Synthesis and characterization of marula nut derived carbon and modified manganese fluorophosphates for electrochemical energy storage applications

By

Bokome Shaku

Student Number: 726829

UNIVERSITY OF THE
WITWATERSRAND,
JOHANNESBURG

Supervisors:

Dr Manoko S. Maubane-Nkadimeng

Prof Neil J. Coville

Prof Kenneth I. Ozoemena

A thesis submitted to the Faculty of Science,

University of the Witwatersrand, Johannesburg,

in fulfilment for the degree of

Doctor of Philosophy in Chemistry

3rd November, 2023.

DECLARATION

I declare that this thesis, which is hereby submitted for a degree of Doctor of Philosophy in the Faculty of Science, School of Chemistry, University of the Witwatersrand, Johannesburg is my own unaided work and has not been submitted for examination at any institution.

UNIVERSITY OF THE
WITWATERSRAND,
JOHANNESBURG

(Signed) Bokome Shaku

On this day of 16th January 2024

DEDICATION

This work is dedicated to my family:

My late loving father (Makate W. Shaku) and my mother (Mokgohloe O. Shaku)

ACKNOWLEDGEMENTS

There are numerous people I would like to thank for contributing to this work. Firstly, I would like to thank the Almighty God for everything in my life. Thank you, dear God, for this good life. I wish to express my warm and sincere thanks to my supervisor, Dr Manoko S. Maubane-Nkadimeng, for giving me huge assistance in designing the research project and equipping me with problem solving skills. Thank you for your endless support, kind and understanding spirit.

I am extremely thankful to my co-supervisors, Prof Neil J. Coville and Prof Kenneth I. Ozoemena, for their valuable guidance and support throughout completing this project.

I extend my gratitude to my mentor, Dr Thapelo Mofokeng for helping me in the laboratory. To the School of Chemistry and also CATMAT, Carbocatalysis and Ozoemena research groups at the University of the Witwatersrand - thanks for the enthusiasm, support and for making the lab a greatest place to be.

I am grateful to the microscopy and microanalysis unit (MMU) for allowing me to make use of their instruments. Many thanks to Dr Rudolph Erasmus for his kind assistance with the Raman spectroscopy analysis. Special thanks to Rhandzu Rikhotso for allowing me to do high resolution transmission electron microscopy (HRTEM) and SEM-EDS analysis through the Council for Scientific and Industrial Research (CSIR) characterization facility.

Special gratitude to the National Research Foundation (NRF) of South Africa, DSI-NRF Centre of Excellence in Strong Materials (CoE-SM) and Post-graduate Merit Award (PMA) for financial assistance. Thanks a lot for settling all my academic fees, stipends, chemicals and conference expenses.

I also acknowledge with a deep sense of reverence, my gratitude towards my parents and members of my family, who gave me endless support. Dear mom and dad, you planted a seed and got to watch it grow. Now your seed is blossoming. Thank you so much for everything.

RESEARCH OUTPUTS

1. B. Shaku, T.P. Mofokeng, N.Coville, K.I. Ozoemena, M.S. Maubane – Nkadimeng. Biomass valorisation of marula nutshell waste into nitrogen-doped activated carbon for use in high performance supercapacitors. Electrochimica Acta 442 (2023) 141828.
2. B. Shaku, T.P. Mofokeng, N.Coville, M.S. Maubane – Nkadimeng, K.I. Ozoemena. Turninng the properties of Mn_2PO_4F by potassium intercalation for asymmetric supercaapcitors (to submit 2023).
3. B. Shaku, T.P. Mofokeng, N.Coville, K.I. Ozoemena, M.S. Maubane – Nkadimeng. Enhanced pseudocapacitance of Li^+/MFP: The effect of alkaline, neutral and ionic electrolyte (to submit 2024).
4. B. Shaku, T.P. Mofokeng, N.Coville, K.I. Ozoemena, M.S. Maubane – Nkadimeng. Hierarchically designed ceria nanorods decorated on sleeping ‘triplite’ material for asymmetric supercaacitors in alkaline and neutral electrolytes (to submit 2024).

CONFERENCES

1. Shaku, B. Coville, N. Ozoemena, K.I and Maubane-Nkadimeng, M., Synthesis and application of activated carbon from Marula husk waste in supercapacitors, Young Chemists Symposium, 8-9th July 2021 (Poster presentation)
2. Shaku, B. Coville, N. Ozoemena, K.I. and M. Maubane-Nkadimeng., Synthesis and application of activated carbon from Marula husk waste in supercapacitors, The 12th Cross Faculty Postgraduate Symposium 2021, 26-30th July 2021 (Poster presentation).
3. Shaku, B. Coville, N. Ozoemena K.I. and Maubane-Nkadimeng. M., Synthesis and application of activated carbon from Marula husk waste in supercapacitors, 72nd Annual Meeting of the International Society of Electrochemistry, 29th August-3rd September 2021 (poster presentation).
4. Shaku, B. Coville, N. Ozoemena, K.I and Maubane-Nkadimeng, M., Synthesis and application of activated carbon from Marula husk waste in supercapacitors, South African nanotechnology Initiative Nano Science Young Researchers (SANI-NYRS), 7-8th October 2021.
5. Shaku, B. Mofokeng, T.P. Coville, N. Ozoemena, K.I and Maubane-Nkadimeng, M., Biomass valorisation of marula nutshell waste into nitrogen doped activated carbon for use in high performance supercapacitors, African Materials Research Society (AMRS), 12-15th December, Dakar, Senegal (Oral presentation)
6. Shaku, B. Mofokeng, T.P. Coville, N. Ozoemena, K.I and Maubane-Nkadimeng, M., Facile preparation of nitrogen -doped activated derived from marula nutshell for supercapacitors, Catalysis Society of South Africa (CATSA) 13-16th November, 2022 (Poster presentation).

AWARDS

1. Awarded the DSI-NRF Centre of Excellence in strong materials, 2020-2023.
2. University of the Witwatersrand, Postgraduate Merit Award (PMA), 2020-2022.

STUDENT SUPERVISION

1. I co-supervised one Honours student at the University of the Witwatersrand, Johannesburg, South Africa.

ABSTRACT

In this thesis, six (6) different electrode materials for supercapacitor applications were created and studied. Electrode materials are one of the most important components in supercapacitors. The increase in energy density requires require electrode materials that have high surface area, conductivity, redox properties. Hence, in this study, the electrochemical characteristics of nitrogen doped activated carbons (N-ACs) material made from marula nuts as a carbon source and melamine as a nitrogen source were studied in both symmetric and asymmetric capacitors. Again, potassium and lithium intercalation in manganese fluorophosphate (MFP) were studied in asymmetric capacitor. Ceria oxide (CeO_2) was used to form a composite with MFP and the electrode material was studied in asymmetric capacitor. All of the synthetic materials' morphology, crystallinity, defects, elemental composition, and structural porosity were examined. Additionally, electrochemical analysis of all materials in different electrolytes were ran to obtain current response, charge and discharge time and charge transfer resistance using two (2) and three (3) electrode systems respectively. Firstly, marula nutshell waste, was used as a source of carbon to form activated carbons (ACs) doped with nitrogen. The high surface area and nitrogen present on the material resulted in energy density that is high (17.2 Wh/kg). Secondly, a novel chemical intercalation synthesis method based on potassium hydroxide-induced hydrothermal process was used to create alkali ion-containing triplite MFP. Research findings in the study indicate that d-spacing increase when intercalating potassium into the triplite structure. An asymmetric supercapacitor was fabricated using potassium intercalated material (K^+/MFP) as a cathode and N-ACs as anode in alkaline and neutral electrolytes. Higher energy density (26.9 Wh/kg) was observed in 1 M KNO_3 than 6 M KOH with 25.2 Wh/kg. Thirdly, assembly of asymmetric supercapacitor of N-ACs and Li^+/MFP was done. The electrode material exhibited energy of 18.8 Wh/kg in 1 M LiFSTI with capacitance retention of 69.5% after 15 000 cycles. N-ACs and MFP-CeO_2 was assembled in 1 M K_2SO_4. The material gave energy of 23.8 Wh/kg with specific power of 525.6 Wh/kg. The MFP-CeO_2//N-ACs had a good cycling stability of 69.8% after 15 000 cycles.

TABLE OF CONTENTS

LIST OF FIGURES

CHAPTER 1:

CHAPTER 2:

CHAPTER 3:

CHAPTER 4:

CHAPTER 5:

CHAPTER 6:

APPENDIX:

LIST OF TABLES

CHAPTER 3:

CHAPTER 4:

CHAPTER 5:

CHAPTER 6:

APPENDIX:

LIST OF SYMBOLS AND ABBREVIATIONS

Ar	Argon
BET	Brunauer-Emmett-Teller
C	Capacitance
CeO_2	Ceria oxide
CVD	Chemical vapour deposition
EDLCs	Electric double layer capacitance
EIS	Electric impedance spectroscopy
E	Energy
F	Farads
G	Gram
GCD	Galvanostatic charge-discharge
h.	Hour
Hz	Hertz
i	Applied current
Kg	Kilogram
KOH	Potassium hydroxide
LiOH	Lithium hydroxide
M	Mass
MFP	Manganese flurophosphate
Min	Minute
N-ACs	Nitrogen doped activated carbons
NMP	N-Methyl-2-pyrrolidone
P_{max}	Maximum power

PVDF	Polyvinylidene fluoride
q^+	Charge on positive electrode
q^-	Charge on negative electrode
Q	Charge
R	Resistance
SEM-EDS	Scanning electron microscope and energy-dispersive spectroscopy
TEM	Transmission electron microscopy
W	Watt
XPS	X-ray photoelectron spectroscopy
XRD	X-ray diffraction

CHAPTER 1

1. Introduction

1.1. Background and motivation

The climate crisis is centred on energy, and energy is essential to finding a solution. While heat and power are generated from usage of fossil fuels, greenhouse gases are also generated from using of fossil fuels [1]. The biggest contributor of climate change comes from coal, gas and oil which generates about 75% emissions while about 90% comes from carbon dioxide [2]. Hence, emissions must be reduced to mitigate contributions of greenhouse gases affecting climate change. To mitigate effects of harmful gases generated by using fossil fuels, we must reduce the use of fossil fuels and start relying on clean, accessible and affordable energy systems. To do this, clean and reliable energy need to be invested in to reduce usage of fossil fuels. However, the ability to supply energy to the population and to simultaneously circumvent environmental issues is a difficult one [3]. A disturbing truth about the supply of energy is also hampered by the fact that there are still billions of people living in the world with a lack of basic energy even as the population increases [4], [5]. The UN Millennium Development Goals (MDGs) are goals to overcome the lack of energy supply [6], [7], [8]. Energy is important to sustain living such as its use in cooking, lighting, transport and information transfer [9]. However, the human population needs to alter the way energy is produced, transported and consumed [10]. The increase in population rate also results in an increase in number of people using cars, this lead to transport emissions to double and lead to environmental pollution since most cars are dependent on fossil fuels [11]. The reliance on energy in the world, as estimated by the World Energy Council, will double by 2050 [12].

Again, South Africa has been relying on coal for generation of about 80 % electricity from ESKOM Company. However, ESKOM has been struggling with debts, mismanagement, failing power plants for the past few years. Due to these, South Africa has been receiving disrupted power supply daily for certain hours. These power cuts affects the living conditions of many people and it slowing economic growth.

Therefore, to avoid uninterrupted supply of energy and also mitigate harmful release of gases when using fossil fuels (coal, gas and oil), the need to develop environment more friendly sources from renewables to produce energy is needed [1].

Renewable energy have abundant sources such as the sun where greenhouse gases are little or not emitted [13], The various sources of renewable energy are shown in Fig 1.1 [13].

Out of the mentioned renewable energy sources indicated in Fig.1, solar and wind energy are the most practical energy sources because they can produce large amounts of energy and can be scaled accordingly [14] . The challenges associated with power storage and transmission are a major barrier to the use of renewable energy, even though it appears to be a growing solution to environmental pollution. In order to integrate renewable technology and ensure the distribution of electricity, grid energy storage is a crucial component.

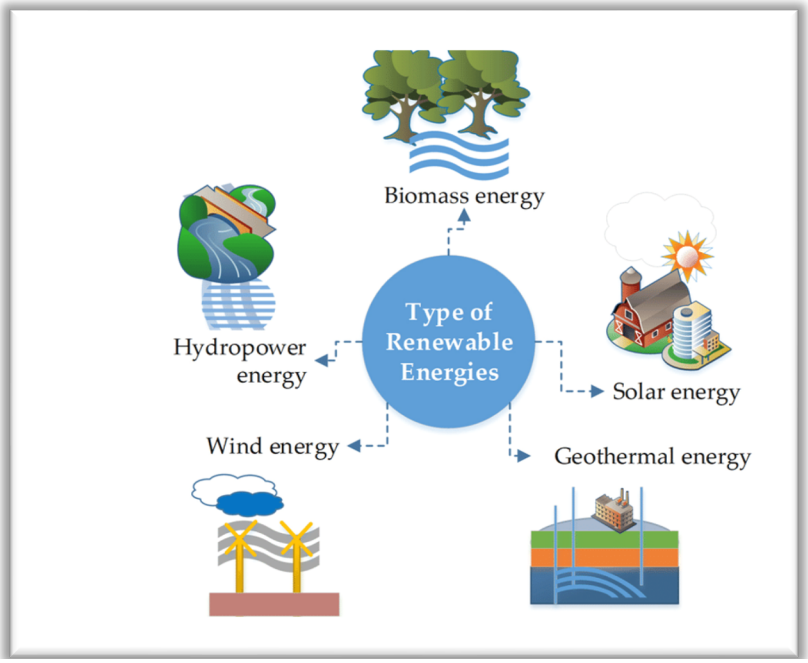

Fig. 1. 1. Image showing different types of renewable energy sources [13].

Traditionally, batteries are used to store energy and provide backup power [15]. Systems for storing energy in batteries rely on secondary batteries, which can be charged and discharged repeatedly without suffering damage [16]. Batteries are electrochemical devices that uses electrical energy conversion into chemical energy to store energy [16]. To create energy, this chemical energy is released once more. There are several significant battery energy storage technologies, some of which are brand-new and some of which are well-established. The lead-acid battery, which is used in automobiles, nickel cadmium batteries, sodium sulfur and lithium ion batteries, are examples of common types [17], [18]. Fast response times for both power absorption and release are a hallmark of battery systems, however, all batteries deteriorate over time and with use. Some gradually lose charge, which restricts their utility for long-term storage. Batteries also suffer from low power density as shown from Ragone plot in Fig. 1.2.

An alternative kind of energy storage system that can be used for high power density applications is supercapacitors (SCs). SCs are known to deliver high power density in a short period of time. Hence, in this study, SCs were explored as energy storage devices. [19].

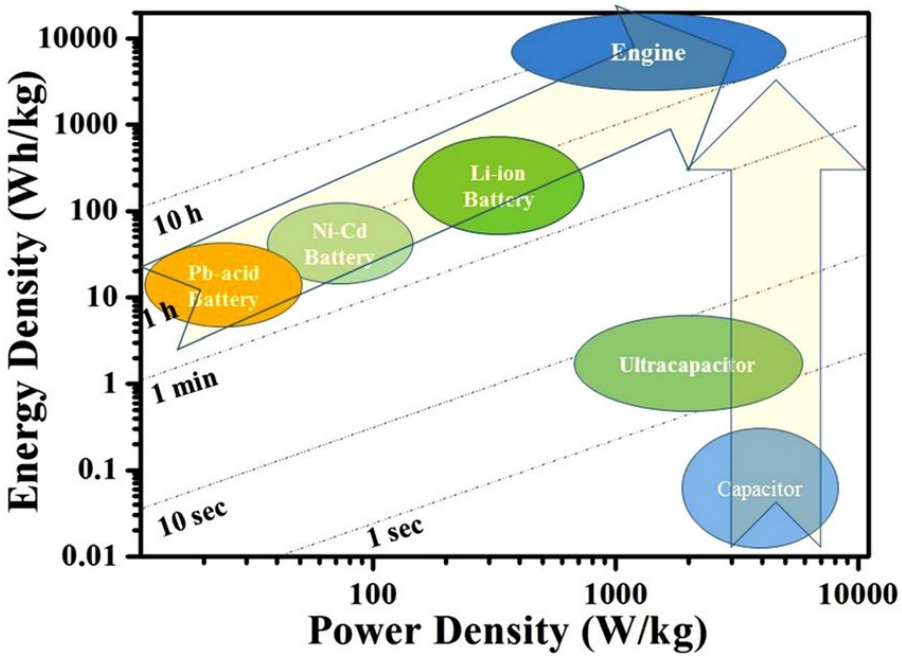

Fig. 1. 2. Ragone plot showing different types of energy storage system [20].

1.2. Supercapacitors as energy storage device

Energy storage has become a main topic in the world due to the massive increase of population.. This also calls for an economical and friendly way to store energy that will be long lasting. Again, the energy need to be outsourced from a variety of materials which are readily available and environmentally friendly at a cheaper cost. Energy storage at a faster charging rate can be overcome by the use of SCs which also offers a longer life cycle [21].

The energy storage in SCs can be improved by lot of factors such as doping to improve the conductivity of the material, using symmetric devices and electrolytes that can operate at wider voltage range [22], [29]. Thus, SCs can not only be applied in suppling backup energy but also as power devices in small appliances such as cell phones, laptops etc. They are also used in transportation such as electric cars. The production of environmentally friendly high energy and high power SCs devices could provide a global path of transportation industry a reality.

Hence, SCs have been studied as an alternative energy storage device as they take shorter periods to charge, can have a long life cycle and have high reliability. SCs are energy storage

devices comprising of two electrodes as cathode and anode, separator immersed in an electrolyte between the electrodes to prevent migration of ions (see Fig 1.3). Electrolyte ions are oriented at the electrolyte/electrolyte interface to build and release electrical double layers (EDLs), which causes electrons movement. SCs consist of three types such as EDLCs, pseudocapacitor and hybrid capacitors. Storage of energy in EDLCs by non faradaic charges (Fig. 1.3), pseudocapacitors by faradaic charges wherelse hybrid capacitors store energy by both faradaic and non-faradaic charges. EDLCs mostly uses are carbon materials because they are cheaper to synthesize, contain surface area that is high and offers stability that is high.

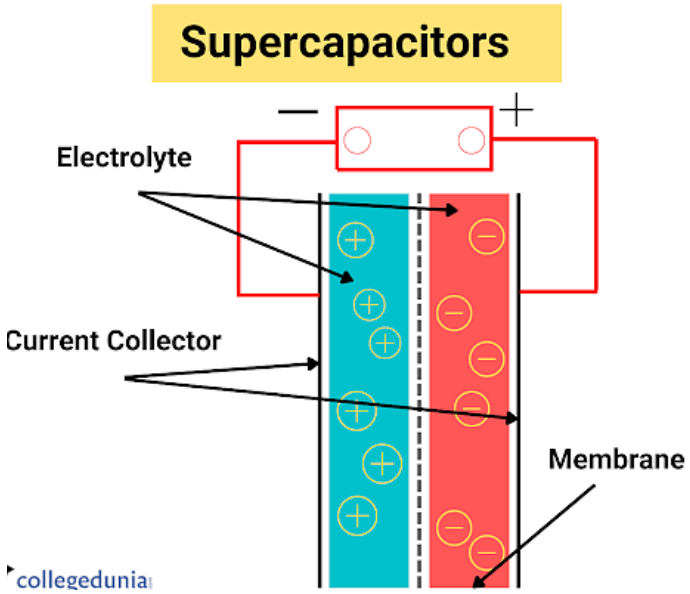

Fig. 1. 3. Diagram of supercapacitor (EDLCs) (copyright permission from M. Winter and R. J. Brodd , 2004). [16].

Activated carbons (ACs) are carbon materials produced at a low cost i.e. biomass and consist of surface area that is high (~2000 m^2/g) and good thermal stability [21], [25]. Their properties are fascinating which makes them suitable for application in SCs [23], [27]. The high surface area facilitates the diffusion of electrolyte ions for storing energy. However, energy storage depends on many factors, such as the availability of micropores and mesopores, ion conductivity, and the type of electrolyte used [28]. Also, the conductivity of ACs has been reported to be low, hence, nitrogen doping can be introduced for further improvement of the conductivity since nitrogen can easily replace carbon as their atomic masses and sizes are similar [29]. Altogether, the process of introducing nitrogen on ACs can improve the energy storage in SCs. Manganese fluorophosphate (MFP) as a pseudocapacitor will be used in the study for energy storage. MFP belongs to the triplite family with a formula Mn_2PO_4F. It has

been reported by Nzimande *et al*.[30] to have an open framework that allow for diffusion of electrolyte ions. Secondly, Mn-based materials are widely recognized as essential components of SCs [31] and battery cathodes [32] etc. because they are massively abundant naturally (especially in South Africa, which has about 80% of the world's manganese reserves) [33]. However, MFP has shown poor electrochemical performance. Hence, in this study, potassium and lithium intercalation will be introduced on MFP because cation doping/intercalation has been reported to stabilize $LiMn_2O_4$ by reducing electrochemically active Mn^{3+}, which is responsible for manganese disproportionate reaction into electrolyte [18]. Again, cation intercalation has been reported to increase volume expansion that can help in more diffusion of electrolyte ions [34].

Due to its non-toxicity to the environment, cerium (Ce) stands out among the lanthanides as the most ideal candidate for coating MFP. CeO_2 is reported as a material to use in SCs due to qualities that have a large band gap of 3.2 eV, strong transparency and outstanding redox properties [35].

1.3. Purpose of the study

1.3.1. Aims of the study

The hypothesis in this study is that the conductivity improves when nitrogen to the carbon electrode is introduced and this will lead to an increase in energy storage. Again, alkali metal intercalation was aimed to improve the d-spacing of MFP and its electrochemical behaviour thus increasing energy storage. Ceria coating was also aimed at improving the redox behaviour of MFP.

1.3.2. Objectives

- ✓ To synthesize activated carbon at different ratios from marula nutshell as a biomass source.
- ✓ To synthesize nitrogen doped activated carbon.
- ✓ To synthesize manganese fluorophosphates (MFP).
- ✓ To intercalate potassium and lithium into MFP.
- ✓ To coat MFP with ceria oxide.
- ✓ The synthesized materials will be characterized using Scanning electron microscopy - energy dispersive spectroscopy (EDS), Brunauer-Emmett-Teller (BET), Thermal

gravimetric analysis (TGA), Raman spectra, X-ray diffraction (XRD) and X-ray photoelectron spectroscopy (XPS).

- ✓ Supercapacitor cell was fabricated using T-type cell and carbon paper coated with the electrode materials.
- ✓ The electrochemical properties of the synthesized materials will be characterized by using cyclic voltammetry (CV), galvanostatic charge-discharge (GCD) and electrochemical impedance spectroscopy (EIS).

Thesis Outline

This work is divided into 7 chapters entailing the aims and objectives of the study, challenges of energy storage and motivation behind the use of activated carbons in the study. Also, the use of supercapacitors is discussed in **Chapter 1**.

Chapter 2 entails the discussion about different types of supercapacitors, their mechanisms of action, and materials used in their construction. It also discusses the synthesis of activated carbons from biomass and different activating agents used to make activated carbons.

The role of nitrogen doping in modifying the electronic properties of SCs is discussed. Finally the use of manganese fluorophosphates (MFP), together with the role of potassium and lithium intercalation and ceria coating of the MFP is discussed.

Chapter 3 discusses the biomass valorisation of marula nutshell waste into nitrogen-doped activated carbon for use in high performance supercapacitors.

Chapter 4 entails the turning of Mn_2PO_4F by potassium intercalation for asymmetric supercapacitors.

Chapter 5 discusses the enhanced pseudocapacitance of Li^+/MFP: The effect of alkaline, neutral and ionic electrolyte.

Chapter 6 discusses hierarchically designed ceria nanorods decorated on a sleeping 'triplite' material for use in asymmetric supercapacitors. In alkaline and neutral electrolytes

Chapter 7: General conclusions and recommendations

References

[1] J. A. Mathews. From Fossil Fuels to Renewable Energy, Greening of Capitalism (2019) 79–113.

[2] J. Macknick. Energy and CO_2 emission data uncertaintier. 2 Carbon management (2011) 189-205.

[3] S. A. Abbasi. RENEWABLE ENERGY SOURCES, Their Impact on Global Warming and Pollution (2011).

[4] OECD. OECD Contribution to the United Nations Commission on Sustainable Development 15: Energy for Sustainable Development; OECD: Paris, France, 2007.

[5] J. Zhang, M. Gu, X. Chen. Supercapacitors for renewable energy applications: A review. Micro and Nano Engineering 21 (2023) 100229.

[6] T. Ma, H.X. Yang, L. Lu. Development of hybrid battery-supercapacitor energy storage for remote area renewable energy systems. Appl. Energy, 153 (2015) 56-62,

[7] A. González, E. Goikolea, J.A. Barrena, R. Mysyk. Review on supercapacitors: technologies and materials. Renew. Sust. Energ. Rev., 58 (2016) 1189-1206.

[8] Y. Guan, J. Yan, K. Hubacek. Burden of the global energy price crisis on households. Nature Energy 8 (2023) 304-316.

[9] A. Muzaffar, M.B. Ahamed, K. Deshmukh, J. Thirumalai. A review on recent advances in hybrid supercapacitors: design, fabrication and applications

Renew. Sust. Energ. Rev., 101 (2019)123-145.

[10] J.L. Espinoza-Acosta, P.I. Torres-Chavez, J.L. Olmedo-Martinez, A. Vega-Rios, S. Flores-Gallardo, E.A. Zaragoza-Contreras. Lignin in storage and renewable energy applications: a review. J. Energy Chem., 27 (2018), pp. 1422-1438.

[11] W. F. Lamb et al., A review of trends and drivers of greenhouse gas emissions by sector from 1990 to 2018. Environmental Research Letters 7 (2021).

[12] C. de Mondial. World Energy Scenarios WORLD ENERGY COUNCIL.

[13] R. Avtar et al., "Remote Sensing and GIS — A Review. Resources 149 (2019) 23.

[14] Y. Tripanagnostopoulos, M. Souliotis, and T. Makris. Combined solar and wind energy systems, AIP Conf Proc (2010) 1025–1030.

[15] D. Chao *et al.* Roadmap for advanced aqueous batteries: From design of materials to applications (2020). [Online]. Available: https://www.science.org

[16] M. Winter and R. J. Brodd. What are batteries, fuel cells, and supercapacitors? Chem Rev 10 (2004) 4245–4269.

[17] Y. Ren, N. Hortance, J. R. McBride, and K. B. Hatzell, "Sodium-Sulfur Batteries Enabled by a Protected Inorganic/Organic Hybrid Solid Electrolyte. ACS Energy Lett 2 (2021) 345–353.

[18] C. G. Han, C. Zhu, G. Saito, and T. Akiyama. Improved electrochemical performance of LiMn2O4 surface-modified by a Mn4+-rich phase for rechargeable lithium-ion batteries. Electrochim Acta (2016) 225–234.

[19] Y. Liang et al. A review of rechargeable batteries for portable electronic devices. InfoMat 1 (2019) 6–32.

[20] R. Zhou et al. Charge Storage by Electrochemical Reaction of Water Bilayers Absorbed on MoS_2 Monolayers. Sci Rep 1 (2019).

[21] H. Peng, G. Ma, K. Sun, Z. Zhang, Q. Yang, and Z. Lei. Nitrogen-doped interconnected carbon nanosheets from pomelo mesocarps for high performance supercapacitors. Electrochim Acta 190 (2016) 862–871.

[22] B. Li et al. Nitrogen-doped activated carbon for a high energy hybrid supercapacitor. Energy Environ Sci 1 (2016) 102–106.

[23] B. Pal, S. Yang, S. Ramesh, V. Thangadurai, and R. Jose. Electrolyte selection for supercapacitive devices: A critical review. Nanoscale Adv. 10 (2019) 3807–3835.

[24] A. S. Alzaydien. Physical, chemical and adsorptive characteristics of local oak sawdust based activated carbons. Asian J Sci Res 2 (2016) 45–56.

[25] A. Chafidz, W. Astuti, D. Hartanto, A. S. Mutia, and P. R. Sari. Preparation of activated carbon from banana peel waste for reducing air pollutant from motorcycle muffler," in MATEC Web of Conferences, EDP Sciences, Feb. 2018.

[26] L. Chen, T. Ji, L. Mu, and J. Zhu. Cotton fabric derived hierarchically porous carbon and nitrogen doping for sustainable capacitor electrode. Carbon 111 (2017) 839–848.

[27] H. Gou, J. He, G. Zhao, L. Zhang, C. Yang, and H. Rao. Porous nitrogen-doped carbon networks derived from orange peel for high-performance supercapacitors. Ionics (Kiel) 9 (2019) 4371–4380.

[28] W. Han et al. Superior nitrogen-doped activated carbon materials for water cleaning and energy storing prepared from renewable leather wastes. Environ Int. 142 (2020).

[29] S. Ahmed, M. Rafat, and A. Ahmed. Nitrogen doped activated carbon derived from orange peel for supercapacitor application. Advances in Natural Sciences: Nanoscience and Nanotechnology 3 (2018).

[30] N. Nzimande, A. Haruna, P. Mwonga, B. Rasche, F. Cummings, and K. I. Ozoemena. Ceria-Spiderweb Nanosheets Unlock the Energy-Storage Properties in the 'Sleeping' Triplite ($Mn_2(PO_4)F$). 4 ACS Appl. Energy. Mater. (2021) 13085-13097.

[31] K. Makgopa et al. A high-rate aqueous symmetric pseudocapacitor based on highly graphitized onion-like carbon/birnessite-type manganese oxide nanohybrids. J Mater Chem A Mater 7 (2015) 3480–3490.

[32] C. J. Jafta, K. Raju, M. K. Mathe, N. Manyala, and K. I. Ozoemena. Microwave Irradiation Controls the Manganese Oxidation States of Nanostructured ($Li[Li_{0.2}Mn_{0.52}Ni_{0.13}Co_{0.13}Al_{0.02}]O_2$) Layered Cathode Materials for High-Performance Lithium Ion Batteries. J Electrochem Soc. 4 (2015) A768–A773.

[33] P. Christmanna. A forward look into rare earth supply and demand: A role for sedimentary phosphate deposits in Procedia Engineering, Elsevier Ltd (2014) 19–26.

[34] N. Recham *et al.* Preparation and characterization of a stable $FeSO_4F$-based framework for alkali ion insertion electrodes. Chemistry of Materials 22 (2012) 4363–4370.

[35] R. Kumar, A. Agrawal, R. K. Nagarale, and A. Sharma. High Performance Supercapacitors from Novel Metal-Doped Ceria-Decorated Aminated Graphene. Journal of Physical Chemistry 6 (2016) 3107–3116

CHAPTER 2: Literature review

2. Introduction: The need for energy storage

The global energy demand increases daily due to the increase in population rate. Households survive on food, water and energy for sustainable growth. Without these, most people in the world would plunge [1]. Historically, the supply of energy has commuted slowly, for example, the use of wood as energy fuel has decreased immensely to coal, oil, gas and shifted now to renewables such as biomass [2]. Electricity generation has been made from natural sources such as the sun. The sustainability to obtain clean energy is still a challenge the world is facing, despite the numerous availability of energy sources in the world [3]. Our increase in reliance on energy has prompted a lot of research on supercapacitors (SCs) as energy storage devices [4], [5]. Energy storage such as SCs have high power density that is delivered in a very short period of time, longer life cycle and good cycling performance [6], [7]. However, the downside use of SCs is the lower energy storage, due to low per cell voltage [8]. As such, a lot of attention has been given on the development of electrode materials for improvement of energy storage [9]. Carbon materials are favourable for use in electric double layer capacitors (EDLCs) because they are cheaper, have different shapes that can be altered by activating, functionalization and doping using heteroatoms such as nitrogen, boron and sulphur to improve the surface area and surface chemistry of the material [9–12]. Different kinds of carbon materials have been used in EDCLs, i.e. activated carbons (ACs) [13], [14], graphene [15] and carbon nanotubes (CNTs) [16]. In this study, ACs has been chosen as an electrode material for use in EDLCs over other carbon materials due to its eco-friendly nature and cheaper cost [17], [18]. High surface (>2000 m^2/g) can be achieved in ACs by activating using different activating agents such as $ZnCl_2$, H_3PO_4, KOH etc [19], [20].

On the other hand, alkali intercalation in manganese-based materials have been used as pseudocapacitive materials due to increase of volume expansion to accumulate large number of electrolytes ions [21]. Furthermore, ceria oxide has also been reported to give outstanding redox behaviour when used as a coating material [22]. This chapter will give an overview on electrode materials and different types of SCs. Detailed discussion on the type of biomass material and its activating agents to produce ACs is also provided.

In addition, manganese based material (Mn_2PO_4F), effect of alkali intercalation and CeO_2 will also be discussed. In this chapter, the key parts and latest improvement of SCs and electrode materials used including different types of electrolytes will be discussed briefly.

2.1.Electrochemical capacitors

Electrochemical capacitors, (ECCs), sometimes known as supercapacitors or ultracapacitors are devices that stores energy with a far larger capacitance and energy density than the conventional dielectric capacitor [23]. Compared to batteries, electrochemical capacitors have a significantly lower energy density and a much larger power capacity. As a result, depending on the application, ECCs can compete with both regular capacitors and batteries. ECCs may generally be a substitute for batteries when the quantity of energy to be stored is too little for a battery and the system's peak power need is greater than its average power consumption [24].

2.1.1. Capacitors vs. supercapacitors

A capacitor is an electrochemical device that supply more power density than SCs via electric field but have less energy [25]. The structure of a capacitor involves two plates which are parallel to each other as shown in Fig. 2.1. Between the two plates, there is a dielectric layer that prevents migration of ions [26]. The charging of the capacitors occurs by first applying voltage across the plates, upon that, positive and negative charges migrate towards the electrode surface of opposite charges.

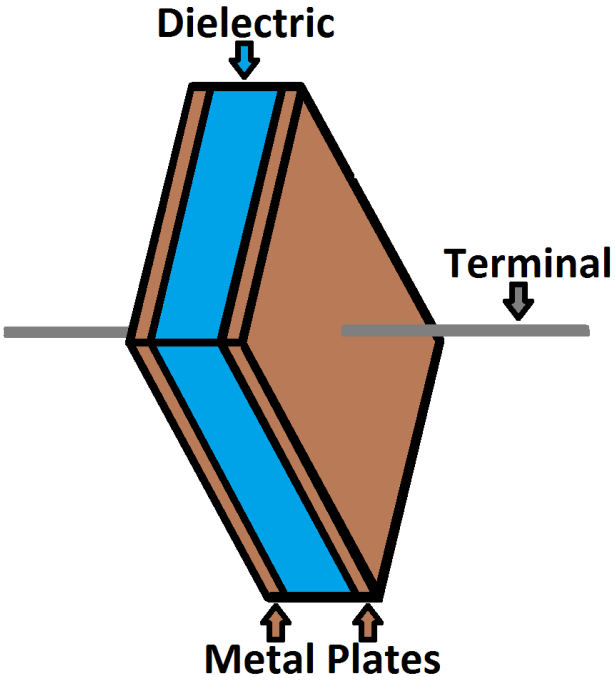

Fig. 2. 1. Illustration of a capacitor [27].

The flow of current then occurs when the system is charged and voltage is applied, which create capacitance [26]. Hence, capacitance (C) in Farads (F) is measured as electric charges flows between two plates where potential (V) is applied. Equation 2.1 is used to measure capacitance in electric capacitors [26]:

$$C = \frac{Q}{V} \qquad \text{eqn 2.1}$$

Capacitance is directly proportional to both area of the electrode and the permittivity of free space when plates are parallel in electric capacitors. However, it is indirectly proportional to the distance between the plates. This can be expressed in equation 2.2 [26].

$$C = \varepsilon_o \varepsilon_r \frac{A}{D} \qquad \text{eqn 2.2}$$

Where the surface area of the electrodes are represented by A (m^2/g), C is the capacitance in farad, permittivity of free space is given as $8.9x10^{-1}$ F/m).

Two essential parameters in capacitors are energy and power density. Energy density is related to the capacitance obtained at a given potential, which can be expressed in equation 2.3 [28].

$$E = \frac{1}{2} CV^2 \qquad \text{eqn 2.3}$$

This explains that an increase in capacitance will lead to an increase in energy density.
Power density is related to the voltage drop (ESR), which can also be expressed in as [29]:

$$P_{max} = \frac{V^2}{4 \times ESR} \quad \text{eqn 2.4}$$

Equation 2.4 shows that a lower ESR will results in higher power density.

SCs are energy storage devices that relies on charging and discharging of electric charges between the electrodes surface of high surface area [30]. The principle of energy storage of capacitors and SCs are similar [31]. However, SCs make use of porous materials with high specific surface areas and dielectrics which are thinner leading to an electric double layer [32]. This leads to a higher capacitance and energy density which is 10,000 greater than of capacitors. This offers a great potential of using SCs commercially.

The difference between capacitors and SCs lie on the type of materials used and the dielectric between the electrodes. SCs make use of electrode that have a higher surface area.

2.1.2. Supercapacitors vs batteries

The difference between SCs and batteries lie in the mechanism of energy storage and the amount of energy and power density both deliver. SCs stores energy via electrostatic charges between the electrodes (non-faradaic) whereas batteries stores energy via chemical reactions (faradaic reactions) at the electrodes [33]. Batteries have higher energy but lower power density than SCs. This is because reactions (non-faradaic reactions) occurring at the electrode surface in batteries are slower, whereas in SCs, the reaction process that leads to double layer is faster [34]. The high amount of energy in batteries and the small weight makes it useful in industries. However, problems associated with the use of a battery is life cycle, shelf life and power density. Hence, there is a need for energy storage devices that can deliver energy in a short period of time [35].

SCs are deemed as promising energy storage devices due to faster charging process in seconds that lead to high power density. Other advantages of using SCs are long life cycle and wider operating voltage [35]. Energy and power are two parameters that are important in electrochemical energy devices. Ragone plot is used to distinguish energy and power density of different types of energy storage systems in a logarithm scale (Fig. 2.2) [36].

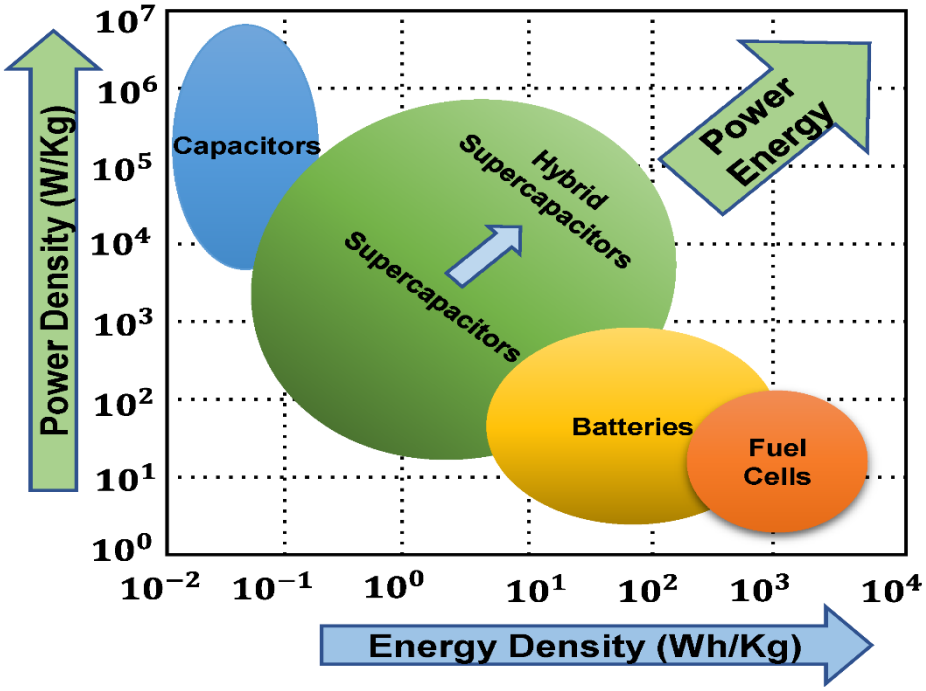

Fig. 2. 2. Ragone plot of different types of electrochemical energy storage devices [36].

As per the Ragone plot, assuming an electric vehicle has gadget with high energy storage (i.e. batteries), the battery makes the vehicle to travel longer distance before getting charged. Whereas, if the vehicle has a SCs device, the acceleration of the vehicle will be faster due to high power density of the device. This means that batteries can last for a day without charging whereas SCs needs charging constantly [37]. However, the volume changes that happens in a battery are due to redox reactions limiting the life cycle thus causing a reduction of power density. Thus, SCs can be used due to the fast charging rate is seconds that lead to high power delivery and energy storage that is lifelong [38].

2.1.3. Working standards and evaluation of different kinds of supercapacitors

Three main categories in capacitors are electrolytic capacitors, non-electrolytic capacitors and supercapacitors [36]. This can be further split into electric double layer capacitor (EDLCs), pseudocapacitors and hybrid capacitors (Figure 2.1).

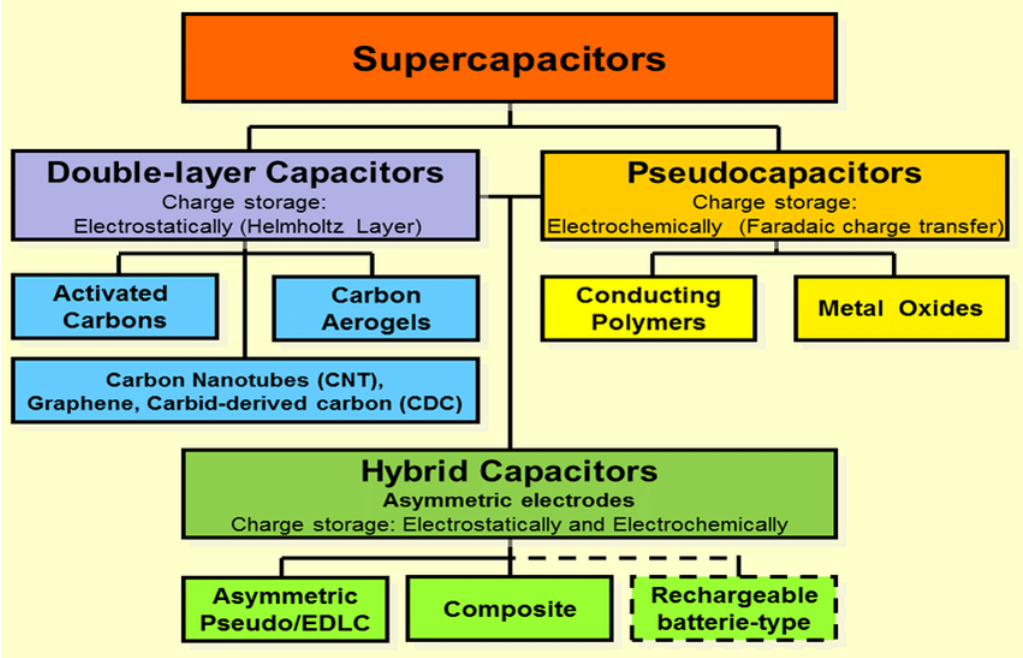

Fig. 2. 3. Classification of different types of supercapacitors [39].

These categories are differentiated by the specific type of materials used. The energy storage in capacitors is through an electrostatic charge between two conducting metal plates. The energy storage is led by the movement of opposite charged electrolyte ions through the opposite charged metal plates. Conventional capacitors are known to store little energy as compared to electric double layer capacitors due to the plate area being limited. The higher amount of energy obtained in EDLCs arises from the larger area and the separation distance between the plates [30].

The energy storage components in SCs are electrodes, current collectors, electrolyte and separator.

2.1.4. Types of supercapacitors

There are three types of supercapacitors namely electric double layer capacitors (EDLCs), pseudocapacitors and hybrid capacitors [39].

2.1.4.1.Electric double layer capacitors (EDLCs)

EDLCs stores charge by non-faradaic charges [30]. The illustration of EDLCs is shown in Fig. 2.4 comprising of porous electrode material separated by a separator submerged in an electrolyte [40]. Between the electrodes, voltage is applied and this led to charges being stored by electrostatic interactions. Electrode materials of choice in EDLCs must be porous in nature

to accumulate charges. The advantage of using EDLCs is high power densities, fast charging in seconds and good cyclic stability [41].

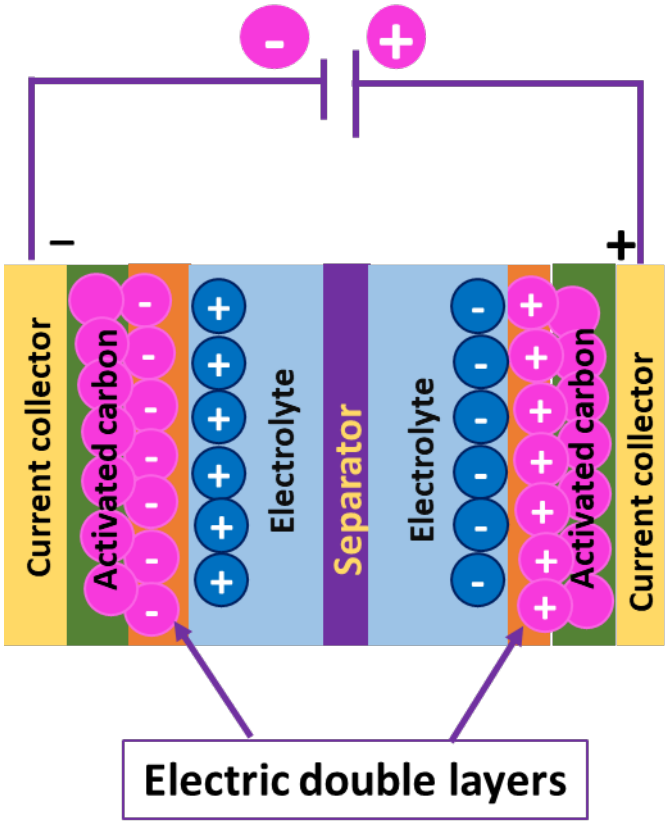

Fig. 2. 4. Schematic illustration of EDLCs [40].

The following equations are used to explain energy storage by ion adsorption on electrode materials:

Positive electrode:

Charging process: $E_{s1} + A^- \longrightarrow E_{s1}^+//A^- + e^-$ eqn 2.5

Discharging process: $E_{s1}^+//A^- + e^- \longrightarrow E_{s1} + A^-$ eqn 2.6

On the negative electrode:

Charging process: $E_{s2} + C^+ \longrightarrow E_{s2}^+//C^+$ eqn 2.7

Discharging process: $E_{s2}^+//C^+ \longrightarrow E_{s2} + C^+ + e^-$ eqn 2.8

Reactions occurring at the cathode and anode electrode are summarized as follows::

Charging process: $E_{s1} + E_{s2} + A^- + C^+ \longrightarrow E_{s1}//A^- + E_{s2}//C^+$ eqn 2.9

Discharging process: $E_{s1}//A^- + E_{s2}//C^+ \longrightarrow E_{s1} + E_{s2} + A^- + C^+$ eqn 2.10

Where Es_1 and E_{S2} represents the first and second electrode surface. The anion electrolyte is A^- and C^+ is the cation. Electrolyte ions interacts with the electrode surface and this process is represented by the sign //. Upon charging the system via the external load, electrons make a way from the negative terminal to positive terminal. The interface between electrode and electrolyte (//) lead to formation of a double layer where there is migration of cations (C^+) towards negative electrode (Es_2) and anions (A^-) towards the positive electrode (E_{s1}). Upon discharging the system, the reverse process occurs. Transfer of charges does not occur between the electrode and electrolyte in this type of process. It is also reported that during the processes occurring in EDLCs, the electrolyte concentration stays constant.

2.1.4.2.Pseudocapacitors

Pseudocapacitors stores energy by reversible faradic reactions or by ion intercalation at the electrode surface [42]. Redox mechanism can occur in materials such as metal oxides and the intercalation process can be due to the insertion of Li^+ into host materials (Fig. 2.5). Although the intercalation process is mainly surface controlled rather than diffusion controlled such as in batteries. The high capacitance in pseudocapacitance is advantageous for an increase in energy storage. However, the disadvantage of pseudocapacitors is the low capacitance retention as compared to EDLCs [43]. The illustration of pseudocapacitors is shown in Fig. 2.5.

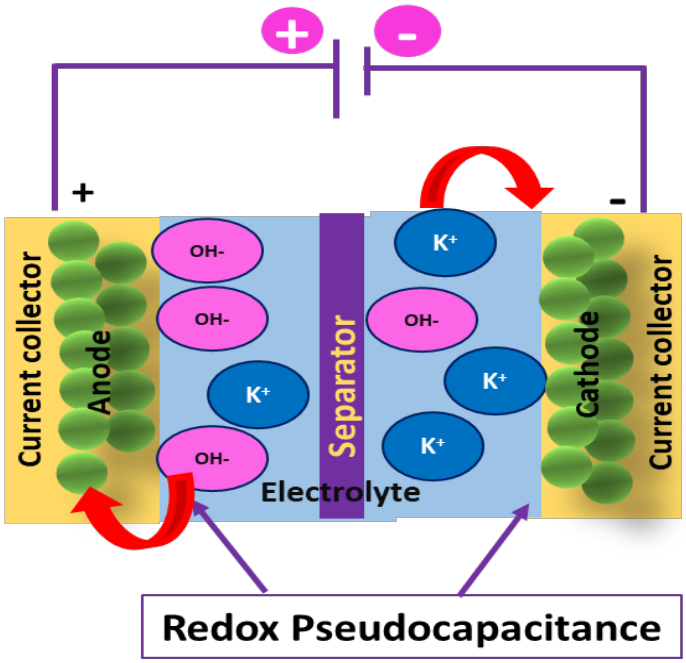

Fig. 2. 5. Schematic illustration of pseudocapacitors [40].

The mechanism of transportation of electrolytes ions to the electrode materials follows a three-step process such as (a) Underpotential mechanism, (b) Redox mechanism and (c) Intercalation of ions [44].

(a) Underpotential process follow a process of adsorption of metal ions above redox potential on the surface of electrode material (see Fig. 2.6a, i.e. adsorption of lead ions (Pb^{2+}) onto Gold (Au)).

(b) Redox mechanism occurs when there is adsorption of ions on the surface by Faradic charges (see Fig. 2.6b),

(c) Intercalation process occurs when electrolyte ions intercalate through the host material without change in the phase structure (see Fig. 2.6c).

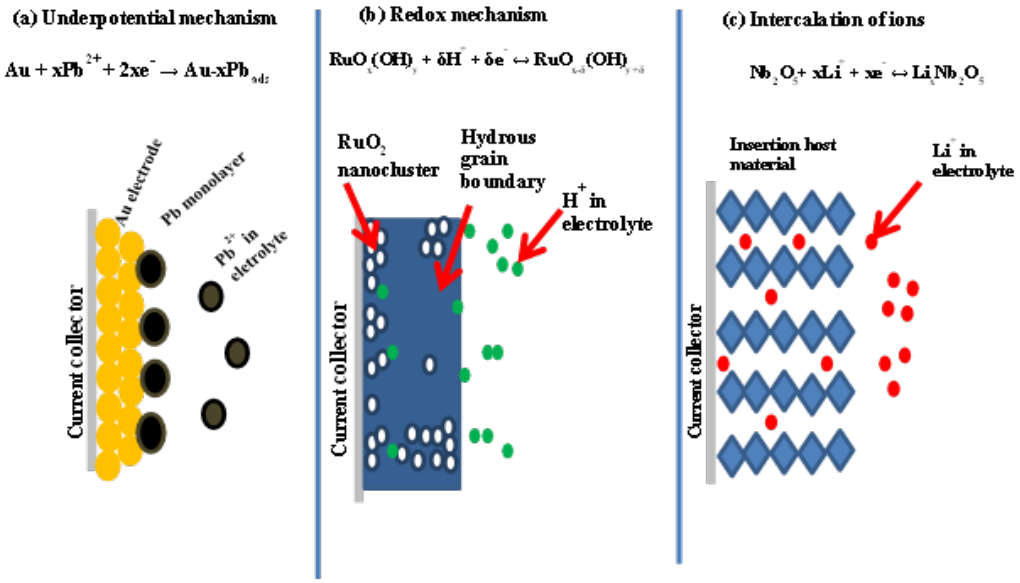

Fig. 2. 6. Three mechanisms in pseudocapacitors [44].

The intercalation process of layered materials (Fig. 2.6c) is driven by redox reactions together with other variations. The other variations that occur in layered materials are pseudodcapacitive mechanism and diffusive intercalation. The two mechanism in layered materials occur at different kinetic regimes. The mechanism of diffusive intercalation in bulk layered materials correspond to battery like behaviour mechanism with phase transition. The redox reaction occur inside the bulk electrode material during phase transition that occur when the interlayer spaces are filled with carrier ions.

However, pseudocapacitive charge storage becomes dominant when redox reactions do not occur inside the bulk electrode material but rather near the surface or interlayer plane. Hence, the charge storage will be dominated by surface controlled mechanism than diffusion controlled. Some of the layered electrode materials reported in literature have pseudocapacitive behaviour due to the nanoscaling of the materials [45]. The nanoscaling of the electrode materials shifts the charge storage from diffusion controlled (battery-like) to surface controlled (capacitor-like) mechanism.

2.1.4.3.Hybrid capacitors

Hybrid capacitors store energy in two ways via faradaic and non-faradaic charges (Fig. 2.7) [46]. The anode materials serves as a capacitive power source such as activated carbons material and the cathode is a battery like material that serves as energy source. Asymmetric SCs uses EDCLs as anode materials and pseudocapacitors as cathode materials. Separator

soaked in electrolyte prevents conduct between the two electrodes. During the charging, discharge process, K^+ ions migrate and intercalate through the cathode as shown in Fig. 2.7. Meanwhile, OH^- are adsorbed on the non-faradaic material.

The energy density obtained in hybrid capacitors is high because of using two different materials with different surface area, conductivity which circumvent each other. Hence, industries are opting for hybrid capacitors because they provide higher energy densities, high stability and longer life cycle.

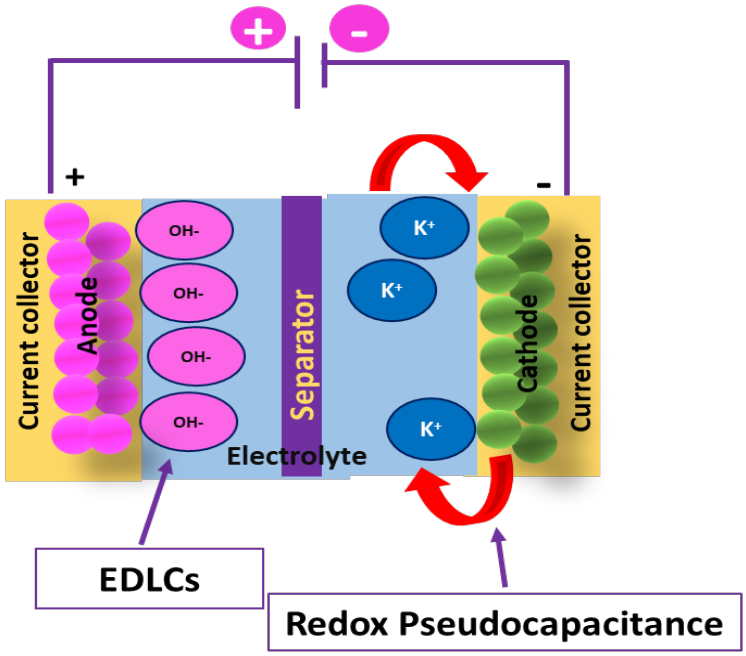

Fig. 2. 7. Schematic illustration of hybrid capacitor [40].

2.2.Energy storage components:

- Electrode: Material of interest where charge storage occur. The material can store charge through different processes such as electric double layer capacitance or via faradaic process [47]. Different materials can be used such as activated carbon, carbon nano-tube, polymers and metal oxides.
- Current collectors: It is used to improve the material's conductivity l by rolling it to a metal sheet. The current collectors consist of non-corrosive metals that are inert [48]. For instance, the use of aluminium collectors in organic electrolytes doesn't lead to corrosion but can corrode when used in aqueous electrolytes. Subsequently similar as ships in the sea, stainless steel in aqueous electrolytes is often used.

- Electrolyte: This is a solution prepared at a desired concentration and it contains different kinds of ions that differ in conductivity and sizes. Separators are immersed inside the electrolyte and used between electrodes materials to form a double layer of faradaic reactions [35]. Electrolyte can be classified in three different ways such as aqueous, organic and ionic electrolytes [49]. The mentioned electrolytes differ in terms of ionic sizes, conductivity and operating voltage [49]. For example, energy storage in terms of aqueous electrolytes (i.e. KOH) is less because of the low operating voltage (~1.2 V) due to water decomposition happening at 1.2 V [50]. However, the stability window in acidic electrolytes (i.e. H_2SO_4) can be improved to 1.6 V to increase the amount of energy storage. However, the use of acid media has its own advantages such as corrosion [40]. Luckily, the corrosion faced with the use of acid media can be mitigated by using neutral electrolytes such as KNO_3, Na_2SO_4, Li_2SO_4 [51]. The use of neutral electrolytes can be deemed as a way of achieving higher energy storage because of the wider operating voltage (~2 V) due to the low oxygen and water decomposition [51]. Again, organic and ionic liquids are used due to the wider voltage range of up to 3 V [52]. Choosing an electrolyte depend on two parameters: conductivity which affect equivalent solution resistance (ESR) and stability window which is used to determine the stability of the voltage window [40].

  Energy density in SCs is directly proportional to the operating voltage. Hence, for an increase in energy density, the electrolyte needs to have both high conductivity and wider operating voltage. However, there are still other parameters that affects the diffusion of electrolytes which affects capacitance such as the sizes of electrolyte ions, the interaction between electrode material and electrolyte, molar concentration of the electrolyte [52]. Electrolyte also determines the internal resistance in SCs, cycle life and toxicity [48]. However, to date, there is no single electrolyte that have all the characteristics for use in SCs. Properties of different electrolyte are discussed below.

2.2.1. Aqueous electrolytes

Aqueous electrolytes are less likely to be used in the industries due to the less amount of energy density delivered in SCs. However, they are mostly explored in SCs because of their high conductivity higher than organic and ionic electrolytes and easy fabrication [53]. There are three types of aqueous electrolytes such as acid, alkaline and neutral solutions. Electrolyte such as H_2SO_4 is mostly used due to higher conductivity of 0.8 S/cm at room temperature [54]. The higher conductivity lead to lower solution resistance thus delivering high power density. The

reported amount of capacitance when using H_2SO_4 electrolyte in activated carbons as electrode materials is around 100-300 F/g [55]. Alkaline electrolytes such as KOH are also studied in research due to their higher conductivity of 0.6 S/cm. Capacitance obtained in activated carbons using alkaline electrolytes is similar to that of acidic electrolytes [55].

To obtain higher energy density, neutral electrolytes such as Li_2SO_4, Na_2SO_4 and K_2NO_3, are often studied due to their wider working potential (1.5-2.0 V) [56–58]. This wider operating voltage obtained in neutral electrolytes is due to lower concentration OH^- and H^+ [57]. Other advantages of using alkaline electrolytes is less corrosion and cost effectiveness. Again, smaller ion sizes in the electrolytes makes it easier for intercalation/de-intercalation onto the electrode material [57].

2.2.2. Organic electrolytes

Organic electrolytes are applied commercially due to the wider operating voltage of 2.5 to 2.8 V leading to a higher energy density as compared to aqueous electrolytes [59]. However, there are a lot of factors to consider when using organic electrolytes because they are quite expensive to use, lower conductivity leading to lower capacitance. Organic electrolytes are also flammable and have high volatility [60]. The ionic sizes of organic electrolytes are relatively large which is the reason for lower capacitance. To enhance the ionic conductivity of the electrolyte, the organic electrolytes are prepared by dissolving the conducting salts in organic solutions.

Preparation of an organic electrolyte can be done by dissolving tetraethylammonium tetrafluoroborate ($TEABF_4$) in acetonitrile (AC) or propylene carbonate (PC) [61]. Sevilla et al. [62] reported a capacitance of 250 F/g at 1 mV/s using this electrolyte at 2.7 V with energy and power density of 30 $Whkg^{-1}$ and 13 kWkg. The higher energy and power density in organic electrolytes are due to the wider voltage. There are also a lot of factors that organic electrolytes are dependent on such as the cations and anions present in the salts, solvents and some bit of water present as part of impurities [63]. A report by Pericconе *et al.* [64] showed that the voltage window can be enhanced to 3.5 V above the normal range (2.5 to 2.8 V).

2.2.3. Ionic liquids

Ionic liquids (ILs) are cations and anions salts in nature that have a low melting point below 100 ℃. This low melting temperature is due to the weak interactions that exists between the cations and anions [65]. The advantages of using ILs in SCs is their wider voltage which leads

to high energy densities. Other properties of ionic liquids are zero or neglible volatility, low melting point, moderate viscosity and they are flammable [66], [67]. There are three different kinds of ILs such as aprotic which are mostly used in lithium ion batteries and SCs, protic in fuel cells and Zwitterion in electrochemical applications [68].

2.3. Electrode materials for supercapacitors

The development of innovative materials that can satisfy the required energy demand is of utmost relevance because of the vital function that active electrode materials play in SCs. One of the most crucial factors for enhancing storage of charge in electrode materials is a combination of surface area that is large and conductivity that is high [69]. However, pore size distribution and structural flaws that are incidental to the large surface area also affect the charge storage capabilities. For instance, surface area promotes the creation of an electrical double layer, whereas a uniform pore size distribution controls the pathway for electrolyte ions in the electrode material's inner core [70]. The behaviour of an electrode material may therefore be explained using the electrochemically active surface area. The most popular electrode materials in SCs are generally carbon, polymers, and transition metal based materials. ACs are used mostly in EDLCs due to large surface area and conductivity. Transition metal oxides are used as pseudocapacitor electrode material due to their redox behaviour [71]. Due to their theoretical capacitance that is high, plentiful supplies, and inexpensive cost, metal oxides, have received a lot of attention [72,73].

Valence state changes can result in phase transformation of a material and its ion diffusion rate which are significant for electrochemical properties because the energy storage mechanisms of transition metal oxide-based electrodes primarily involve the electron transfer in the process of redox reactions and valence state changes of transition metal ions [74]. Such a transition often causes a slow bulk phase reaction and significant volumetric expansion and contraction during the energy storage process, which in turn causes the electrode materials based SCs to have poor cycle stabilities and slow chemical reaction kinetics [74]. Hence, intercalation of alkali metal can be used to increase the volume expansion and improve the stability of transition metals [71]. Again, earth oxides such as CeO_2 can be used to improve the redox behaviour of transition metals [75].

2.3.1. Activated carbon

Materials used in SCs are usually carbon materials and activated carbons (ACs) has shown to be a promising electrode material due to its enormous porous structure [76], [77]. ACs has

other desirable characteristics such as high surface area, high stability and high adsorption capacity [78], [79]. The good characteristics of ACs make it a suitable material for use in different applications. Hence, a lot of focus has been done on ACs since the 20th century due to the expansion in population rate in order to manage environmental pollution. The raw materials used in producing ACs are mostly lignocellulosic materials since they are agricultural wastes that are deemed to be cheaper, available in large quantities and likely to possess a higher content of carbon [8].

Back in the olden days (1500 B.C), charcoal was one of the interesting carbon material and has been used potently in medicinal application [80]. Its power to adsorb gases on the surface has been discovered by Scheele *et al.* in 1773 [80]. ACs as an adsorbent was first reported by Lowitz *et al.* in liquid phase for decolourization process [81]. The First World War in 1914-1918 acquainted harmful gases which drove with breath issues in the military. For this, ACs was then produced from coconut shells [80]. ACs are produced via two steps namely, carbonization and activation [82]. The activation is performed by methods of either physical or chemical or by applying both physical and chemical methods together. Physical activation involves gases like steam or CO_2 as activators from temperatures ranging from 800-1000 ℃ [81]. There are a lot of properties in the material that steam activation affects such as the surface area and oxygen content of the biomass. Properties of ACs produced by physical activation are laboured by several factors such as the type of biomass used, activation time, and activation temperature [83]. ACs produced from physical methods are desirable because the method is easy and cheap [84]. However, the detrimental use of this physical activation method is the low yields of ACs produced which can be an issue in producing large yields of the material in industries [85]. The reasons behind low yields lie in the carbonization and activation processes. The yield is affected by activation temperature and time. This can be explained due to exiting of more volatile compounds from the system at higher carbonization temperature wherein prolonged activation time burns more carbon away because of the presence of more oxygen atoms during steaming which both leads to lower yields of ACs [85]. Longer time of steam exposure to the biomass leads to more burn off of organic compounds leading to lower yield but higher surface areas and pore volume [86].

ACs can also be produced by chemical activation method. Carbon can be activated by chemical agents such as $ZnCl_2$, H_3PO_4, NaOH and KOH [19], [20], [87], [88]. During chemical activation, the biomass is impregnated with the activating agent and dried in an oven. The dried mixture is then transferred to a furnace for carbonization at temperature of 500 to 800 ℃ for 1

to 4 h under flow or argon/nitrogen gas [86]. The reaction between carbon and alkaline activating agents (NaOH and KOH) can be ascribed by the following equations [89]:

$$6NaOH + 2C \leftrightarrow 2Na + 3H_2 + 2Na_2CO_3 \quad \text{eqn (2.11)}$$

$$6KOH + 2C \leftrightarrow 2K + 3H_2 + 2Na_2CO_3 \quad \text{eqn (2.12)}$$

Pores are created when K from KOH intercalates through the material at higher temperatures (> 700℃) which is later removed by acid wash and water [90].

Chemical activation is more convenient to use because the steps are one process. Again, the activation temperature used are low yielding high carbon content than physical activation [91]. However, the method of chemical activation also presents disadvantages because some of the activating agents are not environmentally and can be corrosive to the equipment used in during production of ACs [92]. Again, chemical activation method can be performed by two step process where carbonization of the biomass is done first, followed by activation of the carbon unlike processes that involve one step where reaction of carbonization and activation are done in the same reactor [93], [94]. Properties of ACs produced from chemical activation are high carbon content, high surface area and high level of porosity (see Fig. 2.9) [95].

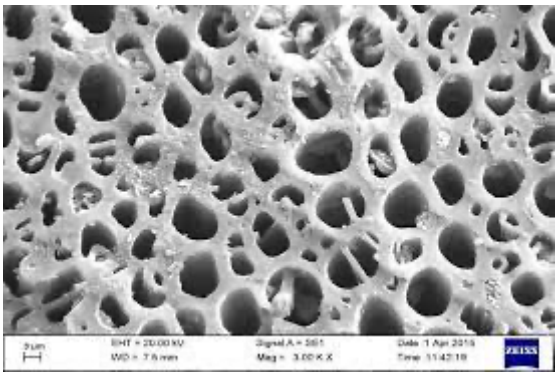

Fig. 2. 8. Image of ACs from green coconut shell [91].

The porosity of the obtained ACs differ with sizes ranging from micropores (< 2 nm), mesopores (2-50 nm) and macropores (> 50 nm) [95]. The types of pores depend on the activating agent used. For example, $ZnCl_2$ is known to create wide micropores and low mesopores wherelse H_3PO_4 creates mesopores that are large and even macropores [96]. Lastly, it has been reported that KOH is known for producing high percentages of micropores to more heterogeneous micropores [95]. Mariet *et al.* [97] reported on the use of lignocellulosic material for making ACs using H_3PO_4 at a temperature above 350 ℃ and their work demonstrated creation of pores example. Again, high surface area ACs from H_3PO_4 activation on kraft black

liquors has been reported by Gonzalez-Serrano *et al.* [98]. The produced ACs was similar to the commercial ones. Comparative study on ACs produced by H_3PO_4 and $ZnCl_2$ activation has been reported using Hura Crepitans Linn seed shells [99]. Their study demonstrated the difference in carbon yield where ACs by $ZnCl_2$ had a lower percentage yield of 31.94% and H_3PO_4 producing a higher percentage yield of 44.90% [99]. However, another claim studied showed that KOH and NaOH can produce a high surface area ACs of more than 1000 m^2/g [100]. This has been followed by a recent study on ACs from rice husk using KOH giving about 2342 m^2/g while the surface area of 885 m^2/g was obtained when activating with NaOH [101]. The reason behind this is that the metallic K from KOH is faster as compared to the metallic Na from NaOH due to its higher boiling point [102].

Carbonization is usually done after impregnation. Carbonization is defined as the removal of non-carbon species through thermal decomposition [103]. During the process of carbonization, charcoal is formed by reducing the volatile content resulting in an increase in carbon percentage. Again, deposition of tars is formed when lignocellulosic matter is decomposed removing non-carbon atoms such as oxygen, nitrogen and hydrogen. This occurs wherein light molecules are decomposed first followed by light aromatics resulting in pore formation. The structure of ACs is different from that one of graphite due to a higher interlayer spacing of 0.34 to 0.35 nm compared to the interlayer spacing of graphite (0.335 nm) [104]. Characterization of ACs is partitioned into two classifications, specifically graphitizing and non-graphitizing carbons [105]. Graphitizing carbons are soft with weak linkages consisting of parallel graphene layers oriented to each other (Fig. 2.10a) while non-graphitizable carbons are hard carbons with well-defined microporous structure that has strong cross linkages (Fig. 2.10b). The non-graphitizable carbon is formed due to insufficient presence of hydrogen or availability of associated oxygen in the raw material [106].

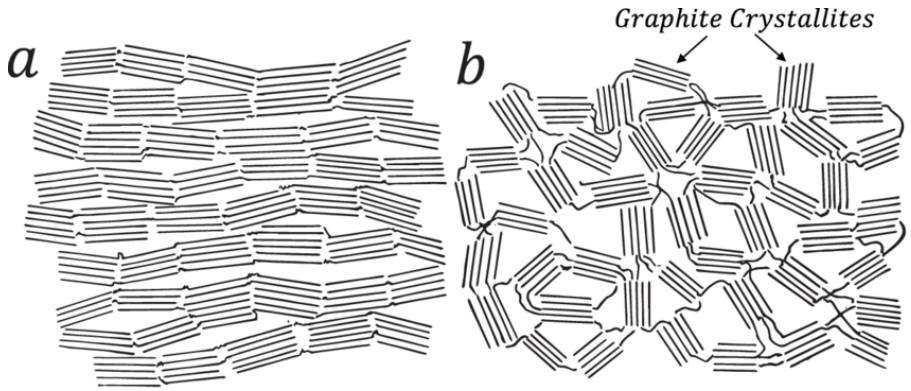

Fig. 2. 9. Structural representation (a) graphitizable carbon and (b) non-graphitizable carbon [107].

2.3.1.1. Effect of impregnation ratio

The stability and surface area of ACs are dependent on the impregnation ration. Impregnation ratio is the mass difference between the raw material and activating agent [108]. Different types of pores are created at different impregnation ratios. The role of impregnation ratio has been observed on processing grape using activating agent such as $ZnCl_2$ [109]. This involved varying different ratios of the activating agent ($ZnCl_2$) to the raw material from 1:1, 2:1, 4:1, 6:1 and 8:1 for 60 min at 500 ℃. Results obtained showed that micropores were formed when lower impregnation ratios were used and mesopores were formed when higher impregnation ratios were used [109]. This can be ascribed to the fact that higher impregnation ratios lead to more release of volatile organic matter widening the pores. At the same time, elimination of volatile matter happens at lower impregnation ratios while also constraining tars from depositing leading to formation of micropores. However, $ZnCl_2$ display disadvantages as it is difficult to remove after impregnating.

Percentage yield of ACs is also affected by impregnation ratio. This can be further supported by the work reported by Prahas *et al.* [20] using H_3PO_4 as an activating agent. The raw material used was jackfruit peel impregnated at different ratios (1:1, 2:1, 3:1 and 4:1) at different temperatures of 350, 450 and 650 ℃, respectively. Their findings recorded a lower yield of the ACs at higher impregnation rations. The trend was similar at the different temperature used. This can be caused by the gasification on carbon material using H_3PO_4.

Again, Chaisit *et al.* [110] reported on KOH impregnation ratios on cassava root from 1:1, 1:3, and 1:5. Their findings recorded a higher surface area of over 1000 m^2/g at all different impregnation ratios at 800 ℃ for 2 h. These different activation agents play a different role in

creation of pores. However, in SCs, micropores are needed for charge accumulation and mesopores for charge transfer [111]. Hence, in this study Marula husk will be implemented for making ACs. Marula husk originates from Marula fruits which are well known fruits used to make an international liquor named Amarula (Distell production, SA).

2.3.1.2. Effect of temperature

Carbonization temperature affect the pore structure of a material yielding a low content of carbon at higher carbonization temperatures [103]. High carbonization temperatures result in a decrease of volatile matter content while increasing the ash content and fixed carbon content. A study by Yorgun *et al.* [112] was reported using Paulownia wood as the raw material at different carbonization temperatures ranging from 300-600 ℃ using H_3PO_4 (4:1) as an activating agent. It was observed that the BET surface area of the AC increases from 300-400 ℃ while it decreases when further increasing the carbonization temperature from 400-600 ℃. This was ascribed to the shrinkage of the material at higher temperature. Siipola and co-workers [113] reported on the difference in carbonization temperature of 260 and 475 ℃ using sscots pine bark and willow as active raw material. The activating agent used was KOH. The highest surface area of 1594 m^2/g was attributed for the willow raw material. This confirms that KOH is commonly used as activating agent producing large surface areas and highly developed microporous structures [87].

2.3.1.3.Marula tree

Sclerocarya birrea subsp. Caffra is a wild fruit that is commonly known as marula in South Africa, and it is also called by other names in other parts of Africa. The marula tree is mostly found in Africa and the fruits are produced from the female tree (7-17 m in height) in warm frost free regions unlike male marula tree that only produces pollen [114]. The tree is found in high lying areas and in the wild, the tree can survive up to 150 years producing about 500 kg of fruits yearly. The natural habitat of marula tree is in the eastern and southern parts of Africa [115], where the southern parts of Africa includes various countries (see Fig. 2.11) [116], [117], [118]

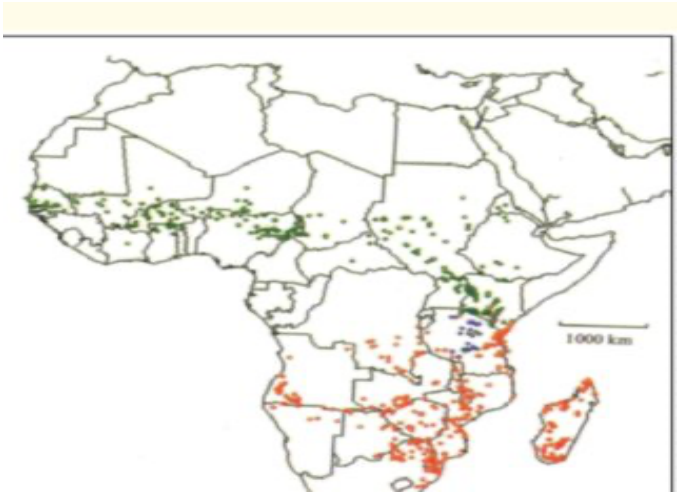

Fig. 2. 10. Map showing the distribution of marula tree (Sclerocarya birrea subsp. Caffra [118].

2.3.1.2. Fruits and husk

The fruits are round and oval and the diameter of ranges from 3-5 cm when the fruits mature (Fig. 2.12a). The fruits consist of a pale yellow color that covers the flesh or pulp (juice content) where the brown husk is found inside containing the nuts. The fruit skin is about 20%, the brown husk is about 30% and 50% is the juice and fibres. The fresh fruits is a source of Vitamin C containing about 400 mg/100 g juice. The marula fruits in South Africa are appreciated by local communities for making income. Women in local communities collect these fruits and sell them to either Distell/Mirma in Phalaborwa (Amarula Cream Liqueur) [119]. The cash income made from selling these Marula fruits is about R35-R40 per 50 kg bag. Some households make beer and sell it or use the nuts for making cosmetic oil [119]. The leaves and bark from the Marula tree also serve a purpose in medicinal usage for treating dysentery, diarrhoea and malaria [120]. Marula fruits in SA are seasonal, fruits starts to grow around mid December-mid January. Around the rainy seasons in February-March, the fruits starts to fall from the tree to the ground and start ripening on the ground to a yellow color. The fruits are mostly collected by locals and can be eaten raw (Fig. 2.12a), like small mangos or can be used to make juice, jams (Fig. 2.13b) or be fermented to make traditional beer or liqueur (see Figure 2.14c [121]. The husk from the fruits can be dried and nuts produced from the husk can be eaten raw or fried.

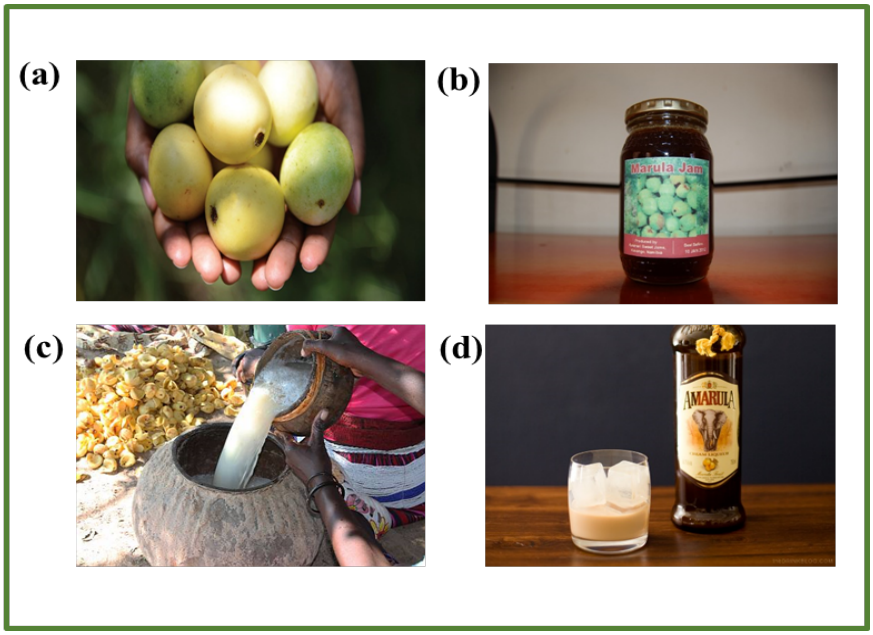

Fig. 2. 11. Figure showing (a) marula fruits, (b) jam, (c) traditional beer and (d) Amarula liquour made from marula fruits [121].

Marula fruits contains a variety of minerals occurring naturally mainly due to a specific geographical area. Elements such as calcium, potassium, magnesium, phosphorous are abundant minerals found in large amounts. The husks/stones/shells coverings the fruits are often used to start a fire hence they are deemed as a good source of fuel [11].

2.3.1.2 Nitrogen doping of activated carbons

ACs has a range of sizes from micro to macro from physical or chemical synthesis. However, their specific capacitance is low despite the high surface area that is obtained from synthesis of up to 3000 m^2/g [11,23]. The development of ACs materials thus requires new activation or preparation techniques that offer a limited pore size distribution and adjustable pore structure. Along with structure tuning, surface functionality also aids in enhancing AC materials' performance. Recently, it was discovered that nitrogen doping effectively increased the specific capacitance of AC materials [23,69,70,122]. Nitrogen is suitable among other dopants to replace carbon atoms in a structure because the atomic size and mass are similar [123]. By associating with the four electrons of carbon and one electron that is free to roam around, nitrogen, which has five valence electrons, can operate as an electron donor. This mechanism alters the Fermi level, resulting in an increase in conductivity [124]. Hence, in this study, ACs was doped with nitrogen to enhance its electrical conductivity.

2.3.2. Manganese fluorophosphate (Mn_2PO_4F)

Open framework materials are of growing interest in research due to their numerous applications in energy storage, catalysis, gas storage etc. [125,126]. Hurlbut's 1936 [127] research on triplite was the first to suggest that it was made up of an isomorphous series of two elements that formed a bivariant series of metals, Fe^{2+} and Mn^{2+}, containing a large amount of Mg and a small amount of Ca. Variations in Fe and Mg were found to have an impact on optical properties, while Mn variation had little of an impact.

In 1969, Waldrop *et al.* [128] showed that MFP is isostructural with the mineral except that there is no disorder in the fluorine site as in triplite. He went on to prove that edge sharing links the Mn(2) and Mn(1) octahedra together to create zigzag chains that are perpendicular to the b axis. Edge sharing also links the Mn(2) and Mn(1) chains together to create chains that are parallel to the b axis and that only their corners are shared by other polyhedral and the phosphate tetrahedra.

Again, Mn_2PO_4F was reported by Rea *et al.* in 1972 [129]. Fig. 2.13 show the fluorine environment in Mn_2PO_4F (MFP).

The manganese atoms lie at the center of highly distorted octahedra. Four oxygen atoms at an average distance of 2.158 Å and two fluorine atoms at 2.113 and 2.534 Å coordinate Mn (1). Four oxygen atoms at an average distance of 2.145 Å and two fluorine atoms at 2.135 and 2.372 Å serve as the coordinates for Mn(2). In both instances, the fluorine atoms are cis.

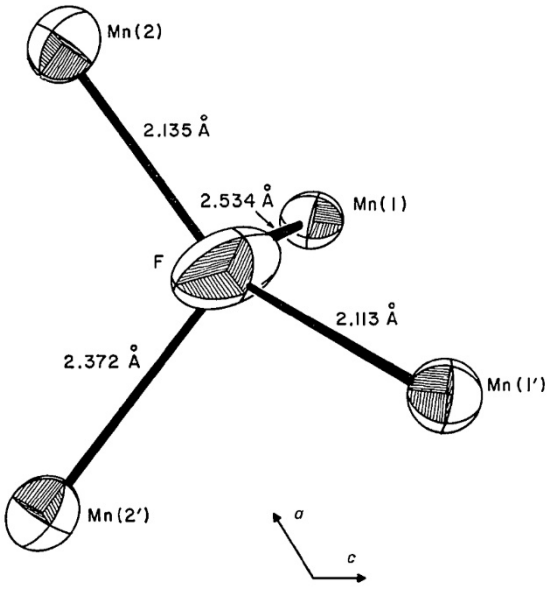

Fig. 2. 12. Schematic representation of $Mn_2(PO_4)F$ showing fluorine environment [129].

Nzimande *et al*.[22] also reported on Mn_2PO_4F for use in rechargeable batteries. MFP in his study showed open framework that allow for diffusion of electrolyte ion. The material was added with ceria oxide and carbon which gave energy density of 195 mAh/g. Hence, in this study, MFP was used as a cathode material for asymmetric SCs. The electrochemical kinetics of the material was improved by potassium and lithium intercalation. Again, ceria oxide was used to improve the electrochemical properties of MFP.

2.3.2.1.Potassium and lithium intercalation

The synergy behind alkali intercalation was to increase the d-spacing of MFP in order to allow more diffusion of electrolyte ions faster thus improving the capacitance of MFP. Stabilizing cations (such as Ag^+, K^+, Li^+, Ba^{2+}, and Mg^{2+}, etc.) are introduced by pre- or post-synthesis to maintain charge neutrality and structural integrity [21]. These cation improves the stability of materials by mitigating the migration of Manganese into the tunnel which can cause irreversible phase transformation. In the tunnel cavity, the cations and water molecules reside. The thermodynamic stability of tunnelled MnO_2 cathodes is said to be improved by increasing the concentration of stabilizing cations (such as K^+) in the tunnels, according to previous experimental research [21,130]. The addition of potassium to $FeSO_4F$, according to Tarascon's group [131], stabilizes the new structure since it has a bigger ionic radius and somewhat altered crystal chemistry.

When lithium was inserted into silicon, McDowell *et al.* [132] found a 300% increase in volume expansion. This led to amorphization, which creates an ideal environment for Li ions to be hosted in the electrode. Na intercalation into $FePO_4$ was the subject of another investigation by Xiang *et al.* [133]which led to a 17% volume expansion with high transformation strains. Thus, K^+ or Li^+ intercalation into triplite material may lead to high capacitance because framework hydration makes the electrolyte more accessible and faster ion diffusion.

2.3.2.2.Ceria oxide coating

Ceria oxide (CeO_2) is among one of the most rare earth oxide because of its abundance and is extensively usage in several fields [134,135]. Recent studies on relative abundance of CeO_2 indicate that the crust of the planet has nearly as many cerium sources as copper sources. Cerium is currently one of the rare earth metals that is most readily available. Advantages of using CeO_2 for coating of MFP includes (i) a high earth abundance worldwide and (ii) a promising redox behavior/transition between Ce^{3+} and Ce^{4+}. CeO_2 is a possibility for the SCs

application due to its fluorite-structure's oxygen mobility, high oxide ion conductivity, and eco-friendliness [136,137]. It has the ability to lose an additional 4f electron to form the 4f empty state, which would result in stable Ce^{4+} in addition to losing one 5d and two 6s electrons to make stable Ce^{3+} like other lanthanide metals. CeO_2, an exceptional redox compound with potential application in SCs, is ensured by its ability to switch between Ce^{3+} and Ce^{4+} [75].

Besides the good properties of CeO_2, it suffers from poor conductivity and structure stability. The lattice of CeO_2 expand when oxidation state changes from 4^+ to 3^+ [75]. As a result, it cannot serve as the only electrode material. Thus, in this study, it will be used for coating on MFP material.

References

[1] Organisation for Economic Co-operation and Development., International Energy Agency., Energy., OECD, 2012.

[2] A.K. Karmaker, M.M. Rahman, M.A. Hossain, M.R. Ahmed. Exploration and corrective measures of greenhouse gas emission from fossil fuel power stations for Bangladesh. J. Clean. Prod 244 (2020) 118645.

[3] J.A. Mathews. From Fossil Fuels to Renewable Energy, Greening of Capitalism. (2019) 79–113.

[4] J. Castro-Gutiérrez, A. Celzard, V. Fierro, Energy Storage in Supercapacitors: Focus on Tannin-Derived Carbon Electrodes, Front Mater. 7 (2020).

[5] P. Sharma, T.S. Bhatti, A review on electrochemical double-layer capacitors, Energy Convers Manag. 51 (2010) 2901–2912.

[6] B. Shaku, T.P. Mofokeng, T.H. Mongwe, N.J. Coville, K.I. Ozoemena, M.S. Maubane-Nkadimeng, Physicochemical Properties of Nitrogen Doped Carbon Nano-onions Grown by Flame Pyrolysis from Grapeseed Oil for Use in Supercapacitors, Electroanalysis. 32 (2020) 2946–2957.

[7] B. Zhao, D. Chen, X. Xiong, B. Song, R. Hu, Q. Zhang, B.H. Rainwater, G.H. Waller, D. Zhen, Y. Ding, Y. Chen, C. Qu, D. Dang, C.P. Wong, M. Liu, A high-energy, long cycle-life hybrid supercapacitor based on graphene composite electrodes, Energy Storage Mater. 7 (2017) 32–39.

[8] Z. Cabrane, M. Ouassaid, M. Maaroufi. Analysis and evaluation of battery-supercapacitor hybrid energy storage system for photovoltaic installation. Int. J. Hydrog. Energy 41 (2016) 20897-20907.

[9] R. Dubey, V. Guruviah, Review of carbon-based electrode materials for supercapacitor energy storage, Ionics (Kiel). 25 (2019) 1419–1445.

[10] H. Gou, J. He, G. Zhao, L. Zhang, C. Yang, H. Rao, Porous nitrogen-doped carbon networks derived from orange peel for high-performance supercapacitors, Ionics (Kiel). 25 (2019) 4371–4380.

[11] L. Guan, L. Pan, T. Peng, C. Gao, W. Zhao, Z. Yang, H. Hu, M. Wu, Synthesis of Biomass-Derived Nitrogen-Doped Porous Carbon Nanosheests for High-Performance Supercapacitors, ACS Sustain Chem Eng. 7 (2019) 8405–8412.

[12] J. Kim, J. Chun, S.G. Kim, H. Ahn, K.C. Roh, Nitrogen and fluorine co-doped activated carbon for supercapacitors, Journal of Electrochemical Science and Technology. 8 (2017) 338–343.

[13] X. Zhu, S. Yu, K. Xu, Y. Zhang, L. Zhang, G. Lou, Y. Wu, E. Zhu, H. Chen, Z. Shen, B. Bao, S. Fu, Sustainable activated carbons from dead ginkgo leaves for supercapacitor electrode active materials, Chem Eng Sci. 181 (2018) 36–45. https://doi.org/10.1016/j.ces.2018.02.004.

[14] M. Zhou, F. Pu, Z. Wang, S. Guan, Nitrogen-doped porous carbons through KOH activation with superior performance in supercapacitors, Carbon N Y. 68 (2014) 185–194.

[15] W.K. Chee, H.N. Lim, Z. Zainal, N.M. Huang, I. Harrison, Y. Andou, Flexible Graphene-Based Supercapacitors: A Review, Journal of Physical Chemistry C. 120 (2016) 4153–4172.

[16] T.P. Mofokeng, Z.N. Tetana, K.I. Ozoemena, Defective 3D nitrogen-doped carbon nanotube-carbon fibre networks for high-performance supercapacitor: Transformative role of nitrogen-doping from surface-confined to diffusive kinetics, Carbon N Y. 169 (2020) 312–326.

[17] M. Olivares-Marín, J.A. Fernández, M.J. Lázaro, C. Fernández-González, A. Macías-García, V. Gómez-Serrano, F. Stoeckli, T.A. Centeno, Cherry stones as precursor of activated carbons for supercapacitors, Mater Chem Phys. 114 (2009) 323–327.

[18] R.J. Mo, Y. Zhao, M. Wu, H.M. Xiao, S. Kuga, Y. Huang, J.P. Li, S.Y. Fu, Activated carbon from nitrogen rich watermelon rind for high-performance supercapacitors, RSC Adv. 6 (2016) 59333–59342.

[19] F. Caturla, M. Molina-Sabio, F. Rodríguez-Reinoso, Preparation of activated carbon by chemical activation with ZnCl2, Carbon N Y. 29 (1991) 999–1007.

[20] D. Prahas, Y. Kartika, N. Indraswati, S. Ismadji, Activated carbon from jackfruit peel waste by H3PO4 chemical activation: Pore structure and surface chemistry characterization, Chemical Engineering Journal. 140 (2008) 32–42.

[21] J. Liu, V. Makwana, J. Cai, S.L. Suib, M. Aindow, Effects of alkali metal and ammonium cation templates on nanofibrous cryptomelane-type manganese oxide octahedral molecular sieves (OMS-2), Journal of Physical Chemistry B. 107 (2003) 9185–9194.

[22] N. Nzimande, A. Haruna, P. Mwonga, B. Rasche, F. Cummings, K.I. Ozoemena, Supporting Information Ceria-Spiderweb Nanosheets Unlock the Energy-Storage Properties in the "Sleeping" Triplite (Mn2(PO4)F), n.d.

[23] M. Inagaki, H. Konno, O. Tanaike, Carbon materials for electrochemical capacitors, J Power Sources. 195 (2010) 7880–7903.

[24] M. Winter, R.J. Brodd. What are batteries, fuel cells, and supercapacitors?, Chem Rev. 104 (2004) 4245–4269.

[25] M. Yaseen, M.A.K. Khattak, M. Humayun, M. Usman, S.S. Shah, S. Bibi, B.S.U. Hasnain, S.M. Ahmad, A. Khan, N. Shah, A.A. Tahir, H. Ullah, A review of supercapacitors: Materials design, modification, and applications, Energies (Basel). 14 (2021).

[26] V.S. Marin Halper James C Ellenbogen, Supercapacitors: A Brief Overview MITRE MITRE MITRE MITRE, 2006.

[27] O.K. Oyeniran, H. Pretoria, Synthesis and characterization of carbon-based nanostructured material electrodes for designing novel hybrid supercapacitors, 2018.

[28] A. Burke, Prospects for the development of high energy density dielectric capacitors, Applied Sciences (Switzerland). 11 (2021).

[29] A. Burke, Ultracapacitors: why, how, and where is the technology, 2000.

[30] M. Yassine, D. Fabris, Performance of commercially available supercapacitors, Energies (Basel). 10 (2017).

[31] A.B. Cultura, Z.M. Salameh, Modeling, Evaluation and Simulation of a Supercapacitor Module for Energy Storage Application, 2015.

[32] Y.A. Maletin, N.G. Stryzhakova, S.O. Zelinskyi, S.I. Chernukhin, Energy Storage Technologies Based on Electrochemical Double Layer Capacitors: A Review, Theoretical and Experimental Chemistry. 57 (2021) 311–324.

[33] M.Z. Iqbal, M.M. Faisal, S.R. Ali, Integration of supercapacitors and batteries towards high-performance hybrid energy storage devices, Int J Energy Res. 45 (2021) 1449–1479.

[34] J. Zhang, Y. Cui, G. Shan, Metal oxide nanomaterials for pseudocapacitors, 2017.

[35] C. Zhong, Y. Deng, W. Hu, J. Qiao, L. Zhang, J. Zhang, A review of electrolyte materials and compositions for electrochemical supercapacitors, Chem Soc Rev. 44 (2015) 7484–7539.

[36] J.P.; Thomas, M.A. Qidwai, The Design and Application of Multifunctional Structure-Battery Materials Systems, 2005.

[37] Y. Gogotsi, P. Simon, True performance metrics in electrochemical energy storage, Science (1979). 334 (2011) 917–918.

[38] J.P. Steffensen, K.K. Andersen, M. Bigler, H.B. Clausen, D. Dahl-Jensen, H. Fischer, K. Goto-Azuma, M. Hansson, S.J. Johnsen, J. Jouzel, V. Masson-Delmotte, T. Popp, S.O. Rasmussen, R. Röthlisberger, U. Ruth, B. Stauffer, M.L. Siggaard-Andersen, Á.E. Sveinbjörnsdóttir, A. Svensson, J.W.C. White, High-resolution greenland ice core data show abrupt climate change happens in few years, Science (1979). 321 (2008) 680–684.

[39] M. Yibowei, J. G. Adekoya, A. A. Adediran, O. Adekomaya. Carbon-based nano-filler in polymeric composites for supercapacitor electrode materials: a review. Environmental Science and Poluttion Research 8 (2021) 26269-26279.

[40] C. Zhong, Y. Deng, W. Hu, J. Qiao, L. Zhang, J. Zhang, A review of electrolyte materials and compositions for electrochemical supercapacitors, Chem Soc Rev. 44 (2015) 7484–7539.

[41] B. Fang, Y.Z. Wei, M. Kumagai, Modified carbon materials for high-rate EDLCs application, J Power Sources. 155 (2006) 487–491.

[42] A. Djire, P. Pande, A. Deb, J.B. Siegel, O.T. Ajenifujah, L. He, A.E. Sleightholme, P.G. Rasmussen, L.T. Thompson, Unveiling the pseudocapacitive charge storage mechanisms of nanostructured vanadium nitrides using in-situ analyses, Nano Energy. 60 (2019) 72–81.

[43] S. Balasubramaniam, A. Mohanty, S.K. Balasingam, S.J. Kim, A. Ramadoss, Comprehensive Insight into the Mechanism, Material Selection and Performance Evaluation of Supercapatteries, Springer Singapore, 2020. https://doi.org/10.1007/s40820-020-0413-7.

[44] V. Augustyn, P. Simon, B. Dunn, Pseudocapacitive oxide materials for high-rate electrochemical energy storage, Energy Environ Sci. 7 (2014) 1597–1614.

[45] Y. Jiang, J. Liu, Definitions of Pseudocapacitive Materials: A Brief Review, Energy and Environmental Materials. 2 (2019) 30–37.

[46] A. Shellikeri, S. Yturriaga, J.S. Zheng, W. Cao, M. Hagen, J.A. Read, T.R. Jow, J.P. Zheng, Hybrid lithium-ion capacitor with LiFePO4/AC composite cathode - Long term cycle life study, rate effect and charge sharing analysis, J Power Sources. 392 (2018) 285–295.

[47] F. Béguin, V. Presser, A. Balducci, E. Frackowiak, Carbons and electrolytes for advanced supercapacitors, Advanced Materials. 26 (2014) 2219–2251.

[48] B.K. Kim, S. Sy, A. Yu, J. Zhang, Electrochemical Supercapacitors for Energy Storage and Conversion, Handbook of Clean Energy Systems. (2015) 1–25.

[49] B. Pal, S. Yang, S. Ramesh, V. Thangadurai, R. Jose, Electrolyte selection for supercapacitive devices: A critical review, Nanoscale Adv. 1 (2019) 3807–3835.

[50] F. Wan, J. Zhu, S. Huang, Z. Niu, High-Voltage Electrolytes for Aqueous Energy Storage Devices, Batter Supercaps. 3 (2020) 323–330.

[51] K. Fic, G. Lota, M. Meller, E. Frackowiak, Novel insight into neutral medium as electrolyte for high-voltage supercapacitors, Energy Environ Sci. 5 (2012) 5842–5850.

[52] P. Simon, Y. Gogotsi, Materials for electrochemical capacitors, Nat Mater. 7 (2008) 845–854.

[53] J.-C. Liu, Z.-H. Huang, T.-Y. Ma, Aqueous Supercapacitor with Ultrahigh Voltage Window Beyond 2.0 Volt, Small Struct. 1 (2020) 2000020.

[54] M. Galiński, A. Lewandowski, I. Stepniak, Ionic liquids as electrolytes, Electrochim Acta. 51 (2006) 5567–5580.

[55] M. Norsuzila Ya'acob, M. Abdullah, Ismail, M. Medina, T.L. Talarico, I.A. Casas, T.C. Chung, W.J. Dobrogosz, L. Axelsson, S.E. Lindgren, W.J. Dobrogosz, L. Kerkeni, P. Ruano, L.L. Delgado, S. Picco, L. Villegas, F. Tonelli, M. Merlo, J. Rigau, D. Diaz, M. Masuelli, We are IntechOpen , the world ' s leading publisher of Open Access books Built by scientists , for scientists TOP 1 %, Intech. 32 (1989) 137–144.

[56] M.P. Bichat, E. Raymundo-Piñero, F. Béguin, High voltage supercapacitor built with seaweed carbons in neutral aqueous electrolyte, Carbon N Y. 48 (2010) 4351–4361.

[57] K. Fic, G. Lota, M. Meller, E. Frackowiak, Novel insight into neutral medium as electrolyte for high-voltage supercapacitors, Energy Environ Sci. 5 (2012) 5842–5850.

[58] D. Chen, Z. Li, J. Jiang, J. Wu, N. Shu, X. Zhang, Influence of electrolyte ions on rechargeable supercapacitor for high value-added conversion of low-grade waste heat, J Power Sources. 465 (2020) 228263.

[59] G.Q.D.E. Souza, and organic electrolytes for lithium- A comparison between aqueous and organic electrolytes for lithium-ion batteries, (2021).

[60] E.P. Roth, C.J. Orendorff, How electrolytes influence battery safety, Electrochemical Society Interface. 21 (2012) 45–49.

[61] R.E. Ruther, F.M. Delnick, J. Nanda, Stable Electrolyte for High Voltage Electrochemical Double-Layer Capacitors, ECS Meeting Abstracts. MA2017-01 (2017) 17–17.

[62] M. Sevilla, A.B. Fuertes, Direct Synthesis of Highly Porous Interconnected Carbon, 1 (2016) 1–10.

[63] S. Ishimoto, Y. Asakawa, M. Shinya, K. Naoi, Degradation Responses of Activated-Carbon-Based EDLCs for Higher Voltage Operation and Their Factors, J Electrochem Soc. 156 (2009) A563.

[64] E. Perricone, M. Chamas, L. Cointeaux, J.C. Leprêtre, P. Judeinstein, P. Azais, F. Béguin, F. Alloin, Investigation of methoxypropionitrile as co-solvent for ethylene carbonate based electrolyte in supercapacitors. A safe and wide temperature range electrolyte, Electrochim Acta. 93 (2013) 1–7.

[65] Y. Kitazawa, K. Iwata, R. Kido, S. Imaizumi, S. Tsuzuki, W. Shinoda, K. Ueno, T. Mandai, H. Kokubo, K. Dokko, M. Watanabe, Polymer Electrolytes Containing Solvate Ionic Liquids: A New Approach to Achieve High Ionic Conductivity, Thermal Stability, and a Wide Potential Window, Chemistry of Materials. 30 (2018) 252–261.

[66] R. Ratti, Ionic Liquids: Synthesis and Applications in Catalysis, Advances in Chemistry. 2014 (2014) 1–16.

[67] M. Armand, F. Endres, D.R. MacFarlane, H. Ohno, B. Scrosati, Ionic-liquid materials for the electrochemical challenges of the future, Nat Mater. 8 (2009) 621–629.

[68] M. Yoshizawa, A. Narita, H. Ohno, Design of ionic liquids for electrochemical applications, Aust J Chem. 57 (2004) 139–144.

[69] B. Li, F. Dai, Q. Xiao, L. Yang, J. Shen, C. Zhang, M. Cai, Nitrogen-doped activated carbon for a high energy hybrid supercapacitor, Energy Environ Sci. 9 (2016) 102–106.

[70] B. Shaku, T.P. Mofokeng, N.J. Coville, K.I. Ozoemena, M.S. Maubane-Nkadimeng, Biomass valorisation of marula nutshell waste into nitrogen-doped activated carbon for use in high performance supercapacitors, Electrochim Acta. 442 (2023).

[71] S.C. Lin, Y.T. Lu, Y.A. Chien, J.A. Wang, P.Y. Chen, C.C.M. Ma, C.C. Hu, Asymmetric supercapacitors based on electrospun carbon nanofiber/sodium-pre-intercalated manganese oxide electrodes with high power and energy densities, J Power Sources. 393 (2018) 1–10.

[72] K. Makgopa, P.M. Ejikeme, C.J. Jafta, K. Raju, M. Zeiger, V. Presser, K.I. Ozoemena, A high-rate aqueous symmetric pseudocapacitor based on highly graphitized onion-like carbon/birnessite-type manganese oxide nanohybrids, J Mater Chem A Mater. 3 (2015) 3480–3490.

[73] C.J. Jafta, K. Raju, M.K. Mathe, N. Manyala, K.I. Ozoemena, Microwave Irradiation Controls the Manganese Oxidation States of Nanostructured (Li[Li 0.2 Mn 0.52 Ni 0.13 Co 0.13 Al 0.02]O 2) Layered Cathode Materials for High-Performance Lithium Ion Batteries , J Electrochem Soc. 162 (2015) A768–A773.

[74] K. Ren, Z. Liu, T. Wei, Z. Fan, Recent Developments of Transition Metal Compounds-Carbon Hybrid Electrodes for High Energy/Power Supercapacitors, Nanomicro Lett. 13 (2021).

[75] H. Zhang, J. Gu, J. Tong, Y. Hu, B. Guan, B. Hu, J. Zhao, C. Wang, Hierarchical porous MnO2/CeO2 with high performance for supercapacitor electrodes, Chemical Engineering Journal. 286 (2016) 139–149.

[76] C. K. Balogoun, Influence of Pretreatment with Soda (NaOH) on the Structural Characteristics of Activated Carbon Prepared by Chemical Means with H₃PO₄ from Rice Bran, American Journal of Physical Chemistry. 5 (2016) 35.

[77] A. Mohammad-Khah, R. Ansari, Activated Charcoal: Preparation, characterization and Applications : A review article, n.d.

[78] F. Barzegar, Synthesis and characterization of activated carbon materials for supercapacitor applications, 2015.

[79] C.L. Lee, K.L. Chin, P.S. H'ng, U. Rashid, M. Maminski, P.S. Khoo, Effect of pretreatment conditions on the chemical–structural characteristics of coconut and palm kernel shell: A potentially valuable precursor for eco-efficient activated carbon production, Environ Technol Innov. 21 (2021).

[80] Sadashiv Bubanale, M Shivashankar, History, Method of Production, Structure and Applications of Activated Carbon, International Journal of Engineering Research And. V6 (2017) 495–498.

[81] W.M. Review, Y. Luka, The Promising Precursors for Development of Activated Carbon: Agricultural Waste Materials- A Review, International Journal of Advances in Scientific Research and Engineering. (2018).

[82] E.M. Mistar, T. Alfatah, M.D. Supardan, Synthesis and characterization of activated carbon from Bambusa vulgaris striata using two-step KOH activation, Journal of Materials Research and Technology. 9 (2020) 6278–6286.

[83] D. Bergna, T. Hu, H. Prokkola, H. Romar, U. Lassi, Effect of Some Process Parameters on the Main Properties of Activated Carbon Produced from Peat in a Lab-Scale Process, Waste Biomass Valorization. 11 (2020) 2837–2848.

[84] L. Wang, M. Li, M. Hao, G.K. Liu, S. Xu, J. Chen, X. Ren, Y.A. Levendis, Effects of Activation Conditions on the Properties of Sludge-Based Activated Coke, ACS Omega. 6 (2021) 22020–22032.

[85] Z. Liu, Y. Huang, G. Zhao, Preparation and characterization of activated carbon fibers from liquefied wood by ZnCl2 activation, Bioresources. 11 (2016) 3178–3190.

[86] A. Baçaoui, A. Yaacoubi, A. Dahbi, C. Bennouna, R. Phan Tan Luu, F.J. Maldonado-Hodar, J. Rivera-Utrilla, C. Moreno-Castilla, Optimization of conditions for the preparation of activated carbons from olive-waste cakes, Carbon N Y. 39 (2001) 425–432.

[87] M. Lillo-Rodenas, D. Cazorla-Amoros, A. Linares-Solanó, U nderstanding chemical reactions between carbons and NaOH and KOH An insight into the chemical activation mechanism, 2003.

[88] Q. Yu, M. Li, P. Ning, H. Yi, X. Tang, Preparation and Phosphine Adsorption of Activated Carbon Prepared from Walnut Shells by KOH Chemical Activation, Separation Science and Technology (Philadelphia). 49 (2014) 2366–2375.

[89] A. Linares-Solano *et al.* NaOH AND KOHF ORPREPARING ACTIVATED CARBON SUSEDINEN ERGYAND ENVIRONMENT ALAPPLICATIONS. Energy, Environmental and Economics 4 (2012) 59-91.

[90] Y. Shen, L. Maurizi, G. Magnacca, V. Boffa, Y. Yue, Tuning porosity of reduced graphene oxide membrane materials by alkali activation, Nanomaterials. 10 (2020) 1–14.

[91] S.M. Anisuzzaman, C.G. Joseph, Y.H. Taufiq-Yap, D. Krishnaiah, V. V. Tay, Modification of commercial activated carbon for the removal of 2,4-dichlorophenol from simulated wastewater, J King Saud Univ Sci. 27 (2015) 318–330.

[92] S.M. Yakout, G. Sharaf El-Deen, Characterization of activated carbon prepared by phosphoric acid activation of olive stones, Arabian Journal of Chemistry. 9 (2016) S1155–S1162.

[93] V. Siipola, T. Tamminen, A. Källi, R. Lahti, H. Romar, K. Rasa, R. Keskinen, J. Hyväluoma, M. Hannula, H. Wikberg, Effects of biomass type, carbonization process, and activation method on the properties of bio-based activated carbons, Bioresources. 13 (2019) 5976–6002.

[94] S.E. Chun, J.F. Whitacre, Formation of micro/mesopores during chemical activation in tailor-made nongraphitic carbons, Microporous and Mesoporous Materials. 251 (2017) 34–41.

[95] V.D. Canh, S. Tabata, S. Yamanoi, Y. Onaka, T. Yokoi, H. Furumai, H. Katayama, Evaluation of porous carbon adsorbents made from rice husks for virus removal in water, Water (Switzerland). 13 (2021) 1–10.

[96] A. Javier Sánchez, Characterization of activated carbon produced from coffee residues by chemical and physical activation., KTH Chemical Science and Engineering. (2011) 66.

[97] J. Gamby *et al.* Studies and characterisations of various activated carbons used for carbon/carbon supercapacitors. Power Sources 1 (2001) 109-116.

[98] E. Gonzalez-Serrano, T. Cordero, J. Rodríguez-Mirasol, J.J. Rodríguez, Development of Porosity upon Chemical Activation of Kraft Lignin with ZnCl2, Ind Eng Chem Res. 36 (1997) 4832–4838.

[99] E. Nsi, A. Akpakpan, U. Akpabio, E.J. Ukpong, Preparation and Characterization of Activated Carbon from Hura Crepitans Linn Seed ShellsPreparation and Characterization of Activated Carbon from Hura Crepitans Linn Seed Shells, The International Journal Of Engineering And Science (IJES). 5 (2016) 38–44.

[100] M.S. Reza, C.S. Yun, S. Afroze, N. Radenahmad, M.S.A. Bakar, R. Saidur, J. Taweekun, A.K. Azad, Preparation of activated carbon from biomass and its' applications in water and gas purification, a review, Arab J Basic Appl Sci. 27 (2020) 208–238.

[101] L. Shrestha, M. Thapa, R. Shrestha, S. Maji, R. Pradhananga, K. Ariga, Rice Husk-Derived High Surface Area Nanoporous Carbon Materials with Excellent Iodine and Methylene Blue Adsorption Properties, C (Basel). 5 (2019) 10.

[102] J. Yang, K. Qiu, Development of high surface area mesoporous activated carbons from herb residues, Chemical Engineering Journal. 167 (2011) 148–154.

[103] M.A. Yahya, Z. Al-Qodah, C.W.Z. Ngah, Agricultural bio-waste materials as potential sustainable precursors used for activated carbon production: A review, Renewable and Sustainable Energy Reviews. 46 (2015) 218–235.

[104] F. Islam, A. Tahmasebi, B. Moghtaderi, J. Yu, Structural investigation of the synthesized few-layer graphene from coal under microwave, Nanomaterials. 12 (2022) 1–12.

[105] D.B. Schuepfer, F. Badaczewski, J.M. Guerra-Castro, D.M. Hofmann, C. Heiliger, B. Smarsly, P.J. Klar, Assessing the structural properties of graphitic and non-graphitic carbons by Raman spectroscopy, Carbon N Y. 161 (2020) 359–372.

[106] P. Ouzilleau, A.E. Gheribi, P. Chartrand, G. Soucy, M. Monthioux, Why some carbons may or may not graphitize? The point of view of thermodynamics, Carbon N Y. 149 (2019) 419–435.

[107] I.Y. Stein, Synthesis and Characterization of Next-Generation Multifunctional Material Architectures: Aligned Carbon Nanotube Carbon Matrix Nanocomposites, (2013).

[108] M. Zięzio, B. Charmas, K. Jedynak, M. Hawryluk, K. Kucio, Preparation and characterization of activated carbons obtained from the waste materials impregnated with phosphoric acid(V), Applied Nanoscience (Switzerland). 10 (2020) 4703–4716.

[109] H. Sayılı, F. Güzel, Y. Önal, Conversion of grape industrial processing waste to activated carbon sorbent and its performance in cationic and anionic dyes adsorption, J Clean Prod. 93 (2015) 84–93.

[110] S. Chaisit, N. Chanlek, J. Khajonrit, T. Sichumsaeng, S. Maensiri, Preparation, characterization, and electrochemical properties of KOH-activated carbon from cassava root, Mater Res Express. 7 (2020).

[111] H. Shi, Activated carbons and double layer capacitance, Electrochim Acta. 41 (1996) 1633–1639.

[112] S. Yorgun, N. Vural, H. Demiral, Preparation of high-surface area activated carbons from Paulownia wood by ZnCl2 activation, Microporous and Mesoporous Materials. 122 (2009) 189–194.

[113] V. Siipola, T. Tamminen, A. Källi, R. Lahti, H. Romar, K. Rasa, R. Keskinen, J. Hyväluoma, M. Hannula, H. Wikberg, Effects of biomass type, carbonization process, and activation method on the properties of bio-based activated carbons, Bioresources. 13 (2019) 5976–6002.

[114] S. Shackleton, Livelihood benefits from the local level commercial-ization of savanna resources: a case study of the new and expanding trade in marula (Sclerocarya birrea) beer in Bushbuckridge, South Africa, n.d.

[115] C. Shackleton, S. Shackleton, The importance of non-timber forest products in rural livelihood security and as safety nets: A review of evidence from South Africa, S Afr J Sci. 100 (2004) 658–664.

[116] R. Leakey, K. Pate, C. Lombard, Domestication potential of Marula (Sclerocarya birrea subsp caffra) in South Africa and Namibia: 2. Phenotypic variation in nut and kernel traits, Agroforestry Systems. 64 (2005) 37–49.

[117] N.C. Mokgolodi, Y. fang Ding, M.P. Setshogo, C. Ma, Y. jun Liu, The importance of an indigenous tree to southern African communities with specific relevance to its domestication and commercialization: A case of the marula tree, For Stud China. 13 (2011) 36–44.

[118] K. Andrew Tapiwa, Assessing the Distribution and Stem Densities of Sclerocarya birrea in Arable and Non-Arable Lands: A Case of Zimbabwe, Acta Scientific Microbiology. 2 (2019) 59–66.

[119] S. Shackleton, C. Shackleton, Use of marula products for domestic and commercial purposes by households in the Bushbuckridge district, Limpopo Province, South Africa Longitudinal studies (2): rural development and livelihood transformations in the Eastern Cape, South Africa View project Iron Age Ecology View project, 2002.

[120] J.N. Eloff, Antibacterial activity of Marula (Sclerocarya birrea (A. rich.) Hochst. subsp. caffra (Sond.) Kokwaro) (Anacardiaceae) bark and leaves, 2001.

[121] S. Shackleton, C. Shackleton, The contribution of marula (Sclerocarya Birrea) fruit and fruit products to rural livelihoods in the bushbuckridge district, South Africa: Balancing domestic needs and commercialisation, Forests Trees and Livelihoods. 15 (2005) 3–24.

[122] H. Peng, G. Ma, K. Sun, Z. Zhang, Q. Yang, Z. Lei, Nitrogen-doped interconnected carbon nanosheets from pomelo mesocarps for high performance supercapacitors, Electrochim Acta. 190 (2016) 862–871.

[123] P. Rani, V.K. Jindal, Designing band gap of graphene by B and N dopant atoms, RSC Adv. 3 (2013) 802–812.

[124] Y. Shao, J. Sui, G. Yin, Y. Gao, Nitrogen-doped carbon nanostructures and their composites as catalytic materials for proton exchange membrane fuel cell, Appl Catal B. 79 (2008) 89–99.

[125] S. Natarajan, S. Mandal, Open-framework structures of transition-metal compounds, Angewandte Chemie - International Edition. 47 (2008) 4798–4828.

[126] J.A. Armstrong, E.R. Williams, M.T. Weller, Manganese(iii) fluorophosphate frameworks, Dalton Transactions. 42 (2013) 2302–2308.

[127] E.W. Heinrich MINERALOGY OF TRIPLITE. 1950.

[128] L. Waldrop, The crystal structure of triplite, $(Mn,Fe)_2FP0_4$, 1969.

[129] J.R. Rea, E. Kostiner, The crystal structure of manganese fluorophosphate, $Mn_2(PO_4)F$. Acta Crystallogr B. 28 (1972) 2525–2529.

[130] S. Fritsch, J.E. Post, S.L. Suib, A. Navrotsky, Thermochemistry of Framework and Layer Manganese Dioxide Related Phases, 1998.

[131] N. Recham, G. Rousse, M.T. Sougrati, J.N. Chotard, C. Frayret, S. Mariyappan, B.C. Melot, J.C. Jumas, J.M. Tarascon, Preparation and characterization of a stable FeSO4F-based framework for alkali ion insertion electrodes, Chemistry of Materials. 24 (2012) 4363–4370.

[132] M.T. McDowell, S.W. Lee, W.D. Nix, Y. Cui, 25th anniversary article: Understanding the lithiation of silicon and other alloying anodes for lithium-ion batteries, Advanced Materials. 25 (2013) 4966–4985.

[133] K. Xiang, W. Xing, D.B. Ravnsbæk, L. Hong, M. Tang, Z. Li, K.M. Wiaderek, O.J. Borkiewicz, K.W. Chapman, P.J. Chupas, Y.M. Chiang, Accommodating High Transformation Strains in Battery Electrodes via the Formation of Nanoscale Intermediate Phases: Operando Investigation of Olivine NaFePO4, Nano Lett. 17 (2017) 1696–1702.

[134] P. Kim, A. Anderko, A. Navrotsky, R.E. Riman, Trends in structure and thermodynamic properties of normal rare earth carbonates and rare earth hydroxycarbonates, Minerals. 8 (2018).

[135] A. Baranik, A. Gagor, I. Queralt, E. Marguí, R. Sitko, B. Zawisza, Determination and speciation of ultratrace arsenic and chromium species using aluminium oxide supported on graphene oxide, Talanta. 185 (2018) 264–274.

[136] S. Ghosh, T. Thomas, G.R. Rao, Zr substitution aided enhancement of pseudocapacitive behavior of ceria, Mater Lett. 266 (2020).

[137] S. Ghosh, G.R. Rao, T. Thomas, Analysis of Charge Storage Behavior in Redox-electrolyte Based Battery-like-systems: A Case Study on Zr-doped Ceria, ChemistrySelect. 5 (2020) 1628–1639.

CHAPTER 3: Biomass valorisation of marula nutshell waste into nitrogen doped activated carbon for use in high performance supercapacitor.

3.1. Introduction

The sustainability of human development through the generation of energy by 'green' methodologies is a tremendous challenge and requires the development of efficient, safe, and high-performance energy storage devices [1–3]. Hence, much research has been undertaken to develop supercapacitors (SCs) for high powered energy storage as one solution to solve this problem [4, 5]. Electric double layer capacitors (EDLCs) store charge by a simple ion-adsorption process (non-faradic) at an electrode/electrolyte interface [6, 7]. EDLCs have been shown to have fast charging-discharging rates and a long life cycle which makes them useful as high powered devices [8, 9]. The efficiency of SCs as electrochemical cells depend on the type of electrode materials used. One material that has been extensively studied as an electrode in SCs is activated carbons (ACs) because of its low cost, high specific surface area (SSA) and high thermal stability [10, 11]. Precursors for making ACs and their optimum synthesis conditions require careful selection in order to achieve desirable properties. Precursors for making ACs commercially are derived from fossil fuels such as coal, polymers, and pitch which can be expensive and/or ecologically unfriendly. Therefore, there is a need to determine whether the synthesis of ACs from renewable waste carbon containing sources that are cheap is possible. The ACs produced will need to compete with ACs produced from waste (i.e. pomelo peel [12], hazel nutshell [13] etc.) in terms of physical properties, reproducibility and cost. Here we report on the use of a local waste, marula nutshells which is found in abundance in South Africa for use as an electrode material making nitrogen doped activated carbons by KOH and melamine (for the first time) in SCs.

South Africa is one of the largest producers of marula fruits, and these fruits are used for producing the international branded Amarula liquour (Distell production, South Africa) [14]. Sclerocarya birrea (marula) produces the fruits in warm frost-free climates, as found in the Northern parts of South Africa. The tree can produce 500 kg of ripe fruits per year with a delightfully juicy acid taste. The fruit contains nut that is removed from the fruit and this marula nutshell generates a waste that is pale brown in colour and has an oval shape [15].

Marula nutshell has been reported to have a carbon content of ~38.2%, a moisture content of ~5.5% and an ash content of ~8.4 % [16]. The low ash content present in the biomass has been reported to have good properties for making good adsorbent ACs with good mechanical strength [16].

Studies of ACs as electrode materials for SCs have shown some limitations. For example, the type of biomass and different precursors used during synthesis can impact on its properties [17]. ACs can be synthesized from different methods such as physical/chemical activation and microwave irradiation [18, 19]. Microwave irradiations are used to heat dielectric materials [20]. Physical activation normally involves pyrolysis at higher temperature (> 500 ℃) followed by activation at higher temperatures (700-1000 ℃) using activating agents such as air, CO_2 and steam [21] . Chemical activation involves treatment of the biomass with an activating agent followed by pyrolysis leading to efficient porosity of the material [22, 23].

Regardless of the method, the improvement of the energy efficiency of the ACs is very important due to the low conductivity of the carbon materials resulting from degree of carbon graphitization. This low conductivity produces a limited amount of energy storage due to the restriction of fast charging-discharging rates [24]. Heteroatom species such as nitrogen, boron, sulphur etc. can be introduced into the carbon matrix to overcome the low conductivity associated with the ACs [25, 26]. In particular, the introduction of nitrogen on, or into, the carbon matrix improves the capacitance due to the enhanced wettability of the material, thus improving the electric contact between the electrode and electrolyte [27, 28]. Nitrogen-doped carbons can be synthesized by in-situ or ex-situ thermal processes using nitrogen containing species such as ammonia gas (NH_3), melamine, urea, acetonitrile etc. [29, 30]. In-situ nitrogen doping involves a one or two pot synthesis. In the one pot synthesis of the biomass, an activating agent and a nitrogen source are mixed together and then carbonized. In the two pot synthesis direct pyrolysis of the material in the presence of a nitrogen containing species followed by activation at high temperatures is used [31, 32].

For example, Ahmed *et al.* [31] reported on the in-situ nitrogen doping of orange peel as a biomass at 700 ℃, using melamine as a nitrogen source and KOH as an activating agent. The nitrogen content decreased as the KOH concentration increased with a highest capacitance of 168 F/g exhibited at 10 mV s^{-1} with an energy density of 5.79 Wh kg^{-1} in 6 M KOH electrolyte. Zhou *et al.* [33] reported on the formation of nitrogen doped porous carbons using ethylenediamine as a nitrogen source and carbon tetrachloride as a carbon source by KOH

activation. The nitrogen doped porous carbon showed a decrease of the nitrogen content from 10.8% to 1.1% as the KOH concentration increased. In another study by Mo *et al.* [34], watermelon rind that contained nitrogen (~2.8%) was used to make ACs. After KOH impregnation, the surface area increased to 2277 m^2 g^{-1} but the nitrogen content decreased to 1.51% and the carbon electrode had a capacitance of 270 F g^{-1} in 6 M KOH electrolyte. The above studies revealed that the surface area and the nitrogen content are two complementary features that influence the SCs properties and that the use of elevated temperatures and increased KOH concentrations decrease the nitrogen content. An alternative method to produce ACs with a high surface area, and with moderate to high nitrogen-content, is by using ex-situ nitrogen doping i.e. the two-pot synthesis approach. Thus, in this study we have made nitrogen-doped ACs from the carbons produced from the marula nutshells that have a moderate nitrogen content and high surface area via the ex-situ two pot doping method.

Energy storage in SCs is not only dependent on active surface area and conductivity, but also the properties of the electrolyte [35]. Another way of increasing the energy density of a SC is by using organic or ionic electrolytes that operate over a wide voltage range [36, 37]. However, it must be kept in mind that organic or ionic liquids suffer from poor conductivity compared to aqueous electrolytes although they have wide operating voltage and high viscosity creating hindrance charge accumulation of electrolyte ions [37]. Hence, aqueous electrolytes can be used because of the high conductivity.

Within this context, the objective of the study is to evaluate marula nutshell as a precursor electrode material for producing ACs under different impregnation ratios of the biomass and KOH. Marula fruits, besides being the main products for producing Amarula liqueur, the material produces marula nutshell which possess adequate characteristics for the production of activated carbon. In the literature, there are no published studies on obtaining nitrogen doped ACs from marula nutshell by KOH activation and melamine as a nitrogen precursor. To this purpose, using KOH as an activating agent and the effect of nitrogen has been investigated. Samples of the activated and nitrogen doped were subjected to electrochemical examination using a three-electrode system in 6 M KOH and 2.5 KNO_3 electrolyte. Due to the wider potential window of KNO_3 [38], the materials were further evaluated in a two electrode system. Neutral electrolytes are used because of their cost effectiveness, corrosion resistance, and electrochemical stability. They also make the EDLCs assembly a simple process [39]. Also, 2.5 M KNO_3 affirmed the possibility of expanding the potential range of the electrolyte to a wide range leading to an efficient capacitor.

3.2. Experimental section

3.2.1. Materials

Marula nut waste used in the experiment were collected from nuts found in the Limpopo province, Modimolle (South Africa). The N-ACs were synthesized using nitrogen (N_2; 99.9% Afrox), potassium hydroxide (KOH; Sigma Aldrich) and melamine (Sigma Aldrich). Microfiber filter paper (ACE chemicals) were used as an electrode separator with 0.18 mm thickness. All other reagents were used without further purification.

3.2.2. Synthesis of activated carbon

Fig. 3.1 shows a schematic representation of the synthesis of the ACs. Marula nuts waste (MNW) was washed with acetone and water to remove dirt and then pulverized into powder. The powdered material was sieved to have a size < 150 µm. About 10.0 g of the sieved material was treated hydrothermally in air in 3% H_2SO_4 using a heating rate of 5 ℃/min to achieve the required temperature (160 ℃, 12 h). This pre-treated material was then washed with distilled water until a neutral pH was achieved. The material was labelled pre-treated marula nuts waste (PMNW) [40]. About 4.0 g of the PMNW was added to KOH using different mass ratios (PMNW:KOH =1:0.5, 1:1, 1:2, 1:3) in 50 mL distilled water. The mixtures were stirred for 24 h at room temperature and oven dried overnight at 80 ℃. About 3.0 g of the dried mixture was placed in a quartz boat in a furnace for 2 h at 800 ℃ (heating rate used: 5 ℃/min) under a flow of nitrogen (250 ml/min). The resulting material was washed with 1.0 M HCl, followed by distilled water until neutral pH [41] (see Fig. 3.1). The PMNW samples were labelled activated marula nuts waste (AMNW-0.5, AMNW-1, AMNW-2, AMNW-3) respectively for the samples made using the different KOH mass ratios (PMNW:KOH =1:0.5, 1:1, 1:2, 1:3).

The final weight percentage of the activated materials was calculated using equation 3.1.

$$\%\text{yield}=\frac{m_f}{m_i} \times 100\% \quad (3.1)$$

where m_i is the initial mass before carbonization and activation, m_f is the final mass after the KOH synthesis step (Table S3.1).

3.2.3 Ex-situ nitrogen doping

Ex-situ nitrogen doping was achieved by mixing AMNW-2 with melamine (1 (AMNW-2):3 (melamine) in 20 mL distilled water (Fig. 3.1). The mixture was stirred for 2 h at room temperature and dried in an oven at 80 ℃ overight. The dried mixture was placed in a quartz

boat in a furnace for 2 h at 800 ℃ (heating rate: 5 ℃/min) under a flow of nitrogen (250 ml/min). The material was washed with distilled water. The resulting materials was labelled ex-situ nitrogen doped activated carbons (N-ACs) [42].

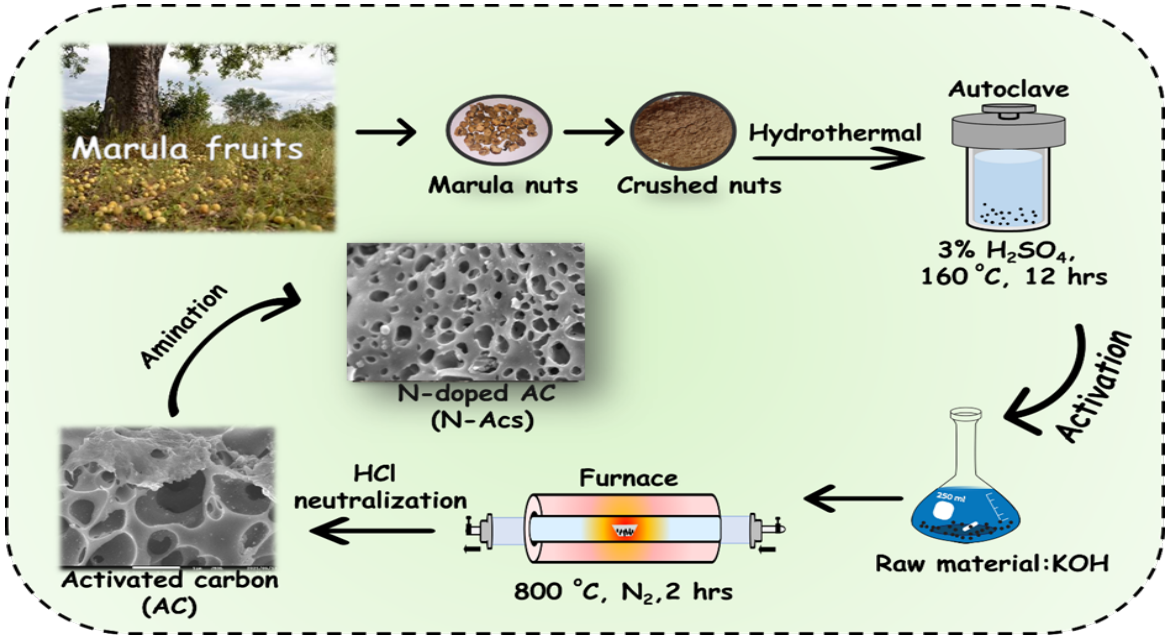

Fig. 3. 1. A schematic depicting the synthetic route to make the activated carbons and nitrogen doped activated carbons.

Table 3. 1. Abbreviations and compositions of activated carbons produced from marula nuts waste.

Abbreviation	PMNW:KOH (wt %)
AMNW-0.5	1:0.5
AMNW-1	1:1
AMNW-2	1:2
AMNW-3	1:3
PMNW	Hydrothermal treatment, no aivation
MNW	No hydrothermal treatment, no activation
N-ACs	AMNW-2:melamine (1:3)

3.2.5 Electrochemical characterization

The working electrode was fabricated by mixing the activated materials (80%) with carbon black (CB, 10 %) and polyvinylidene (PVDF, 10%) in a few drops of methylpyrrolidone

(NMP) [43]. The slurry was sonicated for 30 minutes, pasted on carbon paper and dried in a vacuum oven at 60 ℃ for 12 h. The coated carbon papers were used as working electrodes in the two- and three-electrode systems. The three-electrode system (half-cell) in 6 M KOH and 2.5 M KNO_3 was constructed using nickel foam as a counter electrode and saturated calomel electrode as a reference electrode in a T-type Swagelok cell. The two-electrode (full-cell) system was assembled using a T-type Swagelok cell with a microfiber filter paper between the electrodes that was soaked in a 2.5 KNO_3 electrolyte. The total mass per unit area of active material was around ~1.1 cm^2/mg. All the electrochemical analyses were tested by using cyclic voltammetry (CV), galvanostatic charge-discharge (GCD), and impedance spectroscopy (EIS) procedures using a SP300 potentiostat.

The specific capacitance (C_{sp}), energy density (E_s), power density (P_s) were calculated from the discharge time obtained from GCD curves using equation 3.2-3.7 [44–48].

Equation 3.2 was used to calculate capacitance (F):

$$C = \frac{I \times \Delta t}{\Delta V} \tag{3.2}$$

Where the discharge current is given by I/A, $\Delta t/s$ is the discharge time, $\Delta v/V$ is the potential difference.

Equation 3.3 was used to calculate the specific capacitance, $C_s/F\ g^{-1}$ of the three electrode/half-cell:

$$C_{sp} = \frac{C}{m} \tag{3.3}$$

Where m(g) is the mass of the active electrode material.

The $C_s/F\ g^{-1}$ for a full-cell/symmetric two electrode system, where the counter and working electrode are the same active material has been calculated using equation 3.4:

$$C_{sp} = 4\ \frac{C}{m} \tag{3.4}$$

Where m/g is the total active electrode mass.

Energy density (E_s) 's basic expression in equation 3.5 is in the unit $J\ g^{-1}$.

$$Es = \frac{1}{2} \times C_{sp}(\Delta V)^2 \tag{3.5}$$

Where C_{sp}/ F g^{-1} is the specific capacitance and ΔV/V is the potential window. To convert J g^{-1} to unit Wh g^{-1}, equation 3.5 is divided by a factor of 3600. To convert to Wh kg^{-1}, the units are multiplied by a 1000 to give equation 3.6. Hence, Es/Wh kg^{-1} is given by equation 3.6 and P_s/W kg^{-1} is calculated from equation 3.7.

$$Es=\frac{1}{2} \times C_{sp}(\Delta V)^2 \ =\frac{C\times(\Delta V)^2}{2m} \times \frac{1000}{3600} \quad (3.6)$$

Where C is capacitance, ΔV/V is the cell potential and m/kg is the mass of both active electrodes.

Power density (P_s) was calculated from equation 3.7:

$$P_s=3600\frac{E_s}{\Delta t} \quad (3.7)$$

3.3. Characterization techniques

The morphology of the synthesized materials were characterized by using scanning electron microscopy (SEM) measurements (LEO, Zeiss SEM). The defects present in the material were established by Raman spectroscopy (micro-Raman mode; Jobin-Yvon T64000, λ = 532 nm) at a focal plane of 1.5 μm. The surface area of the materials were determined using the Brunauer-Emmett-Teller (BET) procedure (Micrometrics Tristar 300 analyser). Thermal gravimetric analysis (TGA, Perkin Elmer 6000) was used to measure the stability of the materials. X-ray photoelectron spectroscopy (XPS) data was collected using a Physical Electronics Quantum 2000 instrument at 1486.7 eV using monochromatic a Al Kα source.

3.4 Results and discussion

3.4.1 Influence of PMNW:KOH ratio

The nut waste after acid treatment was treated with KOH. Different PMNW:KOH ratios were used (1:0.5, 1:1, 1:2, 1:3) based on earlier studies on similar carbons [49]. After the impregnation studies with KOH, the samples were heated at 800 ℃ for 2 h to obtain the desired material. As expected, carbon was lost under these conditions (Fig. S3.1). This mass loss is due to the reaction of KOH with the carbon (equation 3.8 and 3.9) [50], [51]

$$6KOH+ 2C \leftrightarrow 2K + 3H_2 + 2K_2CO_3 \quad (3.8)$$

$$K_2CO_3 + 2C \rightarrow 2K + 3CO \quad (3.9)$$

The reaction between carbon and KOH showed that when the impregnation ratio increased from 1:0.5 to 1:3, the % yield of carbon decreased (Fig. S3.1). This is in accordance with work reported by Marsh *et al.* [50] that the reaction between carbon and KOH lead to gasification of volatile matter from the carbon. Reaction between carbon and KOH follows equations 3.8 and 3.9.

3.4.2 Morphology and surface area analysis

SEM images of the marula nuts before and after activation are shown in Fig. 3.2. The MNW sample (Fig. 3.2a) shows agglomerated nanoparticles with a smooth surface. After pre-treatment with 3% H_2SO_4 (Fig. 3.2b), the PMNW showed a morphology change compared to the MNW, and the production of a material with a rough surface. The pre-treatment was used to break down the lignin in the marula nuts and to allow access to the cellulose, and this reaction led to an increase in the surface area (Table S3.2) [52]. After activation of the four AMNM samples, SEM images showed that they all now contained irregular holes (AMNW-2 (Fig. 3.2c), AMNW-0.5 (Fig. S3.2a), AMNW-1 (Fig. S3.2b) and AMNW-3 (Fig. S3.2c). Such holes aid with the diffusion of the electrolyte ions during charge storage.

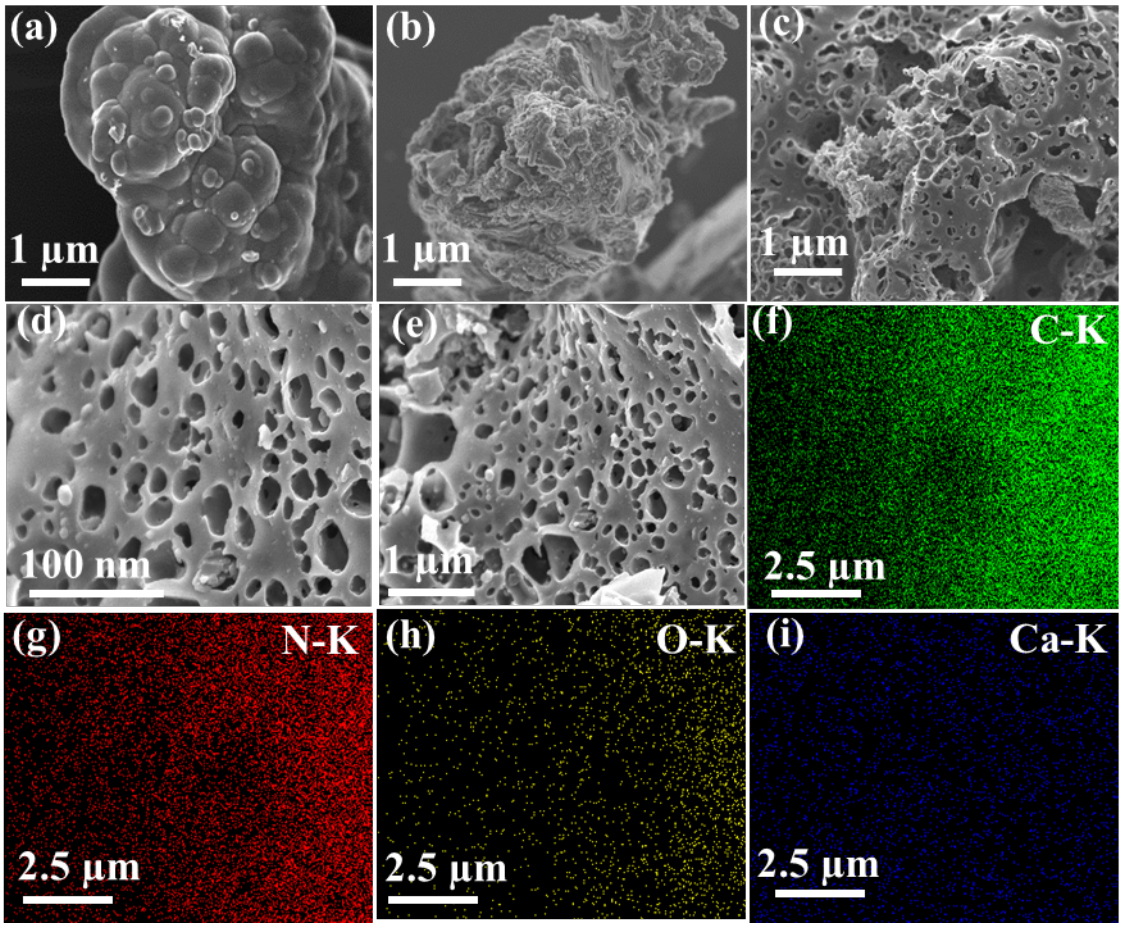

Fig. 3. 2. SEM images of (a) MNW, (b) PMNW, (c) AMNW-2, (d) high, (e) low magnification of N-ACs and the corresponding EDS mapping of for the different elements: (f) C-K, (g) N-K, (h) O-K and (i) Ca-K.

The textural properties of the activated carbons were determined and the N_2 adsorption-desorption data are shown in Fig. 3.3a and b. The adsorption-desorption isotherm of the activated materials all displayed a Type IV isotherm (Fig. 3.3a) according to the IUPAC classification with a H4 hysteresis loop [53], [54]. The hysteresis loop was observed between the adsorption and desorption branches and indicates the presence of mesopores. A Type 1 isotherm was observed for MNW and PMNW (Fig. S3.3).

The surface area of the original material was close to zero m^2/g and after pre-treatment (PMNW), this increased to 31 m^2/g (Table S3.2). After activation, the surface area increased to between 1111 m^2/g and 1353 m^2/g. While treatment of the PMNW with KOH, with the 1:1 AMNW:KOH ratio (AMNW-1), gave the ACs with the largest surface area, increasing the KOH ratio further did not increase the surface area. This indicates that as the impregnation ratio increased from 1 to 3 the excess KOH led to destruction of the carbon structure rather

than creation of a more porous material. This is consistent with the decrease in total pore volume but minimal change in the micropore volume with variation of the KOH ratio (Table S3.2; Fig. 3.3b) [54].

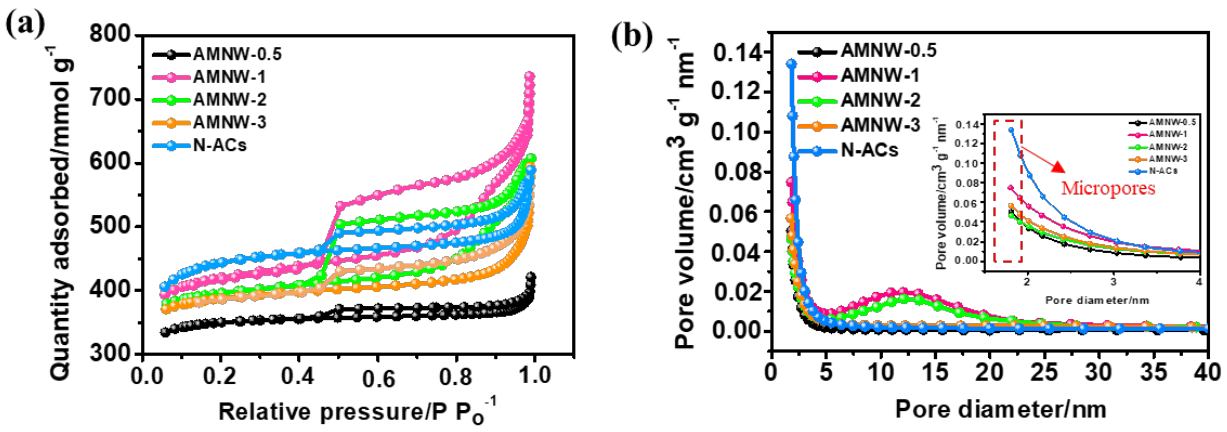

Fig. 3. 3. (a) N_2 adsorption-desorption isotherm and (b) pore size distribution curves.

3.4.3 Raman and TGA analysis

The Raman spectra of the materials are shown in Fig. 3.4a. The Raman spectra were used to evaluate the combined effect of activation and carbonization of the carbons. The Raman shift of all the materials showed the presence of a D-band (~1349 cm^{-1}) (called D_1 in the analysis; see below) and a G-band (~1598-1600 cm^{-1}) [55] (Table S3.3). The presence of the D-band is due to defects in the material and the G-band is a feature of the sp^2 graphitic materials [56]. The deconvoluted spectra of the activated materials also showed the presence of a further vibration (D_3; Fig. S3.4). The D_3 band result from amorphous carbon and disordered graphitic lattice. The D3 band is more visible in AMNW-2 and AMNW-3 due to higher concentration of KOH that led to destruction of the carbon. A measure of the disorder in the materials is given by the D_1/G band intensity ratios. As can be seen (Table S3.3), the disorder increased with the KOH:carbon ratio viz. 2.9 (AMNW-0.5) < 3.9 (AMNW-1) < 4.3 (AMNW-2) < 4.5 (AMNW-3).

Fig. 3.4c,d shows the TGA and TGA-derivative curves of the pristine, pretreated, and activated marula nuts. MNW (Fig. 3.4d) showed three weight losses at 52 °C [57], due to loss of moisture, at 295 °C, due to polymer (cellulose and hemicellulose) degradation [58] and at 356 °C due to lignin loss [58]. The remaining mass of MNW was 11% (Fig. 3.4c) showing the presence of inorganic compounds in the material. The PMNW showed a weight loss at ~63 °C

due to the loss of moisture and two other degradation events at 337 and 471 ℃ due to the breakdown of lignin and removal of most of the inorganic material ca. 1% residue).

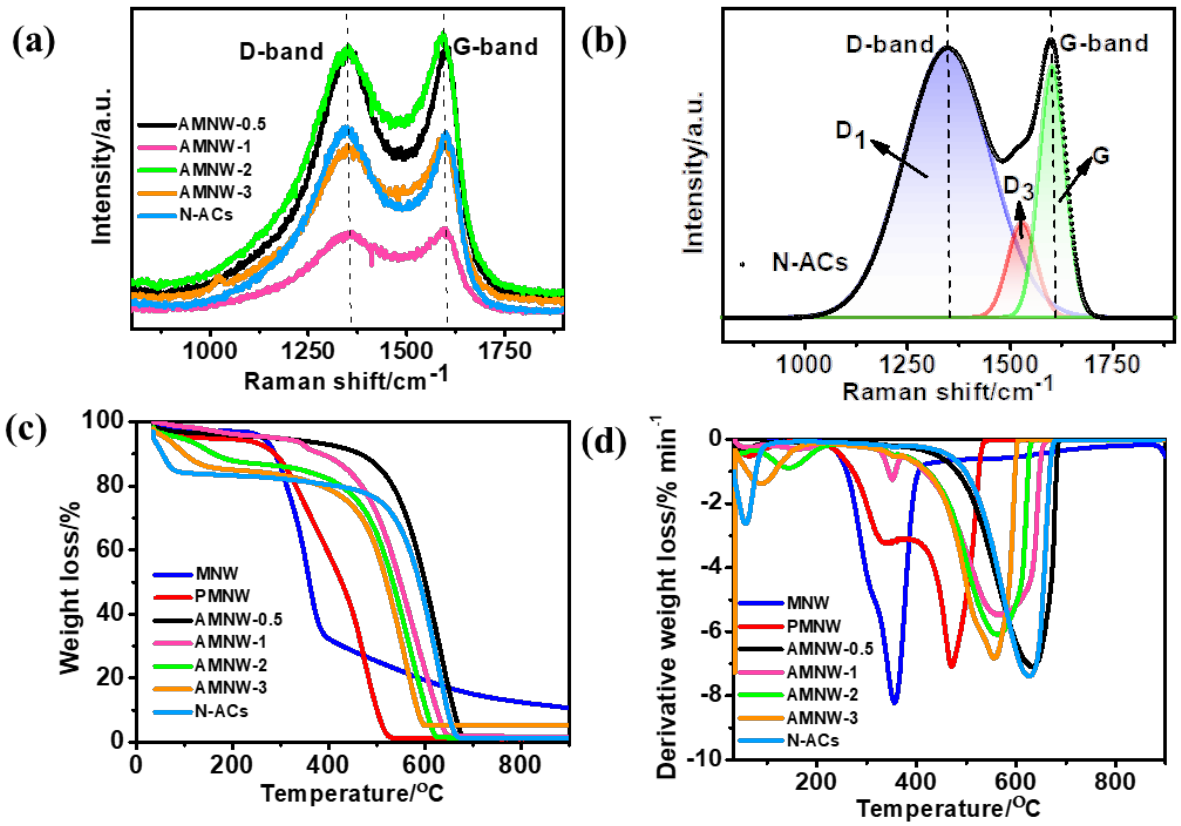

Fig. 3. 4. (a) Raman spectra, (b) Deconvoluted Raman spectra of N-ACs, (c) TGA and (d) TGA-derivatives of activated carbons.

Activation with KOH resulted in removal of carbons that gave rise to the peak at ca. 400 ºC and a shift (and broadening) of the major peak from 620 ºC to ca. 550 ºC with increasing KOH:carbon ratio. This is consistent with the formation of a more porous material with activation. [59]. The small peaks at 351 ℃ (AMNW-1) and 358 ℃ (AMNW-2 and AMNW-3) are due to the presence and degradation of lignin. The materials all showed small amounts (1 -5 %) of residue which can be due to the ash content present in the materials.

3.4.4 Effect of nitrogen-doping on activated carbons

Nitrogen doping was only performed on the AMNW-2 as (i) it showed slightly high number of micropores area that facilitates charge storage and (ii) defects which can improve electron transport.

SEM images of the N-ACs is shown in Fig. 3.2d,e. The SEM image still clearly shows the presence of the irregular holes seen in the SEM image of AMNW-2. Energy dispersive spectroscopy (EDS) mapping was applied to investigate the elements present in the N-ACs. This also showed that the nitrogen was evenly dispersed across the carbon (Fig. 3.2g).

The surface area of AMNW-2 increased from 1266 to 1427 $m^2 g^{-1}$ on N doping (Fig. 3.3a and Table S3.2). This surface area increase suggests that the melamine decomposition, that covers the surface with C and N atoms and does not cover the holes that were formed due to the KOH reaction with carbon [60].

The Raman spectra was recorded and the peaks deconvoluted using a Lorentzian function in order to calculate the intensity ratio of the D-band to the G-band (Fig. 3.4b). Upon introducing nitrogen to AMNW-2, the G-band shifted to a higher wavenumber (Table S3.3) and the D_1/G ratio decreased from 4.3 to 3.5. This observation suggests that even though the addition of N will produce a less graphitized carbon surface, the added annealing at the high temperature is a more important factor in determining the surface structure. The decrease of the D_1/G ratio is also influenced by the increase in the number of carbon atoms introduced from melamine resulting in the further graphitization of the material [60].

TGA was performed on the N-ACs sample. N-ACs was more thermally stable than AMNW-2 with a carbon decomposition temperature at 630 ℃ (Fig. 3.4d) as compared to a temperature of 589℃ for the AMNW-2 material. The high stability of N-ACs might be due to the increase of carbon content from melamine decomposition (Fig. 3.4c).

3.4.5 XPS analysis

The survey XPS scan of N-ACs and AMNW-2 (Fig.3.5a) showed the presence of C1s, N1s and O1s at ca. 284 eV, 399 eV and 532 eV [61]. The presence of N in AMNW-2 indicates that marula nuts waste naturally contains a small amount of nitrogen (0.9%) (Table 3.2). After nitrogen doping of AMNW-2, the nitrogen content of the N-ACs was found to be 5.1 % (Table 3.2).

Table 3. 2. XPS atom % of AMNW-2 and N-ACs.

Type of material	XPS atom %		
	C	O	N
AMNW-2	78.3	16.8	0.9

N-ACs	84.9	7.9	5.1

The C1s peak for AMNW-2 was deconvoluted, resulting in the detection of five different C atom types (Fig. 3.5b). The signals comprise of sp^2 C-C (284.2 eV), sp^3 C-C (285.8 eV), C-O (288.2 eV), C=O (289.8 eV) and O-C=O (292.4 eV) [62, 63]. The O1s peak seen in the survey scan was also deconvoluted and is shown in Fig. 3.5c with metal oxides at 531.2 eV, O-C-O (533.1 eV) and O-C=O (534.1 eV) [64, 65] The N1s peak deconvolution was done, and it showed three peaks which are attributed to pyridinic-N (398.8 eV), pyrrolic-N (399.8 eV) and graphitic-N (402.2 eV) (Fig. 3.5d) [66].

The C1s peak for N-ACs was deconvoluted (Fig. 3.5e) and it showed five carbon signals for sp^2 C-C/sp^2 C-N (284.2 eV), sp^3 C-C/sp^3 C-N (285.2 eV), C-O (286.8 eV), C=O (289.2 eV) and O-C=O/N-C=O (291.7 eV) [62]. The C1s peak for N-ACs showed a decrease of atomic % of C-C sp^2 (31.4%) and C-C sp^3 (18.9%) as compared to C-C sp^2 (52.7%) and C-C sp^3 (26.4%) for AMNW-2 (Table S3.4). This can be attributed to the formation of C-N bonds that are formed when nitrogen is introduced to the activated material. This shows that the decomposition of melamine generates more C-N bonds.

The deconvolution of O1s was also done and it comprises of two signals (Fig. 3.5f) at 531.2 eV and 533.0 eV for O-C-O and O-C=O [64, 67]As seen from Table S3.4, the atomic % of O-C=O oxygen decreased after nitrogen doping. This is due to the removal of oxygen on the surface after reaction with the melamine, to form nitrogen containing surface species. The deconvolution of the N-ACs N1s peak gave rise to five signals (Fig. 3.5g) [68]. The five signals comprises of pyridinic-N at 398.1 eV, pyrrolic-N at 399.6 eV, graphitic-N at 401.4 eV, oxygenated-N at 403.4 eV and chemisorbed-N at 405.8 eV [69, 70]. As seen from Table S3.4, there are mainly pyridinic and pyrrolic species which are chemically active nitrogen bonding configurations enhancing the conductivity of the material, which is essential for improving capacitance. These results are in good agreement with the data reported by Guan et al. for nitrogen doping of activated carbon from pine nut shell using melamine as nitrogen source [71].

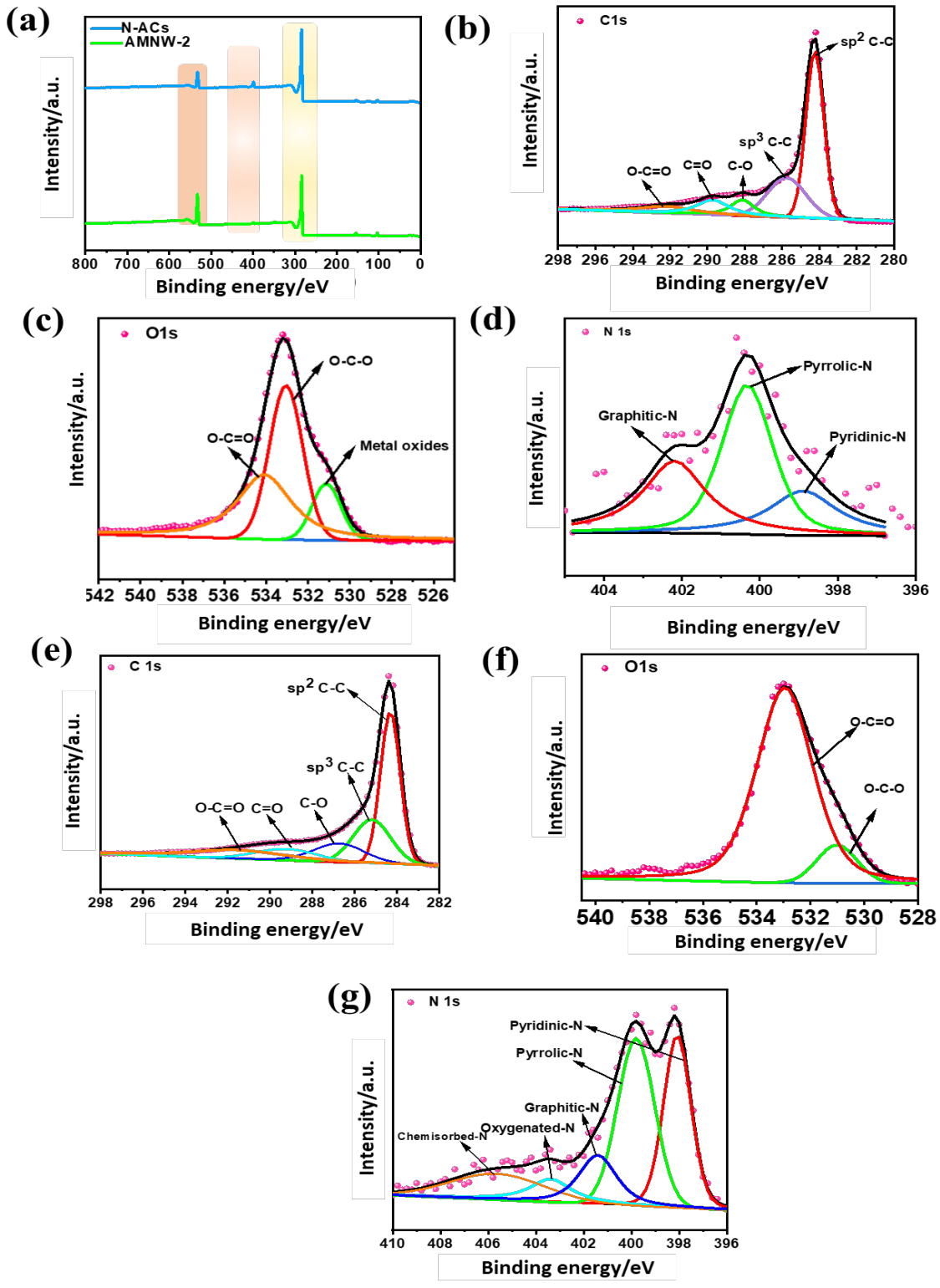

Fig. 3. 5. (a) Survey scans of AMNW-2 and N-ACs, (b) C1s, (c) O1s and (d) N1s deconvoluted spectrum of AMNW-2, (e) C1s, (f) O1s and (g) N 1s deconvoluted spectrum of N-ACs.

3.4.6 Electrochemical analysis

The electrochemical properties of the ACs were analysed in a three-electrode system using 6 M and 2.5 KNO_3 electrolyte in a potential range (E vs SCE/V) of -0.8-0.0 V as shown in Fig. 3.6. Fig. 3.6a,c shows the cyclic voltammograms (CV) of the materials at 30 mV s^{-1} in 6 M KOH (Fig. 3.6a) and 2.5 KNO_3 (Fig. 3.6c). All the CV curves have a rectangular shape demonstrating an electric double layer capacitance [72]. AMNW-2 showed a higher current response than the other ACs in both 6 M KOH and 2.5 M KNO_3. This was not directly related to surface area since AMNW-1 had the highest surface area (1353 m^2 g^{-1}). This is not unexpected since the surface area is not directly proportional to capacitance as capacitance depends on other factors such as conductivity, porosity and the type of electrolyte used [73]. AMNW-2 had the highest micropore volume and this could have been the important property that determined the current response that serve as charge storage as compared to mesopores which facilitates charge movement [74].

Fig. 3.6b, d shows the charge-discharge curves for activated carbons materials at 1 A g^{-1} and this figure displays a triangular shape which is characteristic of an ideal capacitor [75]. AMNW-2 displayed a higher discharge time than the other undoped activated carbons in both 6 M KOH and 2.5 M KNO_3.

Upon doping AMNW-2 with nitrogen, the current response improved in both 6 M and 2.5 KNO_3 due to an improved conductivity (see EIS data below). Comparing N-ACs in both 6 M KOH and 2.5 M KNO_3, the N-ACs had a high current response (Fig. 3.6a), a long discharge time (Fig. 3.6b), and a high specific capacitance (Fig. 3.6e) in 6 M KOH than in 2.5 M KNO_3. N-ACs performed better in 6 M KOH than in 2.5 KNO_3.

The calculated capacitance of all the materials are listed in Table S3.5. Table S3.5 shows that increasing current densities leads to limited amount of charge stored hence the decrease in capacitance (Fig. 3.6e,f).

The high capacitance of the materials in 6 M KOH than in 2.5 M KNO_3 is attributed to the high ionic conductivity of the KOH electrolyte. According to previous studies [76, 77], the excellent electrochemical performance of carbon materials in 6 M KOH can be due to ionic mobility, conductivity, and electrolyte pH. Table 3.3 summarizes the parameters of the electrolytes showing that KOH have higher conductivity and high ionic mobility hence the higher capacitances. Again, the high amount of charge stored in N-ACs can be attributed to an

improved conductivity [78]. Wang et al. [79] also reported an increase in capacitance due to the influence of nitrogen on activated carbons, implying that nitrogen doping improved the conductivity of the material.

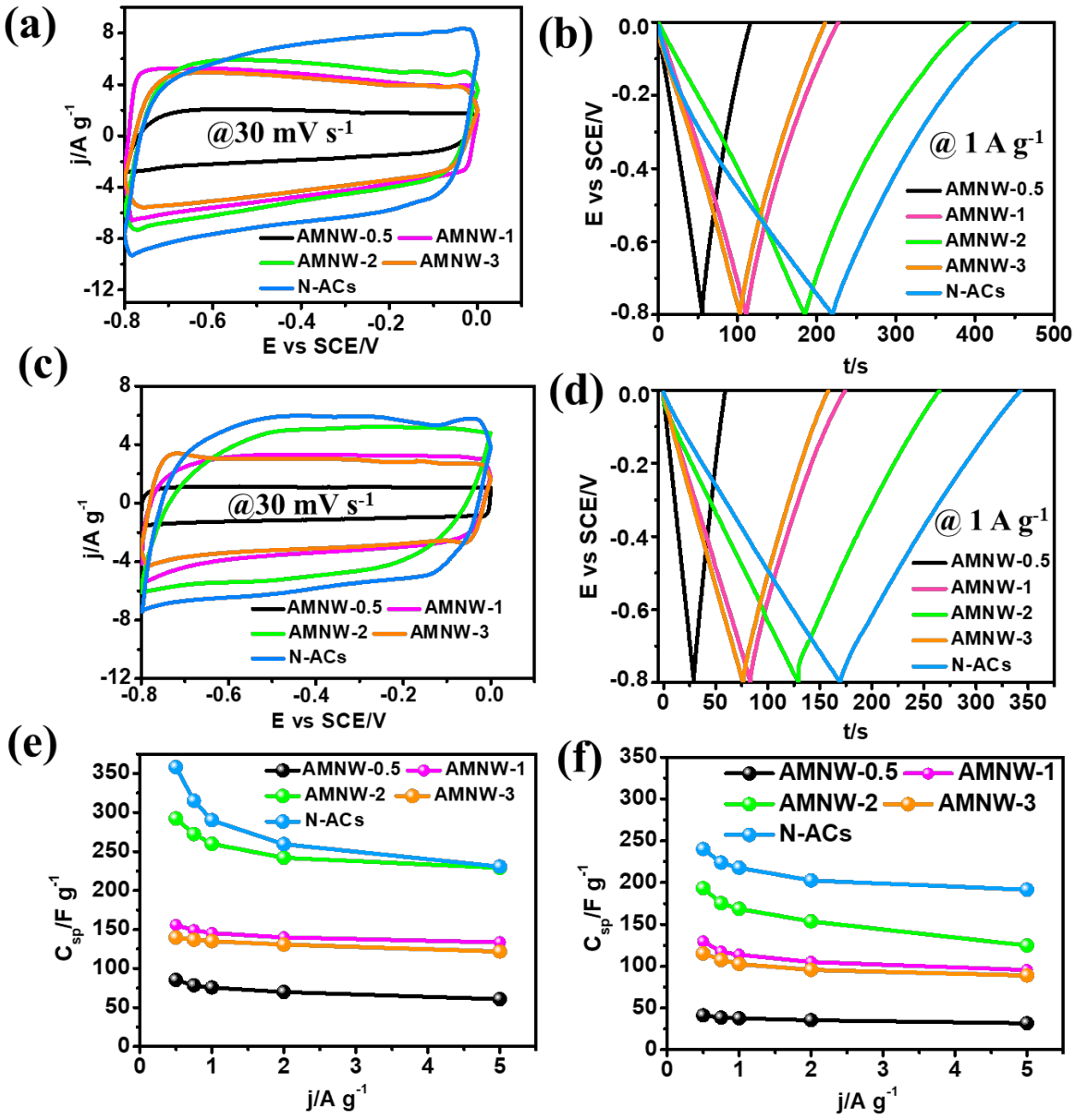

Fig. 3. 6. (a) CV, (b) GCD, (e) Csp VS current density in 6 M KOH, (c) CV, (d) GCD , (e) and (f) Csp VS current density in 2.5 M KNO_3 of ACs and N-ACs.

Table 3. 3. Summary of the sizes of ions [80].

Type of ion	Size of bare ion/Å	Size of hydrated ion/Å	Ionic conductivity/Scm^2 mol^{-1}
K^+	1.15	3.31	73.5
OH^-	1.76	3.00	198
NO^{3-}	2.64	3.35	71.42

The high conductivity (198 Scm^2 mol^{-1}) and smaller hydrated size (3.00 Å) of OH^- ions compared to NO^{3-} ions explains why KOH has a higher ion mobility and conductivity than NO^{3-} [80]. Hence, the high capacitance values of the materials when using KOH electrolyte.

However, operating the cell in a wider voltage in 6 M KOH is limited due to the water decomposition at 1.23 V [78]. When compared to alkaline electrolytes (i.e. KOH), neutral electrolytes (i.e. KNO_3) can be operated at a high voltage (~2 V) because the H^- and OH^- concentrations are lower, resulting in a potential shift of the hydrogen and oxygen evolution to a wider stable potential window, that increases the amount of energy stored. For example, Sheng et al. reported on the use of a 1 M Na_2SO_4 neutral electrolyte with an operating voltage up to 1.6 V giving an energy density of 25.7 Wh kg^{-1} [78]. Neutral electrolytes have been reported to have a higher voltage window and to be less corrosive than alkaline electrolytes [81]. As a result, carbon-based materials in symmetric devices using neutral electrolytes have been considered as a possible way to achieve higher energy density while reducing the impact of corrosive effects on the device. Hence, in this study, a symmetric device was assembled and operated at a wider potential using 2.5 M KNO_3 to enhance the energy density.

Due to the wide potential window of the neutral electrolyte, N-ACs was run at different cell potential from 1.5-2.0 V as shown from CV curves (Fig.3.7a) and GCD curves (Fig. 3.7b) in 2.5 M KNO_3 electrolyte. Both CV and GCD curves show that the cell potential becomes stable up to 1.8 V and further increasing the potential up to 2 V changes the CV and GCD shape due to the polarization of the material as the electrolyte decomposes at high potential range (> 1.8 V). Hence, the material was further run at different scan rates and current densities at a cell

potential of 1.8 V. The cell potential of neutral electrolytes can reach up to 1.8 V due to the low concentrations of H^+ and OH^-, given that increased oxygen and dihydrogen evolution increases the electrolyte stability window [82]. The wider stability window of neutral electrolytes can be explained by the high overpotential as effects of ion hydration fundamentals processes [83–85]. This is due to the fact that neutral electrolytes lack free H^+ and OH^- resulting in high overpotential on both hydrogen evolution reaction (HER) and oxygen evolution reaction (OER). This notion was used by Hong et al. by comparing linear weep voltammetry of 1 M HCl, KOH, and KCl, where the water electrolysis happening in KCl had similar onset potentials as the OER in HCl to HER in KOH solutions [84].

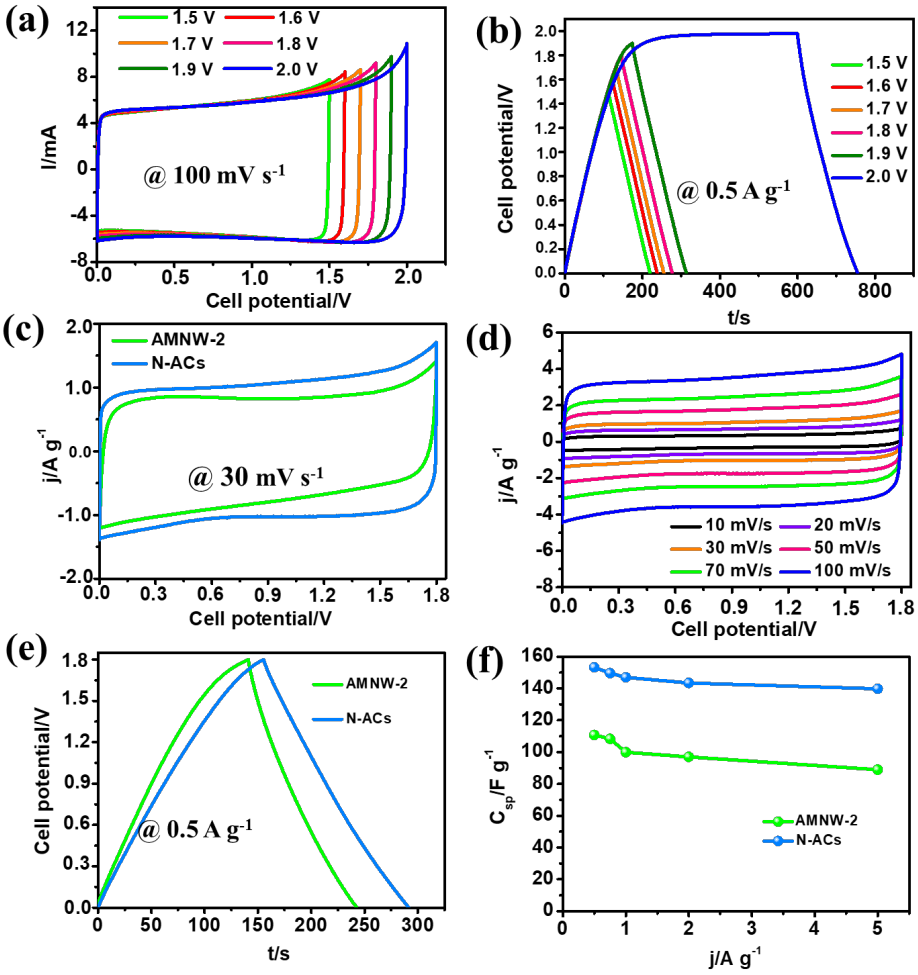

Fig. 3. 7. (a) CV tests of N-ACs at different cell potential (b) GCD curves of N-ACs at different cell potential, (c) CV curves comparison of AMNW-2 and N-ACs at 30 mV s^{-1}, (d) CV curves ACs at different scan rates, (e) GCD and (f) specific capacitance comparison of AMNW-2 and N-ACs current densities in 2.5 M KNO_3.

This perception implied that HER and OER occurred through direct oxidation/reduction of water molecules[86]. The amount of reactant for water decomposition can be depleted by reducing the concentration of water which further widen the electrochemical stability.

The CV curves of AMNW-2 and N-ACs were then compared at 30 mV s^{-1} (see Fig. 3.7c). N-ACs showed a high current response which can be attributed to the higher conductivity of the material arising from the high nitrogen content of 5.1% [87]. CV curves of N-ACs were ran at different scan rates from (Fig. 3.7d) and showed the rectangular shape of an ideal capacitor. GCD curves of the materials (Fig. 3.7e) were compared at 0.5 A g^{-1} and they showed a triangular shape which is that of an ideal capacitor. N-ACs showed a higher charge-discharge time which is in good agreement with the high current from the CV curves. The GCD curves of N-ACs were ran at current densities from 0.5-5 A g^{-1} (Fig. S3.5) and showed a triangular shape which is that of an ideal capacitor indicating reversible adsorption and desorption of electrolyte ions.

The specific capacitance was calculated from these GCD curves using equation 3.4 and the capacitance decreased as the current density increased which indicates a good rate capability (Fig. 3.7f). The capacitance of N-ACs obtained at 0.5 A g^{-1} was 153.3 F g^{-1} and 139.8 F g^{-1} at 5 A g^{-1}.

The Nyquist plots (Fig. 3.8a) of AMNW-2 and N-ACs were modelled before and after 6 000 cycles. The material's bulk properties were shown by the presence of the solution resistance (R_s) (i.e. electrodes, electrolytes, current collectors and separators), charge transfer resistance (R_{ct}), internal resistance (R_{int}), double layer capacitance (Cd_{ll}) and the constant phase element (CPE) [61,88]. The impedance power law relationship of CPE (ZCPE) is shown in equation 3.10:

$$Z_{CPE} = [Q\ (j\omega)^n]^{-1} \tag{3.10}$$

where Q represents the frequency-independent constant, j = $\sqrt{-1}$, radial frequency is represented by symbol ω, and n lies between -1 and 1 ($-1 \leq n \leq 1$) which is the slope of Log Z vs. Log f.

The CPE becomes a pure resistor when n=0, while the CPE is that of a pure capacitor when n=1, and when n=-1, the CPE is that of an inductor. However, when n=0.5, the CPE can be regarded as equivalent to a Warburg impedance (Z_w) [47]. From Table 4, the value of n=0.77 for N-ACs after cycling demonstrates the nature of N-ACs as an EDCLs material.

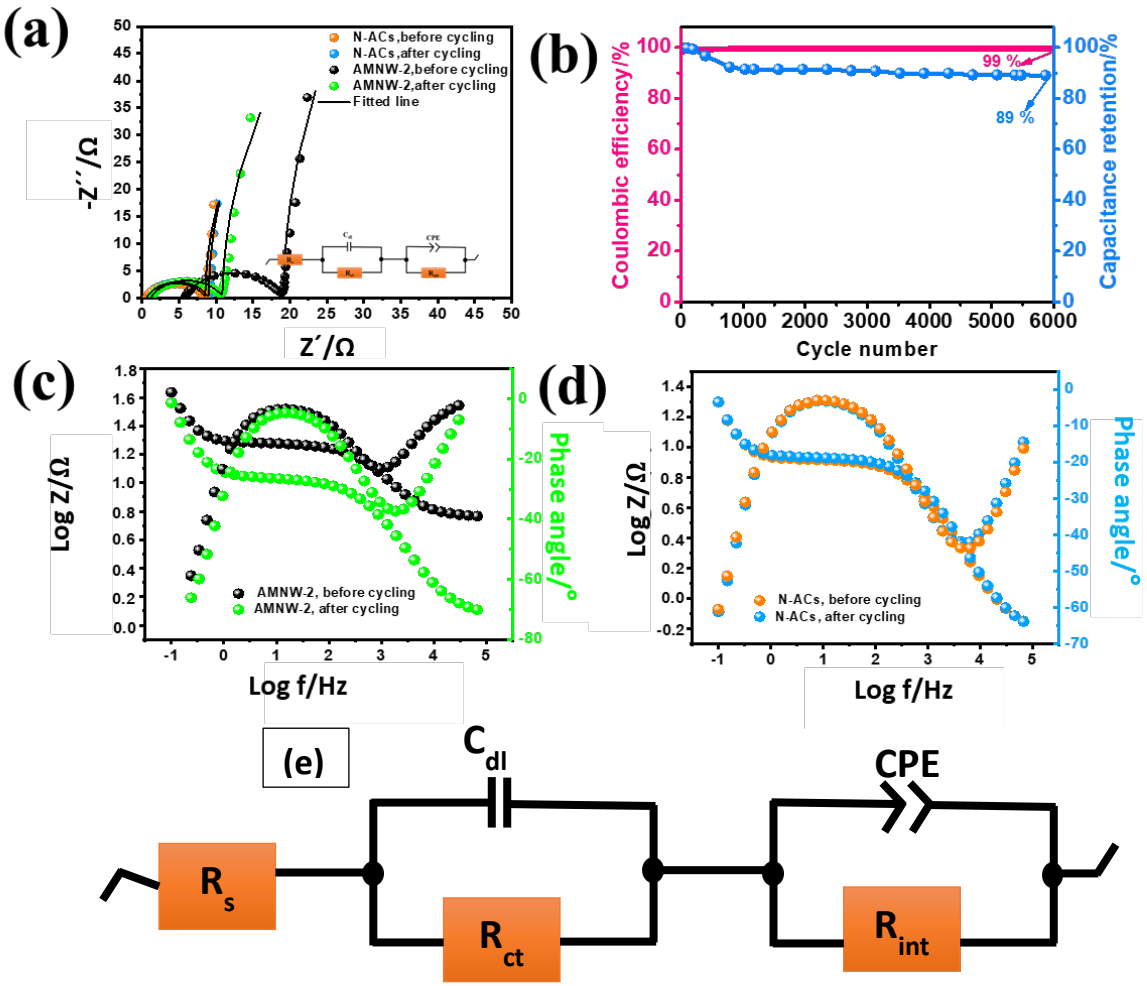

Fig. 3. 8. (a) Nyquist plots of AMNW-2 and N-ACs obtained before and after 6,000 cycles with electrical equivalent circuit used to fit Nyquist plots, (b) cyclic stability of N-ACs, (c,d) Bode plots before and after 6,000 cycles of the AMNW-2 and N-ACs symmetric cells and (e) electrical equivalent circuit used to fit Nyquist plots.

The R_s value of N-ACs is 0.59 Ω, which is lower than the R_s value of AMNW-2 (1.18 Ω) after cycling and suggests that nitrogen improved the solution resistance of the ACs. The R_{CT} value of the N-ACs was also smaller (7.99 Ω) than that of the AMNW-2 (9.77 Ω), which is due to the improved conductivity resulting in better electrode/electrolyte surface contact from the nitrogen doping [89, 90]. Interestingly, the Cd_{ll} for N-ACs was higher before and after cycling than AMNW-2 which indicates that nitrogen doping made the carbon materials more capacitive. The R_{int} obtained for N-ACs after cycling was smaller (~ 186 Ω) than AMNW-2 (~235 Ω). Given that R_{int} is mainly due to the ohmic drop (IR drop) and diffusion rate of electrolytes ions [91], hence N-ACs gave a smaller R_{int} than AMNW-2 due to the improved surface contact of the material and electrolytes ions. The knee frequency (f_o / Hz) from the EIS

data (Table 3.4) was estimated and gave the power capability of the materials. A high value of the f_o / Hz indicates the capability of a material to have a high power density and to provide energy density in a short time frame. The EIS parameters in Table 3.4 show that N-ACs gave a higher f_o (ca. 25.1 Hz, response time, τ of 40 ms) after 6000th cycles. This is important if one considers that high powered supercapacitors available commercially operate at less than 1 Hz. The phase angles of the symmetric cells after cycling, as determined by Bode plots (Fig. 3.8c & d), demonstrated that the AMNW-2 symmetric cell (69º) cell has a higher phase angle at low frequencies, implying decreased ionic permeability and thus insulating characteristics. The high ionic permeability of the N-ACs symmetric cell (60 º) cell occurs at low frequencies, which is indicative of poor insulation, revealing that the N-ACs electrode material is permeable to solution ions.

The cyclic stability of N-ACs for the symmetric device was tested using charge-discharge up to 6000 cycles at a current density of 5 A/g (Fig. 3.8b). A Coulombic efficiency of 99 % was obtained with a capacitance retention of 89 %. The excellent capacitance retention of the material is due to its structural stability that permits the re-usability of the material.

Table 3. 4. EIS parameters of the synthesized materials for two-electrode system in 2.5 M KNO_3.

EIS parameters	Electrode material for the symmetric supercapacitor			
	AMNW-2		N-ACs	
	Before cycling (1st cycle)	After cycling (6,000th cycle)	Before cycling (1st cycle)	After cycling (6,000th cycle)
R_s / Ω	5.70 ± 0.47	1.18± 0.47	0.60 ± 0.46	0.59 ± 0.47
ESR (R_{ct}) / Ω	13.48 ± 0.82	9.77 ±0.84	8.44 ± 0.79	7.99 ± 0.81
C_{dl} / μF	41.26 ± 3.61	45.54 ± 4.45	89.19 ± 0.02	90.67 ± 0.02
R_{int} / Ω	344.70 ± 277.10	235.3 ± 158.1	224.3 ± 558.6	186.01 ± 384.0
CPE /mF s^(a-1)	0.13 ± 0.11	0.21 ± 0.28	0.15 ± 0.24	0.17 ± 0.30
N	0.77	0.76	0.79	0.77
f_o / Hz	11.4	16.9	25.1	25.1
τ / ms	88	59	40	40
Phase angle	59º	66º	61º	60º

The evaluation of the amount of charge stored and the rate at which it was delivered can be determined by two parameters: energy and power density. A Ragone plot of the materials is shown in Fig. 3.9. The N-ACs demonstrated a higher energy density of 17.2 Wh kg^{-1} and a power density of 448.7 W kg^{-1}, than that of AMNW-2 (12.5 Wh kg^{-1}). The improved energy density of N-ACs is due to the improved conductivity and total surface area of the material. The energy density of ACs from marula nuts waste in this study is comparable to activated carbons from hazel nutshell with an energy density of 11.1 Wh kg^{-1} in 1.0 M Na_2SO_4 electrolyte [92]. In addition, the single device was connected to a light emitting diode (LED, 1.6 V) and this device successfully lit up a red LED (see inset in Fig. 3.9) for over a minute after charging for 20 s.

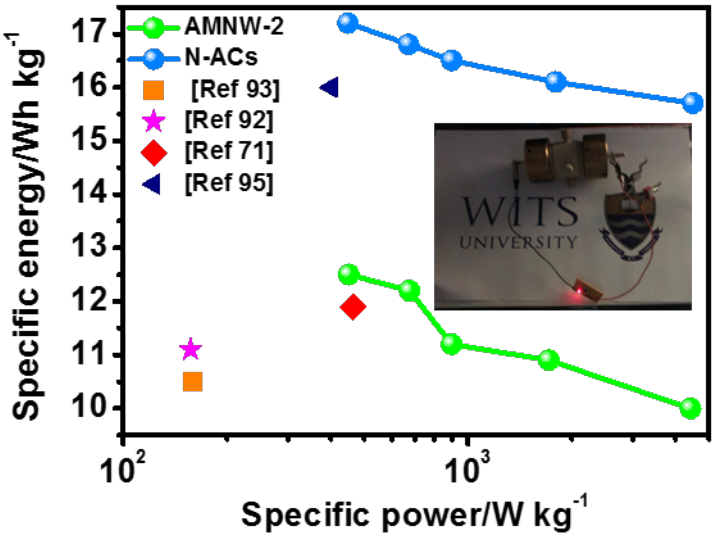

Fig. 3. 9. Ragone plot of AMNW-2 and N-ACs. The inset shows an image of a red LED powered by the N-ACs electrode-based device.

Our results indicate that nitrogen improves the specific capacitance of carbon. To place these current findings into perspective, the findings on activated carbons and nitrogen-doped activated carbons from the use of biomass in SCs, as well as their energy densities, is given in Table 3.5. The specific energy and power obtained in this study was comparable to other studies and in some cases found to be higher to other undoped porous carbons and nitrogen doped porous carbons. These results show that energy density depends on many factors such as activating agent, surface area, type of electrolyte, etc.

Table 3. 5. Summary of energy and power densities of activated carbons in SCs.

Biomass	Precursor	Surface area (m^2 g^{-1})	Electrolyte	Cell potential (V)	Current density (A g^{-1})	Specific energy (W h kg^{-1})	Specific power (W kg^{-1})	Reference
Activated carbons								
Marula nuts shell	KOH	1266	2.5 M KNO_3	2.0	0.5	12.5	451.4	This study
Hazel nutshell	MgO	552	1M Na_2SO_4	2.0	0.25	11.1	156.8	[92]
Eucalyptus bark	KOH	1003	1M Na_2SO_4	1.8	0.2	10.5	159.5	[93]
Cotton fiber	$ZnCl_2$	2549	1 M Na_2SO_4	1.8	0.5	13.75	-	[94]
		Nitrogen doping						
N-ACs	KOH/melamine	1427	2.5 M KNO_3	2.0	0.5	17.2	448.7	This study
Pine nut shells	KOH/melamine	1806	1 M $NaSO_4$	1.8	1.0	11.9	463.6	[71]
Orange peel	$FeCl_3$/Urea	1514.2	0.5 M Li_2SO_4	1.6	0.5	16	400	[95]

Cellulose	NaOH/urea	2245	1 M Na_2SO_4	1.8	0.5	17.24	452	[96]

3.5 Conclusions

Nitrogen-doped activated carbons with a high porous surface area of 1427 m^2 g^{-1} and high nitrogen content of 5.1% was successfully synthesized from marula nuts via KOH activation and carbonization at 800 ℃ using melamine as a nitrogen source. Electrochemical characterizations of the materials were tested for supercapacitor applications using 6 M KOH and 2.5 M KNO_3 in three electrode system. AMNW-2 and N-ACs performed better in 6 M KOH than 2.5 M KNO_3 than the other activated materials due to the higher conductivity of the alkaline electrolyte. For a two-electrode system, the AMNW-2 and N-ACs were examined using 2.5 M KNO_3 with a wider cell voltage window of 1.8 V. The activated material gave an energy density of 12.5 Wh/kg which improved to 17.2 Wh/kg after doping with nitrogen. These results in a neutral 2.5 M KNO_3 electrolyte are fascinating, empowering, and demonstrate the feasibility of using marula nut waste to produce porous carbons, demonstrating the exciting potential for producing activated carbons at low cost, which could pique industry interest for possible application in energy storage.

References

[1] M.U. Sasmaz, E. Sakar, Y.E. Yayla, U. Akkucuk, The relationship between renewable energy and human development in OECD countries: A panel data analysis, Sustainability (Switzerland). 12 (2020) 1–16.

[2] Y. Li, X. Han, T. Yi, Y. He, X. Li, Review and prospect of NiCo2O4-based composite materials for supercapacitor electrodes, Journal of Energy Chemistry. 31 (2019) 54–78.

[3] Q. Geng, H. Wang, J. Wang, J. Hong, W. Sun, Y. Wu, Y. Wang, Boosting the Capacity of Aqueous Li-Ion Capacitors via Pinpoint Surgery in Nanocoral-Like Covalent Organic Frameworks, Small Methods. 6 (2022).

[4] C. Cai, Y. Zou, C. Xiang, H. Chu, S. Qiu, Q. Sui, F. Xu, L. Sun, A. Shah, Broccoli-like porous carbon nitride from ZIF-8 and melamine for high performance supercapacitors, Appl Surf Sci. 440 (2018) 47–54.

[5] F.W. Richey, C. Tran, V. Kalra, Y.A. Elabd, Ionic liquid dynamics in nanoporous carbon nanofibers in supercapacitors measured with in operando infrared spectroelectrochemistry, Journal of Physical Chemistry C. 118 (2014) 21846–21855.

[6] Q. Wang, J. Yan, Y. Wang, T. Wei, M. Zhang, X. Jing, Z. Fan, Three-dimensional flower-like and hierarchical porous carbon materials as high-rate performance electrodes for supercapacitors, Carbon N Y. 67 (2014) 119–127.

[7] Z.S. Wu, K. Parvez, X. Feng, K. Müllen, Graphene-based in-plane micro-supercapacitors with high power and energy densities, Nat Commun. 4 (2013).

[8] M. Passalacqua, D. Lanzarotto, M. Repetto, M. Marchesoni, Advantages of using supercapacitors and silicon carbide on hybrid vehicle series architecture, Energies (Basel). 10 (2017) 1–14.

[9] D. Pech, M. Brunet, H. Durou, P. Huang, V. Mochalin, Y. Gogotsi, P.L. Taberna, P. Simon, Ultrahigh-power micrometre-sized supercapacitors based on onion-like carbon, Nat Nanotechnol. 5 (2010) 651–654.

[10] M. Olivares-Marín, J.A. Fernández, M.J. Lázaro, C. Fernández-González, A. Macías-García, V. Gómez-Serrano, F. Stoeckli, T.A. Centeno, Cherry stones as precursor of activated carbons for supercapacitors, Mater Chem Phys. 114 (2009) 323–327.

[11] X. Zhu, S. Yu, K. Xu, Y. Zhang, L. Zhang, G. Lou, Y. Wu, E. Zhu, H. Chen, Z. Shen, B. Bao, S. Fu, Sustainable activated carbons from dead ginkgo leaves for supercapacitor electrode active materials, Chem Eng Sci. 181 (2018) 36–45.

[12] C. Peng, J. Lang, S. Xu, X. Wang, Oxygen-enriched activated carbons from pomelo peel in high energy density supercapacitors, RSC Adv. 4 (2014) 54662–54667.

[13] N. Sinan, E. Unur, Hydrothermal conversion of lignocellulosic biomass into high-value energy storage materials, Journal of Energy Chemistry. 26 (2017) 783–789.

[14] S. Shackleton, Livelihood benefits from the local level commercialization of savanna resources: A case study of the new and expanding trade in marula (Sclerocarya birrea) beer in Bushbuckridge, South Africa, S Afr J Sci. 100 (2004) 651–657.

[15] C. Shackleton, S. Shackleton, The importance of non-timber forest products in rural livelihood security and as safety nets: A review of evidence from South Africa, S Afr J Sci. 100 (2004) 658–664.

[16] T. Mkungunugwa, S. Manhokwe, A. Chawafambira, M. Shumba, Synthesis and Characterisation of Activated Carbon Obtained from Marula (Sclerocarya birrea) Nutshell, J Chem. 2021 (2021).

[17] Q. Chen, X. Tan, Y. Liu, S. Liu, M. Li, Y. Gu, P. Zhang, S. Ye, Z. Yang, Y. Yang, Biomass-derived porous graphitic carbon materials for energy and environmental applications, J Mater Chem A Mater. 8 (2020) 5773–5811.

[18] A. Javier Sánchez, Characterization of activated carbon produced from coffee residues by chemical and physical activation., KTH Chemical Science and Engineering. (2011) 66.

[19] A.S. Alzaydien, Physical, chemical and adsorptive characteristics of local oak sawdust based activated carbons, Asian J Sci Res. 9 (2016) 45–56.

[20] W. Li, L. bo Zhang, J. hui Peng, N. Li, X. yun Zhu, Preparation of high surface area activated carbons from tobacco stems with K2CO3 activation using microwave radiation, Ind Crops Prod. 27 (2008) 341–347.

[21] J. Pallarés, A. González-Cencerrado, I. Arauzo, Production and characterization of activated carbon from barley straw by physical activation with carbon dioxide and steam, Biomass Bioenergy. 115 (2018) 64–73.

[22] G. Lota, T.A. Centeno, E. Frackowiak, F. Stoeckli, Improvement of the structural and chemical properties of a commercial activated carbon for its application in electrochemical capacitors, Electrochim Acta. 53 (2008) 2210–2216.

[23] V. Ruiz, C. Blanco, E. Raymundo-Piñero, V. Khomenko, F. Béguin, R. Santamaría, Effects of thermal treatment of activated carbon on the electrochemical behaviour in supercapacitors, Electrochim Acta. 52 (2007) 4969–4973.

[24] B. Fang, Y.Z. Wei, M. Kumagai, Modified carbon materials for high-rate EDLCs application, J Power Sources. 155 (2006) 487–491.

[25] J. ichi Ozaki, N. Kimura, T. Anahara, A. Oya, Preparation and oxygen reduction activity of BN-doped carbons, Carbon N Y. 45 (2007) 1847–1853.

[26] X. Yan, Y. Jia, X. Yao, Defects on carbons for electrocatalytic oxygen reduction, Chem Soc Rev. 47 (2018) 7628–7658.

[27] W. Han, H. Wang, K. Xia, S. Chen, P. Yan, T. Deng, W. Zhu, Superior nitrogen-doped activated carbon materials for water cleaning and energy storing prepared from renewable leather wastes, Environ Int. 142 (2020) 105846.

[28] B. Li, F. Dai, Q. Xiao, L. Yang, J. Shen, C. Zhang, M. Cai, Nitrogen-doped activated carbon for a high energy hybrid supercapacitor, Energy Environ Sci. 9 (2016) 102–106.

[29] X. Wang, Y. Liu, L. Zhu, Y. Li, K. Wang, K. Qiu, N. Tippayawong, P. Aggarangsi, P. Reubroycharoen, S. Wang, Biomass derived N-doped biochar as efficient catalyst supports for CO2 methanation, Journal of CO2 Utilization. 34 (2019) 733–741.

[30] Y. Ding, Y. Li, Y. Dai, X. Han, B. Xing, L. Zhu, K. Qiu, S. Wang, A novel approach for preparing in-situ nitrogen doped carbon via pyrolysis of bean pulp for supercapacitors, Energy. 216 (2021) 119227.

[31] S. Ahmed, M. Rafat, A. Ahmed, Nitrogen doped activated carbon derived from orange peel for supercapacitor application, Advances in Natural Sciences: Nanoscience and Nanotechnology. 9 (2018).

[32] M. Sevilla, G.A. Ferrero, N. Diez, A.B. Fuertes, One-step synthesis of ultra-high surface area nanoporous carbons and their application for electrochemical energy storage, Carbon N Y. 131 (2018) 193–200.

[33] M. Zhou, F. Pu, Z. Wang, S. Guan, Nitrogen-doped porous carbons through KOH activation with superior performance in supercapacitors, Carbon N Y. 68 (2014) 185–194.

[34] R.J. Mo, Y. Zhao, M. Wu, H.M. Xiao, S. Kuga, Y. Huang, J.P. Li, S.Y. Fu, Activated carbon from nitrogen rich watermelon rind for high-performance supercapacitors, RSC Adv. 6 (2016) 59333–59342.

[35] K. Kierzek, G. Gryglewicz, Activated carbons and their evaluation in electric double layer capacitors, Molecules. 25 (2020).

[36] A. Lewandowski, A. Olejniczak, M. Galinski, I. Stepniak, Performance of carbon-carbon supercapacitors based on organic, aqueous and ionic liquid electrolytes, J Power Sources. 195 (2010) 5814–5819.

[37] F. Béguin, V. Presser, A. Balducci, E. Frackowiak, Carbons and electrolytes for advanced supercapacitors, Advanced Materials. 26 (2014) 2219–2251.

[38] H. Jiang, Y. Tian, M. Liu, X. Zhou, R. Xue, Influence of KNO3 on Capacitive Properties of Active Carbon in Potassium Ferricyanide Solutions, Int J Electrochem Sci. 17 (2022) 1–12.

[39] C. Zhong, Y. Deng, W. Hu, J. Qiao, L. Zhang, J. Zhang, A review of electrolyte materials and compositions for electrochemical supercapacitors, Chem Soc Rev. 44 (2015) 7484–7539.

[40] C.L. Lee, K.L. Chin, P.S. H'ng, U. Rashid, M. Maminski, P.S. Khoo, Effect of pretreatment conditions on the chemical–structural characteristics of coconut and palm kernel shell: A potentially valuable precursor for eco-efficient activated carbon production, Environ Technol Innov. 21 (2021).

[41] Y. Guo, Z. Zeng, Y. Liu, Z. Huang, Y. Cui, J. Yang, One-pot synthesis of sulfur doped activated carbon as a superior metal-free catalyst for the adsorption and catalytic oxidation of aqueous organics, J Mater Chem A Mater. 6 (2018) 4055–4067.

[42] L. Chen, T. Ji, L. Mu, J. Zhu, Cotton fabric derived hierarchically porous carbon and nitrogen doping for sustainable capacitor electrode, Carbon N Y. 111 (2017) 839–848.

[43] E. Zhen, J. Jiang, C. Lv, X. Huang, H. Xu, H. Dou, X. Zhang, Effects of binder content on low-cost solvent-free electrodes made by dry-spraying manufacturing for lithium-ion batteries, J Power Sources. 515 (2021).

[44] W. Yang, Z. Gao, J. Wang, J. Ma, M. Zhang, L. Liu, Solvothermal one-step synthesis of Ni-Al layered double hydroxide/carbon nanotube/reduced graphene oxide sheet ternary nanocomposite with ultrahigh capacitance for supercapacitors, ACS Appl Mater Interfaces. 5 (2013) 5443–5454.

[45] W. Sun, Y. Zhang, F. Yang, Tuning electrochemical performance of carbon-sphere-based supercapacitors by compressive stress, Electrochim Acta. 357 (2020).

[46] K. Makgopa, P.M. Ejikeme, C.J. Jafta, K. Raju, M. Zeiger, V. Presser, K.I. Ozoemena, A high-rate aqueous symmetric pseudocapacitor based on highly graphitized onion-like carbon/birnessite-type manganese oxide nanohybrids, J Mater Chem A Mater. 3 (2015) 3480–3490.

[47] T.P. Mofokeng, Z.N. Tetana, K.I. Ozoemena, Defective 3D nitrogen-doped carbon nanotube-carbon fibre networks for high-performance supercapacitor: Transformative role of nitrogen-doping from surface-confined to diffusive kinetics, Carbon N Y. 169 (2020) 312–326.

[48] K. Makgopa, P.M. Ejikeme, K.I. Ozoemena, Graphene oxide-modified nickel (II) tetra-aminophthalocyanine nanocomposites for high-power symmetric pseudocapacitor, Electrochim Acta. 212 (2016) 876–882.

[49] H.M. Yang, D.H. Zhang, Y. Chen, M.J. Ran, J.C. Gu, Study on the application of KOH to produce activated carbon to realize the utilization of distiller's grains, IOP Conf Ser Earth Environ Sci. 69 (2017).

[50] Harry. Marsh, F. Rodríguez-Reinoso, Activated carbon, Elsevier, 2006.

[51] J. Andas, M.L.A. Rahman, M.S.M. Yahya, Preparation and Characterization of Activated Carbon from Palm Kernel Shell, in: IOP Conf Ser Mater Sci Eng, Institute of Physics Publishing, 2017.

[52] G. Brodeur, E. Yau, K. Badal, J. Collier, K.B. Ramachandran, S. Ramakrishnan, Chemical and physicochemical pretreatment of lignocellulosic biomass: A review, Enzyme Res. 2011 (2011).

[53] W. Zhou, S. Lei, S. Sun, X. Ou, Q. Fu, Y. Xu, Y. Xiao, B. Cheng, From weed to multi-heteroatom-doped honeycomb-like porous carbon for advanced supercapacitors: A gelatinization-controlled one-step carbonization, J Power Sources. 402 (2018) 203–212.

[54] K. Dujearic-Stephane, M. Gupta, A. Kumar, V. Sharma, S. Pandit, P. Bocchetta, Y. Kumar, The effect of modifications of activated carbon materials on the capacitive performance: surface, microstructure, and wettability, Journal of Composites Science. 5 (2021) 1–26.

[55] Y. Wang, D.C. Alsmeyer, R.L. McCreery, Raman Spectroscopy of Carbon Materials: Structural Basis of Observed Spectra, Chemistry of Materials. 2 (1990) 557–563.

[56] J.R. Dennison, M. Holtz, Raman spectroscopy of carbon materials, Spectroscopy (Santa Monica). 11 (1996) 38–46.

[57] J.N. Edokpayi, S.S. Ndlovu, J.O. Odiyo, Characterization of pulverized Marula seed husk and its potential for the sequestration of methylene blue from aqueous solution, BMC Chem. 13 (2019).

[58] D.L. Postai, C.A. Demarchi, F. Zanatta, D.C.C. Melo, C.A. Rodrigues, Adsorption of rhodamine B and methylene blue dyes using waste of seeds of Aleurites Moluccana, a low cost adsorbent, Alexandria Engineering Journal. 55 (2016) 1713–1723.

[59] T. Krahnstöver, J. Plattner, T. Wintgens, Quantitative detection of powdered activated carbon in wastewater treatment plant effluent by thermogravimetric analysis (TGA), Water Res. 101 (2016) 510–518.

[60] L.D. Yao, F.Y. Li, J.X. Li, C.Q. Jin, R.C. Yu, Study of the products of melamine (C 3N 6H 6) treated at high pressure and high temperature, Physica Status Solidi (A) Applications and Materials Science. 202 (2005) 2679–2685.

[61] B. Shaku, T.P. Mofokeng, T.H. Mongwe, N.J. Coville, K.I. Ozoemena, M.S. Maubane-Nkadimeng, Physicochemical Properties of Nitrogen Doped Carbon Nano-onions Grown by Flame Pyrolysis from Grapeseed Oil for Use in Supercapacitors, Electroanalysis. 32 (2020) 2946–2957.

[62] R.J.J. Jansen, H. van Bekkum, XPS OF NITROGEN-CONTAINING FUNCTIONAL GROUPS ON ACTIVATED CARBON, 1995.

[63] Y. Kang, Z. Chu, D. Zhang, G. Li, Z. Jiang, H. Cheng, X. Li, Incorporate boron and nitrogen into graphene to make BCN hybrid nanosheets with enhanced microwave absorbing properties, Carbon N Y. 61 (2013) 200–208.

[64] L. Százdi, J. Gulyás, B. Pukánszky, Surface characterization of electrochemically oxidized carbon fibers: Surface properties and interfacial adhesion, Compos Interfaces. 9 (2002) 219–232.

[65] Y. Lu, D. Wu, Y. Qin, Y. Xie, Y. Ling, H. Ye, Y. Zhang, Facile construction of BiOBr/CoAl-LDH heterojunctions with suppressed Z-axis growth for efficient photoreduction of CO2, Sep Purif Technol. 302 (2022).

[66] F. Kapteijn, J.A. Moulijn, S. Matzner, H.-P. Boehm, The development of nitrogen functionality in model chars during gasification in CO and O, 1999.

[67] C. Lin, H. Liu, M. Guo, Y. Zhao, X. Su, P. Zhang, Y. Zhang, Plasmon-induced broad spectrum photocatalytic overall water splitting: Through non-noble bimetal nanoparticles hybrid with reduced graphene oxide, Colloids Surf A Physicochem Eng Asp. 646 (2022).

[68] W. Han, H. Wang, K. Xia, S. Chen, P. Yan, T. Deng, W. Zhu, Superior nitrogen-doped activated carbon materials for water cleaning and energy storing prepared from renewable leather wastes, Environ Int. 142 (2020).

[69] X. Zhang, H. Li, G. Wang, Q. Ji, T. Liang, Preparation and Characterization of Bio-Nitrogen-Doped Activated Carbon, (2021).

[70] B. Shaku, T.P. Mofokeng, T.H. Mongwe, N.J. Coville, K.I. Ozoemena, M.S. Maubane-Nkadimeng, Physicochemical Properties of Nitrogen Doped Carbon Nano-onions Grown by Flame Pyrolysis from Grapeseed Oil for Use in Supercapacitors, Electroanalysis. 32 (2020) 2946–2957.

[71] L. Guan, L. Pan, T. Peng, C. Gao, W. Zhao, Z. Yang, H. Hu, M. Wu, Synthesis of Biomass-Derived Nitrogen-Doped Porous Carbon Nanosheests for High-Performance Supercapacitors, ACS Sustain Chem Eng. 7 (2019) 8405–8412.

[72] Y. Lin, H. Zhao, F. Yu, J. Yang, Design of an extended experiment with electrical double layer capacitors: Electrochemical energy storage devices in green chemistry, Sustainability (Switzerland). 10 (2018).

[73] R. Heimböckel, F. Hoffmann, M. Fröba, Insights into the influence of the pore size and surface area of activated carbons on the energy storage of electric double layer capacitors with a new potentially universally applicable capacitor model, Physical Chemistry Chemical Physics. 21 (2019) 3122–3133.

[74] V. Pavlenko, S. Kalybekkyzy, D. Knez, Q. Abbas, Z. Mansurov, Z. Bakenov, A. Ng, Revisiting the carbon mesopore contribution towards improved performance of ionic liquid–based EDLCs at sub-zero temperatures, Ionics (Kiel). (2021).

[75] M. Fahim, A. ul H.A. Shah, S. Bilal, Highly stable and efficient performance of binder-free symmetric supercapacitor fabricated with electroactive polymer synthesized via interfacial polymerization, Materials. 12 (2019).

[76] Y. Lu, S. Zhang, J. Yin, C. Bai, J. Zhang, Y. Li, Y. Yang, Z. Ge, M. Zhang, L. Wei, M. Ma, Y. Ma, Y. Chen, Data on high performance supercapacitors based on mesoporous activated carbon materials with ultrahigh mesopore volume and effective specific surface area, Data Brief. 18 (2018) 1448–1456.

[77] F. Barzegar, A. Bello, O. Guellati, D.Y. Momodu, A. Harat, J.K. Dangbegnon, M. Guerioune, N. Manyala, Effect of addition of different carbon materials on hydrogel derived carbon material for high performance electrochemical capacitors, Electrochim Acta. 186 (2015) 277–284.

[78] Z. Sheng, X. Lin, H. Wei, Y. Zhang, Z. Tian, C. Wang, D. Xu, Y. Wang, Green synthesis of nitrogen-doped hierarchical porous carbon nanosheets derived from polyvinyl chloride towards high-performance supercapacitor, J Power Sources. 515 (2021).

[79] X. Wang, M. Lou, X. Yuan, W. Dong, C. Dong, H. Bi, F. Huang, Nitrogen and oxygen dual-doped carbon nanohorn for electrochemical capacitors, Carbon N Y. 118 (2017) 511–516.

[80] C. Zhong, Y. Deng, W. Hu, J. Qiao, L. Zhang, J. Zhang, A review of electrolyte materials and compositions for electrochemical supercapacitors, Chem Soc Rev. 44 (2015) 7484–7539.

[81] L. Demarconnay, E. Raymundo-Piñero, F. Béguin, A symmetric carbon/carbon supercapacitor operating at 1.6 v by using a neutral aqueous solution, Electrochem Commun. 12 (2010) 1275–1278.

[82] S.T. Vindt, E.M. Skou, The buffer effect in neutral electrolyte supercapacitors, Appl Phys A Mater Sci Process. 122 (2016) 1–6.

[83] A. Virya, K. Lian, A review of neutral pH polymer electrolytes for electrochemical capacitors: Transitioning from liquid to solid devices, Materials Reports: Energy. 1 (2021) 100005.

[84] M.S. Hong, S.H. Lee, S.W. Kim, Use of KCl aqueous electrolyte for 2 V manganese oxide/activated carbon hybrid capacitor, Electrochemical and Solid-State Letters. 5 (2002).

[85] Q. Gao, L. Demarconnay, E. Raymundo-Piñero, F. Béguin, Exploring the large voltage range of carbon/carbon supercapacitors in aqueous lithium sulfate electrolyte, Energy Environ Sci. 5 (2012) 9611–9617.

[86] H. Tomiyasu, H. Shikata, K. Takao, N. Asanuma, S. Taruta, Y.Y. Park, An aqueous electrolyte of the widest potential window and its superior capability for capacitors, Sci Rep. 7 (2017).

[87] J. Kim, J. Chun, S.G. Kim, H. Ahn, K.C. Roh, Nitrogen and fluorine co-doped activated carbon for supercapacitors, Journal of Electrochemical Science and Technology. 8 (2017) 338–343.

[88] H.S. Magar, R.Y.A. Hassan, A. Mulchandani, Electrochemical impedance spectroscopy (Eis): Principles, construction, and biosensing applications, Sensors. 21 (2021).

[89] A. Gopalakrishnan, T.D. Raju, S. Badhulika, Green synthesis of nitrogen, sulfur-co-doped worm-like hierarchical porous carbon derived from ginger for outstanding supercapacitor performance, Carbon N Y. 168 (2020) 209–219.

[90] C. Chen, M. Zhao, Y. Cai, G. Zhao, Y. Xie, L. Zhang, G. Zhu, L. Pan, Scalable synthesis of strutted nitrogen doped hierarchical porous carbon nanosheets for supercapacitors with both high gravimetric and volumetric performances, Carbon N Y. 179 (2021) 458–468.

[91] A.T. Chidembo, K.I. Ozoemena, B.O. Agboola, V. Gupta, G.G. Wildgoose, R.G. Compton, Nickel(ii) tetra-aminophthalocyanine modified MWCNTs as potential nanocomposite materials for the development of supercapacitors, Energy Environ Sci. 3 (2010) 228–236.

[92] N. Sinan, E. Unur, Hydrothermal conversion of lignocellulosic biomass into high-value energy storage materials, Journal of Energy Chemistry. 26 (2017) 783–789.

[93] K. Li, J. Luo, M. Wei, X. Yao, Q. Feng, X. Ma, Z. Liu, Functional porous carbon derived from waste eucalyptus bark for toluene adsorption and aqueous symmetric supercapacitors, Diam Relat Mater. 127 (2022) 109196.

[94] G. Ma, D. Guo, K. Sun, H. Peng, Q. Yang, X. Zhou, X. Zhao, Z. Lei, Cotton-based porous activated carbon with a large specific surface area as an electrode material for high-performance supercapacitors, RSC Adv. 5 (2015) 64704–64710.

[95] H. Gou, J. He, G. Zhao, L. Zhang, C. Yang, H. Rao, Porous nitrogen-doped carbon networks derived from orange peel for high-performance supercapacitors, Ionics (Kiel). 25 (2019) 4371–4380.

[96] P. Song, X.P. Shen, X.M. He, K.H. Feng, L.R. Kong, Z.Y. Ji, L.Z. Zhai, G.X. Zhu, D.Y. Zhang, Cellulose-derived nitrogen-doped hierarchically porous carbon for high-performance supercapacitors, Cellulose. 26 (2019) 1195–1208. “

CHAPTER 4: Tuning the properties of Mn_2PO_4F by potassium intercalation for asymmetric supercapacitors

4.1. Introduction

The high increase in energy demand requires measures to bring forward current systems for energy storage [1,2]. High power and high energy density are two necessities required for the current energy storage system [3]. Among various energy storage systems, metal-ion batteries (MIBs) and supercapacitors (SCs) are considered to be promising energy and power storage systems [4,5]. Materials used in MIBs show faradaic reactions which is favourable in energy density. However, MIBs materials have poor life cycle and low power density due to the diffusion of ions at a slower rate and volumetric changes that occur during charging and discharging [6]. The poor life cycle and low power density associated with MIBs can be overcome through the use of SCs. The high-power density and longer life cycle associated with SCs is through diffusion/release of ions on the materials' surface [7]. Although SCs has desirable characteristics, they suffer from low energy density [8]. Hence, it is highly desirable to blend both the advantages of MIBs and SCs into novel energy storage systems. The configuration of hybrid capacitors/asymmetric capacitors involves using a battery/pseudocapacitor type as a positive electrode and capacitor type as negative electrode [9].

However, the mismatch of kinetics and capacity can lead to poor overall performance of asymmetric capacitor due to different mechanisms occurring at the cathode and anode [10]. A great effort has been made to improve the sluggish kinetics at the cathode by developing advanced materials that enable diffusion of ions. For example, Ding *et al.* [11] synthesized a cathode composite material composed of VS_4 material preintercalated with potassium and nitrogen doped tubular graphene (VS_4/N-TG). Their study reported that K^+ ions also acts as "pillars" to improve the stability structure due to the enlarged interplanar spacing. Manganese fluorophosphate (MFP), which belongs to the triplite family was used as the cathode material. MFP is a fluorophosphate mineral with a formula Mn_2PO_4F and was first reported in 1972 by Rea et al. [12] and recently by Nzimande et al. [13] for use in rechargeable aqueous metal-ion batteries. Manganese based materials are well known and used in SCs and battery cathode materials and are hugely naturally abundant (especially in South Africa, which controls 80% of the global manganese reserves) [14–16]. This material possesses open-framework crystal structure, which can exhibit diffusion of electrolyte ions. However, Mn_2PO_4F has been reported

to be a ‘sleeping triplite’ material with poor capacity, conductivity and stability [13]. This study seeks to improve the electrochemical properties of Mn_2PO_4F for use in supercapacitors by pre-intercalating metal alkali ions. This will increase the volume expansion of Mn_2PO_4F to allow flexibility to distortion of the lattice and also provide room adsorption of electrolyte ions.

A study by McDowell *et al.* [17] reported an increase of volume expansion of 300% when inserting lithium ions into silicon, and this resulted in amorphization which gives a desirable environment in the electrode to host Li ions. Another study by Xiang *et al.* [18] on Na^+ intercalation into $FePO_4$ resulted in 17% volume expansion with high transformation strains. Another study by Tarascon’s group reported that potassium into $FeSO_4F$ stabilize the new structure due to a larger ionic radius and somewhat different crystal chemistry [19].

In this study, using a "hydrothermal potassium insertion" technique, we tailored a novel K^+/MFP interplanar spacing to improve the electrochemical performance as the cathode for asymmetric SCs in alkaline and neutral electrolytes. As a result, the use of K^+ increase the interlayer distance, with K^+/MFP displaying a large lattice spacing of 0.49 nm which would allow for more diffusion of electrolytes ions and maintain the structural stability during the cycling process. Furthermore, extensive electrochemical measurements demonstrated that the wider interlayer spacing plays a crucial role in the fast reaction kinetics. Additionally, the K^+ that is added can electrostatically stabilize the crystal structure during the cycle. Therefore, the use of K^+/MFP with nitrogen doped activated carbons (reported in Chapter 3 [19]) in asymmetric SCs system displays a fantastic energy density of 26.9 W h kg^{-1} in 1 M KNO_3 and 25.2 W h kg^{-1} in 6 M KOH.

4.2. Methodology

4.2.1. Materials

Potassium intercalated manganese fluorophosphate (K^+/MFP) was synthesized using Lithium fluoride (LiF, Sigma Aldrich), ammonium dihydrogen phosphate, $NH_4H_2PO_4$, Sigma Aldrich), Manganese(II) nitrate tetrahydrate ($Mn(NO_3)_2.4H_2O$, Sigma Aldrich) and potassium hydroxide (KOH).

4.2.2. Electrochemical characterization

Working electrode was prepared by making slurry of MFP, K^+/MFP (80 %), carbon black (10 %) and 10% of polyvinylidene (PVDF, 10%). Methylpyrrolidone (NMP), about few drops were added [20]. Sonication for about 30 minutes was done to make uniform slurry. The slurry

was used on a carbon paper by drop casting. The coated carbon paper was dried in a vacuum oven for 12 h at 60 ℃. The three and two electrode system were performed using the coated coated carbon papers. The counter and reference electrode used were nickel foam and Ag/AgCl Microfiber filter paper was soaked in 6 M KOH and 1 M KNO_3 electrolytes and used as separator. The type of cell used was T-type Swagelok. The calculated active mass per area coated on the carbon paper was around ~1.5-1.7 mg/cm^2. VSP-300 potentiostat was used to run cyclic voltammetry (CV), galvanostatic charge-discharge (GCD), and electrochemical impedance spectroscopy (EIS) of the materials.

The specific capacitance (C_{sp}), energy density (E_s), power density (P_s) were calculated from the discharge time obtained from GCD curves using equation 4.1-4.6 [21–25].

Equation 4.1 was used to calculate capacitance (F):

$$C = \frac{I \times \Delta t}{\Delta V} \tag{4.1}$$

Where the discharge current is given by I/A, $\Delta t/s$ is the discharge time, $\Delta v/V$ is the potential difference.

Equation 4.2 was used to calculate the specific capacitance, C_s/F g^{-1} of the three electrode/half-cell:

$$C_{sp} = \frac{C}{m} \tag{4.2}$$

Where m(g) is the mass of the active electrode material.

Charge balancing was done using the mass ratio balancing of the cathode to anode electrode (obtained from three electrode system) using equation 4.3 & 4.4:

$$q^{+}=q^{-} \tag{4.3}$$

Where q+ is the charge at the cathode and q- is the charge at the anode. The optimal mass ratio was obtained using equation 4.4:

$$\frac{m^{+}}{m^{-}} = \frac{C^{-}}{C^{+}} \times \frac{\Delta V^{-}}{\Delta V^{+}} \tag{4.4}$$

Where mass, voltage window and specific capacitance of the cathode are represented by m^{+}/g, $\Delta V+/V$, and C^{+}/F g^{-1}, while m^{-}/g, $\Delta V/V^{-}$, and C^{-}/F g^{-1} are mass, voltage window and specific capacitance of the anode.

The C_s/F g^{-1} for a asymmetric two electrode system, where the counter and working electrode are different active material has been calculated using equation 4.5:

$$C_{sp} = 4\ \frac{C}{m} \tag{4.5}$$

Where m/g is the total active electrode mass.

Energy density (E_s) 's basic expression in equation 4.6 is in the unit J g^{-1}.

$$Es = \frac{1}{2} \times C_{sp}(\Delta V)^2 \tag{4.6}$$

Where C_{sp}/ F g^{-1} is the specific capacitance and ΔV/V is the potential window. To convert J g^{-1} to unit Wh g^{-1}, equation 4.5 is divided by a factor of 3600. To convert to Wh kg^{-1}, the units are multiplied by a 1000 to give equation 4.7. Hence, Es/Wh kg^{-1} is given by equation 7.7 and P_s/W kg^{-1} is calculated from equation 4.8.

$$Es = \frac{1}{2} \times C_{sp}(\Delta V)^2 = \frac{C \times (\Delta V)^2}{2m} \times \frac{1000}{3600} \tag{4.7}$$

Where C is capacitance, ΔV/V is the cell potential and m/kg is the mass of both active electrodes.

Power density (P_s) was calculated from equation 4.8:

$$P_s = 3600\ \frac{E_s}{\Delta t} \tag{4.8}$$

4.2.3. Characterization techniques

LEO, Zeiss scanning electron microscopy (SEM) was used to study the morphology of the synthesized materials and a Tecnai G2 30ST high transmission electron microscopy (HRTEM) operated at 200 kV.). Bruker D2 phaser (Cu-Kα radiation at 30 kV and 10 mA) was used to obtain XRD patterns. A monochromatic Al Kα source Physical Electronics Quantum 2000 instrument was used to obtain X-ray photoelectron spectroscopy (XPS) data.

4.2.4 .Synthesis of MFP

MFP was synthesized by dissolving 1.17 g of LiF in 20 mL distilled water and stirred for 30 min at room temperature (Solution A). About 5.18 g of $NH_4H_2PO_4$ was dissolved in 20 mL distilled water at room temperature and stirred for 30 min (Solution B). Solution B was added into solution A to make solution C and stirred for 1 h. About 22.6 g $Mn(NO_3)_2.4H_2O$ was added

in 30 ml deionized water and stirred for 30 min at room temperature (solution D). Solution C was added into solution D and stir for 24 h at room temperature. The mixture was then subjected to microwave irradiation for 45 min at 180 ℃ (300 W). The prepared gel was the centrifuged, washed with distilled water and ethanol to remove impurities. The mixture was kept in an oven at 60 ℃ for 12 h. The material was grounded by pestle and mortar and heated under argon flow (100 mL/min) for 4 h at 350 ℃. Again, subjected to 800 ℃ for 8 h (ramping temperature 10 ℃/min) to form MFP (Fig. 4.1) [13]. What were the yields?

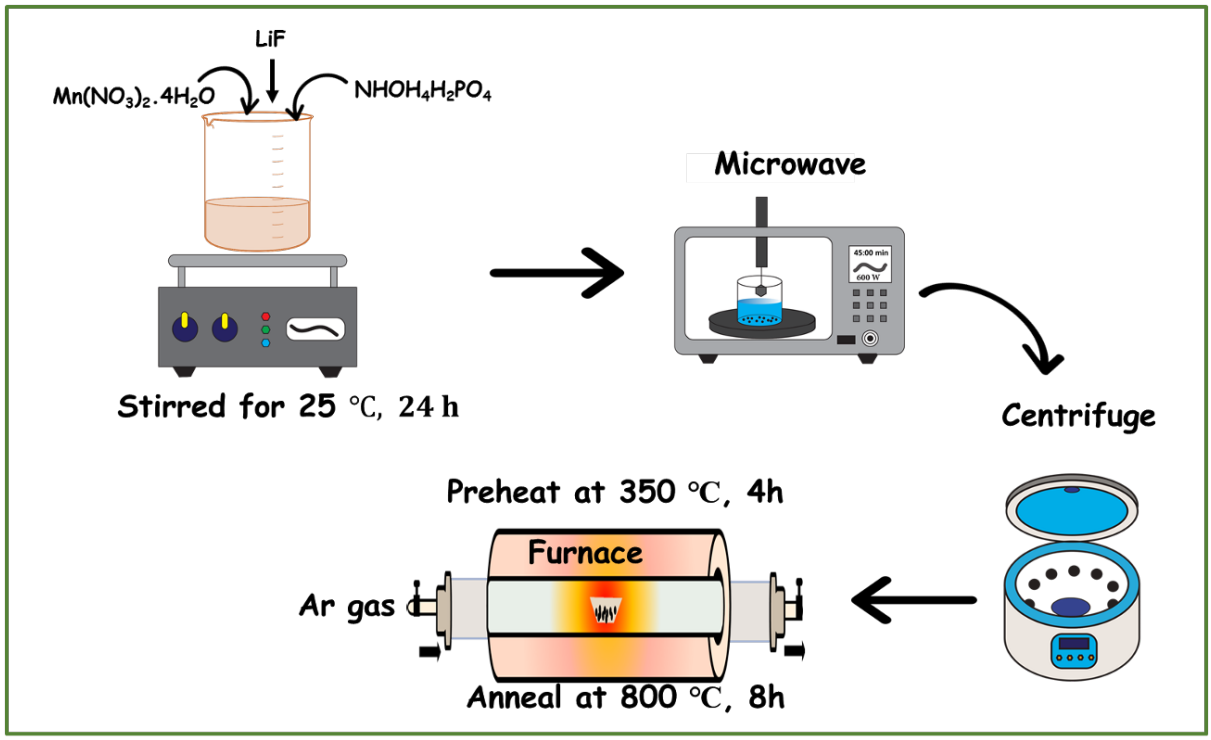

Fig. 4. 1. Scheme showing synthesis of MFP.

4.2.5 Synthesis of K^+/MFP

Fig. 4.2 show synthesis scheme for $K^{+/}$MFP. K^+/MFP was synthesized by mixing 900 mg of MFP with 30 mL of 8 M KOH. The mixture was stirred for 24 h at 25 ℃. Again, the mixture was hydrothermally treated in an autoclave for 12 h at 180 ℃. The resulting mixture was centrifuged and washed with distilled water to form K^+/MFP. The final yield was about ~350.3 mg (~38.9 %).

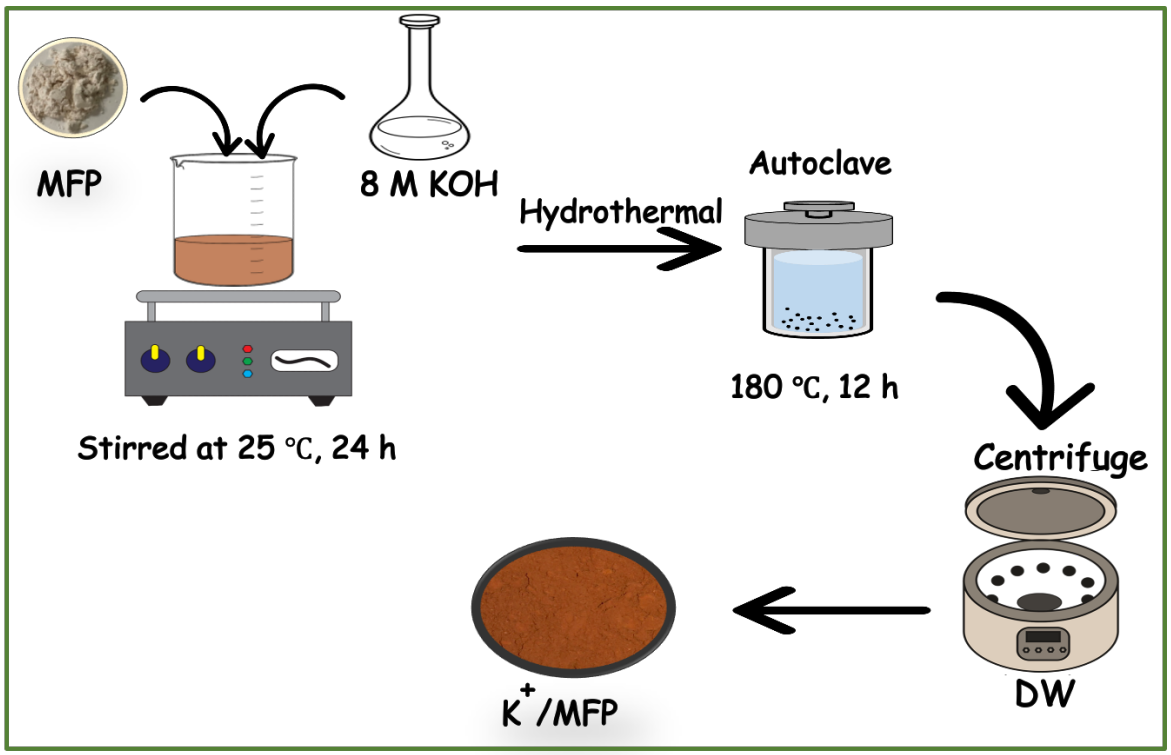

Fig. 4. 2. Scheme showing synthesis of K^+/MFP.

4.3. Results and discussion

In Fig. 4.3, the XRD spectra of MFP and K^+/MFP are displayed. The pure phase of Mn_2PO_4F is confirmed by Rietveld fits of the PXRD patterns. The crystallographic data of the triplite Mn_2PO_4F, which was first structurally clarified in 1972 by Rea and Kostiner [12], was corroborated by the Braggs peaks, which were entirely indexed to the crystal structure of the monoclinic symmetry corresponding to the space group C2/c (15). K^+/MFP show the presence of very few and new crystalline characteristic peaks which are due to the presence of MFP reacting with KOH. It is suggested that the introduction of K^+ caused recrystallization of the sample. Furthermore, these grains accumulated in preferred orientation of 120 ($MnPO_4$) in $K^+/Mn_2(PO_4)F$ as a result of the recrystallization process. Hence, the change in the preferred orientation 021 in $Mn_2(PO_4)F$ to 120 ($MnPO_4$) in $K^+/Mn_2(PO_4)F$. All these caused the change in presence of diffraction peaks in the two samples. There was structural phase transition after the introduction of K^+, which caused disappearance of some of the peaks in XRD pattern of $K^+/Mn_2(PO_4)F$. The peaks 422, 323, 710 in $Mn_2(PO_4)F$ shifted lower angles in $K^+/Mn_2(PO_4)F$, perhaps due to larger K^+ radius than Mn^{2+}. This work is similar to Ding *et al.* [11] were K^+ pre-intercalated into VS_4 shifted the diffraction peak of (110) facet for $K0.20VS_4$/N-TG towards

the lower diffraction angle, indicating K^+ was pre-intercalated into VS4/N-TG lattice, can enlarge the interplanar spacing of VS_4.

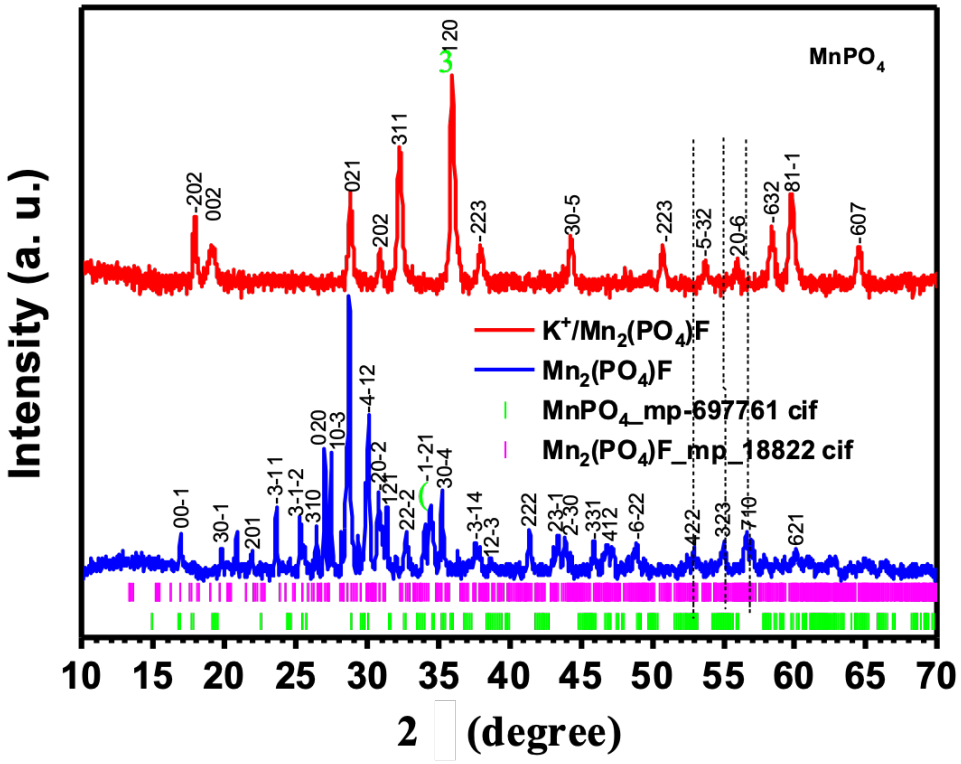

Fig. 4. 3. XRD spectra of MFP and K^+/MFP.

Fig. 4.4 presents the typical TEM images of MFP (a, b) and K^+/MFP (c, d). MFP (Fig. 4a) show no definite morphology. The HRTEM image of MFP (Fig. 4b) show lattice fringes with a d-spacing of ~0.31 nm. After intercalation with potassium ion, the morphology of K^+/MFP (Fig. 4c) changed and resulted in hexagonal and quasi rectangular shapes which indicates deformations in the particles upon K-ion insertion. The change in morphology is due to the use of high concentration of KOH which results in mostly different shapes after synthesis. The calculated d-spacing of 0.49 nm for K^+/MFP (Fig. 4.4d) show that intercalation of potassium increases volume expansion which helps with diffusion of electrolyte ions hence higher energy storage. Similar observations were reported by Ding et al. [11] with an increase in d-spacing after K^+ intercalation.

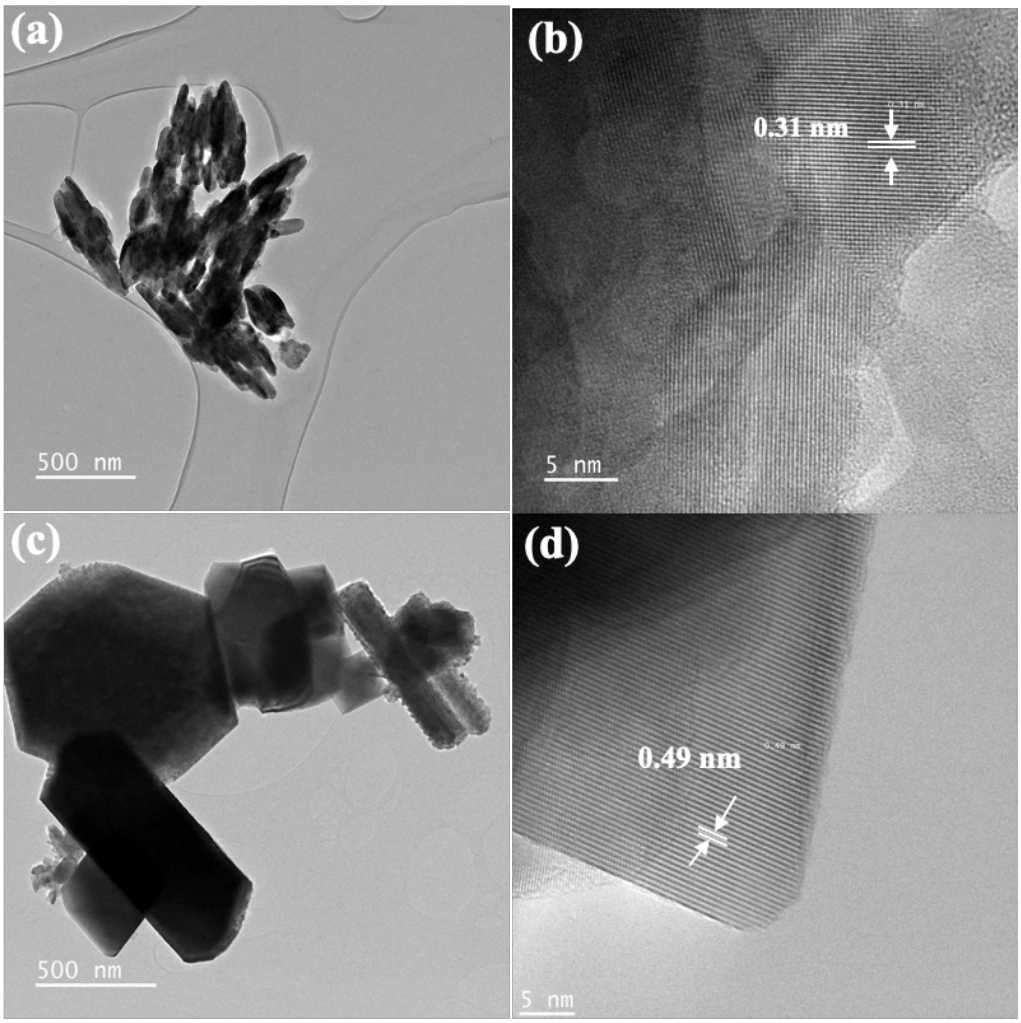

Fig. 4. 4. (a, b) Low and (b, d) high magnification TEM images of MFP (a, b) and K^+/MFP (c, d).

The morphologies of MFP and K^+/MFP were further investigated by SEM-EDS. Fig. 4.5a show SEM image of MFP with a bulk structure. The morphology of K^+/MFP (Fig. 4.5b) show small nanomaterials with hexagonal structures (red square) which supports the TEM images. The formation of different structures (i.e. octahedral) has been observed by Fatima *et al.* [26] by varying different KOH concentrations on Fe_3O_4 nanoparticles and the study showed the type of precursor and concentrations of surfactant are the major contribution in the type of shapes formed. The main driving force for formation of octahedron shapes was the increase in OH^- concentration (1 M) with an average diameter ranging from 200-300 nm. The formation of octahedral shapes is favourable at higher KOH concentrations due to the increase of OH- ions that lead to generation of greater chemical potential within the solution. Another study by Wang *et al.* [27] suggested that the crystal growth of octahedron shapes structure along [111] favourable at higher KOH concentrations. The shapes of nanocrystals were also studied by

Swaminathan *et al.* [28] at different planes and their study suggested that octahedral shapes are formed at a faster crystal growth along [111] while cubes are formed at a faster crystal growth along [100] plane.

The elemental mapping of MFP (Fig. S4.1) show elements Mn, O, F, P that are uniformly distributed throughout the material. K^+/MFP (Fig. 4.5c-h) show uniform distribution of elements of Mn, O, F, P and K. Additionally, the results confirms that potassium ions are located within the structure of MFP.

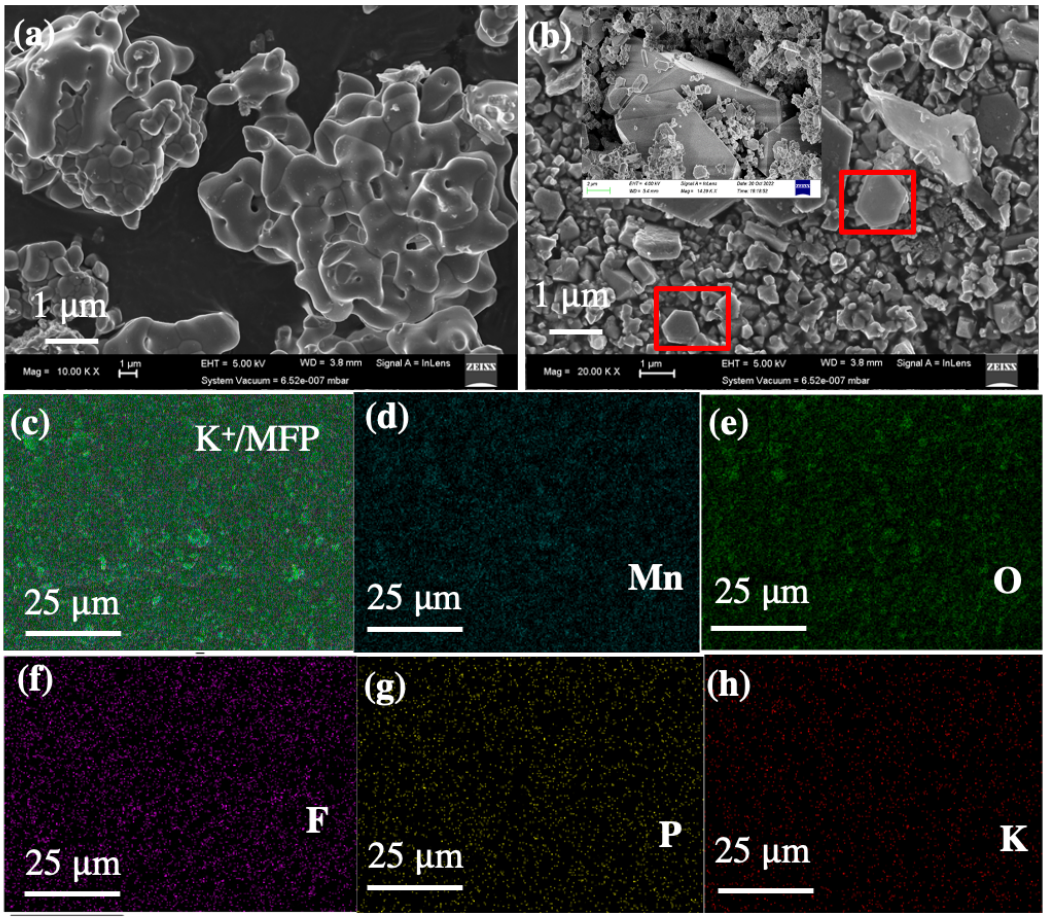

Fig. 4. 5. SEM images of (a) MFP, (b) K^+/MFP, EDS mapping (c-h) of K^+/MFP

The XPS survey scans of MFP show all elements (Mn 2p, O1s, F1s, P2p3) and K^+/MFP (Mn 2p, O1s, F1s, P2p3, K2s) at their respective binding energies as shown in Fig. 4.6. The presence of manganese occurs at a binding energy of 641.4-642.8 eV due to the presence of Mn-O bond in the triplite material [28,29]. The fluoride F1s occur at binding energy of 685.7-687.5 eV

[30,31], P2p3 occurred at a binding energy of 132.7-133.4 eV [32], O1s at 530.0-531.9 eV [33] and K2s at 567.9 eV [34]. Table 4.1 show XPS atom % for all elements present in both MFP and $K^{+/}$MFP. The atom % for elements present in K^{+}/MFP decreases due to interaction with KOH with only an increase in Mn2p. The shows that the treatment of MFP with KOH exposes Mn atoms.

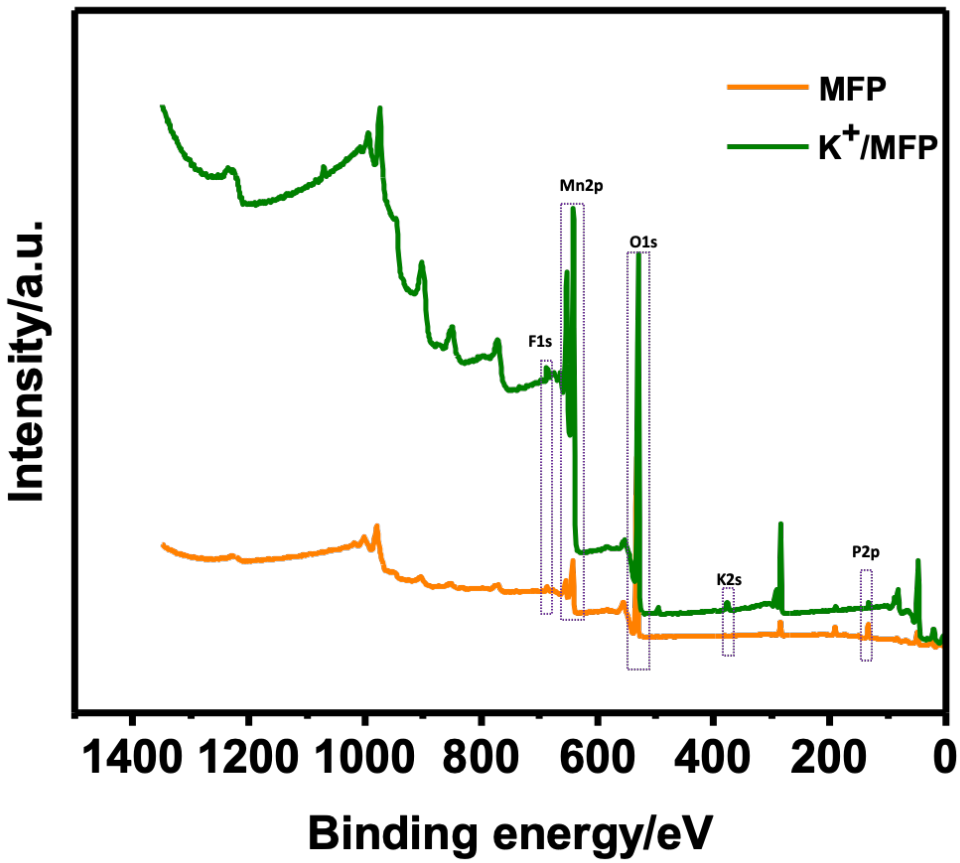

Fig. 4. 6. XPS survey scan of MFP and K^{+}/MFP.

Table 4. 1. XPS data of MFP and K^+/MFP.

Type of material	XPS atom %				
	K2s	Mn2p	O1s	P2p	F1s
MFP	-	12.9	54.5	13.9	1.6
K^+/MFP	1.9	20.2	49.6	1.2	0.6

The deconvoluted Mn2p of MFP is shown in Fig. 4.7a with two main peaks at 642.1 eV for $Mn2p_{3/2}$ and at 654.2 eV for $Mnp_{1/2}$ spin orbitals [29]. The deconvoluted Mn2p of K^+ /MFP is shown in Fig. 4.7b with two main peaks attributed to $Mn2p_{3/2}$ and $Mnp_{1/2}$. $Mn2p_{3/2}$ also show another third peak at 646.2 eV due to satellite shape up [30]. Mn2p (K^+/MFP) was deconvoluted and shown in Fig. 4.7b with two main peaks for $Mn2p_{3/2}$ and $Mn2p_{1/2}$. In $Mn2P_{3/2}$, Mn^{2+}, Mn^{3+} and satellite are at 643.1, 641.7, and 640.6 eV. $Mn2p_{3/2}$ is deconvoluted into two peaks at 643.2 eV for Mn^{2+} and 641.9 eV for Mn^{3+}. The concentration % of Mn^{2+} (77.9%) is higher compared to Mn^{3+} (22.1%) from K^+/MFP as compared to MFP with Mn^{3+} with a higher concentration (73.6%) than Mn^{2+} (26.4%). This shows that cation doping stabilize the MFP structure by reducing the amount of electrochemically active Mn^{3+}, which is reported to for Manganese disproportionate reaction into the electrolyte.

The deconvoluted O1s spectra of MFP is shown in Fig. 4.7c with two peaks attributed to Mn-O-Mn and Mn-O-H at 531.3 eV) and 532.8 eV. The deconvoluted O1s spectra for K^+/MFP (Fig. 7d) gave rise to three peaks attributed to Mn-O-Mn (529.5 eV), OH radical (531.0 eV) and lattice oxygen at 532.6 eV [31].Fig. 4.7e,f show $P2p_{3/2}$ for MFP (133.3 eV) and K^+/MFP (132.3 eV). K2P in K^+/MFP material was deconvoluted and it gave rise to two peaks at 292.eV ($K2p_{1/2}$) and at 295.0 eV ($K2p_{3/2}$) [32]. Fig. S4.2a,b show the presence of F1s for MFP (685.7 ev) and K^+/MFP (687.5 eV). XPS clearly confirms that all elements are present in the material before and after intercalation which corroborates SEM-EDS data.

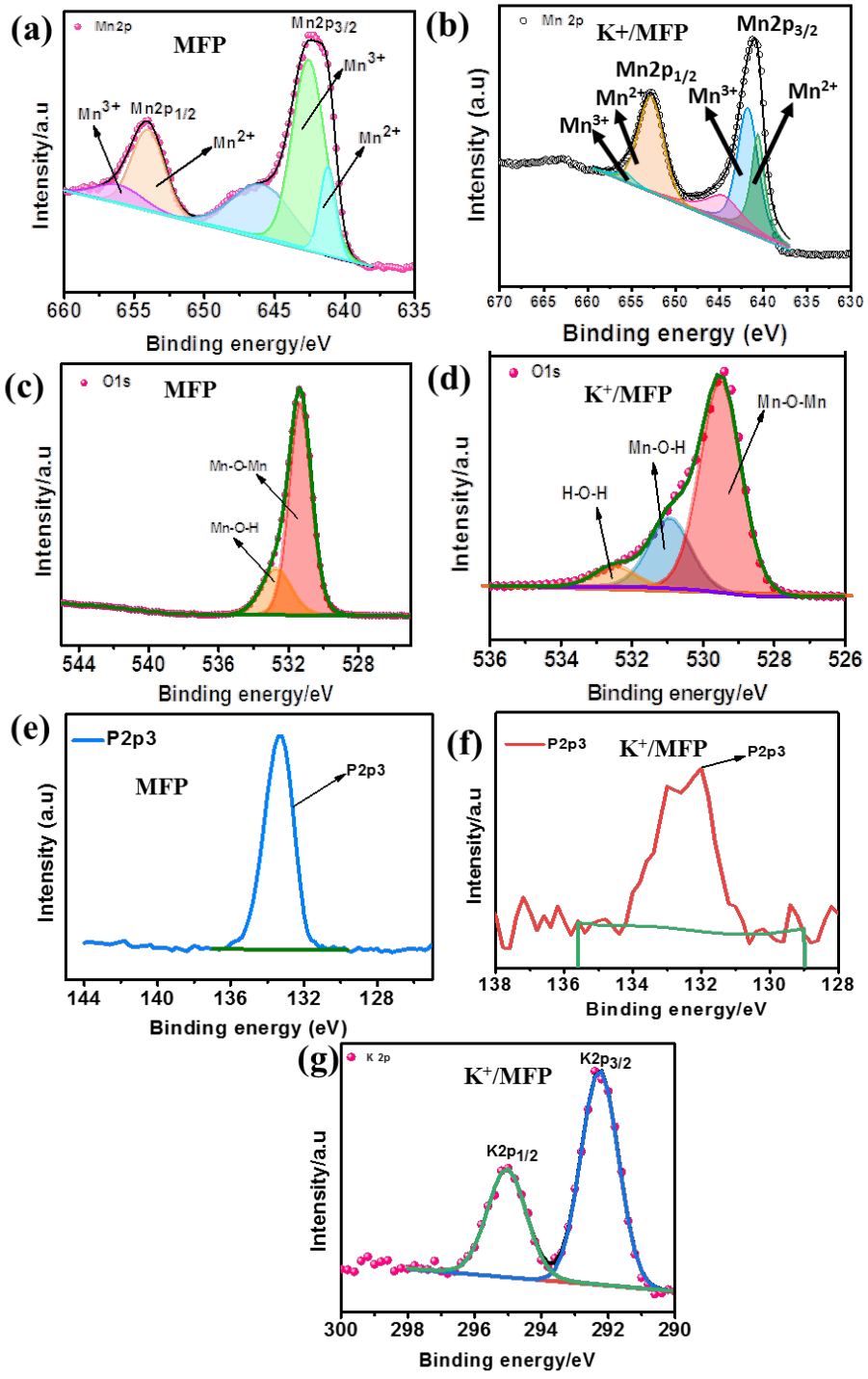

Fig. 4. 7. Mn2p spectra of (a) MFP, (b) K^+/MFP, O1s spectra of (c) MFP, (d) K^+/MFP,P2p3 spectra of (e) MFP, (f) K^+/MFP and (g) K2p spectrum of K^+/MFP.

4.4. Electrochemical measurement

4.4.1. Three electrode system of MFP and K^+/MFP in 6 M KOH electrolyte

Cha.ge storage in materials occur through two possible mechanisms. The first one is due to pseudocapacitive interaction which involves non-faradaic charge transfer. During this mechanism, the alkali metal cation from the electrolyte (here K^+) will diffuse through the open framework of K^+/MFP and intercalate through it [33].

$K^+/Mn_2PO_4F + K^+ + e^+ \rightarrow K^+/MnPO_4F\text{-}Mn\text{-}K$

The second charge storage mechanism is based on electric double layer capacitance which there is no involvement of charge transfer and the charges from the electrolyte ions only accumulate at the surface of the electrode material [34].

$K^+/Mn_2PO_4F + K^+ + e^- \rightarrow K^+/Mn_2PO_4F\text{-}K^+$

The electrochemical performance of MFP and K^+/MFP as a cathode materials were evaluated in a three electrode system using 6 M KOH and 1 M KNO_3. The typical cyclic voltammetry (CV) curves of MFP showed the material can be operated from 0-0.8 V (Fig. 4.8a) and K^+/MFP at 0-0.9 V in 6 M KOH. MFP show poor current response with no obvious redox peaks as compared to $K^{+/}$MFP (Fig. 4.8a). However, after intercalation, the current response improved and the two oxidation and reduction peaks can be assigned to Mn^{2+}/Mn^{3+} redox pair [35] through reversible intercalation and deintercalation of electrolyte ions into and from the electrode material. The CV curves of K^+/MFP consist of four redox peaks in the regions ~0.57 V-0.70 V and ~0.40 V-0.60 V. The redox couple at the lower voltages (anodic peaks ~0.42 V and cathodic peak ~ 0.57 V) is due to Mn^{2+}/Mn^{3+} redox reaction. The presence of Mn^{3+} reveals that the material have some degree of disordered phase. GCD curves were ran at 0.5 A g^{-1} and compared as shown in Fig. 4.8b. and K^+/MFP showed improved discharge time. Improved current response and discharge time is due to the monovalent ions from pre-intercalated potassium that are easily embed into the host structure because of their low charge density and their large ionic radius that increase the interlayer spacing after insertion, thereby improving the electrochemical performance. The specific capacitance calculated (Fig. 4.8c) for MFP were at 29.1 F g^{-1} (at 0.5 A g^{-1}), 22.1 F g^{-1} (at 0.75 A g^{-1}), 16.8 F g^{-1} (at 1 A g^{-1}), 8.4 F g^{-1} (at 2 A g^{-1}) and 2.5 F g^{-1} (5 A g^{-1}), lower compared to K^+/MFP with capacitance values of at 206.2 F g^{-1} (at 0.5 A g^{-1}), 144.2 F g^{-1} (at 0.75 A g^{-1}), 120 F g^{-1} (at 1 A g^{-1}), 68 F g^{-1} (at 2 A g^{-1}) and 42 F g^{-1} (at 5 A g^{-1}). The improvement of the electrochemical performance after K^+ pre-intercalation

can produce the coordination effect of a multi-electron reaction and structural stability in a typical intercalated MFP.

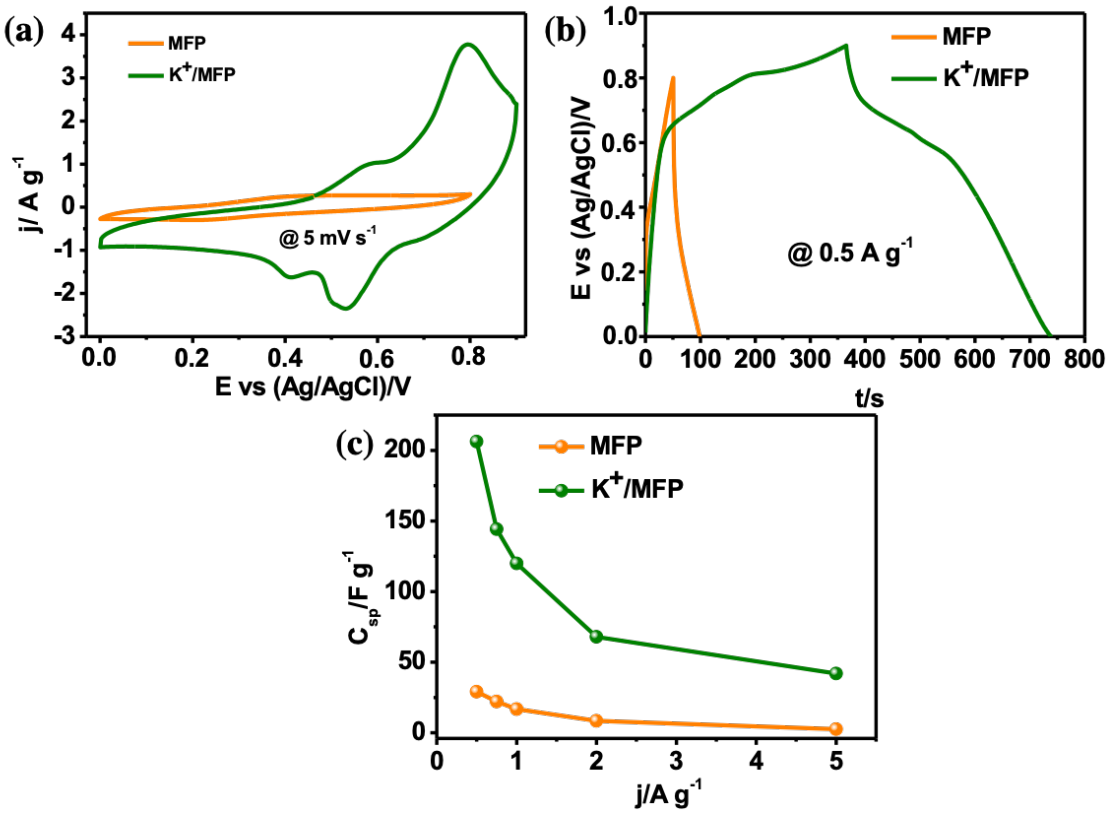

Fig. 4. 8. (a) CV, (b) GCD and (c) Csp VS current density in 6 M KOH.

4.4.2. Three electrode system of MFP and K^+/MFP in 1 M KNO_3

Again, MFP and K^+/MFP were evaluated in a three-electrode system using 1 M KNO_3 electrolyte. As shown from the CV curves in Fig. 4.9a. MFP can be operated to a voltage range of 0.0-0.9 V as compared to K^+/MFP at 0.0-1.2 V (Fig. 4.9b, c). This shows that K^+/MFP exhibit a higher energy storage. From the CV curves shown in Fig. 4.9c, MFP showed no obvious redox peaks as compared to K^+/MFP, which showed redox peaks around 0.6 and 1.1 V attributed to the $Mn^{2+/}Mn^{3+}$ redox pair. GCD curves (Fig. 4.9d) of K^+/MFP showed redox behaviour of the material as compared to MFP with a longer discharge time. Fig. 4.9e show the specific capacitance values of the materials and K^+/MFP exhibited higher capacitance of 145.4 F g^{-1} (at 0.5 A g^{-1}), 119.7 F g^{-1}(at 0.75 A g^{-1}), 109.6 F g^{-1} (1 A g^{-1}), 90.0 F g^{-1}(at 2 A g^{-1}) and 65.4 F g^{-1} (at 5 A g^{-1}) as compared to MFP with capacitance values of 9.2 F g^{-1} (at 0.5 A g^{-1}), 5.8 F g^{-1} (at 0.75 A g^{-1}), 4.0 F g^{-1}(at 1 A g^{-1}), 1.1 F g^{-1} (at 2 A g^{-1}) and 0.04 F g^{-1} (at 5 A g^{-1}). The improved current response and discharge time is attributed to enhanced conductivity to

allow diffusion of electrolyte ions thus enhancing ionic reaction kinetics. The high capacitance values of K^+/MFP in both electrolytes could be because the prepared K^+/MFP has higher d-spacing which could allow more diffusion of electrolyte ions. In our work, the as-prepared K^+/MFP exhibits quasi rectangular, square and hexagonal morphology allowing the solvated K^+ to easily approach the K^+/MFP surface, particularly the inner surface, leading to a high pseudocapacitance. As a result, the electrolyte ions were unable to properly interact with the inner surface of the MFP, which resulted in no redox behaviour. As a result, the stronger redox peaks imply that more electrons are contributing to the K^+/MFP cathode's reaction throughout the electrolyte insertion/extraction process.

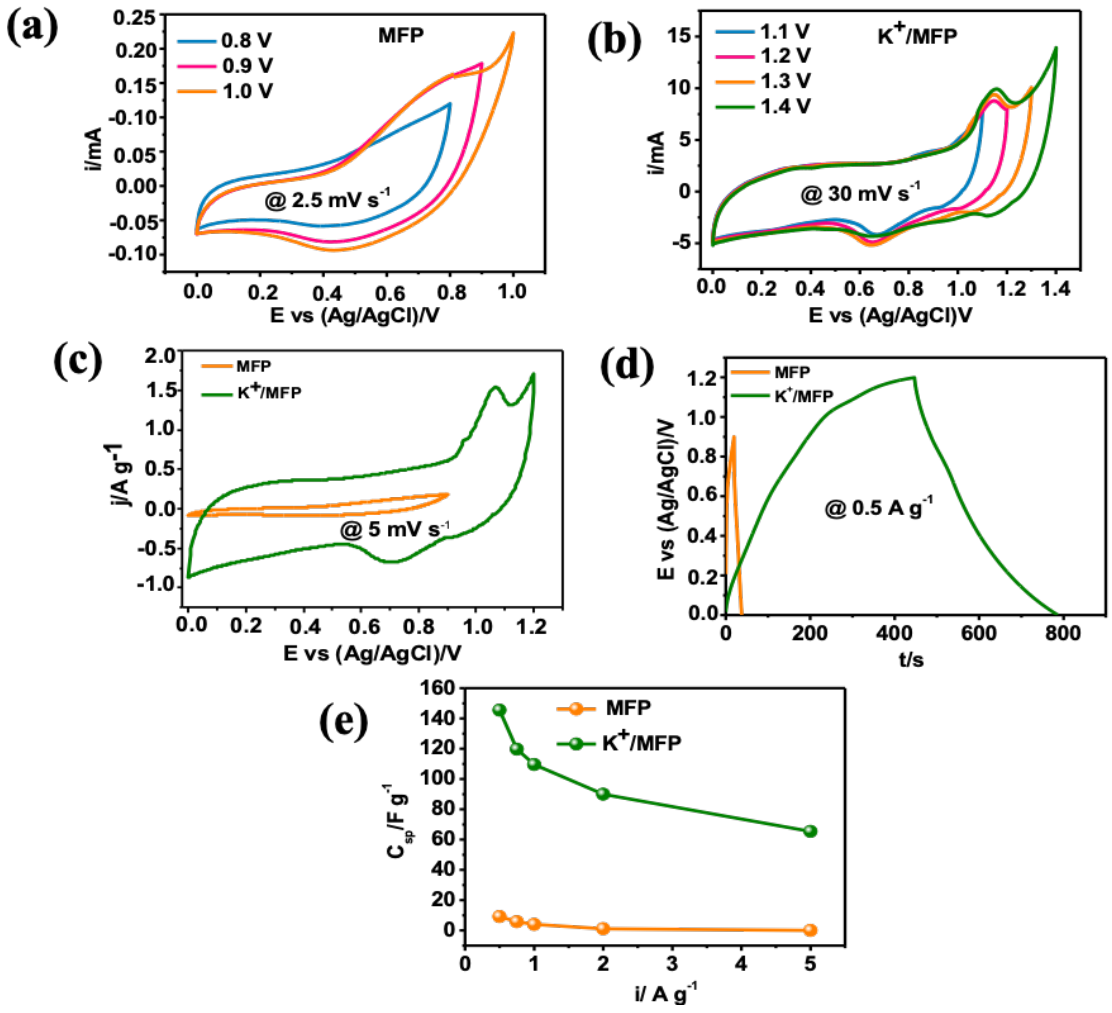

Fig. 4. 9. (a) CV of MFP, (b) CV of K^+/MFP, (c) comparison CV, (d) comparison GCD and (e) Csp VS current density of MFP and K^+/MFP in 1 M KNO_3.

Furthermore, K^+/MFP delivers a higher capacitance when K^+ acts as pillars, which enhances an easy process for electrolyte reversible insertion/extraction into or from K^+/MFP cathode. The anodic peaks of K^+/MFP shift to a lower potential along with electrolyte extraction, and the cathodic peaks shift to a higher potential in response to the insertion of electrolyte in K^+/MFP material which could be due to change of structure.

4.4.3. Asymmetric assemble of K^+/MFP and N-ACs in alkaline and neutral electrolytes

The application of K^+/MFP in asymmetric supercapacitor was evaluated as the cathode material and N-ACs as anode in 6 M KOH (Fig. 4.10a). Evaluation of a three-electrode system showed that K^+/MFP can be operated up to 0.0-0.9 V vs Ag/AgCl at a scan rate of 30 mV s^{-1} and N-ACs from -0.8-0.0 V vs Ag/AgCl (Fig. 4.10a). This show that the potential window of the asymmetric device assembled with K^+/MFP and N-ACs can be extended up to 1.7 V. The voltage window stability was evaluated using CV curves (Fig. 4.10b) and GCD (Fig. 4.10c) with no obvious oxygen evolution until the voltages reaches 1.7 V. Hence, electrochemical measurements system were evaluated at this voltage (1.7 V). The total mass after charge balancing was 3.0 mg. CV curves (Fig. 4.10d) show non-rectangular shape due to the redox behaviour of K^+/MFP from $Mn^{2+/}Mn^{3+}$. Increasing the scan rates to 50 mV s^{-1} results in CV curve shapes retained showing fast charge/discharge characteristics. GCD curves (Fig. 4.10e) show redox peaks supporting the CV curves. The capacitance of K^+/MFP//N-ACs were 283.1 F g^{-1} at 0.5 A g^{-1}, 249.4 F g^{-1} at 0.75 A g^{-1}, 225 .0 F g^{-1} at 1.0 A g^{-1}, 173.0 F g^{-1} at 2.0 A g^{-1} and 107.5 F g^{-1} at 5.0 A g^{-1} as shown in Fig. 4.10f.

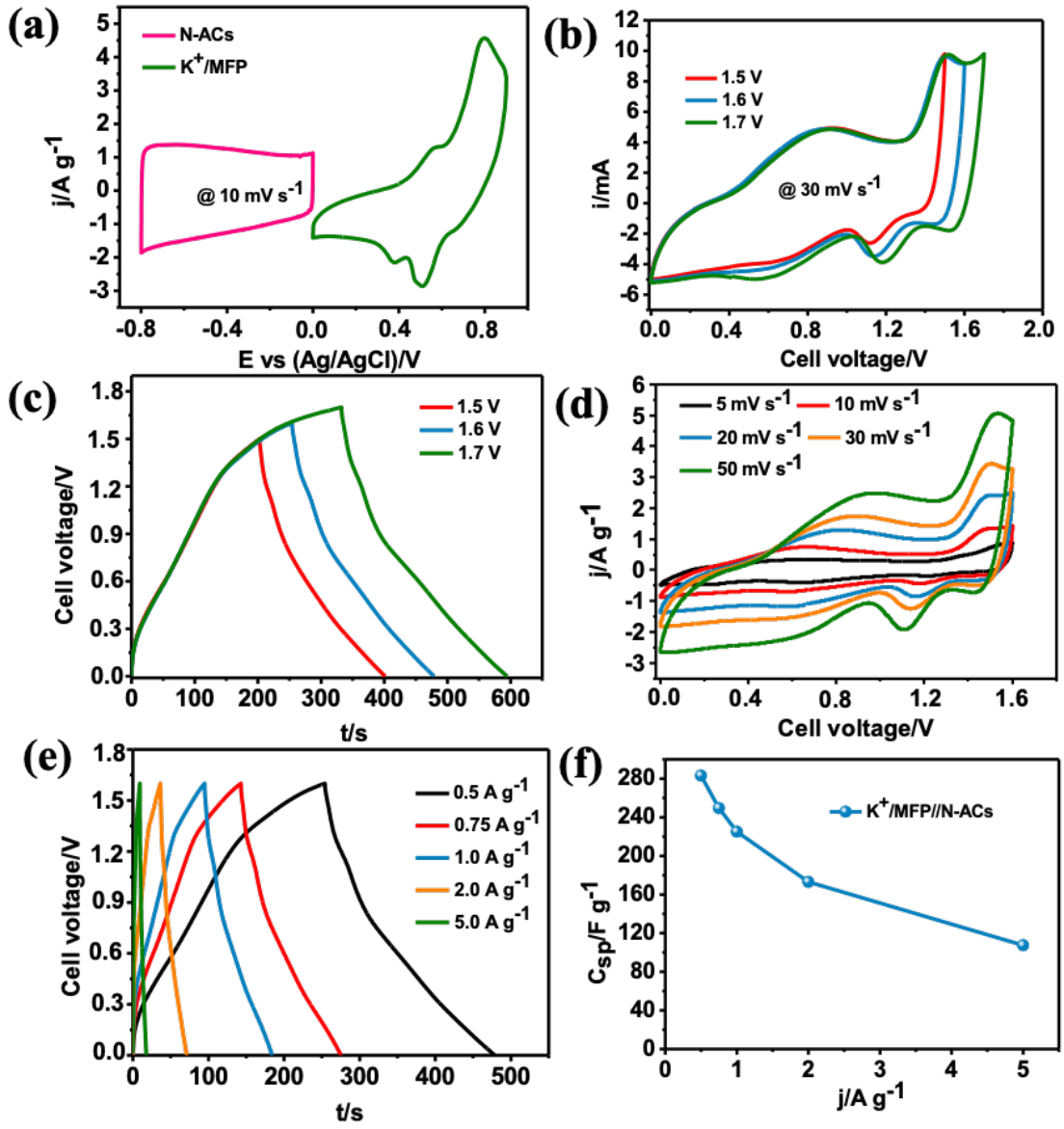

Fig. 4. 10. (a) CV of MFP, (b) CV tests, (c) GCD tests at different voltage window, (d) CV curves at different scan rates, (e) GCD and (f) C_{sp} VS current density of K^+/MFP//N-ACs in 6 M KOH.

K^+/MFP//N-ACs was also evaluated in 1 M KNO_3 (Fig. 4.11). N-ACs in 1 M KNO_3 show that it can be operated in the negative potential from -0.8-0.0 V and K^+/MFP in the positive potential from 0.0-1.2 V (Fig. 4.11a) which indicates that the asymmetric assembly of the materials can lead up to a 2 V voltage range. The total mass after charge balancing was 3.2 mg. The electrochemical stability window was evaluated and the material was ‘’stable up to a voltage of 1.8 V’’ as shown from the CV (Fig. 4.11b) and GCD (Fig. 4.11c) curves. Different scan

rates of the material was ran at different scan rates and the CV curves shapes were retained up to 50 mV s which showed the assembly of the materials are stable (Fig. 4.11d).

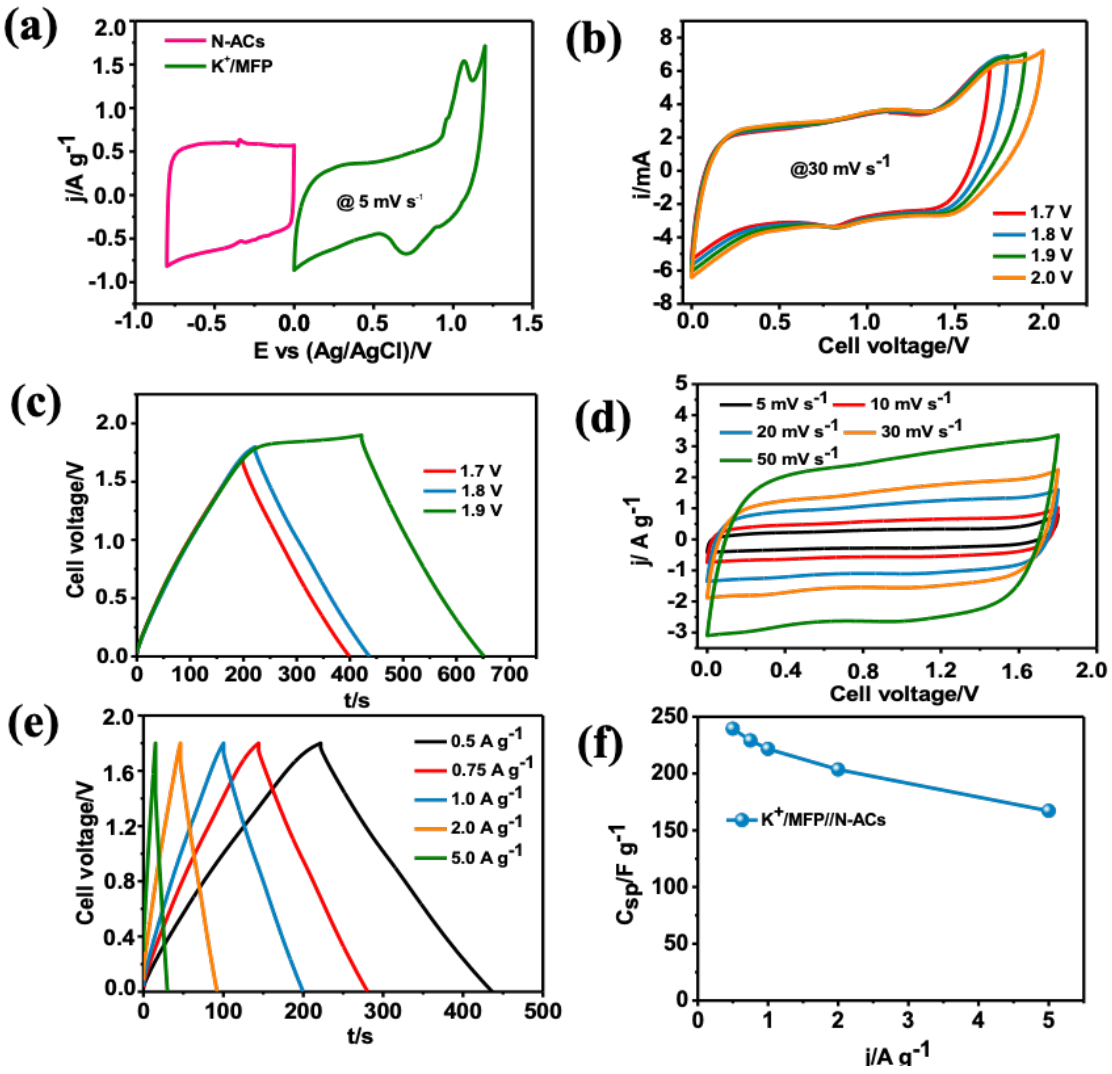

Fig. 4. 11. (a) CV, (b) CV tests, (c) GCD tests at different voltage window, (d) CV curves at different scan rates, (e) GCD ND (f) C_{sp} VS current density of K^+/MFP//N-ACs in 1 M KNO_3.

CV curves (Fig. 4.11d) show redox behaviour from the contribution of Mn^{2+}/Mn^{3+} with an ideal rectangular shape due to EDL capacitance [35,36]. GCD curves (Fig. 4.11e) were ran at different current densities and the discharge time decreases as the current densities increases which show that at higher current densities, there is insufficient time for diffusion of electrolyte ions. The GCD curves at high current densities retained their good quasi triangle with small redox behaviour which is consistent with the CV test results, indicating good supercapacitor behaviour and excellent electrochemical reversibility. Capacitance values (Fig. 4.11f) of the

asymmetric assembled material were 239.5 F g^{-1} at 0.5 A g^{-1}, 229.1 F g^{-1} at 0.75 A g^{-1}, 221.6 F g^{-1} at 1.0 A g^{-1}, 203.5 F g^{-1} at 2.0 A g^{-1} and 167.1 F g^{-1} at 5.0 A g^{-1}.

Analysis of the EIS is essential to understanding how the electrodes behave. Fig. 4.12a,b shows the Nyquist impedance plot, which shows a small arc in the high and middle frequency range signifying charge transfer resistance (R_{CT}) and a nearly vertical line in the low frequency range signifying ideal capacitive behaviour. The solution resistance (R_S), which includes the total resistance of the ionic resistance of the electrolyte, the intrinsic resistance of the active materials, and the contact resistance at the interface between the active electrode material and current collector, intersects with the real Z' axis from Nyquist. The R_s of the material is lower after cycling (0.12 Ω) in 6 M KOH than 1 M KNO_3 with R_s value of 0.33 Ω after cycling due to better contact of the electrode material and electrolyte. The R_{CT} of the material in 6 M KOH is lower (0.96 Ω) compared to 1 M KNO_3 with R_{CT} value of 10.33 Ω after cycling. The smaller R_{CT} value in 6 M KOH is due to higher conductivity. The material in 6 M KOH gave R_{int} of 589.80 Ω after cycling which was higher than before cycling (332.40 Ω) due to the increase in ohmic drop or limited diffusion of electrolyte ions after many cycles.

As shown in Table 4. 2, the values of n in alkaline are greater than in neutral electrolyte which shows that the material in 6 M KOH behaves more of a capacitor after many cycles. The CPE_{CT} and CPE_{cs} fluctuation implies the variation of the material in both electrolytes. As seen from the increase of capacitance retention vs cycling (see Fig. 4.13).

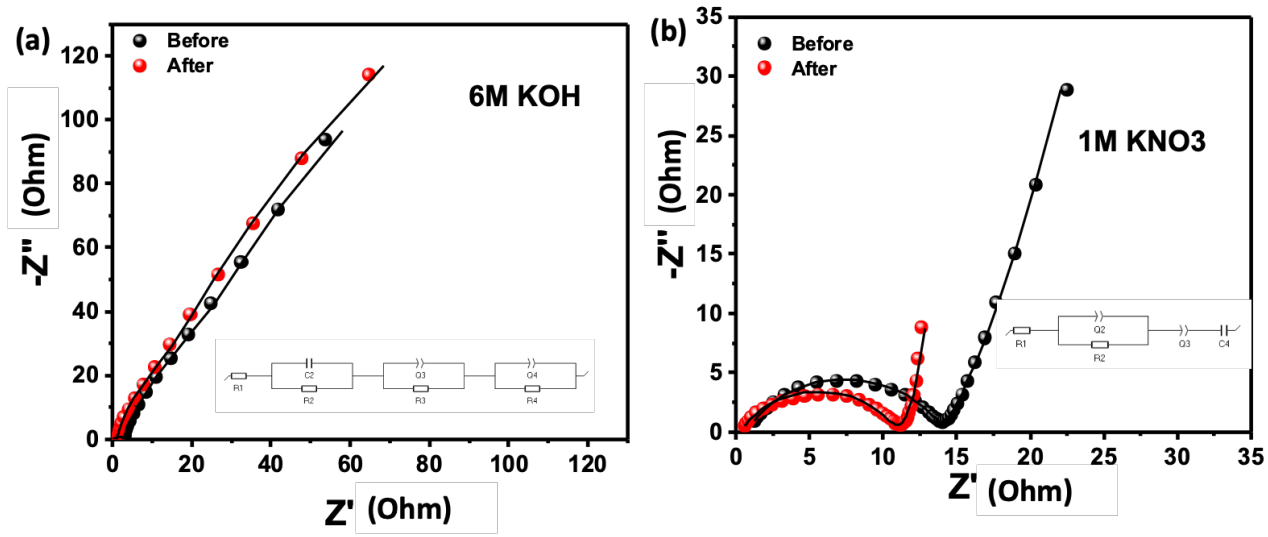

Fig. 4. 12. Nyquist plots of K^+/MFP//N-ACs before and after cycling in (a) 6 M KOH and (b) 1 M KNO_3.

Table 4. 2. EIS parameters of K^+/MFP//N-ACs before and after cycling in 6 M KOH and 1 M KNO_3.

Electrolytes	1 M KNO_3		6 M KOH	
Parameters	Before	After	Before	After
R_s (Ω)	0.81 ± 0.19	0.33 ± 0.13	0.62 ± 0.05	0.12 ± 0.07
R_{ct} (Ω)	13.07 ± 1.84	10.33 ± 2.53	2.08 ± 0.01	0.96 ± 0.04
R_{sei} (Ω)	-	-	35.69± 5.31	8.22 ± 0.11
R_{int} (Ω)	-	-	332.40 ± 26.34	589.80 ± 20.83
C_{dl} (mF)	95.21 ± 1.61	217.40 ± 0.27	16.77 ± 1.97	16.75 ± 0.49
CPE_{ct} (uF. s^(a-1))	52.9 ± 10.01	121.50 ± 32.82	85.46 ± 1.22	10.42 ± 3.67
A	0.76	0.74	0.84	0.84
CPE_{cs} (uF. s^(a-1))	91.26 ± 0.16	459.60 ± 0.44	13.30 ± 0.16	32.69 ± 0.46
A	0.62	0.37	0.82	1.00

It is important to note that the E and P of energy storage systems have a big impact on their effectiveness. The effectiveness of the material in different electrolytes were compared using Ragone plots shown in Fig. 4.13a,c. Ragone plot shown in Fig. 4.13a compares the performances of K^+/MFP//N-ACs in 6 M KOH and Fig. 14.3c in 1 M KNO_3. The material in 6 M KOH gave energy density of 25.2 W h kg^{-1} with power density of 405.3 W kg^{-1} as compared to energy density of 26.9 W h kg^{-1} with power density of 449.4 W kg^{-1}in 1 M KNO_3. The high energy densities in both alkaline and neutral electrolytes is due to the intercalation of potassium resulting in generation of numerous open framework that facilitates diffusion of electrolyte ions. Again, intercalation of potassium assisted in evoking about rich faradic reactions for pseudocapacitance of redox Mn. In addition, a single device was connected to a light emitting diode (LED, 1.6 V) and this device successfully lit up a red LED (see inset Fig. 13a, c) for over a minute after charging for 20 s.

More intriguingly, the assembled asymmetric SCs based on K^+/MFP//N-ACs has high stability, with over 100% capacitance retention for up to 15 000 (Fig. 4.13b, 6 M KOH) and 10 000 (Fig. 4.13d, 1 M KNO_3) GCD cycles at 5 A g^{-1}. The high capacitance retention in both electrolytes indicates outstanding rate capability of the material in asymmetric SCs. The increase in

capacitance retention over many cycles is due to the accessibility of active sites via continuous diffusion of electrolyte ions into the structure.

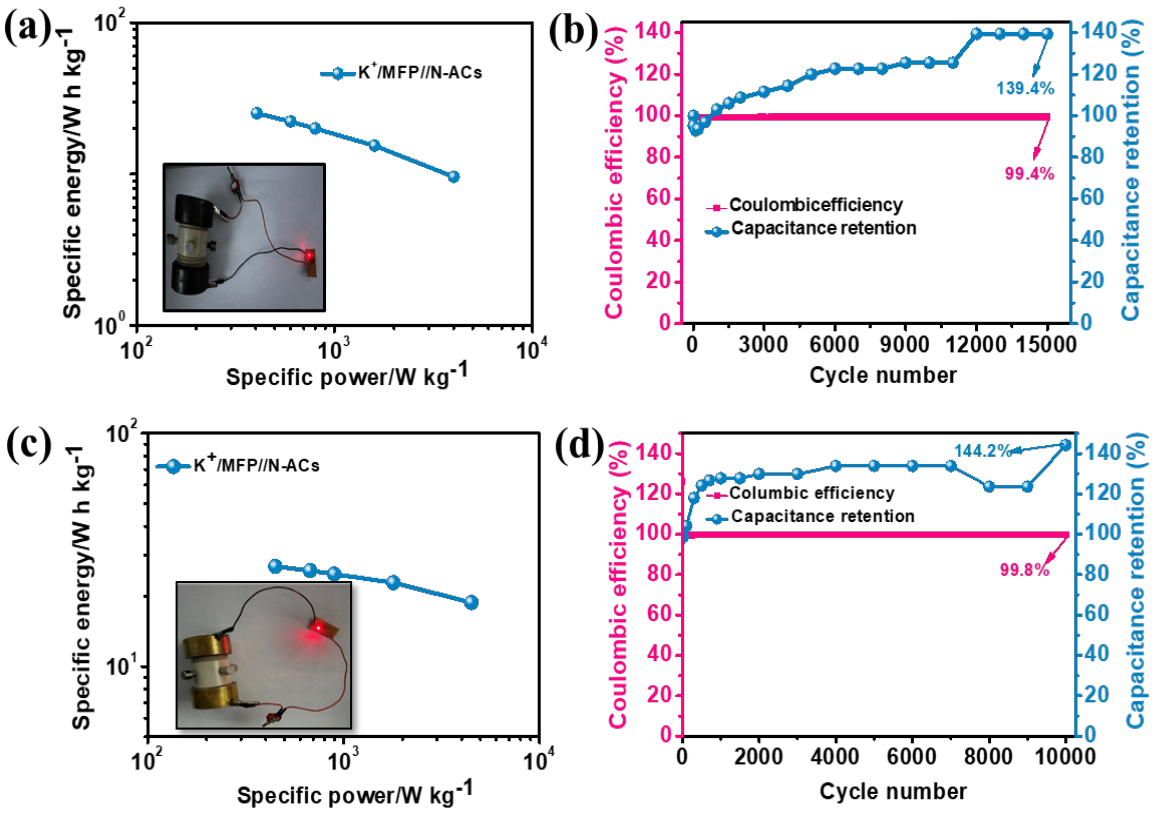

Fig. 4. 13. Ragone and cyclic stability of K^+/MFP//N-ACs in (a, b) 6 M KOH and (c, d) 1 M KNO_3. The insets shows an image of a red LED powered by K^+/MFP//N-ACs electrode based device.

4.4.3 Comparison of K^+/MFP in 6 M KOH and 1 M KNO_3

Three electrode system of K^+/MFP in 6 M KOH showed that the material has higher capacitance values than K^+/MFP in 1 M KNO_3 as shown in Fig. 4.9c and Fig. 4.10e.

The disparity of the performance of materials in the two different electrolytes could be due to the difference of electrolyte pH and the redox contribution that arises from the material. For example, neutral electrolytes (here 1 M KNO_3) has fewer oxygen and hydrogen ions as compared to alkaline electrolyte (here 6 M KOH), so the pH of neutral electrolytes is balanced on the oxygen and hydrogen ions such that there is no biased reaction occurring from the electrolyte ions and electrolyte material in any preferred potential [37,38]. However, alkaline

and acidic electrolytes have abundance of oxygen and hydrogen ions which could allow biased reaction between electrolyte ions and electrode material in a given potential. Other parameters that play a role during the interaction of electrolyte ions and electrode material are the sizes of ionic radii, ionic conductivities, mobility of the ions. The parameters are listed in Table 4.3. From the Table 4.3, the radius of hydration sphere decreases in this order: OH^-< NO^{3-} < $SO4^{2-}$ and the conductivities increases in this order: OH^- > SO_4^{2-} > NO_3^-, so the difference in electrochemical performance of K^+/MFP in 6 M KOH and 1 M KNO_3.

For investigations on the charge storage mechanism of K^+/MFP, the varied electrochemical behaviour of K^+/MFP in the two electrolytes mentioned above shows that the cations and anions are really engaged in the reaction of the K^+/MFP electrode.

Table 4. 3. Summary of the sizes of ions [39]

Type of ion	Size of bare ion (Å)	Size of hydrated ion (Å)	Ionic conductivity ($Scm^2\ mol^{-1}$)
K^+	1.15	3.31	73.5
OH^-	1.76	3.00	198
NO^{3-}	2.64	3.35	71.42

According to our findings, potassium intercalation increases MFP material's specific capacitance. The results on K^+/MFP and nitrogen-doped activated carbons from the utilization of biomass in asymmetric SCs as well as their energy densities, are provided in Table 4.4. To put these recent findings into context, the specific energy and power achieved in this investigation were comparable to those from prior studies and, in some cases, were even higher than those from other alkali intercalation into manganese/metal-based materials. These findings demonstrate how the energy density is influenced by a variety of variables, including the type of alkali metal used for intercalation, electrolyte and the nature of the parent material.

For example, K^+/MFP//N-ACs in 1 M KNO_3 has a higher energy of 26.9 W h Kg^{-1} than Na_xMnO_2@CNF (21.0 W h kg^{-1}) [40] and comparable energy density of nitrogen doped porous carbon in asymmetric SC with potassium intercalated into WO_3 (CBC-1//$K0.3WO_3$) (26.3 W h kg^{-1}).

Table 4. 4. Summary of energy and power density of intercalated alkali ions into manganese base materials and other metal-base materials.

Type of material	Electrolyte	Cell voltage (V)	Current density (A/g)	Specific energy (Wh/kg)	Specific power (W/kg)	Capacitance retention	Reference
K^+/MFP//N-ACs	6 M KOH	1.6	0.5	25.2	405.3	139.4	This study
K^+/MFP//N-ACs	1 M KNO_3	1.8	0.5	26.9	449.4	144.2	This study
Na_xMnO_2@CNF	1 M Na_2SO_4 and 4 mM $NaHCO_3$	2.0	1.0	21	1000	75.2	[40]
CBC-1//K0.3WO_3	1 M H_2SO_4	1.6	0.5 M	26.3	404.2	80	[41]
$LiFePO_4$//mesoporous carbon	1 M LiTFSI	2.1	0.1	17.9	-	-	[42]
K^+/MnO_2//ACs	0.5 M K_2SO_4	2.3	0.5	42.9	4.7	76	[43]

4.4. Conclusions

A novel, scalable synthesis approach that includes a hydrothermal treatment, carried out in an aqueous environment, has been successful in producing alkali metal ion intercalated in fluorophosphates triplite material. The synthesis process parameters were found to ensure the pure triplite phase formation with 1.9% potassium. The intercalated potassium triplite material formation was confirmed by structural characterization; however, SEM imaging shows distinct morphological variations. Intercalated MFP show different quasi rectangular and hexagonal morphology compared to parent MFP with bulk-like structure morphology. Analysis of K^+/MFP showed greater capacitance values in 6 M KOH and 1 M KNO_3 in three electrode system than parent MFP. Again, K^+/MFP showed higher capacitance values of 26.2 F g^{-1} (at 0.5 A g^{-1}) in 6 M KOH than 145.4 F g^{-1} (at 0.5 A g^{-1}) in 1 M KNO_3 electrolyte in a three-electrode system due to the high conductivity of KOH.

Again, K^+/MFP//N-ACs gave rise to capacitance value of 283.1 F g^{-1} at 0.5 A g^{-1} in 6 M KOH as compared to 239.5 F g^{-1} at 0.5 A g^{-1}. However, high energy density was observed in 1 M KNO_3 (26.9 W h kg^{-1}) than 25.2 W h kg^{-1} in 6 M KOH due to the wider voltage range of 1.8 V in 1 M KNO_3 than 1.6 V of 6 M KOH. This study reports the first complete synthesis of alkali ion intercalated triplite material via hydrothermal method and their electrochemistry in alkali and neutral electrolytes energy storage systems.

References

[1] M.U. Sasmaz, E. Sakar, Y.E. Yayla, U. Akkucuk, The relationship between renewable energy and human development in OECD countries: A panel data analysis, Sustainability (Switzerland). 12 (2020) 1–16. https://doi.org/10.3390/SU12187450.

[2] Y. Li, X. Han, T. Yi, Y. He, X. Li, Review and prospect of NiCo2O4-based composite materials for supercapacitor electrodes, Journal of Energy Chemistry. 31 (2019) 54–78. https://doi.org/10.1016/j.jechem.2018.05.010.

[3] M. Zhou, F. Pu, Z. Wang, S. Guan, Nitrogen-doped porous carbons through KOH activation with superior performance in supercapacitors, Carbon N Y. 68 (2014) 185–194. https://doi.org/10.1016/j.carbon.2013.10.079.

[4] D. Chao, W. Zhou, F. Xie, C. Ye, H. Li, M. Jaroniec, S.-Z. Qiao, Roadmap for advanced aqueous batteries: From design of materials to applications, 2020. https://www.science.org.

[5] Q. Gao, L. Demarconnay, E. Raymundo-Piñero, F. Béguin, Exploring the large voltage range of carbon/carbon supercapacitors in aqueous lithium sulfate electrolyte, Energy Environ Sci. 5 (2012) 9611–9617. https://doi.org/10.1039/c2ee22284a.

[6] F. Zhan, H. Wang, Q. He, W. Xu, J. Chen, X. Ren, H. Wang, S. Liu, M. Han, Y. Yamauchi, L. Chen, Metal-organic frameworks and their derivatives for metal-ion (Li, Na, K and Zn) hybrid capacitors, Chem Sci. 13 (2022) 11981–12015. https://doi.org/10.1039/d2sc04012c.

[7] J.-C. Liu, Z.-H. Huang, T.-Y. Ma, Aqueous Supercapacitor with Ultrahigh Voltage Window Beyond 2.0 Volt, Small Struct. 1 (2020) 2000020. https://doi.org/10.1002/sstr.202000020.

[8] C. Liu, Z. Yu, D. Neff, A. Zhamu, B.Z. Jang, Graphene-based supercapacitor with an ultrahigh energy density, Nano Lett. 10 (2010) 4863–4868. https://doi.org/10.1021/nl102661q.

[9] W.G. Pell, B.E. Conway, Peculiarities and requirements of asymmetric capacitor devices based on combination of capacitor and battery-type electrodes, J Power Sources. 136 (2004) 334–345. https://doi.org/10.1016/j.jpowsour.2004.03.021.

[10] Y. Li, Y. Yang, P. Zhou, T. Gao, Z. Xu, S. Lin, H. Chen, J. Zhou, S. Guo, Enhanced Cathode and Anode Compatibility for Boosting Both Energy and Power Densities of Na/K-Ion Hybrid Capacitors, Matter. 1 (2019) 893–910. https://doi.org/10.1016/j.matt.2019.04.003.

[11] S. Ding, X. Dai, Y. Tian, B. Song, L. Wang, G. Li, S. Li, J. Huang, Z. Li, A. Meng, Insight into the coordinating mechanism of multi-electron reaction and structural stability induced by K+ pre-intercalation for magnesium ions batteries, Nano Energy. 93 (2022). https://doi.org/10.1016/j.nanoen.2021.106838.

[12] J.R. Rea, E. Kostiner, The crystal structure of manganese fluorophosphate, Mn 2 (PO 4)F , Acta Crystallogr B. 28 (1972) 2525–2529. https://doi.org/10.1107/s0567740872006417.

[13] N. Nzimande, A. Haruna, P. Mwonga, B. Rasche, F. Cummings, K.I. Ozoemena, Ceria-Spiderweb Nanosheets Unlock the Energy-Storage Properties in the “Sleeping” Triplite ($Mn_2(PO_4)F$). ACS Appl. Energy Mater. 4 (2021) 13085-13097.

[14] C.J. Jafta, M.K. Mathe, N. Manyala, W.D. Roos, K.I. Ozoemena, Microwave-assisted synthesis of high-voltage nanostructured LiMn 1.5Ni0.5O4 spinel: Tuning the Mn3+ content and electrochemical performance, ACS Appl Mater Interfaces. 5 (2013) 7592–7598. https://doi.org/10.1021/am401894t.

[15] C.J. Jafta, K. Raju, M.K. Mathe, N. Manyala, K.I. Ozoemena, Microwave Irradiation Controls the Manganese Oxidation States of Nanostructured ($Li[Li_{0.2}Mn_{0.52}Ni_{0.13}Co_{0.13}Al_{0.02}]O_2$) Layered Cathode Materials for High-Performance Lithium Ion Batteries , J Electrochem Soc. 162 (2015) A768–A773. https://doi.org/10.1149/2.0931504jes.

[16] G. Nelson, S.R. Criswell, J. Zhang, J. Murray, B.A. Racette, Research capacity development in South African manganese mines to bridge exposure and neuropathologic outcomes, Neurotoxicology. 33 (2012) 683–686. https://doi.org/10.1016/j.neuro.2012.01.003.

[17] M.T. McDowell, S.W. Lee, W.D. Nix, Y. Cui, 25th anniversary article: Understanding the lithiation of silicon and other alloying anodes for lithium-ion batteries, Advanced Materials. 25 (2013) 4966–4985. https://doi.org/10.1002/adma.201301795.

[18] K. Xiang, W. Xing, D.B. Ravnsbæk, L. Hong, M. Tang, Z. Li, K.M. Wiaderek, O.J. Borkiewicz, K.W. Chapman, P.J. Chupas, Y.M. Chiang, Accommodating High Transformation Strains in Battery Electrodes via the Formation of Nanoscale Intermediate

Phases: Operando Investigation of Olivine NaFePO4, Nano Lett. 17 (2017) 1696–1702. https://doi.org/10.1021/acs.nanolett.6b04971.

[19] N. Recham, G. Rousse, M.T. Sougrati, J.N. Chotard, C. Frayret, S. Mariyappan, B.C. Melot, J.C. Jumas, J.M. Tarascon, Preparation and characterization of a stable FeSO4F-based framework for alkali ion insertion electrodes, Chemistry of Materials. 24 (2012) 4363–4370. https://doi.org/10.1021/cm302428w.

[20] E. Zhen, J. Jiang, C. Lv, X. Huang, H. Xu, H. Dou, X. Zhang, Effects of binder content on low-cost solvent-free electrodes made by dry-spraying manufacturing for lithium-ion batteries, J Power Sources. 515 (2021). https://doi.org/10.1016/j.jpowsour.2021.230644.

[21] W. Yang, Z. Gao, J. Wang, J. Ma, M. Zhang, L. Liu, Solvothermal one-step synthesis of Ni-Al layered double hydroxide/carbon nanotube/reduced graphene oxide sheet ternary nanocomposite with ultrahigh capacitance for supercapacitors, ACS Appl Mater Interfaces. 5 (2013) 5443–5454. https://doi.org/10.1021/am4003843.

[22] W. Sun, Y. Zhang, F. Yang, Tuning electrochemical performance of carbon-sphere-based supercapacitors by compressive stress, Electrochim Acta. 357 (2020). https://doi.org/10.1016/j.electacta.2020.136874.

[23] K. Makgopa, P.M. Ejikeme, C.J. Jafta, K. Raju, M. Zeiger, V. Presser, K.I. Ozoemena, A high-rate aqueous symmetric pseudocapacitor based on highly graphitized onion-like carbon/birnessite-type manganese oxide nanohybrids, J Mater Chem A Mater. 3 (2015) 3480–3490. https://doi.org/10.1039/c4ta06715k.

[24] T.P. Mofokeng, Z.N. Tetana, K.I. Ozoemena, Defective 3D nitrogen-doped carbon nanotube-carbon fibre networks for high-performance supercapacitor: Transformative role of nitrogen-doping from surface-confined to diffusive kinetics, Carbon N Y. 169 (2020) 312–326. https://doi.org/10.1016/j.carbon.2020.07.049.

[25] K. Makgopa, P.M. Ejikeme, K.I. Ozoemena, Graphene oxide-modified nickel (II) tetra-aminophthalocyanine nanocomposites for high-power symmetric pseudocapacitor, Electrochim Acta. 212 (2016) 876–882. https://doi.org/10.1016/j.electacta.2016.07.027.

[26] H. Fatima, D.W. Lee, H.J. Yun, K.S. Kim, Shape-controlled synthesis of magnetic Fe3O4 nanoparticles with different iron precursors and capping agents, RSC Adv. 8 (2018) 22917–22923. https://doi.org/10.1039/c8ra02909a.

[27] Z.L. Wang, Transmission electron microscopy of shape-controlled nanocrystals and their assemblies, Journal of Physical Chemistry B. 104 (2000) 1153–1175. https://doi.org/10.1021/jp993593c.

[28] R. Swaminathan, M.A. Willard, M.E. McHenry, Experimental observations and nucleation and growth theory of polyhedral magnetic ferrite nanoparticles synthesized using an RF plasma torch, Acta Mater. 54 (2006) 807–816. https://doi.org/10.1016/j.actamat.2005.10.015.

[29] P.W. Menezes, A. Indra, V. Gutkin, M. Driess, Boosting electrochemical water oxidation through replacement of Oh Co sites in cobalt oxide spinel with manganese, Chemical Communications. 53 (2017) 8018–8021. https://doi.org/10.1039/c7cc03749j.

[30] M.A. Langell, C.W. Hutchings, G.A. Carson, M.H. Nassir, High resolution electron energy loss spectroscopy of MnO(100) and oxidized MnO(100), Journal of Vacuum Science & Technology A: Vacuum, Surfaces, and Films. 14 (1996) 1656–1661. https://doi.org/10.1116/1.580314.

[31] R. Tholkappiyan, A.N. Naveen, K. Vishista, F. Hamed, Investigation on the electrochemical performance of hausmannite Mn3O4 nanoparticles by ultrasonic irradiation assisted co-precipitation method for supercapacitor electrodes, Journal of Taibah University for Science. 12 (2018) 669–677. https://doi.org/10.1080/16583655.2018.1497440.

[32] K. Rajkumari, D. Das, G. Pathak, L. Rokhum, Waste-to-useful: A biowaste-derived heterogeneous catalyst for a green and sustainable Henry reaction, New Journal of Chemistry. 43 (2019) 2134–2140. https://doi.org/10.1039/c8nj05029e.

[33] L. Guan, L. Yu, G.Z. Chen, Capacitive and non-capacitive faradaic charge storage, Electrochim Acta. 206 (2016) 464–478. https://doi.org/10.1016/j.electacta.2016.01.213.

[34] B. Fang, Y.Z. Wei, M. Kumagai, Modified carbon materials for high-rate EDLCs application, J Power Sources. 155 (2006) 487–491. https://doi.org/10.1016/j.jpowsour.2005.04.012.

[35] H. Jung, M. Taillefert, J. Sun, Q. Wang, O.J. Borkiewicz, P. Liu, L. Yang, S. Chen, H. Chen, Y. Tang, Redox Cycling Driven Transformation of Layered Manganese Oxides to Tunnel Structures. J. Am. Chem. Soc. 5 (2020) 2506-2513.

[36] S. Ishimoto, Y. Asakawa, M. Shinya, K. Naoi, Degradation Responses of Activated-Carbon-Based EDLCs for Higher Voltage Operation and Their Factors, J Electrochem Soc. 156 (2009) A563. https://doi.org/10.1149/1.3126423.

[37] S.T. Vindt, E.M. Skou, The buffer effect in neutral electrolyte supercapacitors, Appl Phys A Mater Sci Process. 122 (2016) 1–6. https://doi.org/10.1007/s00339-015-9563-8.

[38] Z. Sheng, X. Lin, H. Wei, Y. Zhang, Z. Tian, C. Wang, D. Xu, Y. Wang, Green synthesis of nitrogen-doped hierarchical porous carbon nanosheets derived from polyvinyl chloride towards high-performance supercapacitor, J Power Sources. 515 (2021). https://doi.org/10.1016/j.jpowsour.2021.230629.

[39] C. Zhong, Y. Deng, W. Hu, J. Qiao, L. Zhang, J. Zhang, A review of electrolyte materials and compositions for electrochemical supercapacitors, Chem Soc Rev. 44 (2015) 7484–7539. https://doi.org/10.1039/c5cs00303b.

[40] S.C. Lin, Y.T. Lu, Y.A. Chien, J.A. Wang, P.Y. Chen, C.C.M. Ma, C.C. Hu, Asymmetric supercapacitors based on electrospun carbon nanofiber/sodium-pre-intercalated manganese oxide electrodes with high power and energy densities, J Power Sources. 393 (2018) 1–10. https://doi.org/10.1016/j.jpowsour.2018.05.019.

[41] G. Ma, Z. Zhang, K. Sun, E. Feng, H. Peng, X. Zhou, Z. Lei, High-performance aqueous asymmetric supercapacitor based on K0.3WO3 nanorods and nitrogen-doped porous carbon, J Power Sources. 330 (2016) 219–230. https://doi.org/10.1016/j.jpowsour.2016.09.022.

[42] P.F.R. Ortega, G.A. Dos Santos Junior, L.A. Montoro, G.G. Silva, C. Blanco, R. Santamaría, R.L. Lavall, LiFePO4/Mesoporous Carbon Hybrid Supercapacitor Based on LiTFSI/Imidazolium Ionic Liquid Electrolyte, Journal of Physical Chemistry C. 122 (2018) 1456–1465. https://doi.org/10.1021/acs.jpcc.7b09869.

[43] L. Chen, Y. Zhang, C. Hao, X. Zhang, Q, Sun, Y. Wei, B. Li, L. Ci, J. Wei. Interlayer Engineering of K_xMnO_2 Enables Superior Alkali Metal Ion Storage for Advanced Hybrid Capacitors. 9 ChemElectroChem (2022). https://doi.org/10.1002/celc.202200059

CHAPTER 5: Enhanced pseudocapacitance of Li^+/MFP: The effect of alkaline, neutral and ionic electrolyte

5.1. Introduction

The use of the electrode materials is obviously constrained by the fact that the majority of transition metal-based materials store charges through surface Faradaic reactions [1]. Therefore, to further increase energy density, the development of effective electrode materials with broad potential windows and high bulk utilisation at the atomic level is necessary. However, manganese base materials suffer from capacity fading because of Mn dissolution. Furthermore, the well-known Jahn-Teller effect in Mn^{3+} promotes Mn dissolution by generating Mn^{2+} by the disproportionation reaction of Mn^{3+} [2, 3]. Numerous research studies having confirmed the Mn dissolving mechanisms have led to the progressive development of a number of techniques, including surface modification, atom doping, ion or molecule pre-intercalation, electrolyte optimisation, and others [4,5]. A potassium manganese hexacyanoferrate cathode with an in situ cation engineered surface that substitutes iron for manganese was created by Lu and his coworkers [6]. With this alternate approach, the stability of the electrode structure and the surface chemical characteristics may both be improved while the dissolution of manganese would be reduced. Even if the stability of Mn-based materials may be significantly increased by the work reported by Lu's group [6], several new issues are raised, including a decrease in the capacity of Mn active components, a loss of energy density, and complicated preparation procedures. In order to ensure high capacity, it is essential to create manganese-based materials with a very robust structure using straightforward and practical methods.

Hence, in this study, simple hydrothermal insertion of lithium ions using LiOH was introduced in manganese fluorophosphate (MFP) to improve the stability of the material and retain Mn active components to facilitates an increase in energy density. In this study, lithium ions were intercalated into MFP material to improve reaction kinetics of the material by increasing the volume expansion to allow for faster diffusion of electrolyte ions. Stabilizing cations such as Li^+ can be used to provide charge neutrality and enhance structural stability in MFP [7, 8].

Another cause of low energy density is narrow voltage window [8]. According to the equation used to calculate energy density, $E = \frac{1}{2}CV^2$, increasing specific capacitance (C) or cell voltage (V) are two possible approaches to increase energy density [9, 10]. The ideal way to use the

distinct voltage windows of the cathode and anode for building asymmetric supercapacitors (ASCs) is to dramatically increase the voltage, which may even reach over 2.0 V in neutral electrolytes [11, 12]. Due to the potential water electrolysis voltage at 1.23 V, the voltage for ASC devices is often constrained to 2 V [13].

Additionally, it is clear that electrolytes have an impact on the possible voltage window for aqueous ASCs. Neutral electrolytes such as K_2SO_4, Na_2SO_4 and Li_2SO_4 can attain a greater stable potential window when compared to acid or alkaline electrolytes because of the essential ion dehydration energy and the same concentration of protons and hydroxyl groups at neutral pH, hydrogen/oxygen evolution may be efficiently suppressed in neutral aqueous electrolytes [13, 14].

High electrochemical stability window (ESW) values have recently been reported for various electrode types in so-called "water-in-salt" (WIS) electrolytes, which are more specifically salt to water mass (m_{salt}/m_{water}) or volume (V_{salt}/V_{water}) ratios greater than 1 [15]. The most commonly used salt for this purpose is lithium bis(trifluoromethanesulfonyl)imide (LiTFSI) [15]. Again ionic liquids have been reported to have wider voltage window than aqueous electrolytes. Among various ionic liquids, LiFSTI has been a focus recently due to its good ionic conductivity, increased thermal and electrochemical stabilities [15, 16].In this study, Li^+/MFP was used as a cathode with nitrogen doped activated carbons (N-ACs) as an anode. In this context, the main objective of the present study was to determine the effect of alkaline, neutral and ionic liquids in Li^+/MFP.

5.2. Methodology

5.2.1. Materials

Lithium intercalated manganese fluorophosphate (Li^+/MFP) was synthesized using lithium fluoride (LiF, Sigma Aldrich), ammonium dihydrogen phosphate ($NH_4H_2PO_4$, Sigma Aldrich), manganese (II) nitrate tetrahydrate $(Mn(NO)_3)_2.4H_2O$, Sigma Aldrich) and lithium hydroxide (LiOH, Sigma Aldrich). Microfiber filter paper (ACE chemicals) were used as an electrode separator with 0.18 mm thickness. All other reagents were used without further purification.

5.2.2. Methodology

MFP was synthesized by a procedure discussed in Chapter 4. Li^+/MFP was synthesized by mixing 900 mg of MFP with 8 M LiOH [17]. The mixture was stirred for 24 h at room

temperature. The mixture was then subjected to hydrothermal treatment for 12 h at 180 ℃. The resulting solution was washed with distilled water and dried for 12 at ℃ (see Fig. 5.1).

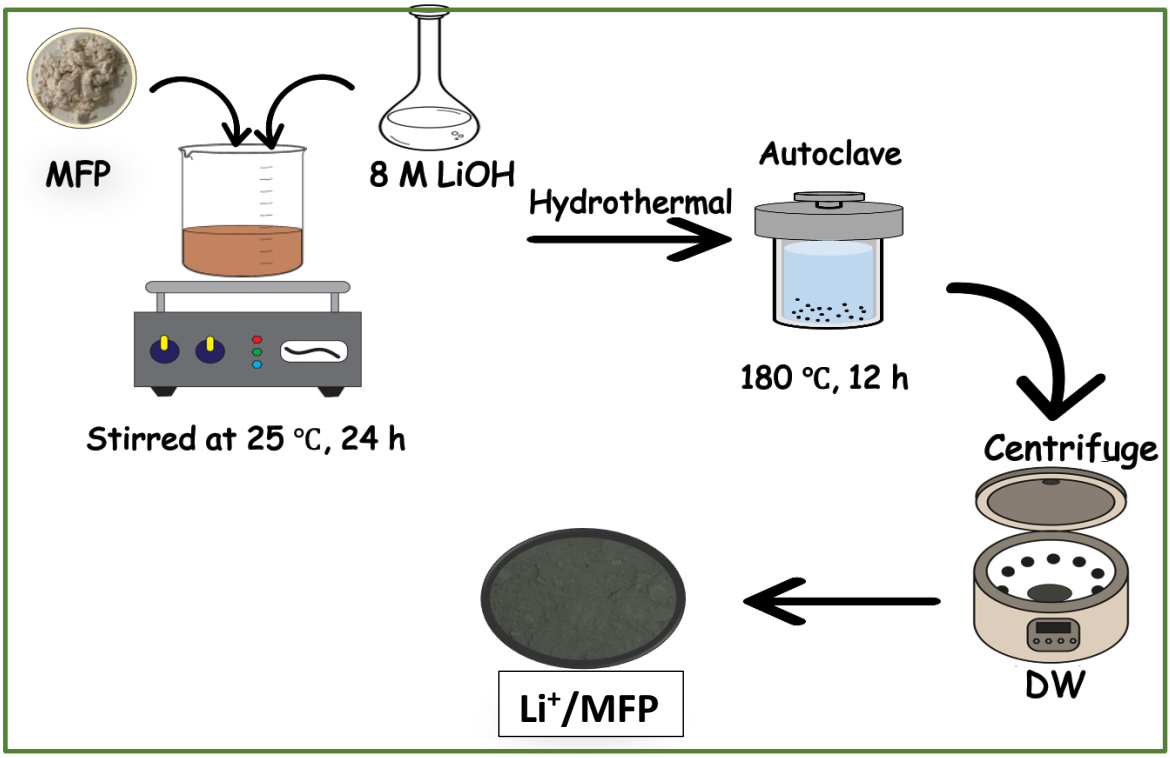

Fig. 5. 1. Schematic representative showing the synthesis of Li^+/MFP.

5.2.3. Electrochemical characterization

A Bio-Logic SP300 electrochemical workstation with EC-lab software was used to perform the electrochemical measurements. Slurry was formed by adding the active materials Li^+/MFP/, MFP, carbon black and N-methylpyrrolidone (NMP) (80:10:10) together and the mixture was stirred for 12 h [18, 19]. The working electrode was prepared by coating the slurry on carbon paper followed by drying in a vacuum oven for 12 h at 60 ℃. The mass loading of a single electrode was 1.4-1.5 mg. The counter electrode used was Ni foam, Ag/AgCl as a reference electrode and 6 M LiOH, 1 M LiTFSI and 1 M Li_2SO_4 as an electrolyte. The assembly of the asymmetric device was achieved using Li^+/MFP as a cathode and N-ACs as an anode.

All the electrochemical analyses were tested by using cyclic voltammetry (CV), galvanostatic charge-discharge (GCD), and electrochemical impedance spectroscopy (EIS) procedures with 10 mV amplitude AC voltage in the frequency range of 0.1 Hz to 100 100 kHz.

5.3. Results and discussion

The XRD spectra of MFP and Li^+/MFP is shown in Fig. 5.2. Rietveld fits of the XRD patterns provide evidence that Mn_2PO_4F is in its pure phase (see Chapter 4). New peaks for Li^+/MFP were observed with phases (202) and (002). However, there was a shift of the other peaks with increase or decrease in intensities after reaction with LiOH. This could be due to the material resulting in smaller particles and change of morphology. [20]. Again,, the peaks of Li^+/MFP becomes broader might be due to lattice defects and crystallite size becomes smaller. Different structures or phases can be formed by different metal hydroxide. These can due to electrolyte ions diffusing in the MFP material in alkaline medium [21, 22]. Another possible explanation could be due to more chemically facets favoured than crystalline facets of the material growth of the manganese-based material on a [22].

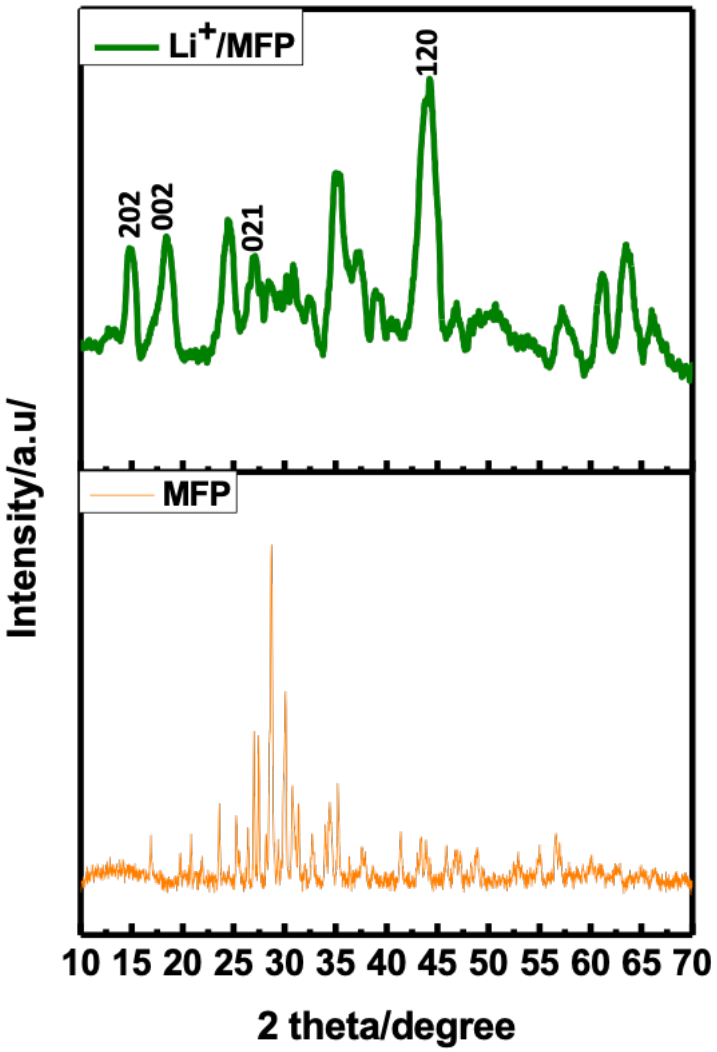

Fig. 5. 2. XRD spectra of MFP and Li^+/MFP.

The typical TEM images of MFP (Fig. 5.3a) and Li^+/MFP (Fig. 5.3b,c) show clusters or agglomerates of big particles for MFP with lattice fringes and a d-spacing of 0.31 nm (see Chapter 4). The d-spacing increases to 0.37 nm after treatment with LiOH (Fig. 5.3d). The cluster morphology of MFP after reaction with LiOH slightly changed the morphology to smaller particles for Li^+/MFP. This shows that treatment of the material with LiOH has a slight impact on the morphology of MFP (compared to KOH, discussed in Chapter 4). The introduction of LiOH changes the morphology of MFP from bulk to smaller particles. This is expected, as LiOH is less strong base compared to KOH. These results are consistent with work reported by Balan et al. [23] where increasing LiOH concentration to 7.8 mM, the morphology of MnO_2 changes from nanoflower to nanocubes.

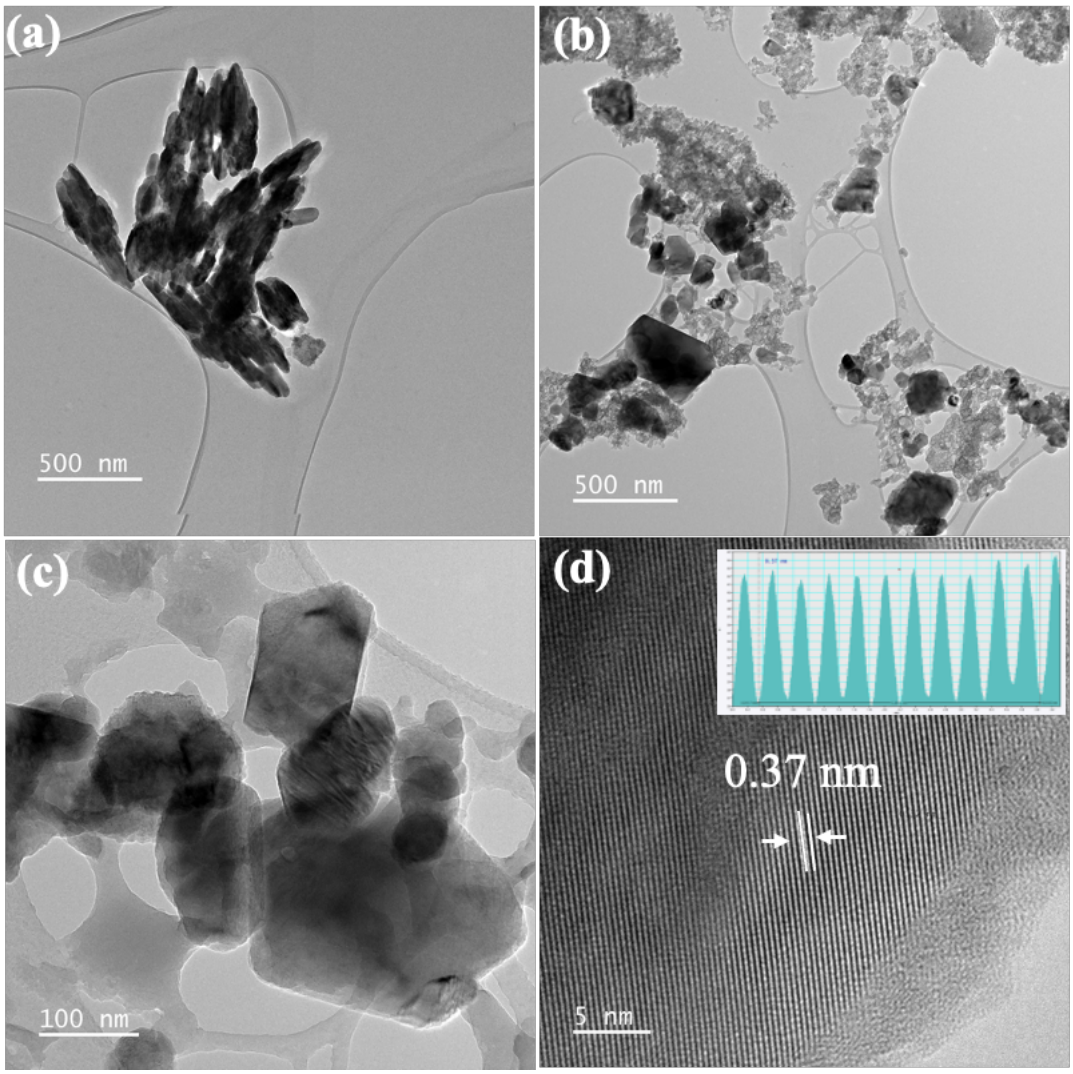

Fig. 5. 3. TEM images of (a) MFP and (b-d) Li^+/MFP.

SEM images of the materials are shown in Fig. 5.4. After treatment of MFP with LiOH, the morphology changed showing smaller particles with quasi rectangular shapes for Li^+/MFP (Fig. 5.4b). Again, Li^+/MFP show aggregates of particles on top of the quasi-rectangular shape structure (Fig. 5.4b, see inset). The formation of aggregates covering the particles could be due to the reaction of the material with LiOH. The elemental mapping of Li^+/MFP show that the elements are uniformly distributed throughout the material. Li^+/MFP (Fig. 5c-g) show uniform distribution of elements of Mn, P, O and F.

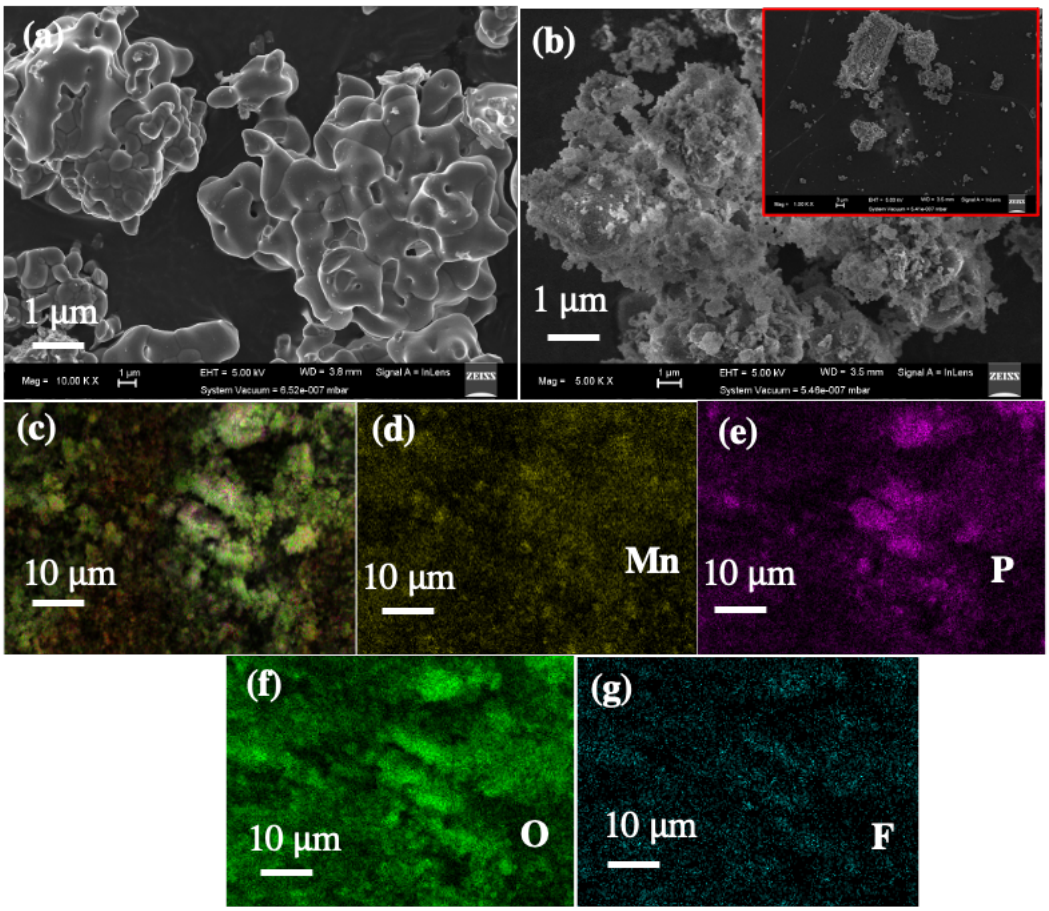

Fig. 5. 4. SEM images of (a) MFP, (b) Li^{+}/MFP, EDS mapping (c-g) of Li^{+}/MFP.

The formation of both MFP and Li^{+}/MFP is further supported by Raman spectrum (Fig. 5.5). The Raman bands are identified in terms of the vibrating units of PO_4^{2-}. The P-O stretching modes of PO_4^{2-} anion appear in the range 954-1046 cm^{-1} for MFP. The symmetric stretching vibration are observed at vibrations labelled ν5-6 (1012.4-1046.5 cm^{-1}), while the asymmetric vibration are observed at 959.9-978.8 cm^{-1} (ν3-4) [21, 24]. The peaks that appear at these regions for PO_4^{2-} vibrations disappear in Li^{+}/MFP which is due to the change in structure and decrease of phosphate atoms on the surface of the material as shown in XPS spectra discussed below (Table 5.1). The broad peak at 646.2 eV (ν1) for Li^{+}/MFP is due to asymmetric vibration of the phosphate group.

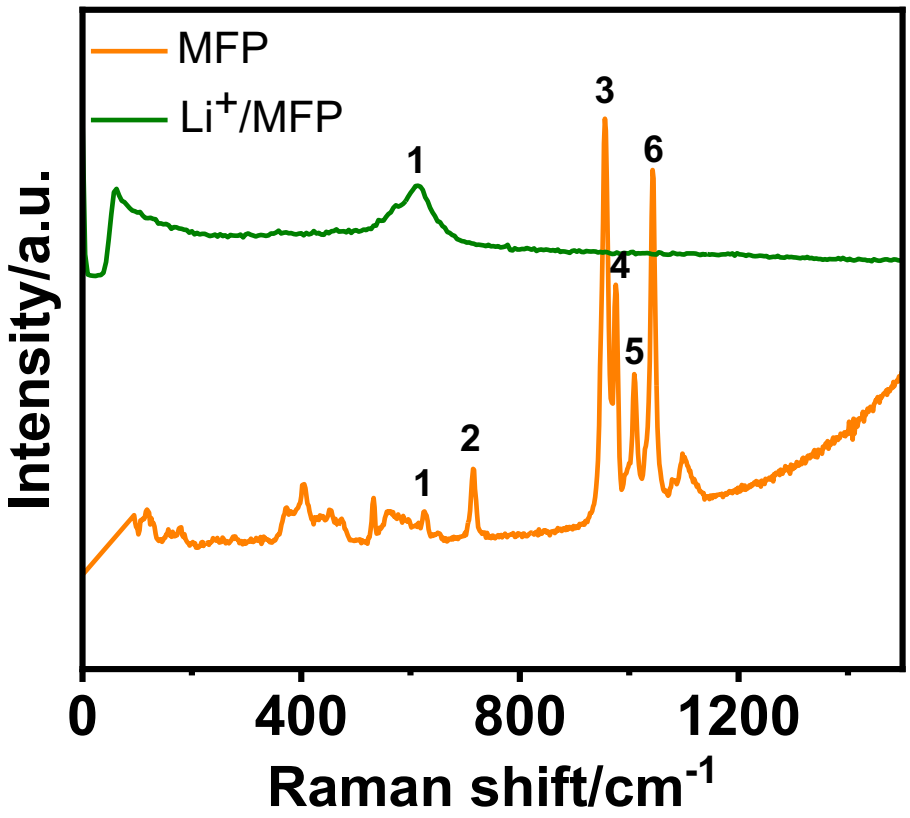

Fig. 5. 5. Raman spectra of MFP and Li^+/MFP.

According to Fig. 5.6, all elements (Mn 2p, O1s, F1s, P2p3, and Li1s) are present at their respective binding energies for Li^+/MFP. Due to the presence of M-O bond in the Li^+/MFP material, manganese oxide is present at a binding energy of 641.4-642.8 eV. The binding energy of fluoride F1s is at 690.2 eV, O1s at 532.9 eV and Li1s at 51.5 eV [21]. All the elements in MFP are present (see Chapter 4). Table 5.1 displays the XPS atom % for each element found in MFP and Li^+/MFP.

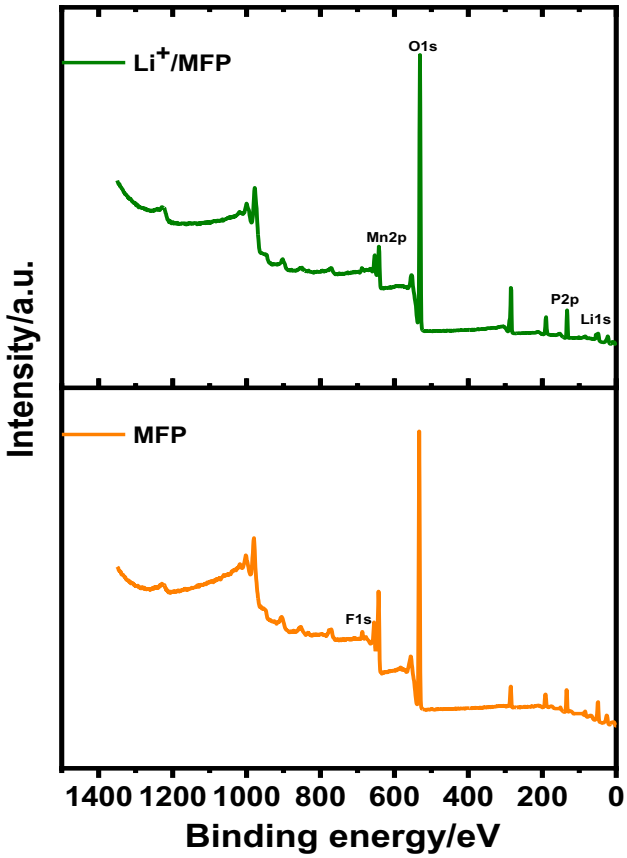

Fig. 5. 6. Survey scan of MFP and Li^+/MFP.

Table 5. 1. XPS % atom of elements present in MFP and Li^+/MFP.

Type of material	XPS atom %				
	Li1s	Mn2p	O1s	P2p	F1s
MFP	-	12.9	54.5	13.9	1.6
Li^+/MFP	3.2	14.9	50.3	7.6	0.5

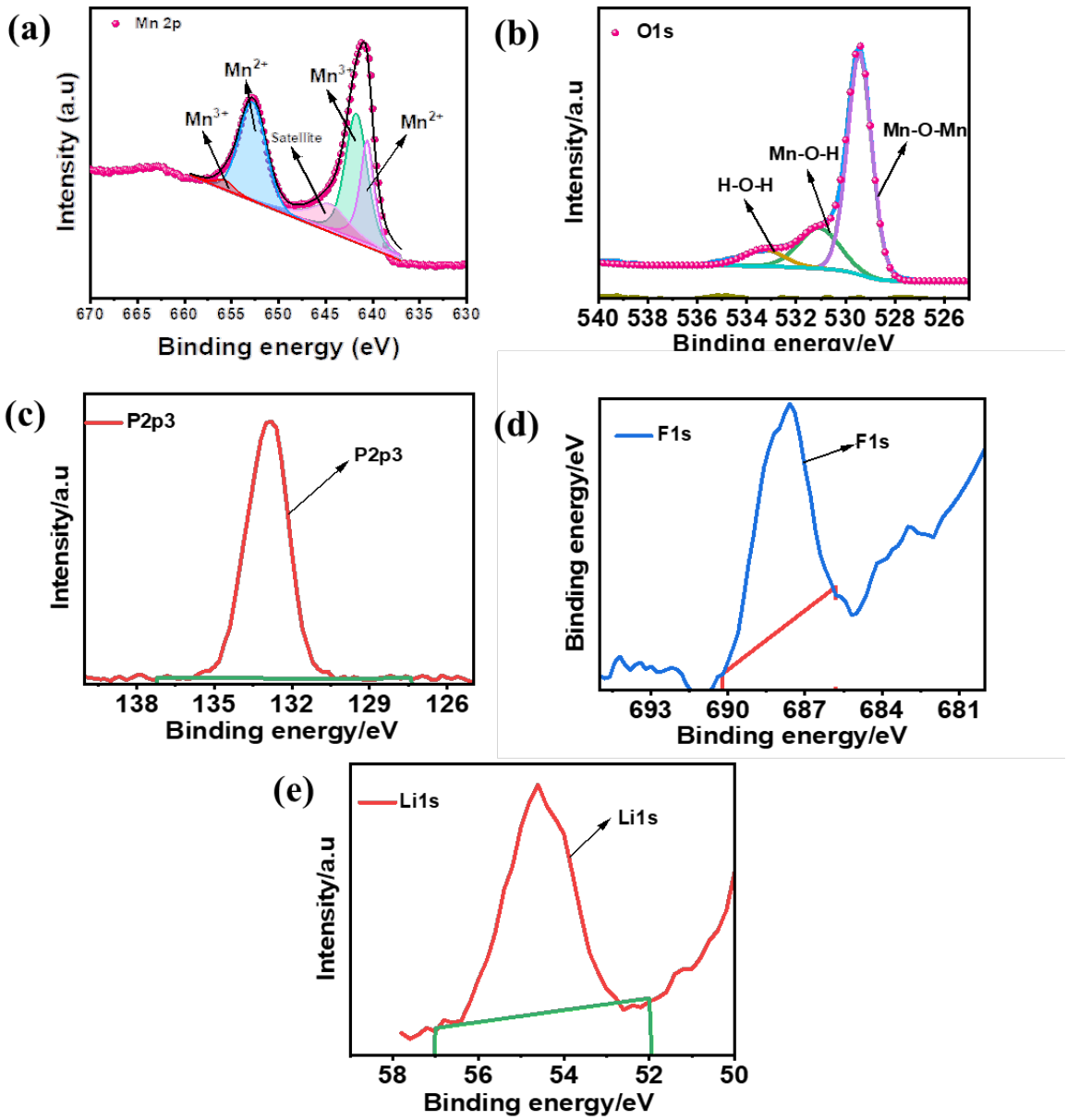

Fig. 5. 7. (a) Mn2p, (b) O1s, (c) P2p3, (d) F1s and (e) Li1s spectra of Li^+/MFP.

Fig. 5.7a depicts the deconvoluted Mn2p for Li^+/ MFP, which has two primary peaks at 642.3 eV for $Mn2p_{3/2}$ and 654.4 eV for $Mn2p_{1/2}$ spin orbitals, respectively. For Li^+/MFP, $Mn2p_{3/2}$ is deconvoluted and has three peaks for Mn^{2+}, Mn^{3+} and a satellite peak. $Mn2p_{1/2}$ is divided into two peaks for Mn^{2+} at lower binding energy and at higher binding energy for Mn^{3+} [25, 26].

Fig. 5.7b depicts the deconvoluted O1s spectrum of Li^+/MFP, which has three peaks that have been identified as Mn-O-Mn (529.4 eV), Mn-OH radical (531.2 eV), and lattice oxygen at 533.4 eV [27]. P2p3 is shown in Fig. 5.7c at 132.4 eV [28]. The presence of F1s for Li^+/MFP is shown in Fig. 5.7d at 687.6 eV and Li1s at 55.2 eV (Fig. 5.7e) [29, 30].

From the characterization techniques, TEM images show that lithium was successfully intercalated in MFP due to the increase in d-spacing. XRD, SEM and Raman data show that the structure of the materials changes after introduction of LiOH. Lastly, XPS show that lithium was successfully introduced into the parent MFP material.

5.4. Electrochemical analysis

5.4.1. Three electrode system of MFP and Li^+/MFP in 6 M LiOH

The electrochemical behaviour of MFP and Li^+/MFP were analysed using CV and GCD. Li^+/MFP show oxygen evolution at 0-1.0 V (Fig. 5.8a), hence the CV and GCD were ran at 0.0-0.9 V. CV and GCD of Li^+/MFP (Fig. 5.8b, c) show high current response and discharge time than MFP, which show that lithium intercalation improves the electrochemistry of the pristine MFP. The improvement of MFP after intercalation could be due to exposure of more manganese atoms as shown from Table 5.1 which could be facilitating the redox behaviour of MFP. Again, the increase in d-spacing of Li^+/MFP facilitates more accumulation of electrolytes ions than narrow d-spacing of MFP. Two pairs of redox peaks on both cathodic (0.18 and 1.77 V) and anodic (0.43 and 0.85 V) sweeps can be observed, from CV curves [31, 32].

The following reaction occurs at cathodic peaks:

Mn (III) +e-→ Mn (II)

and the reaction below correspond to anodic peaks reactions:

Mn (II) -e-→ Mn (III)

The calculated specific capacitance were compared (Fig. 5.8d) and Li^+/MFP showed higher capacitance values of 110.1, 94.2, 77.4, 69.1 and 59.8 F g^{-1} from 5-50 mV s^{-1} than capacitance of MFP (47.4, 36.8, 28.4, 24.3 and 15.8 F g^{-1}). These results show that lithium intercalation evokes the redox properties of MFP.

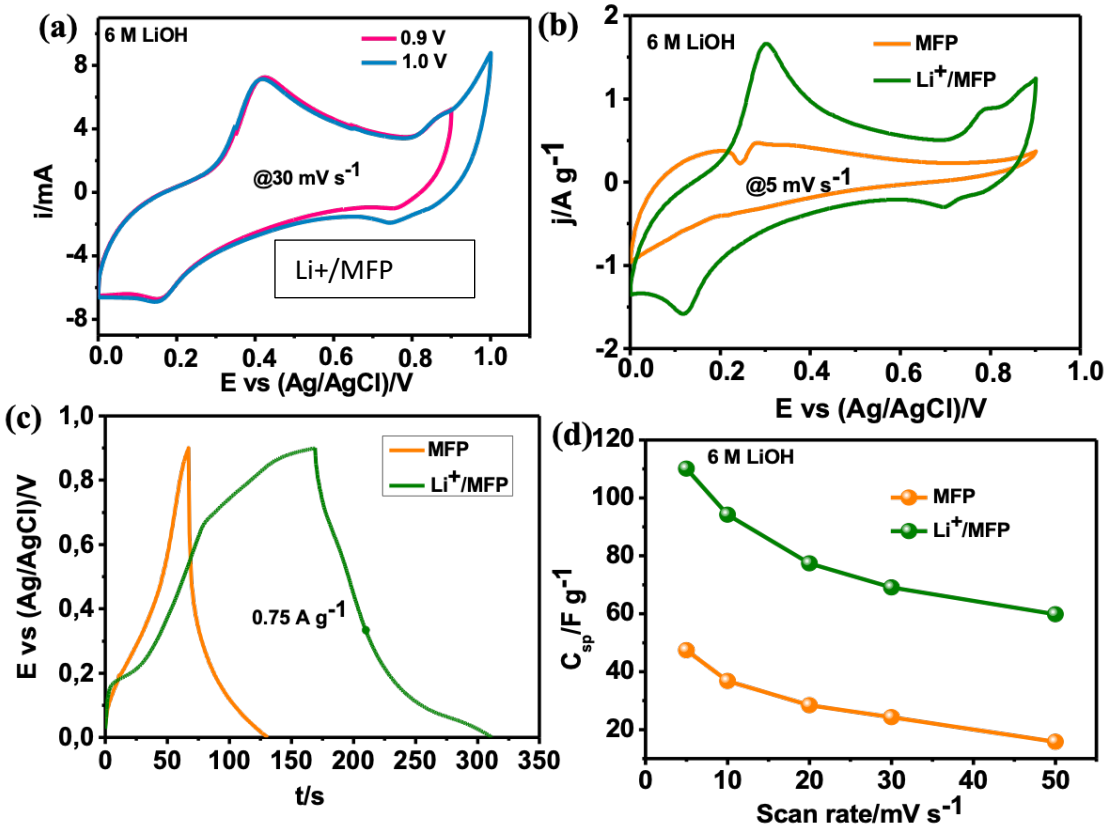

Fig. 5. 8. (a) CV of Li^+/MFP, (b) comparison CV, (c) GCD and (d) C_{sp} vs scan rate of MFP and Li^+/MFP.

5.4.2. Three electrode system of MFP and Li+/MFP in Li_2SO_4

Li^+/MFP as a cathode electrode material was ran in three-electrode system using 1 M Li_2SO_4 electrolyte and the corresponding results are represented in Fig 5.9. Fig 5.9a show CV profiles of MFP and Li^+/MFP at 30 mV s^{-1} with voltage window from 0-0.8 V for MFP and 0-1.4 V for Li^+/MFP (vs Ag/AgCl). As observed, there are evident redox peaks on the CV profile for both MFP and Li^+/MFP revealing typical pseudocapacitive nature of the materials. Li^+/MFP show redox peaks at a more positive voltage which is essential for more energy storage. GCD curves are shown in Fig 5.8b with redox behaviour which is consistent with CV curves. Li^+/MFP has a higher discharge time which indicates higher capacitance values.

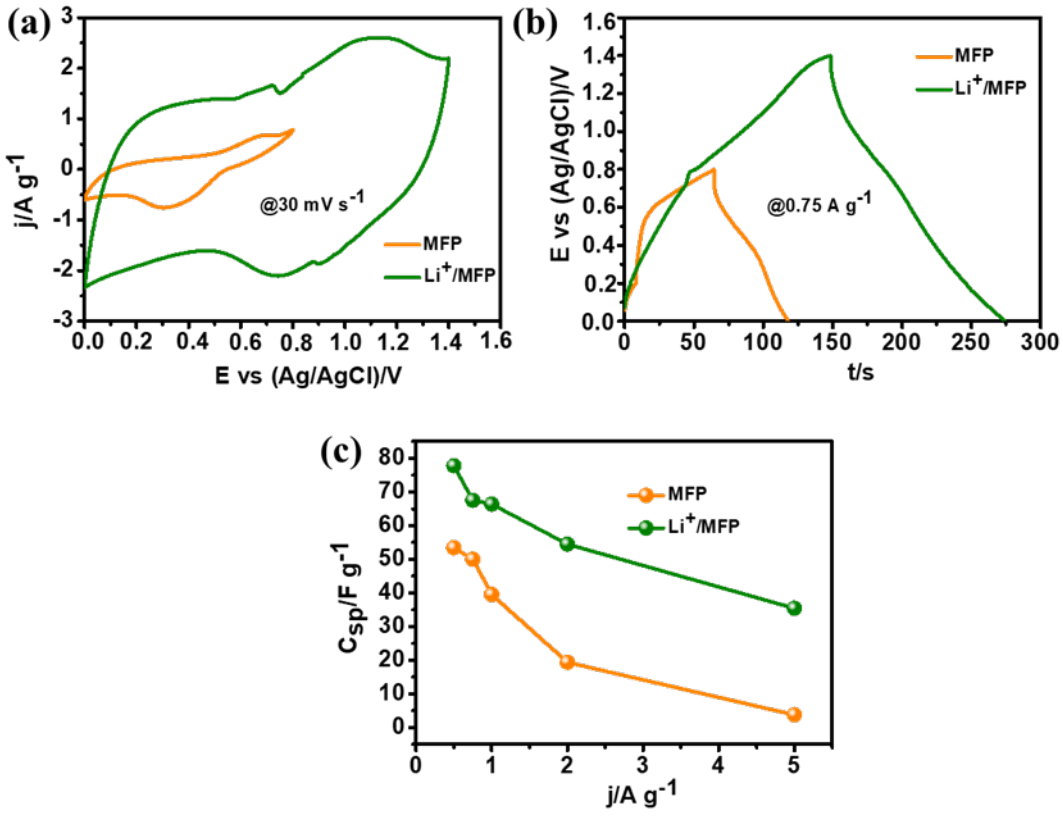

Fig. 5. 9. (a) CV, (b) GCD and (c) C_{sp} VS current density in 1 M Li_2SO_4.

By integrating the CV curves to produce so-called voltametric charges, the specific capacitance values of the MFP and Li^+/MFP were determined. Fig. 5.9c illustrates how the scan rate affects the capacitance of the materials. The capacitance of the electrode materials were calculated and the results are shown in Fig 5.9c. Li^+/MFP has higher capacitance values of 81.2 F g^{-1} (at 5 mV S^{-1}), 60.2 F g^{-1} (at 10 mV S^{-1}), 53.6 F g^{-1} (at 20 mV S^{-1}), 48.9 F g^{-1} (at 30 mV S^{-1}) and 42.8 F g^{-1} (50 mV S^{-1}) as compared to MFP with capacitance values of 27.1 F g^{-1} (at 5 mV S^{-1}), 18.2 F g^{-1} (at 10 mV S^{-1}), 11.5 F g^{-1} (at 20 mV S^{-1}), 8.3 F g^{-1} (at 30 mV S^{-1}) and 7.0 F g^{-1} (at 50 mV S^{-1}). The high capacitance values of Li^+/MFP might be due the defective quasi-rectangular shape (TEM images) of the produced material after treatment with LiOH. Again, the increase in d-spacing and surface chemistry of Li^+/MFP would result in improved current response. The Li^+/MFP is generated with smaller particles that makes it simple for solvated Li^+ to access the material surface, particularly the inner surface, leading to a high pseudocapacitance value. As a result, the inner surface of the MFP was not properly contacted by the Li ions, resulting in poor behaviour.

5.4.3. Three electrode system of MFP and Li^+/MFP in 1 M LiFSTI

The electrochemical study of MFP and Li^+/MFP were further analysed in a three electrode system using 1 M LiTFSI. To examine the behaviour of the charge storage mechanism, CV of Li^+/MFP was ran at a scan rate of 30 mV s^{-1} (Fig. 5.10a) and maximum voltage window was at 0.0-1.2 V. Fig. 5.10b show the comparison CV of MFP and Li^+/MFP and the high current response of Li^+/MFP show that lithium intercalation improves the charge storage of pristine MFP. Both MFP and Li^+/MFP show redox behaviour from Mn^{2+}/Mn^{3+} [32]. GCD curves (Fig. 5.10c) show higher discharge time for Li^+/MFP which supports the CV curves. It is clearly shown in Fig. 5.10d that Li^+/MFP has higher capacitance values of 115.5, 98.1, 80.0, 67.1 and 50.6 F g^{-1} than MFP with capacitance values of 64.4, 43.7, 31.9, 19.4 and 10.7 F g^{-1} from 5-50 mV s^{-1}. The electrochemical performance of these distinct crystallographic phases of Li^+/MFP was found to be different and the higher d-spacing, than pristine MFP which might be due to the improved performance after lithium intercalation.

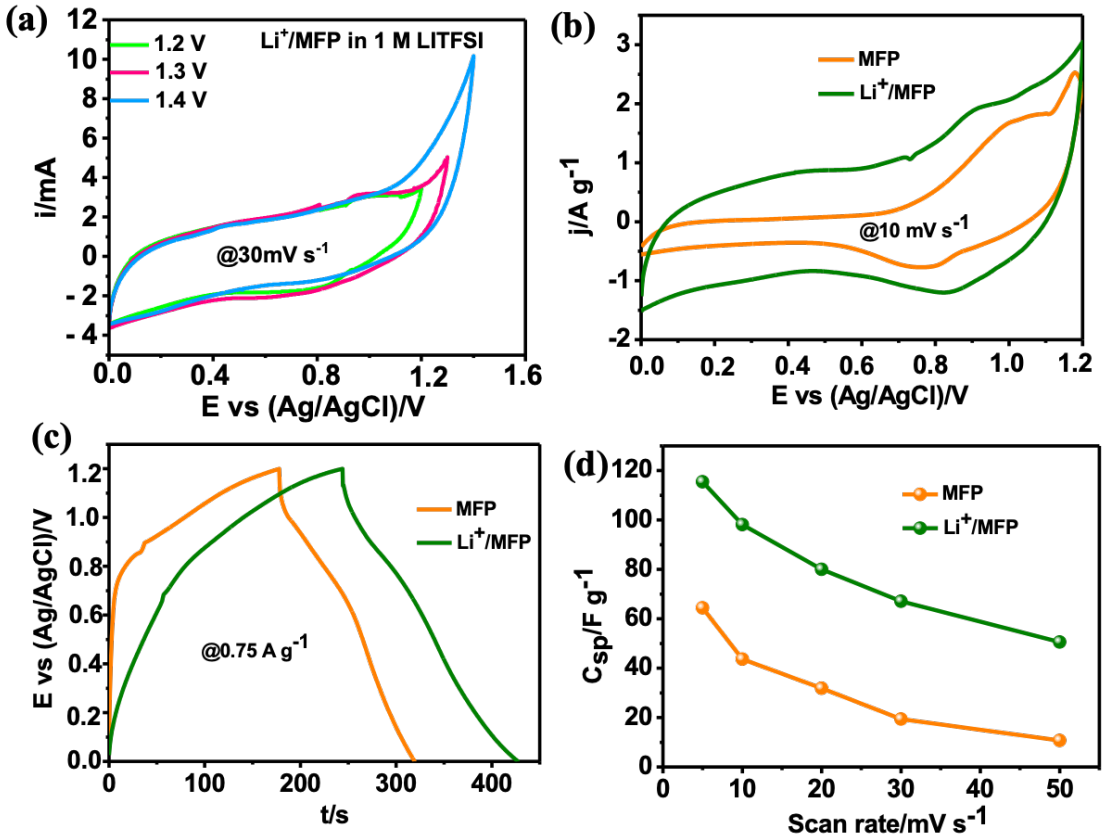

Fig. 5. 10. (a) CV of Li^+/MFP, (b) comparison CV, (c) GCD (c) and (d) Csp vs scan rate of MFP and Li^+/MFP.

5.4.4 Comparison of Li^+/MFP in 6 M LiOH, 1 M Li_2SO_4 and 1 M LiTFSI

Three electrode system of Li^+/MFP was compared in alkaline, neutral and ionic electrolytes. CV and GCD (Fig. 5.11 a, b) show that Li^+/MFP is operated in different voltages due to the type of electrolyte used. For example, alkaline (6 M LiOH) was operated at a voltage window of 0.0-0.9 V due to the water decomposition at 1.23 V [33]. However, neutral (1 M Li_2SO_4) and ionic (1 M LiTFSI) electrolytes can be operated at wider voltage window due to fewer hydrogen and oxygen evolution [34]. According to Table 5.2, OH^- has smaller hydrated size and higher conductivity than SO_4^{2-} hence the higher capacitance of LiOH than in Li_2SO_4 in Fig. 5.11c.

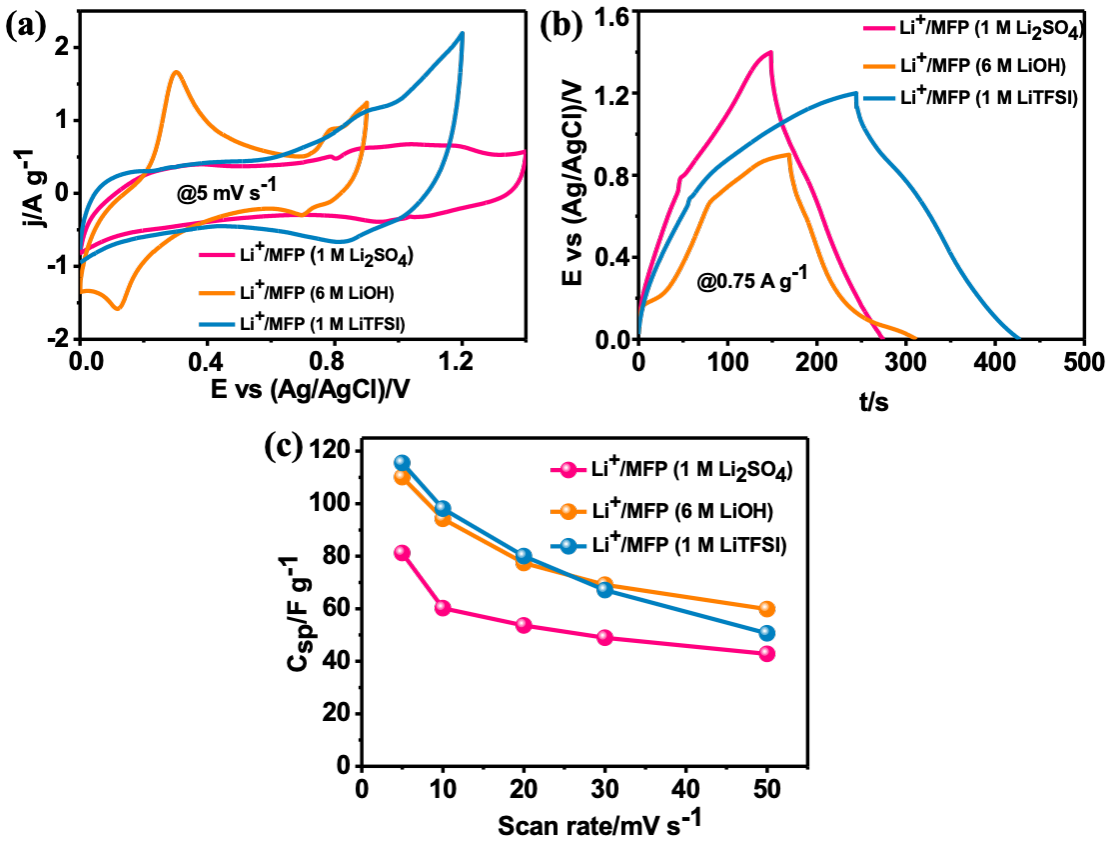

Fig. 5. 11. (a) Comparison CV, (b) GCD and (c) C_{sp} vs scan rate (c) of Li^+/MFP in 6 M LiOH, 1 M Li_2SO_4 and 1 M LiTFSI.

The capacitance values of LiOH and LiTFSI are comparable at scan rate of 5-30 mV s^{-1}. The material in LiTFSI show that it is not stable with about 50% decrease of capacitance than LiOH and Li_2SO_4. However, due to the high capacitance and wide potential window of LiTFSI, asymmetric assembly was operated in this electrolyte to obtain high energy density.

Table 5. 2. The ion size and ionic conductivity values [35, 36].

Ion	Size (Å)	Hydrated ion size (Å)	Ionic Conductivity (S cm^2 mol^{-1})
Li^+	0.60	3.82	38.69
OH^-	1.76	3.00	198
SO_4^{2-}	2.90	3.79	160
$TFSI^-$	2.36	-	-

5.4.5. Two electrode system of Li^+/MFP//N-ACs in 1 M LiTFSI

The asymmetric electrode system was evaluated in 1 M LiTFSI using Li^+/MFP as a positive electrode and N-ACs as a negative electrode. The results are shown in Fig 5.12. As shown in Fig 5.12a, N-ACs has stable voltage window from -0.8-0.0 V (vs Ag/AgCl) and Li^+/MFP has a stable voltage window from 0.0-1.2 V (vs Ag/AgCl) at 10 mV s^{-1}. Therefore, it is expected that the voltage window can be extended up to 2.0-2.3 V when the materials are assembled in asymmetric supercapacitors. CV (Fig 5.12b) and GCD (Fig 5.12c) curves of Li^+/MFP//N-ACs asymmetric SCs were evaluated at different voltage range (2.2-2.4 V) to check the stability window and the assembled asymmetric SCs was stable up to 2.3 V which show that Li^+/MFP//N-ACs can be cycled reversibly in the voltage range of 0.0-2.3 V. Moreover, the CV curves (Fig 5.12d) at different scan rates (5-50 mV s^{-1}) show both quasi rectangular shape indicating ideal capacitor from N-ACs and redox behaviour from Li^+/MFP. Additionally, the GCD curves (Fig 5.12e) at different current densities (0.5-5.0 A g^{-1}) show symmetric shape which is of an ideal capacitor and redox characteristics which is consistent with CV curves. The redox behaviour of Li^+/MFP is due to Mn^{2+}/Mn^{3+}. The calculated capacitance values from GCD curves was 102.6 F g^{-1} at 0.5 F g^{-1} (Fig. 5.12f). The capacitance decreases as the current density decreases due to limited diffusion of electrolyte ions at high current. These results show that lithium intercalation provides more active sites to MFP [37].

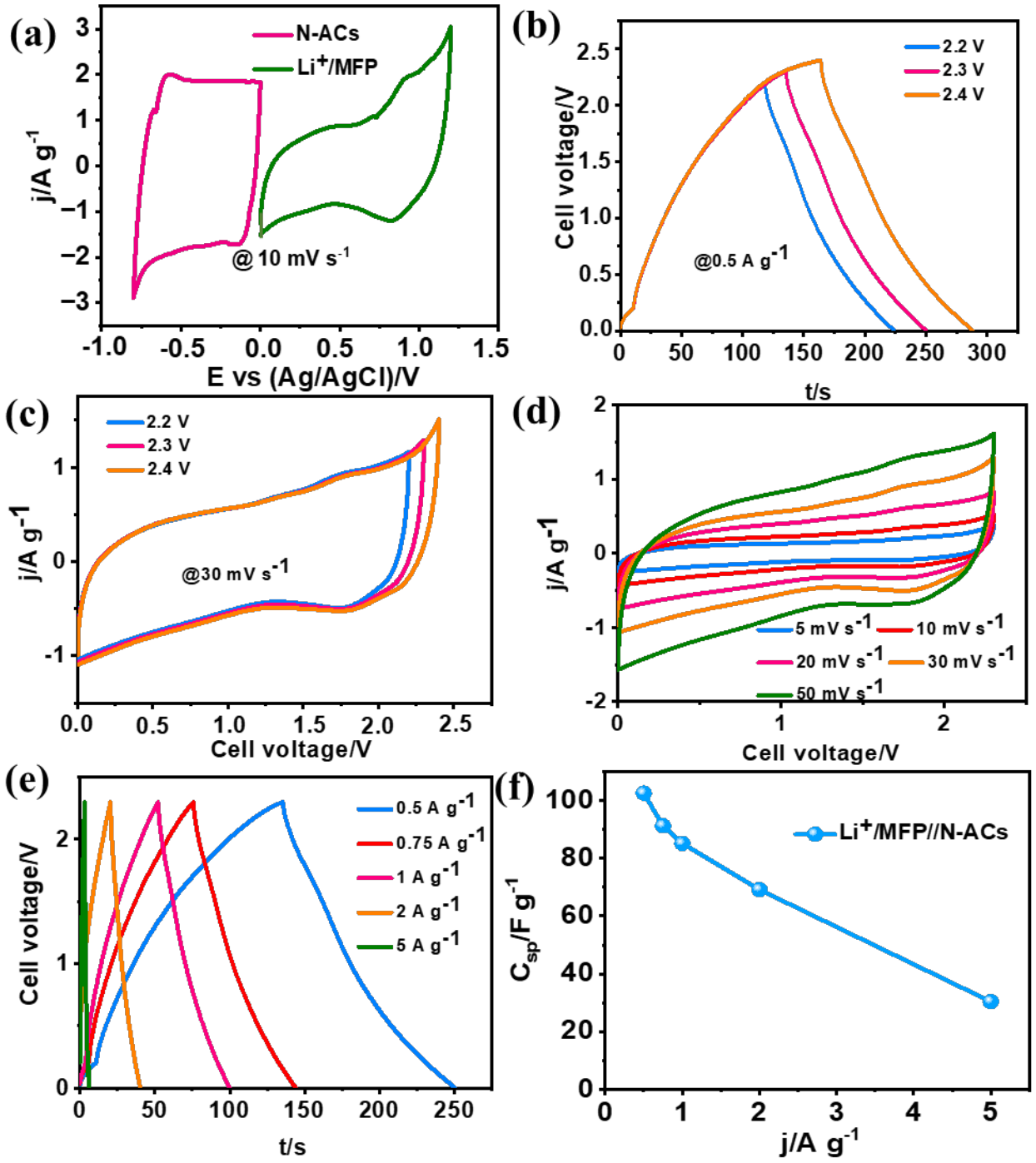

Fig. 5. 12. (a) CV, (b) CV tests, (c) GCD tests at different voltage window, (d) CV curves at different scan rates, (e) GCD and (f) C_{sp} VS current density of Li^+/MFP//N-ACs in 1 M LiTFSI.

Fig. 5.13a depicts the cyclic stability of the material tested at 5 A g^{-1} in a voltage window of 0.0-2.3 V. After 15000 cycles, Li^+/MFP//N-ACs maintains capacitance retention of 69.5%, indicating that the device exhibits good electrochemical cycling stability. The Coulombic efficiency was maintained at 98.7% showing long-term electrochemical cycling. An essential

parameter for examining the electrochemical characteristics of various materials is electrochemical impedance spectroscopy (EIS). With an electrical equivalent circuit (EEC, Fig. 5.13b, inset), the interfacial electrochemistry and cycle stability are best understood via EIS. Fig. 5.13b examines the Nyquist graphs produced prior to and after the 15 000 cycles. The simple Randles electrical equivalent circuit (EEC) was used to model the EIS parameters before and after 15 000 cycles. The parameters include (i) the bulk resistance (R_b) resulting from the sum of resistances from the current collectors, electrodes, electrolyte, and separator; (ii) the charge-transfer resistance (R_{ct}) resulting from electron transport; and (iii) the CPE resulting from the TEM's irregular structures [38, 39].

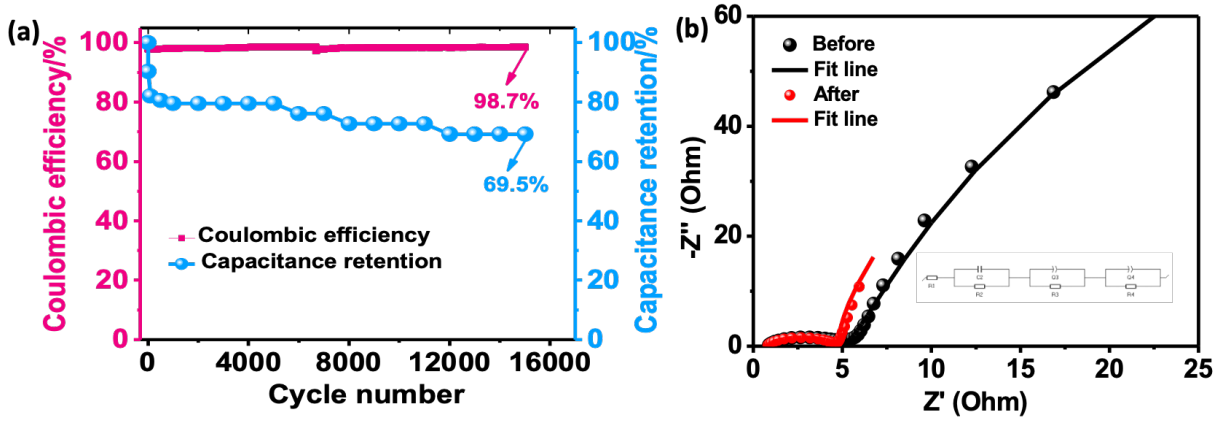

Fig. 5. 13. (a) Cyclic stability and (b) Nyquist plots of Li^+/MFP//N-ACs obtained before and after 15 000 cycles with (b) electrical equivalent circuit used in the fitting of Nyquist plots.

The R_s value increased after cycling (from 0.78 to 0.81 Ω), while R_{CT} decreases from 4.55 to 2.81 Ω as shown from Table 5.3.. The "a'' value of the CPE increased after cycling material does not maintains its of redox mechanism where a=1 is of a pure EDLC process, a=0.5 is of a pure faradaic process [40].

The CPE_{CT} and CPE_{cs} decreases after cycling which implies the efficiency of the material decreases after long cycling.

Table 5. 3. EIS parameters of Li^+/MFP//N-ACs.

Parameters	Before	After
R_s (Ω)	0.78 ± 0.34	0.81 ± 0.66
R_{ct} (Ω)	4.55 ± 1.97	2.81± 1.01
R_{sei} (Ω)	157.1± 7.56	60.22± 1.16

R_{int} (Ω)	274.29 ± 23.56	784.2± 30.83
C_{dl} (mF)	5.75± 2.97	0.334± 0.44
CPE_{ct} (uF. s^(a-1))	85.55± 7.1	79.3 ± 9.56
A	0.80	0.86
CPE_{cs} (uF. s^(a-1))	530.1 ± 0.43	52.1± 1.12
A	0.78	0.92

It is crucial to note that in energy storage systems, the E and P significantly affect how effective the system can be. Using the Ragone plots depicted in Fig. 5.14, the material's efficiency in 1 M LITFSI was contrasted. Li^+/MFP//N-ACs show energy density of 18.8 W h kg^{-1} at a power density of 573.6 W kg^{-1} and a power density of 5249.4 W kg^{-1} at an energy density of 5.6 W h kg^{-1}. Additionally, the single device successfully lighted up a red LED (see inset Fig. 5.10) for more than 3 minutes after charging for 20 s when it was attached to a light emitting diode (LED, 1.6 V). These results show that lithium intercalation results in the reversible insertion/extraction properties of lithium being key findings in lithium-based electrolytes chemistry.

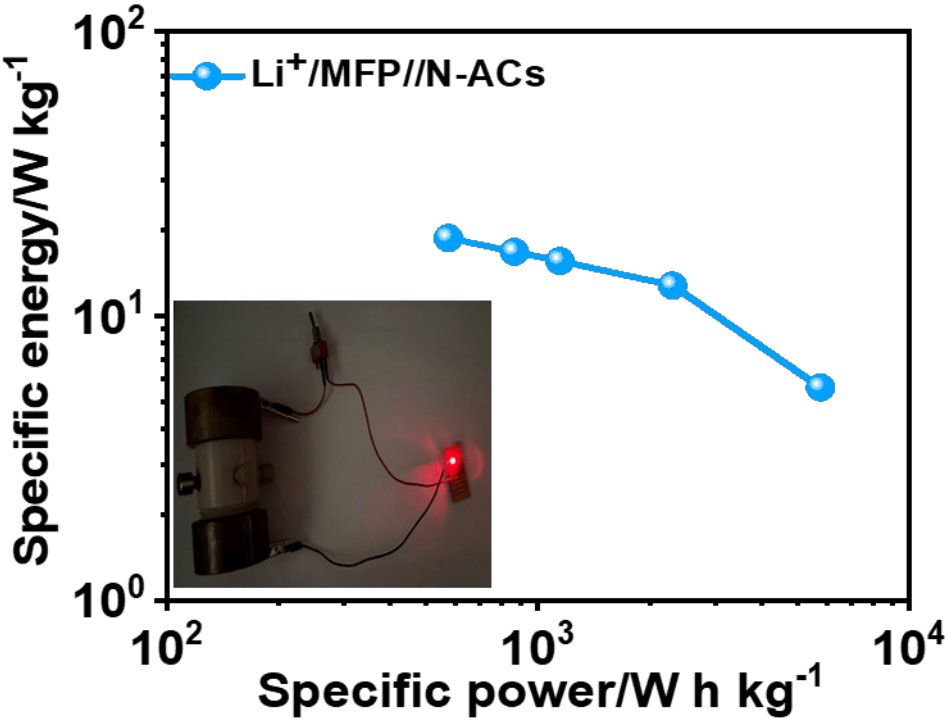

Fig 5. 14. Ragone plot of Li^+/MFP//N-ACs. The insets shows an image of a red LED powered by Li^+/MFP//N-ACs electrode based device in 1 M Li_2SO_4.

Our results show that lithium intercalation enhances the specific capacitance of MFP material. Table 5.4 lists the outcomes for Li^+/MFP and nitrogen-doped activated carbons from the use of biomass in asymmetric SCs along with their energy densities. The specific energy and power obtained in this experiment were comparable to those from earlier investigations [40, 41] and, in some cases, were even greater than those from previous alkali intercalation into manganese/metal based materials,. These results show that the energy density depends on a number of factors, such as the parent material's properties, the electrolyte, and the type of alkali metal employed for intercalation. For example, our material showed higher energy density of 18.8 Wh/kg in a voltage range of 0.0-2.3 V than $LiFePO_4$//mesoporous carbons with energy density of 17.9 Wh/kg [41]. However, the energy density in our study was less as compared to $LiTi_2(PO_4)_3$/AC (24.4 Wh/kg) operated at a voltage range of 0.0-1.6 V [42].

Table 5. 4. Summary of energy and power density of intercalated alkali ions into manganese base materials and other metal-base materials.

Type of material	Electrolyte	Cell voltage (V)	Current density (A/g)	Specific energy (Wh/kg)	Reference
Li^+/MFP//N-ACs	1 M Li_2SO_4	2.3	0.5	18.8	This study
$LiFePO_4$/mesoporous carbons	1 M LiTFSI	2.1	0.1	17.9	[41]
$LiTi_2(PO_4)_3$/AC	1 M Li_2SO_4	1.6	2mA/cm2	24.4	[42]
$NaxMnO_2$@CNT//AC-CNT	1 M Na_2SO_4	1.8	1.0	16.38	[43]

5.5. Conclusions

We have employed hydrothermal lithium insertion method using LiOH to investigate the effect of the alkali metal in the structure of MFP. Our results indicate that LiOH changes the structure of MFP into smaller particles and less formation aggregates particles as shown from TEM and SEM images. XRD also show that LiOH does alter the triplite material's crystal structure.

Electrochemical analysis show that introduction of Li ions into the structure improves the current response and results in a wider voltage range as compared to the parent MFP. Effect of different electrolytes show that Li^+/MFP performed better in 1 M LiTFSI with capacitance and

potential of having a wider voltage range than 6 M LiOH and 1 M Li_2SO_4. Asymmetric assembly of Li^+/MFP with N-ACs gave a powerful energy density of 18.8 W h kg^{-1} in 1 M LiTFSI while powering 1.6 LED bulb for over 3 minutes. These results demonstrate the feasibility of using lithium intercalation into structures for possible energy storage.

References

1. M.N. Sakib, S. Ahmed, S. M. Rahat, S.B. Shuchi. A review of recent advances in manganese-based supercapacitors. Journal of Energy storage 44 (2021) 103322.
2. S. Z. Huang , Z. H. Wang , Y. V. Lim , Y. Wang , Y. Li , D. H. Zhang and H. Y. Yang . Recent Advances in Heterostructure Engineering for Lithium–Sulfur Batteries. Adv. Energy Mater., 11 (2021) 2003689.
3. W. J. Hyun , C. M. Thomas , N. S. Luu and M. C. Hersam. Layered Heterostructure Ionogel Electrolytes for High-Performance Solid-State Lithium-Ion Batteries. Adv. Mater. 33 (2021) 2007864.
4. H. Z. Lv , Y. Song , Z. M. Qin , M. Y. Zhang , D. Yang , Q. Pan , Z. H. Wang , X. J. Mu , J. M. Meng , X. Q. Sun and X. X. Liu. Disproportionation enabling reversible MnO_2/Mn^{2+} transformation in a mild aqueous Zn-MnO_2 hybrid battery. Chem. Eng. J., 430 (2022) 133064.
5. H. Y. Shi , Y. Song , Z. M. Qin , C. C. Li , D. Guo , X. X. Liu and X. Q. Sun , Angew. Inhibiting $VOPO_4 \cdot x\, H_2O$ Decomposition and Dissolution in Rechargeable Aqueous Zinc Batteries to Promote Voltage and Capacity Stabilities. Chem., Int. Ed., 58 (2019) 16057 -16061.
6. J. Ge , L. Fan , A. M. Rao , J. Zhou and B. Lu. Surface-substituted Prussian blue analogue cathode for sustainable potassium-ion batteries. Nat. Sustainability 5 (2022) 225 -234.
7. Z. Guan, Y. Wang, M. Zhang, J. Liu, S. Li, D. Guo and X. Liu. Engineering a manganese-based oxide heterostructure cathode for high-performance aqueous potassium-ion storage. Mater. Adv., 4 (2023) 2174.
8. J. Yan, Q. Wang, T. Wei et al. Recent advances in design and fabrication of electrochemical supercapacitors with high energy densities. Adv Energy Mater. 4 (2014) 1300816
9. S. Yazar, M.B. Arvas, Y. Sahin. An ultrahigh-energy density and wide potential window aqueous electrolyte supercapacitor built by polypyrrole/aniline 2-sulfonic acid modified carbon felt electrode. Energy research 6 (2022) 8042-8060.
10. Y. Song et al. Facile hydrothermal synthesis of cobaltosic sulfide nanorods for high performance supercapacitors. RSC Adv. 12 (2022) 11665–11670.

11. A. Ali, R. Shakoor, A. Raheem, H. Abd dul Muqeet, Q. Awais, A.A. Khan, M. Jamil. Latest Energy Storage Trends in Multi-Energy Standalone Electric Vehicle Charging Stations: A Comprehensive Study. Energies 13 (2022) 4727.
12. L. Xiao, L. Zhao, Y. Jiayuan, L. Xiaoyan, Z. Xiaoli, L. Hong, Z. Weijia. Water Splitting: From Electrode to Green Energy System. Nano micro Letters 131 (2020).
13. Z. Cheng, Y. Deng, H. Wenbin, Q. Jinli, Z. Lei Z, J. Zhang. A review of electrolyte materials and compositions for electrochemical supercapacitors. Chem. Soc. Rev. 21 (2015) 7482-7539.
14. Q. Gao, Optimizing carbon/carbon supercapacitors in aqueous alkali sulfates electrolytes. Energy Chemistry 9 (2019) 219-224.
15. P. Ratajczak, K. Jurewicz, P. Skowron, Q. Abbas, F. Béguin. Effect of accelerated ageing on the performance of high voltage carbon/carbon electrochemical capacitors in salt aqueous electrolyte. Electrochim. Acta 130 (2014) 344-350.
16. D. Weingarth, A. Foelske-Schmitz, R. Kötz. Cycle versus voltage hold – Which is the better stability test for electrochemical double layer capacitors. Power Sources 225 (2013) 84-88.
17. D. Wang, S. Zhang, C. Li, X. Chen et al. Engineering the interplanar spacing of K-birnessite for ultra-long cycle Zn-ion battery through “hydrothermal potassium insertion” strategy. Chem. Eng. (2022) 134754.
18. W. Yang, Z. Gao, J. Wang, J. Ma, M. Zhang, L. Liu. Solvothermal one-step synthesis of Ni-Al layered double hydroxide/carbon nanotube/reduced graphene oxide sheet ternary nanocomposite with ultrahigh capacitance for supercapacitors. ACS Appl. Mater. Interface., 5 (2013) 5443-5454
19. K. Makgopa, P.M. Ejikeme, C.J. Jafta, K. Raju, M. Zeiger, V. Presser, K.I. Ozoemena . A high-rate aqueous symmetric pseudocapacitor based on highly graphitized onion-like carbon/birnessite-type manganese oxide nanohybrids. J. Mater. Chem. A Mater., 3 (2015) 3480-3490
20. S. Li, H. Huang, J. Li, N. Kobayashi et al. The effect of 3D carbon nanoadditives on lithium hydroxide monohydrate based composite materials for highly efficient low temperature thermochemical heat storage. RSC Advances 8 (2018) 8199-8208.
21. N. Nzimande, A. Haruna, P. Mwonga, B. Rasche, F. Cummings and K. I. Ozoemena. Supporting Information Ceria-Spiderweb Nanosheets Unlock the Energy-Storage

Properties in the “Sleeping” Triplite (Mn2(PO4)F). ACS Appl. Energy Mater. 11 (2021).

22. I.V. Zatovsky, N.Y. Strutyriska, I. Ogorodriyk, V.N. Baumer. Peculiarity of formation of the NASICON-related phosphates in the space group R32: synthesis and crystal structures of $Na_4MIIAl(PO_4)_3$ (MII–Mg, Mn). Structural Chemistry 1 (2016).
23. L. Balan, C.M. Ghimbeu, L. Vidal, C. Vix-Guterl. Photoassisted synthesis of manganese oxide nanostructures using visible light at room temperature. Green `chemistry 8 (2013).
24. X. Hu, L. Liu, S. Zhai. The structure-Raman spectra relationships of $Mg_3(PO_4)_2$ polymorphs: A comprehensive experimental and DFT study. Spectrochimica Acta Part A: Molecular and Biomolecular Spectroscopy 245 (2021) 118906.
25. X. Hu, l. Liu, S. Zhai. Ferromagnetic and Transport Properties of Mn-Doped ZnO. Korean Physical Society 1 (2008) 106-111.
26. J. Pereira, J.N. Lacerdia, I.F. Coelho, C. Nogueira. Tuning morphology of manganese oxide nanostructures for obtaining both high gravimetric and volumetric capacitance. Materials Advances 7 (2020).
27. G. Xie, Q. Li, Y. Li, L.Z. Qin, X. Liu, H. Lin, M. Nie. The evolution of α-MnO2 from hollow cubes to hollow spheres and their electrochemical performance for supercapacitors. Materials Science 52 (2017) 1-12.
28. P.S. humal, M.A. Bhakare, K.D. Lokhande,et al. Bio-waste derived, phosphorus decorated composite for highly efficient flame retardant for cotton fabric. Cellulose 29 (2022) 8879–8888.
29. S. Sarkar, S. Garain, D. Mandal, K.K. Chattopadhyay. Electro-active Phase Formation in PVDF-BiVO4 Flexible Nanocomposite Films for High Energy Density Storage Application. RSC Advances 4 (2019).
30. H. Zhao, L. Dondgong, Y. Wang, F. Li et al. Sol-Gel Synthesis of Silicon-Doped Lithium Manganese Oxide with Enhanced Reversible Capacity and Cycling Stability. Materials 8 (2018) 1445.
31. Gazi Jahirul Islam, H.M. Naseem Akhtar, M.A. Mamun, M.Q. Ehsan. Investigations on the redox behaviour of manganese in manganese(II)–saccharin and manganese(II)–saccharin– 1,10-phenanthroline complexes. Journal of Saudi Chemical Society13 (2009) 177–183.

32. D. Feng, T. Gao, L. Zhang, B. Guo, S. Song, Z. Qiao, S. Dai. Boosting High-Rate Zinc-Storage Performance by the Rational Design of Mn_2O_3. Nano-Micro Lett. 12 (2020).
33. Z. Sheng, X. Lin, H. Wei, Y. Zhang, Z. Tian, C. Wang, D. Xu, Y. Wang. Green synthesis of nitrogen-doped hierarchical porous carbon nanosheets derived from polyvinyl chloride towards high-performance supercapacitor. Power Source 515 (2021).
34. L. Demarconnay, E. Raymundo-Piñero, F. Béguin. A symmetric carbon/carbon supercapacitor operating at 1.6 v by using a neutral aqueous solution. Electrochem Commun. 12 (2010) 1275-1278.
35. C. Zhong, Y. Deng, W. Hu, J. Qiao, L. Zhang, J. Zhang. A review of electrolyte materials and compositions for electrochemical supercapacitors. Chem. Soc. Rev. 44 (2015) 7484-7539.
36. C. Zhong, J. Qiao, D. Yida, L. Zhang. A review of electrolyte materials and compositions for electrochemical supercapacitors. Chem. Soc. Rev. (2015).
37. F. Zhan, H. Wang, Q. He, W. Xu, J. Chen, X. Ren. Metal–organic frameworks and their derivatives for metal-ion (Li, Na, K and Zn) hybrid capacitors. Chem. Sci. 13 (2022) 11981.
38. H.S. Magar, R.Y.A. Hassan, A. Mulchandani. Electrochemical impedance spectroscopy (Eis): principles, construction, and biosensing applications. Sensors 21 (2021)
39. G.P. Scisco, M.E. Orazem, K.J. Ziegler, K.S. Jones. On the rate capability of supercapacitors characterized by a constant-phase element. J. Power Source 516 (2021).
40. T. P. Mofokeng, A.K. Ipadeola, Z. N. Tetana, K. I. Ozoemena. Defect-Engineered Nanostructured Ni/MOF-Derived Carbons for an Efficient Aqueous Battery-Type Energy Storage Device. ACS Omega 32 (2020) 20461-20472 .
41. P.F.R . Ortega, G.A. dos Santos Juniou, L.A. Montoro et al. $LiFePO_4$/Mesoporous Carbon Hybrid Supercapacitor Based on LiTFSI/Imidazolium Ionic Liquid Electrolyte. Phys. Chem. C 2018, 122, 3, 1456–1465.
42. J. Luo, Y. Xia. Electrochemical profile of an asymmetric supercapacitor using carbon-coated $LiTi_2(PO_4)_3$ and active carbon electrodes. Journal of Power Sources 1 (2009) 224-227.

43. J. Wang, C. Ma, C. Hu. Constructing a high-performance quasi-solid-state asymmetric supercapacitor: NaxMnO$_2$@CNT/WPU-PAAK-Na$_2$SO$_4$/AC-CNT. Electrochimica Acta 334 (2019) 135576.

CHAPTER 6: Ceria nanorods decorated on sleeping 'triplite' material for asymmetric supercapacitors in alkaline and neutral electrolytes

6.1. Introduction

To address the issues of poor energy density, new electrochemical supercapacitors (SCs) electrode materials have recently been developed such as activated carbons (ACs), metal oxides and polymers [1–3]. This has been accomplished by either completely replacing the carbon materials with electrochemically active redox materials or hybridizing the electrode materials by adding electrochemically active redox materials to an energy storage (ES) electrode layer based on carbon particles or forming composites of redox materials [2,4,5]. The enhancement of SCs can be done by using materials with high porosity, high surface area and redox properties [6].

The high cost, limited supply, and severe toxicity of ruthenium and iridium oxides have a significant impact on their uses despite their intrinsic properties [7]. Because of these shortcomings, researchers have focused a lot of emphasis on the investigation of electrode materials including CeO_2, MnO_2, NiO, Co_3O_4, and Fe_2O_3 [8–10]. Due to its low toxicity, availability, and exceptional redox characteristics, CeO_2 has instead shown to be a practical, beneficial, and promising electrode material for SCs [9].

Several authors reported on CeO_2 composites, such as graphene-CeO_2 [11], CeO_2/CNTs [12], with reported higher capacitances than undoped with CeO_2.Coating electrode material with CeO_2 is a promising strategy in this study to improve the electrochemical performance of manganese fluorophosphate (MFP). With a ground state valence of 4f15d16s2, CeO_2 stands out as a cheap and plentiful rare earth element. As a result, it not only generating stable Ce^{3+} by losing one 5d and two 6s electrons but also stable Ce^{4+} by losing an additional 4f electron. The ease with which the oxidation state of CeO_2 may be changed from Ce^{3+} to Ce^{4+} makes it an excellent redox material for use in SCs. The potential for energy-related applications may be demonstrated by the efficient properties, such as structural defects that rely on the partial pressure of oxygen and high oxygen vacancy mobility. As a result, the assembly in combination with MFP and nanostructured CeO_2 opens new avenues for the creation of electrode materials for high-performance SCs, including the following possibilities: (i) demonstrates improved electrical conductivity; (ii) improves contact between the electrode and electrolyte [13,14]. In

addition, CeO_2 nanostructures with high porosity and surface area may be produced, and it is simple to modify their form of structure [13]. Jeyaranjan *et al.* [15] studied different morphology of CeO_2 and found that nanorods had the highest capacitance. Hence, in the study, CeO_2 nanorods were formed for coating on MFP to better the redox properties of the material and its stability. The combination of MFP and CeO_2 takes advantage of open framework of MFP that allow for accumulation of charge and redox property of CeO_2.

One of the most important factors in how well supercapacitors operate is electrolytes [16]. Aqueous electrolytes enable a better power density for electrode materials than other based electrolytes at the price of offering energy density that is lower. When aqueous electrolytes are contrasted with other different electrolytes, the electrochemical capacitors tested can provide additional advantages including cheap cost, safety, and environmental friendliness. In turn, aqueous electrolytes can be classified as acidic, basic, or neutral. While the working potential window in neutral electrolytes is increased above 1.23 V and reaches a value of 2.2 V, it is constrained to 1.2 V in acidic and basic electrolytes [17]. The specific capacitances are high for acidic, followed by alkaline and neutral.

In this study, CeO_2 was used to coat MFP to form a composite. The composite was used in three electrode and this work report the effect of alkaline (6 M LiOH and 6 M KOH) and neutral electrolytes (1 M Li_2SO_4 and 1 M K_2SO_4). Due to the higher conductivity of 1 M K_2SO_4 and higher capacitance than 1 M Li_2SO_4, and wider voltage range than alkaline electrolytes, asymmetric device was assembled in 1 M K_2SO_4.

6.2. Methodology

6.2.1. Materials

MFP-CeO_2 was synthesized using ceria nitrate ($Ce(NO_3)_3.6H_2O$, Sigma Aldrich), ammonium dihydrogen phosphate ($NH_4H_2PO_4$, Sigma Aldrich), manganese(II) nitrate tetrahydrate ($Mn(NO_3)_2.4H_2O$, Sigma Aldrich). Microfiber filter paper (ACE chemicals) were used as an electrode separator with 0.18 mm thickness. All other reagents were used without further purification.

6.2.2. Electrochemical characterization

Working electrode was prepared by making slurry of MFP, MFP-CeO_2 (80 %), carbon black (10 %) and polyvinylidene (PVDF, 10%) in a few drops of methylpyrrolidone (NMP) [18]. The slurry was sonicated for 30 minutes, pasted on carbon paper and dried in a vacuum oven at 60

℃ for 12 h. The coated carbon papers were used as working electrodes in a two- and three-electrode systems. A three-electrode system (half-cell) in 6 M KOH, 6 M LiOH, 1 M K_2SO_4 and 1 M Li_2SO_4 was constructed using nickel foam as a counter electrode and Ag/AgCl as a reference electrode in a T-type Swagelok cell. The two-electrode (full-cell) system was assembled using a T-type Swagelok cell with a microfiber filter paper between the electrodes that was soaked in 1 M K_2SO_4 electrolyte. The total mass per unit area of active material was around ~1.5-1.8 mg. All the electrochemical analyses were tested by using cyclic voltammetry (CV), galvanostatic charge-discharge (GCD), and impedance spectroscopy (EIS) procedures using a VSP potentiostat. The specific capacitance (C_{sp}), energy density (E_s), power density (P_s) were calculated from equation shown in Section 4.2.2.

6.2.3. Synthesis of MFP-CeO_2

MFP-CeO_2 was synthesized by a method shown in Fig. 6.1 [19]. In a standard reaction, $Ce(NO_3)_3.6H_2O$ was added to MFP (See Section 4.2.4 for the synthesis of MFP) and stirred in 30 mL distilled water for 24 h at room temperature. The mixture was subjected to hydrothermal treatment for 12 h at 180 ℃. The resulting composite was washed with distilled water and dried for 12 h at 60 ℃.

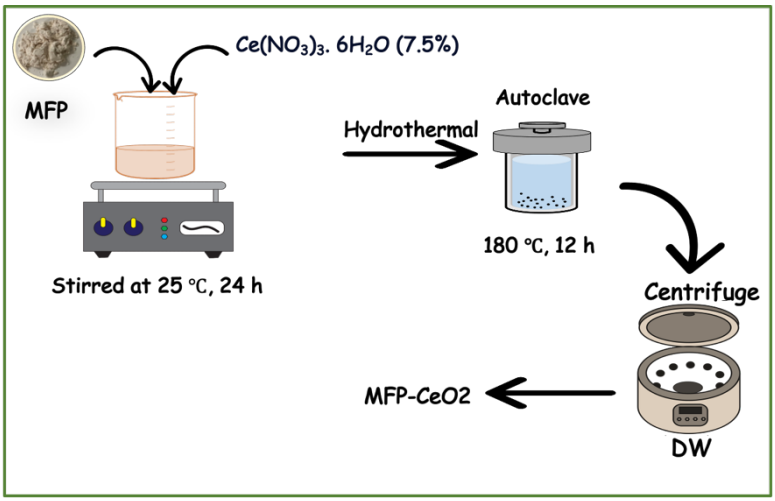

Fig. 6. 1. Graphical representation for the synthesis of MFP-CeO_2.

6.3. Results and discussion

XRD of MFP and MFP-CeO_2 is shown in Fig. 6.2. The XRD patterns show that after addition of CeO_2, the lattice parameters changed slightly, indicating that coating MFP with CeO_2 did

not significantly affect the structure or lattice positions of the atom but maintains the integrity of the pristine MFP. Whereas the XRD pattern for CeO_2 were not easily detectable due to the high intensity of MFP diffraction planes. The intense peak at 29.4° for MFP decreased in intensity due to the coating of CeO_2.

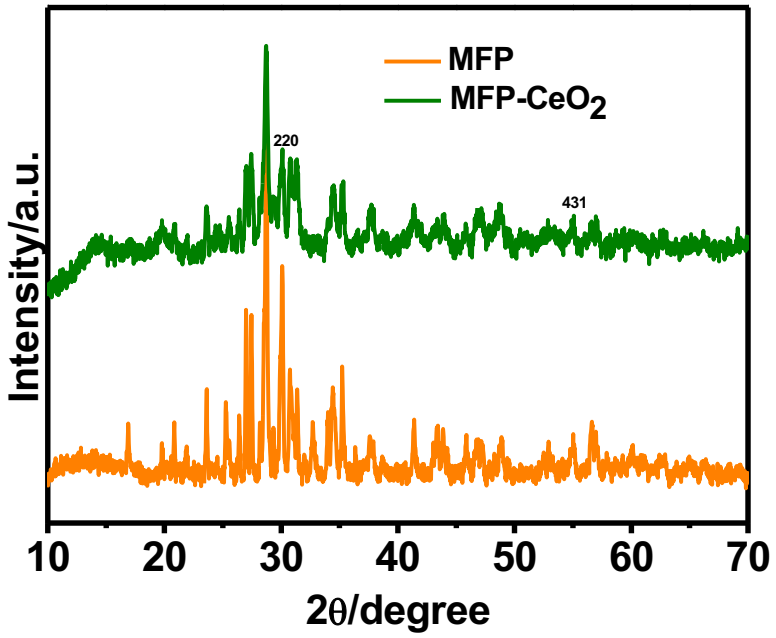

Fig. 6. 2. XRD of MFP and MFP-CeO_2.

Raman spectra of MFP and MFP-CeO_2 are shown in Fig. 6.3. The Raman bands did not show major change after coating with CeO_2 which significantly support XRD that coating with CeO_2 did not change the structure of pristine MFP. The PO_4^{2-} anion's P-O stretching modes are found in the 954–1046 cm^{-1} range. Asymmetric stretching vibrations are seen at v3-4 (1012.4–1046.5 cm^{-1}) and symmetric stretching vibrations at v1–2 (959.99–978.8 cm^{-1}).

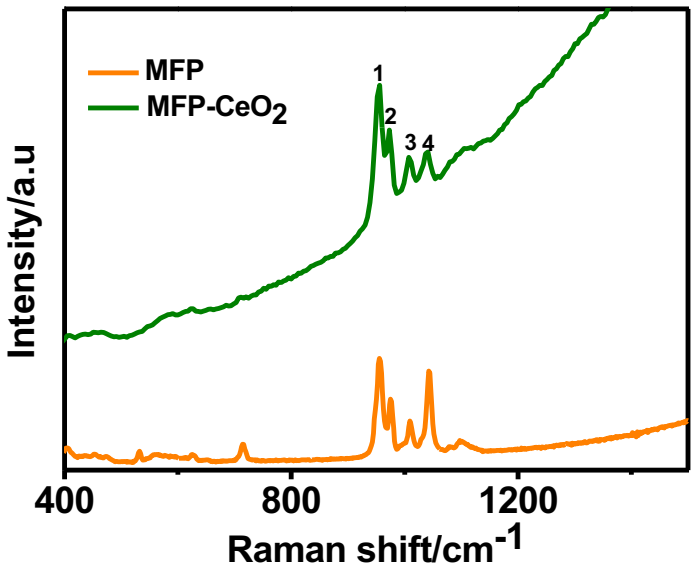

Fig. 6. 3. Raman spectra of MFP and MFP-CeO_2.

The detailed morphology of MFP and MFP-CeO_2 are shown in Fig. 6.4. It can be seen that nanorods of CeO_2 are formed on top or near the surface of MFP (Fig. 6.4b). Fig. 6.4b,c show that the CeO_2 nanorods (small nanorods) are attached to MFP (big dark particles) with a red square in Fig. 6.4c (clearly shown in Fig. 6.4e). The nanorods particles are clearly seen in Fig. 6.4c-f attached to MFP.

The type of ceria containing salt and supersaturation level may be responsible for the varied growth rate. The supersaturation level of the synthesis system regulates the nucleation and crystal growth rates, according to the traditional crystallization process [20–22]. Low supersaturation results in bigger crystals because crystals grow more quickly than they form. In contrast, nucleation predominates during crystal development at greater supersaturations, which eventually results in the creation of more tiny particles. Faster nucleation and hence shorter CeO_2 nanorods will occur at greater Ce nitrate concentrations and other parameters such as temperature and reaction time, which correlate to higher supersaturation values.

Temperature also has an impact on the type of morphology CeO_2 nanoparticles forms. The observed variation in length and aspect ratio on CeO_2 crystallization was caused by temperature [20]. A greater number of tiny nuclei were created because a higher temperature sped up nucleation. At higher temperatures, shorter CeO_2 nanorods were produced for a given quantity of the synthesis precursor.

These findings contrast significantly from those in the literature, where CeO_2 nanorods are frequently only capable of being produced at low temperatures (≤100 °C) [20,23,24]. The temperature impact can be highly confusing since in some circumstances, depending on the hydrothermal treatment period and synthesis mixture composition, multiple morphologies may be formed at the same temperature or vice versa. The diverse synthesis compositions and circumstances employed in each system are the reason why the current study differs from those reported in the literature.

Again, pH also has an impact on the growth of CeO_2 nanoparticles. CeO_2 nanorods only develop in acidic circumstances, as demonstrated by experiments reported by Ji's group [22] with pH ranges of 2 to 12, and within the acidic pH range, the nanorods grew longer at a lower pH.

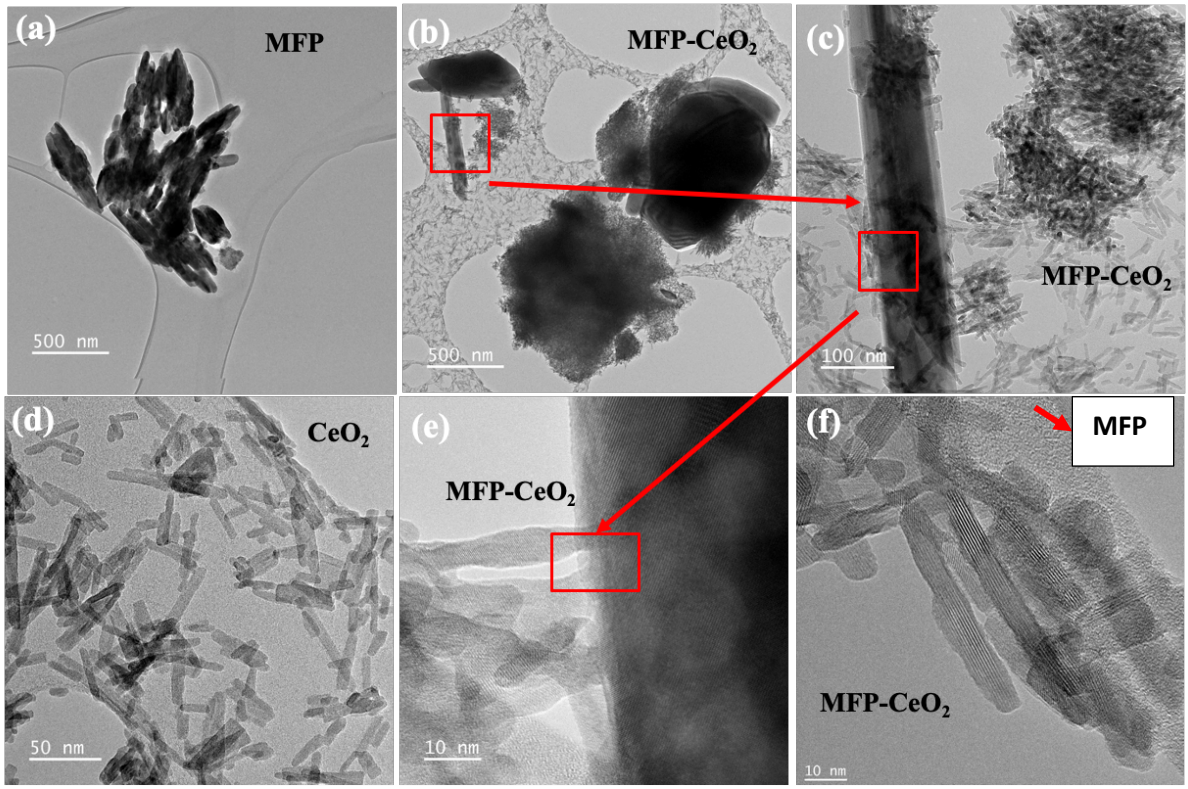

Fig. 6. 4. TEM images of (a) MFP, (b, c, e, f) MFP-CeO_2 and (d) CeO_2.

According to SEM images (Fig. 6.5a, b), CeO_2 nanorods were successfully formed coating the MFP. This is clearly seen from Fig. 6.5b with a clear surface of MFP surrounded by CeO_2 nanorods particles. The nanorods ceria particles has been reported with many attractive properties, such as tunable pore sizes, abundant defects and adjustable surface chemistry, which greatly expand their potential applications in energy storage in this study. Fig. 6.5c-h shows the

compositions and elemental observations of MFP-CeO_2 nanorods particles. The EDS mapping show homogenous distribution of elements Mn, P, O, F and Ce. In the case of hybridization of MFP with the ceria phase, the Mn from MFP surface aid chemical bonding for better attachment and contact with the oxygen vacancies from Ceria. Moreover, the nature of functional groups can influence the degree of structural connection between MFP and ceria.

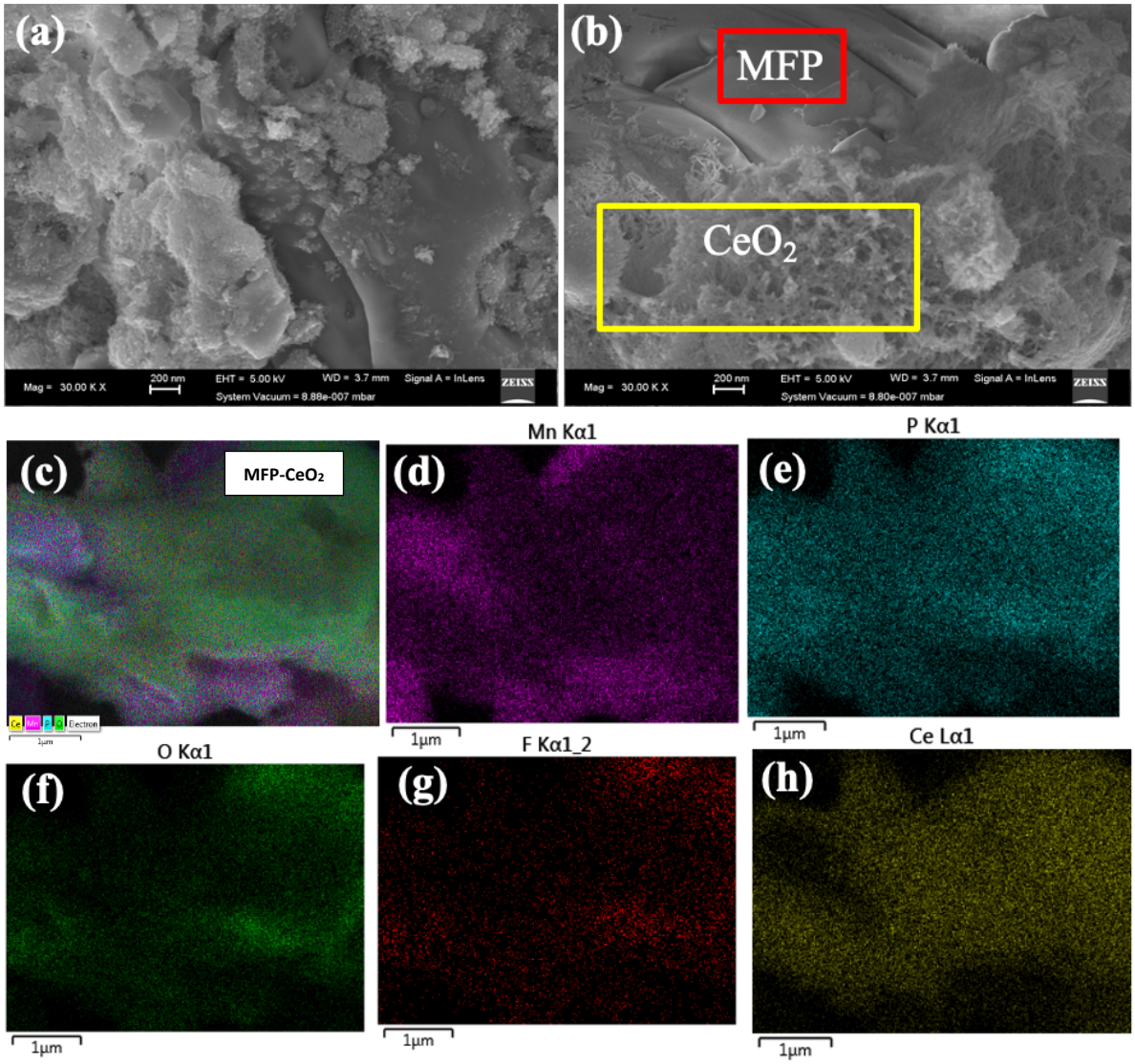

Fig. 6. 5. SEM images (a, b) and EDS mapping (c-h) of MFP-CeO_2.

The presence of several elements and their oxidation states could be identified using XPS analysis. The survey scan of MFP and MFP-CeO_2 is shown in Fig. 6.6. MFP-CeO_2 show that all elements previously present in MFP (Mn2p at 642 eV, O1s at 531.1 eV, P2p at 133.2 eV and F1s at 689.2 eV) [25,26] are still shown with addition of Ce3d at 884.9 eV [8]. The atom

% of Ce3d in the material was found to be at 5.9%. The increase in in oxygen vacancy after coating with CeO_2 may account for the enhancement of energy storage.

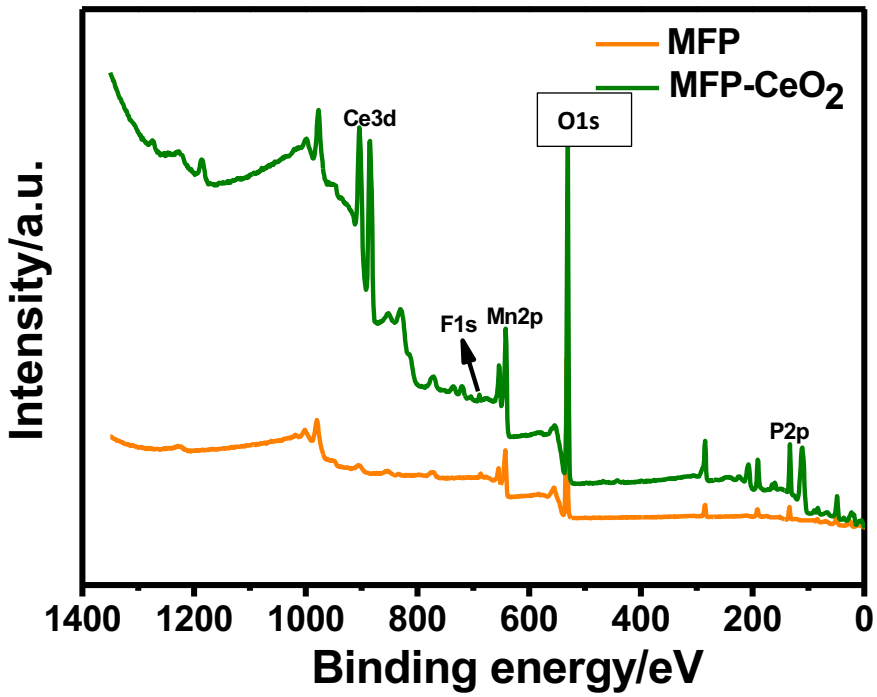

Fig 6. 6. Survey scan of MFP and MFP-CeO_2.

Table 6. 1. XPS atom % of MFP and MFP-CeO_2.

Type of material	XPS atom %				
	Ce3d	Mn2p	O1s	P2p	F1s
MFP	-	12.9	54.5	13.9	1.6
MFP-CeO_2	5.9	7.9	57.6	12.3	0.7

XPS was further used to evaluate the oxidation states of the elements present in MFP-CeO_2 as shown in Fig. 6.7. $Mn2p_{3/2}$ (Fig. 6.7a) is deconvoluted and has three peaks for Mn^{2+}, Mn^{3+} and a satellite peak. $Mn2p_{1/2}$ is divided into two peaks for Mn^{2+} at lower binding energy and at higher binding energy for Mn^{3+} [27]. O1s deconvolution is shown in Fig. 6.7b and the peaks had three overlapping peaks which were due to the presence of oxygen from CeO_2 as well as from Mn-O. The three peaks were observed at 528.5 531.3 and 533.1 eV. The most intense peak appeared at 531.3 eV due to the metal oxides [8,28].

P2p3 is shown in Fig. 6.7c at 133.2 eV. The presence of F1s is shown in Fig. 6.7d at 689.2 eV and Ce3d at 884.9 eV in Fig. 6.7e. In the XPS spectrum of cerium ions, the peaks of $Ce^{3+}3d_{3/2}$ (at binding energies of 900.7 and 907.8 eV) are less stronger than $Ce^{3+}3d_{5/2}$ (883.5 and 886.9 eV) [8]. The estimated density of ions Ce^{3+} in the sample is 58% from the total volume, ions Ce^{4+} − 42%. This suggests that the Ce^{3+} ions are mostly present on the MFP's surface.

In summary, XRD, Raman, TEM, SEM-EDS and XPS confirm successful synthesis of MFP with CeO_2 coating.

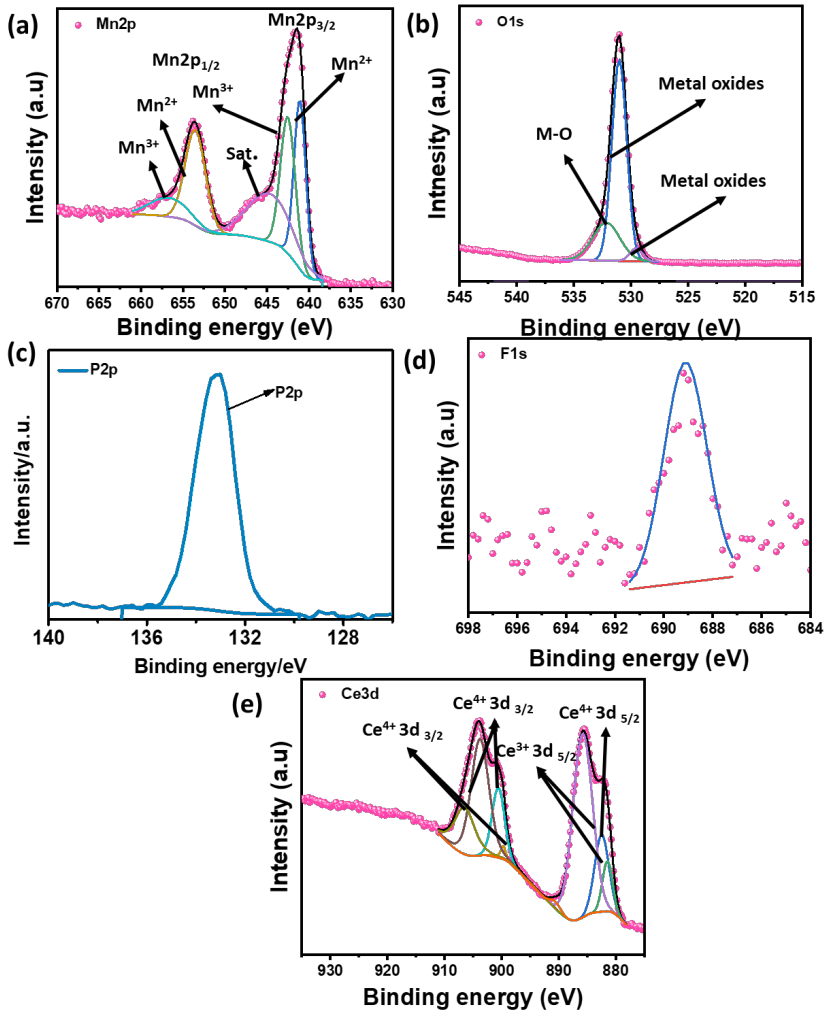

Fig. 6. 7. (a) Mn2p, (b) O1s, (c) P2p3, (d) F1s and (e) Ce3d spectra of MFP-CeO_2.

6.4. Electrochemical analysis of the electrode materials in alkaline and neutral electrolytes

6.4.1. Electrochemical analysis of MFP and MFP-CeO_2 in 6 M LiOH electrolyte

The electrochemical performance of MFP and MFP-CeO_2 were evaluated using CV and GCD in three electrode system using 6 M LiOH. The CV curves of MFP and MFP-CeO_2 across a potential range of 0.0 to 0.9 V at 30 mV s^{-1} is shown in Fig. 6.8a. The CV curve of MFP-CeO_2 show redox peaks due to the presence of manganese and CeO_2 [15,29]. The GCD curves of the electrode material were shown in Fig. 6.8b. It was found that MFP-CeO_2 had a significantly greater area under the CV curve than MFP and indicating that it had better charge storage properties. GCD curves corroborates the CV curves that MFP-CeO_2 has better charge storage due to higher discharge time than pristine MFP. The calculated specific capacitance of the

materials as a function of scan rate are 47.4, 36.8, 28.4, 24.3 and 15.8 F g^{-1} for MFP and 140.1, 118.9, 99.8, 91.2 and 70.7 F g^{-1} for MFP-CeO_2 at scan rate of 5, 10, 20, 30 and 50 mV s^{-1}, respectively. The improvement of current response after interaction of MFP with CeO_2 is due to the tuning of the oxygen vacancies in CeO_2 which implies a useful role as oxygen buffer. This indicates that CeO_2 improves the electron transfer rate and electron cloud which generates faradaic current across MFP as shown from the CV curves that the redox peaks of MFP are evoked after forming MFP-CeO_2 composite.

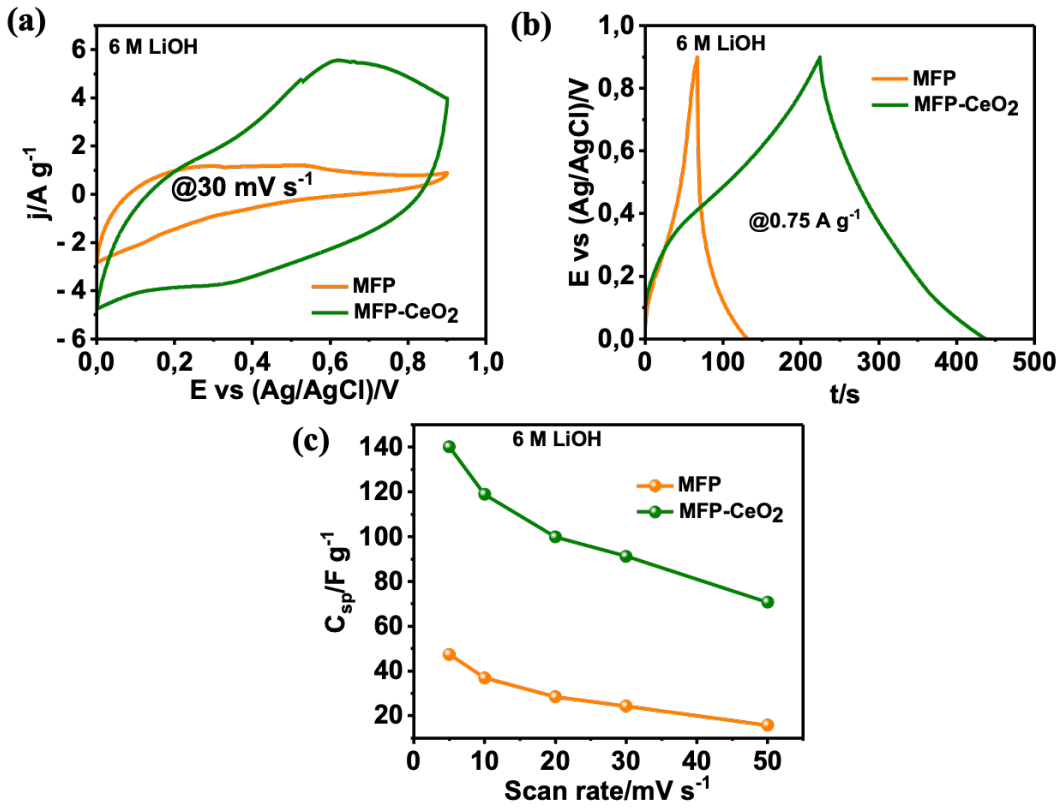

Fig. 6. 8. (a) CV, (b) GCD and (c) C_{sp} vs scan rate of three electrode system in 6 M LiOH.

6.4.2 Electrochemical analysis of MFP and MFP-CeO_2 in 6 M KOH electrolyte

Electrochemical analysis of MFP and MFP-CeO_2 were further evaluated in a three-electrode system using 6 M KOH electrolyte. The CV curves of the electrode materials are shown in Fig. 6.9a with prominent redox peaks due to the presence of Mn and CeO_2 on the surface of MFP. GCD curves are shown in Fig. 6.9b which show that MFP-CeO_2 has a higher discharge time than MFP which corroborates the CV curves with higher current response. These results clearly indicates that CeO_2 indeed improves the electrochemical properties of MFP due to its outstanding redox properties. Fig. 6.9c show the calculated capacitance of the electrode

materials at different scan rates of 5-50 mV s^{-1}. MFP-CeO_2 had the highest capacitance values of 209.1, 156.6, 119.9, 9, 105.9 and 91.2 F g^{-1} than MFP with capacitance values of 94.0, 57.3, 43.3, 38.7 and 18.8 F g^{-1}.

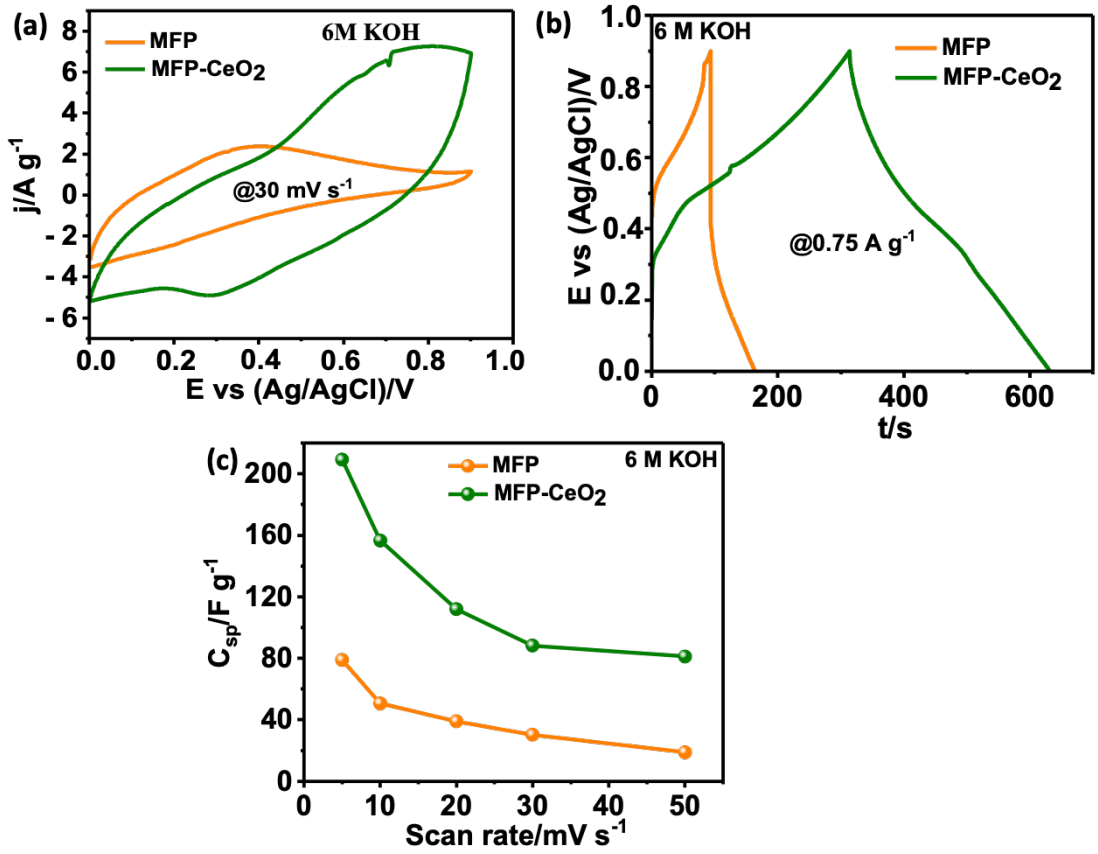

Fig. 6. 9. CV, GCD and Csp vs scan rates of three electrode system in 6 M KOH.

6.4.3 Comparison of 6 M LiOH and 6 M KOH electrolytes

CV and GCD curves (Fig. 6.10a, b) of MFP-CeO_2 are compared and the material show high area under the CV curve and higher discharge time in 6 M KOH. The capacitance values (Fig. 6.10c) are higher for 6 M than 6 M LiOH.

Alkali ions are strongly hydrated in aqueous conditions, and the sizes of their ion-hydrated complexes increase in the following order: $K^+ < Na^+ < Li^+$ (Table 1) [30]. As a result, alkali metal ions become more mobile in the following order: $Li^+ < Na^+ < K^+$. The best capacitance performance of MFP-CeO_2 electrodes in the KOH electrolyte is consistent with this.

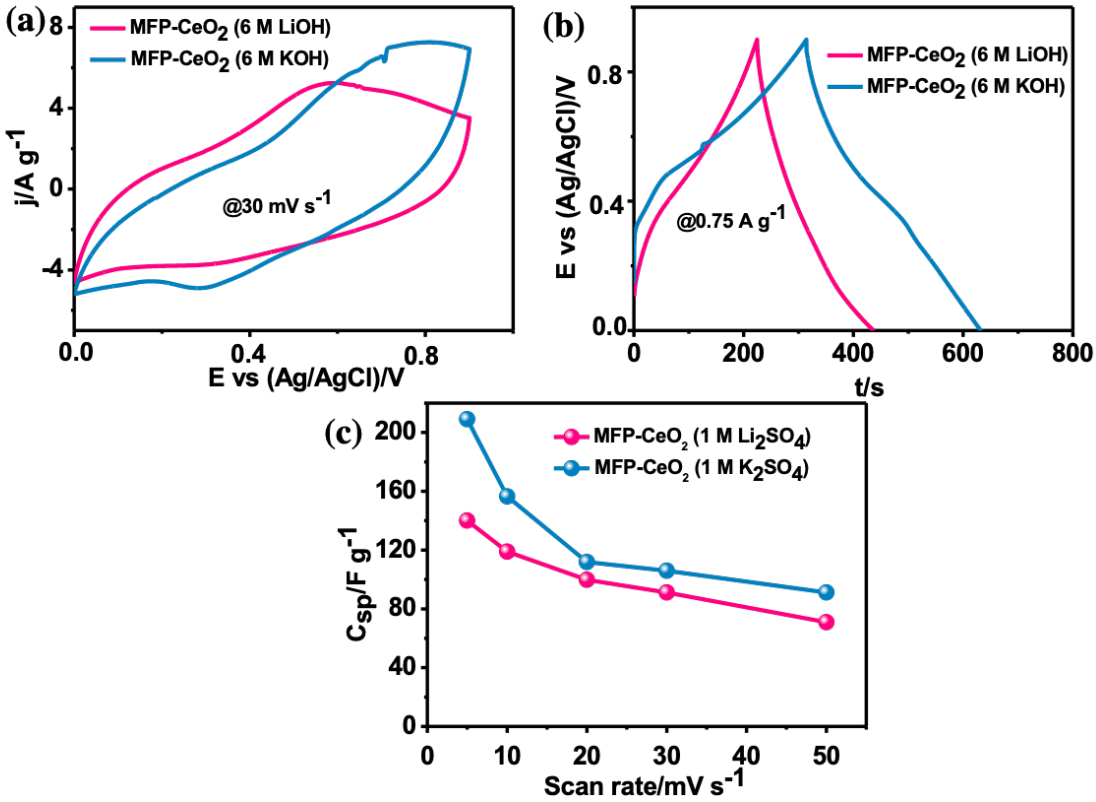

Fig. 6. 10. Comparison CV, GCD and Csp vs scan rate of MFP-CeO_2 in 6 M LiOH and 6 M KOH.

Table 6. 2. Size and conductivity of electrolytic bare and hydrated ions [30].

Type of Ion	Size of bare ion (Å)	Size of hydrated ions (Å)	Ionic conductivity (S cm^2mol^{-1})	MFP-CeO_2 Csp, Fg^{-1}
Li^+	0.60	3.82	38.69	140.1
Na^+	0.95	3.58	50.11	-

Type of Ion	Size of bare ion (Å)	Size of hydrated ions (Å)	Ionic conductivity (S cm^2mol^{-1})	MFP-CeO_2 Csp, Fg^{-1}
K^+	1.33	3.31	73.50	209.1

6.4.4. Electrochemical analysis of MFP and MFP-CeO_2 in 1 M Li_2SO_4 electrolyte

Electrochemical analysis of MFP and MFP-CeO_2 were evaluated in three electrode system in 1 M Li_2SO_4. CV curves of the electrode materials are shown in Fig. 6.11a with MFP-CeO_2 showing high current response compared to MFP and CeO_2. This show that the combination of both MFP and CeO_2 has an impact on each due to the bulk opening of MFP that allow access of electrolyte ions and the redox activities of CeO_2. The oxidation and reduction peaks in the anodic and cathodic regions in the Li_2SO_4 electrolyte are attributed to the reversible faradaic process between Mn^{2+}/Mn^{3+} anions, respectively (Fig. 6.11b). This show that the redox peaks of MFP-CeO_2 are both from MFP and CeO_2 [14]. GCD curves (Fig. 6.11c) show that MFP-CeO_2 performs better with a high discharge time which support the CV data. The CV and GCD curves show that incorporating CeO_2 to MFP also improves the electrochemical voltage window which is needed for energy storage. The calculated capacitance are shown in Fig. 6.8d which indicates that charge storage was higher in MFP-CeO_2 from 5-50 mV s^{-1} with high capacitance values of 51.6 F g^{-1} at 5 mV s^{-1} than MFP with 27.1 F g^{-1} and CeO_2 with 5.6 F g^{-1}.

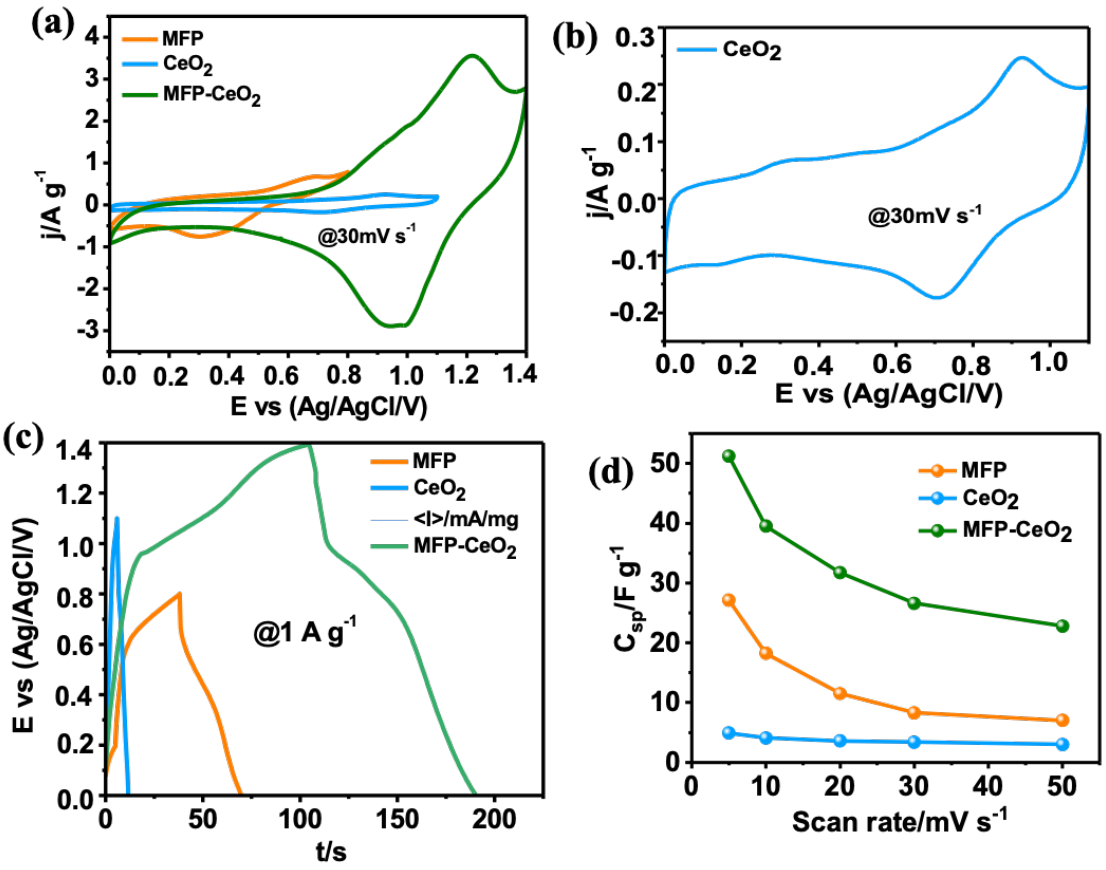

Fig. 6. 11. CV curves (a,b), GCD (c) and Csp vs scan rate for MFP, CeO_2 and MFP-CeO_2 in 1 M Li_2SO_4.

6.4.5. Electrochemical analysis of MFP and MFP-CeO_2 in 1 M K_2SO_4 electrolyte

Electrochemical analysis of MFP and MFP-CeO_2 were evaluated in a three-electrode system using 1 M K_2SO_4. The CV and GCD curves (Fig. 6.12a, b) of the materials were compared and MFP-CeO_2 showed high current response and high discharge time than MFP indicating high charge storage. Again, MFP-CeO_2 showed higher capacitance values of 98.9, 79.4, 86.7, 70.9 and 60.3 F g^{-1} than MFP with capacitance values of 43.75, 33.9, 26.9, 23.3 and 19.9 F g^{-1} from 5-50 mV s^{-1}. These results indicate that CeO_2 play a huge role in improving the charge storage of pristine MFP due to the fluctuation of oxidation state between 3^+ and 4^+, which can aid superconductivity. Again, the coating of CeO_2 on pristine MFP improves the 'sleeping' triplite material as seen from CV and GCD curves. It is suggested that CeO_2 and MnO_2 have a synergistic impact. The CeO_2 cores serve as an accelerator during the electrochemical test. Due to the necessary potential difference, CeO_2 and manganese (Mn) release their electrons simultaneously throughout the oxidation process. However, CeO_2 is easily oxidized and

reduced throughout the oxidation-reduction process due to its high activity. As a result, CeO_2 continuously depopulate electrons from Mn, increasing the degree of oxidation and improving electrochemical performance.

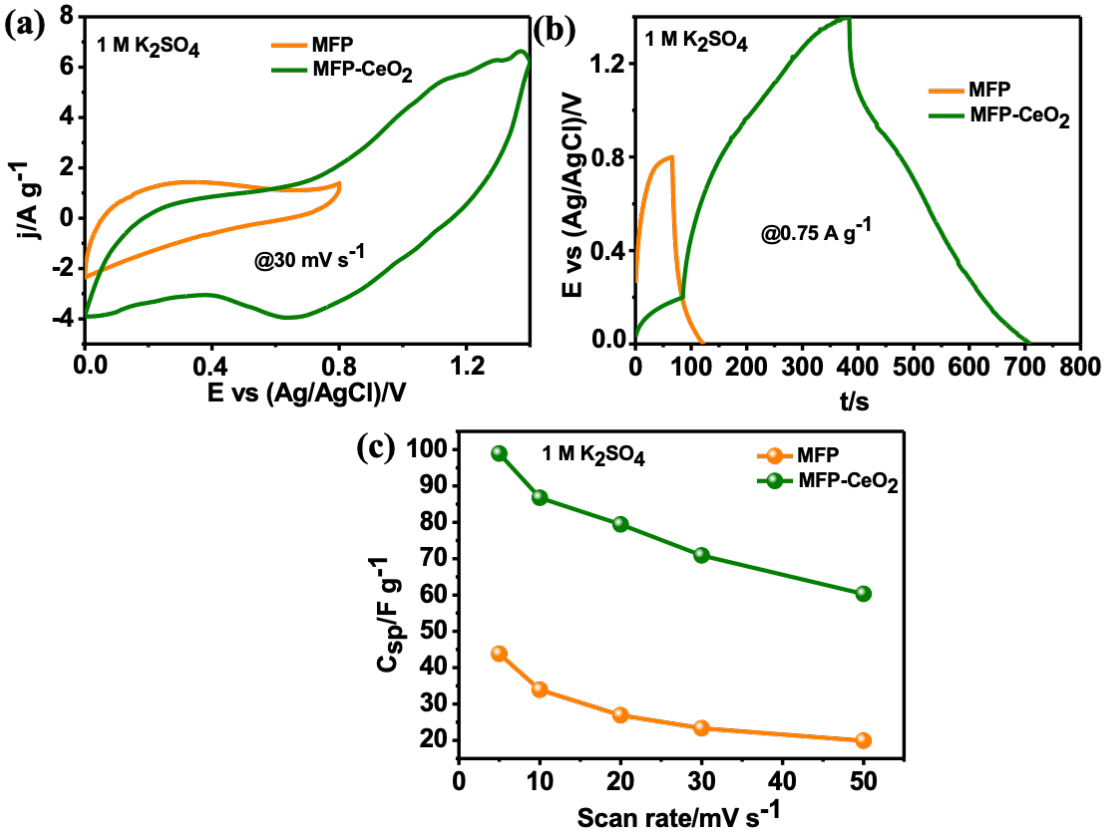

Fig. 6. 12. CV (a), GCD (b) curves and C_{sp} vs scan rate of MFP and MFP-CeO_2 in three electrode system using 1 M K_2SO_4.

6.4.6. Comparison of Li_2SO_4 and K_2SO_4 electrolytes

CV and GCD curves of MFP-CeO_2 in 1 M Li_2SO_4 and 1 M K_2SO_4 were compared in Fig. 6.13a,b. The CV curves in 1 M K_2SO_4 show higher current response than in 1 M Li_2SO_4. Also, the GCD in 1 M K_2SO_4 show higher discharge current than in 1 M Li_2SO_4. The specific capacitance of MFP-CeO_2 in 1 M K_2SO_4 show higher capacitance values of 98.9 F g^{-1} at 5 mV s^{-1}n (Fig. 6.12c) than in 1 M Li_2SO_4 with capacitance value of 51.6 F g^{-1} (Fig. 6.11d). The higher capacitance values of MFP-CeO_2 in K_2SO_4 is due to the higher conductivity of K_2SO_4 than Li_2SO_4 as listed in Table 6.2.

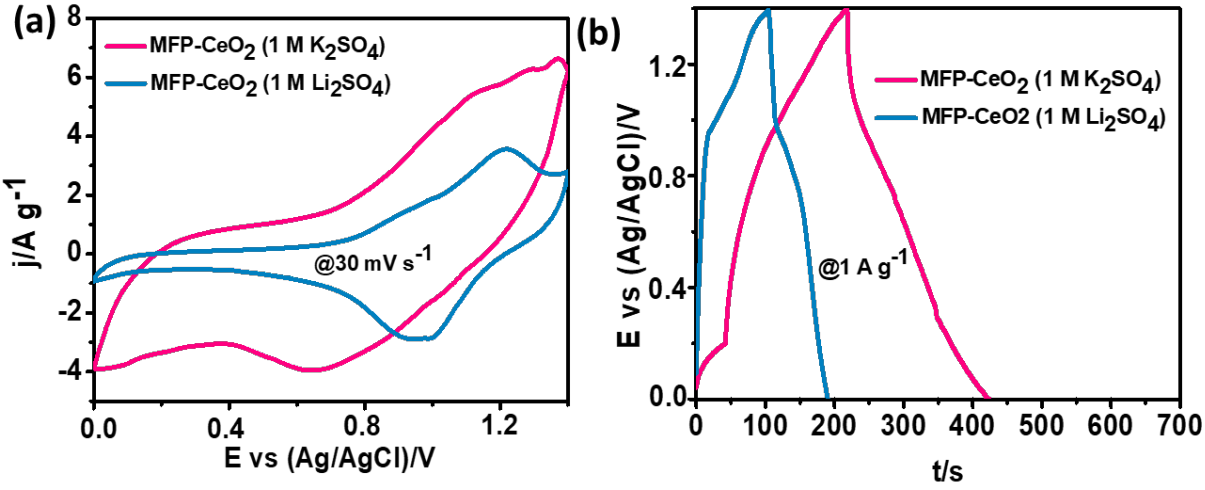

Fig. 6. 13. Comparison (a) CV and (b) of MFP-CeO_2 in 1 M K_2SO_4 and 1 M Li_2SO_4.

Comparing all the electrochemical results in three electrode system using alkaline and neutral electrolytes, the alkaline electrolytes have higher capacitance than neutral electrolytes due to the higher conductivity. However, MFP-CeO_2 in alkaline electrolytes have smaller voltage window (0.0-0.9 V) as compared to higher voltage window of 0-1.4 V in neutral electrolytes. The smaller voltage window of alkaline electrolytes is due to water decomposition occurring at 1.23 V as compared to neutral electrolytes that can be operated at higher voltage window due to H^- and OH^- concentration being lower, resulting in a potential shift of the hydrogen and oxygen evolution to a wider stable potential window, that increases the amount of energy storage [31].

Hence, asymmetric assembly was conducted in 1 M K_2SO_4 electrolyte.

6.4.7. Two electrode system of MFP-CeO_2 in 1 M K_2SO_4

Electrochemical performance of MFP-CeO_2 was evaluated in asymmetric SCs using CV, GCD and EIS in 1 M K_2SO_4 electrolyte. As shown in Fig. 6.14a, CV measurements were performed using a typical three-electrode setup to assess the electrochemical performance of both MFP-CeO_2 and N-ACs electrodes. The MFP-CeO_2 electrode demonstrate a mix of EDLC and pseudocapacitance behavior and was measured in the potential window of 0 to 1.4 V (vs. Ag/AgCl). An ideal EDLC characteristic is demonstrated for N-ACs by the electrode's contribution of the potential window from -0.8 to 0 V (vs. Ag/AgCl) with a symmetrical rectangular CV curve. The total mass ratios of the negative electrode and positive electrode

based on charge balance theory was ~3.1 mg. Fig. 6.14b,c displays the CV and GCD curves of the built MFP-CeO_2//N-ACs asymmetric cell at various potential windows (1.8-2.2 V).

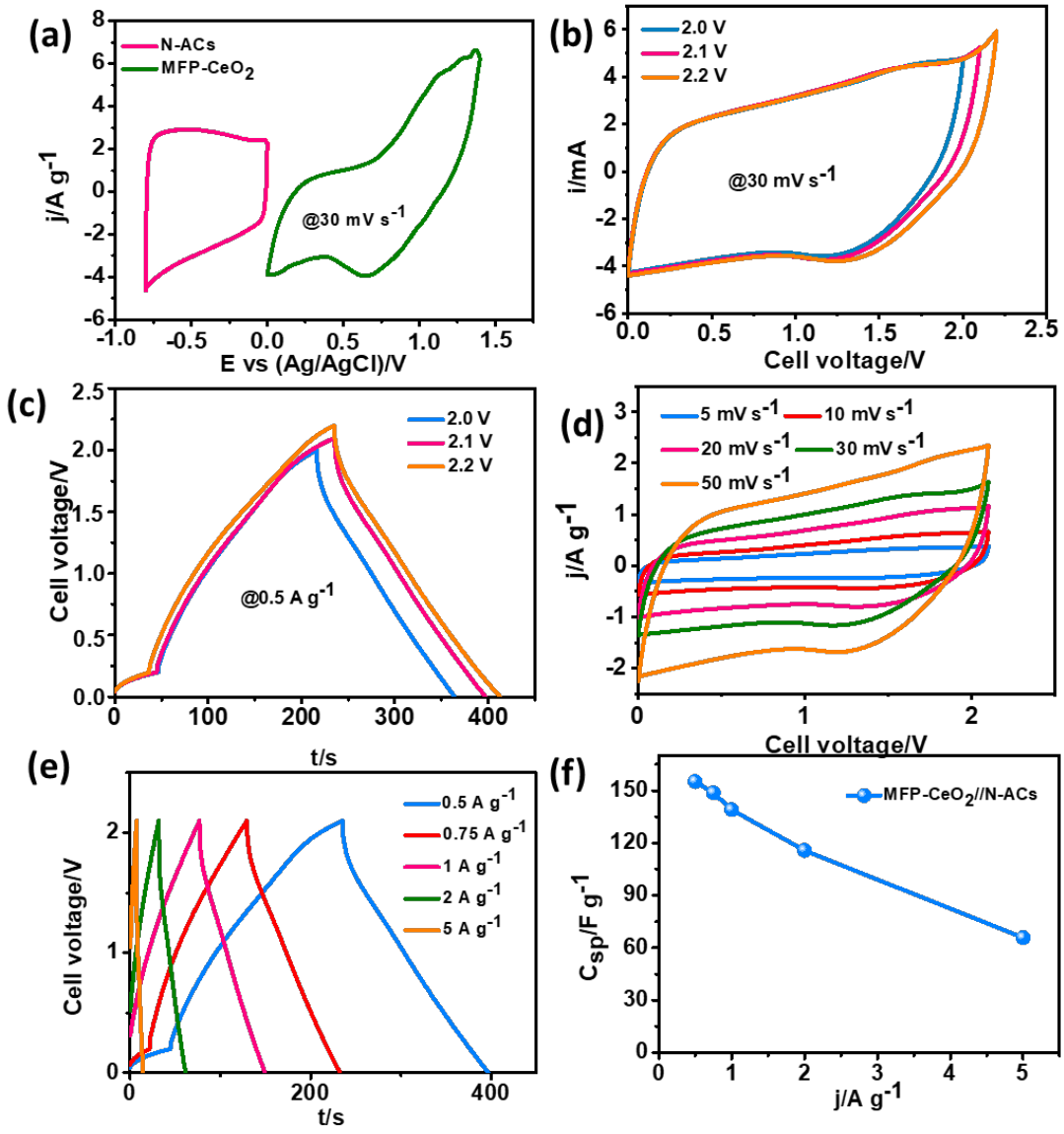

Fig. 6. 14. (a) CV, (b) CV tests, (c) GCD tests at different voltage window, (d) CV curves at different scan rates, (e) GCD and (f) C_{sp} VS current density of MFP-CeO_2//N-ACs in 1 M K_2SO_4.

It is evident that the asymmetric cell can function steadily down to a 2.1 V potential window. The CV curves were ran at different scan rates (Fig. 6.14d) and the CV shapes are preserved, which is consistent with good supercapacitive behaviour. The CV curves show a contribution of EDLCs and pseudocapacitor from Mn^{2+}/Mn^{3+} and CeO_2.

The CV curves show a pair of redox peaks which correspond to oxidation (1.75 V) and reduction (1.33 V) of nano CeO_2 ($Ce^{4+} \leftrightarrow Ce^{3+}$). The redox process is the basis of charge storage and this mechanism can be expressed by the following faradaic reaction:

$$Ce^{IV}O_2 + K^+ + e^- \leftrightarrow Ce^{III}O.OK^+ \quad (6.1)$$

When the electrode is submerged in the electrolyte, two additional mechanisms besides the redox process may be responsible for charge storage: The first sort of charge storage is the traditional EDLC type. This non-faradaic mechanism develops as a result of electrolyte ions building up at the electrode surface/electrolyte contact. The second is a different faradaic mechanism that results from the electrolyte cations' reversible electrochemical adsorption on the electrode surface.

This can be expressed as follows:

$$(CeO_2)surf + K^+ + e^- \leftrightarrow (CeO_2K^+)surf \quad (6.2)$$

Nevertheless, redox type charge storage (pseudocapacitance) is not limited to the electrode material's surfaces and can also take place in the sub-surface redox active sites [32]. The GCD curves in Fig. 6.14e were ran at different current densities from 0.5-5 A g^{-1} and they show redox behaviour mechanism which supports the CV data. The specific capacitance of the full cell as a function of current densities are shown in Fig. 6.14f with capacitance values of 155.2 F g^{-1} at 0.5 A g-^{1} to 65.9 F g^{-1} at 5 A g^{-1}. The specific capacitance decreases as the current densities decreases because the electrolyte ions are unable to permeate into the active material and can only reach the material's outer surface, which causes the specific capacitance to drop.

Using EIS measurements, the electrochemical characteristics of asymmetric supercapacitors was further examined, and the Nyquist plots are displayed in Fig. 6.15a with the EIS parameters in Table 6.3. The symbols Q represents charge, r for resistance and c for capacitance (see Fig. 6.15b). High frequency and low frequency zones make up the two regions in Nyquist plots. The semicircle arc and the intercept of the real axis (Z') at high frequency, respectively, represent the charge transfer resistance (R_{ct}) and equivalent series resistance (ESR). The R_s of the material is nearly the same before cycling (1.26 Ω) with Rs value of 1.27 Ω after cycling (Table 6.3). The R_{CT} of the material is lower after cycling (1.94 Ω) compared to before cycling (5.81 Ω). The smaller R_{CT} value after cycling is due to better contact between the electrolyte and electrode as cycling over time. Given that R_{int} is mainly due to the ohmic drop (IR drop) and diffusion rate of electrolytes ions the material after cycling gave R_{int} of 621.5 Ω which was

smaller than before cycling (834.3 Ω) due to the decrease in ohmic drop or more access of diffusion of electrolyte ions after many cycles. The increase in CPE values after cycling show that the material remains stable through charging and discharging.

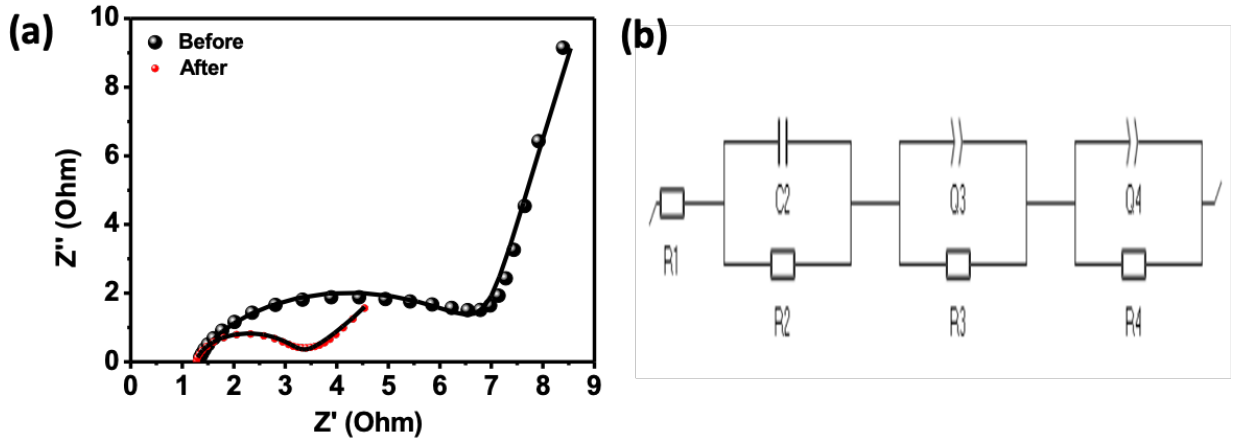

Fig. 6. 15. (a) Nyquist plots of MFP-CeO_2 obtained before and after 15 000 cycles with (b) electrical equivalent circuit used in the fitting of Nyquist plots.

Table 6. 3. EIS parameters of MFP-CeO_2//N-ACs before and after 15 000 cycles.

Parameters	Before	After
R_s (Ω)	1.26 ± 0.44	1.27± 0.23
R_{ct} (Ω)	5.81 ± 1.54	1.94± 0.65
R_{sei} (Ω)	55.04± 9.86	242.50± 10.67
R_{int} (Ω)	834.30 ± 24.36	621.50± 22..73
C_{dl} (mF)	7.18± 6.24	95.1± 24.3
CPE_{ct} (mF. s^(a-1))	0.15± 0.75	0.59± 0.92
a	0.76	0.88
CPE_{cs} (mF. s^(a-1))	5.72± 2.32	100.6± 21.08
a	0.85	0.98

MFP-CeO_2//N-ACs, seen in Figure 6.16a, was further tested for cyclic stability at a high current density of 5 A g^{-1} for up to 15 000 cycles. More than 60 % of the capacitance retention was seen after 15000 cycles, further demonstrating this material's supremacy in real-world high

power density applications. The excellent mechanical strength of the N-ACs, which can efficiently increase the cyclability throughout the charging/discharging process, is primarily responsible for the good long-term cycle stability of the device.

Fig. 6.16b show the Ragone plot (specific energy vs specific power) of MFP-CeO_2//N-ACs asymmetric cell which exhibits maximum specific energy of 23.8 Wh/kg with a specific power of 525.6 W kg^{-1} at a current density of 0.5 A g^{-1}. Furthermore, the specific energy obtained is superior as compared to the reported values for other Mn and CeO_2 based nanomaterials. For example, Nagamuthu *et al.* [33] reported energy density of 17.2 W h kg^{-1} on Mn based material with CeO_2 in 1 M Na_2SO_4 electrolyte with a maximum voltage of 2 V. Again, Ortega *et al.* [34] reported energy density of 17.9 Wh kg^{-1} using $LiFePO_4$//mesoporous carbon in 1 M LiTFSI. Furthermore, the inset in Fig. 6.16 show an LED bulb powered for more than 2 min 54 s.

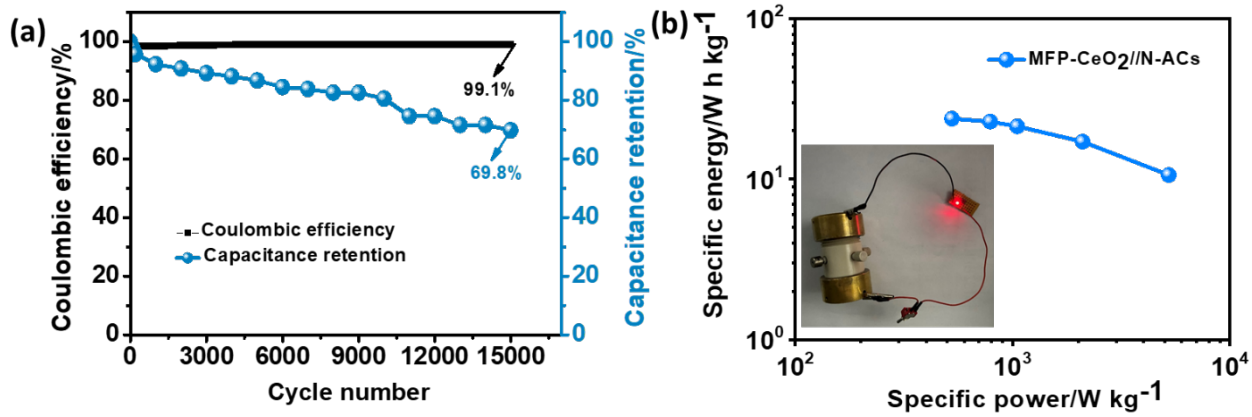

Fig. 6. 16. (a) Cyclic stability and (b) Ragone plot of MFP-CeO_2//N-ACs. The insets shows an image of a red LED powered by MFP-CeO_2//N-ACs electrode based device

Thus, our results were compared to other CeO_2 and manganese-based materials as shown in Table 6.4.

Table 6. 4. Comparison energy density of various CeO_2 and Mn based materials in different electrolytes.

Type of material	Electrolyte	Cell voltage (V)	Current density (A/g)	Specific energy (Wh/kg)	Reference
MFP-CeO_2//N-ACs	1 M K_2SO_4	2.1	0.5	23.8	This study
CeO_2-$LaMnO_3$//ACs	1 M Na_2SO_4	2.0	1.0	17.2	[33]
$LiFePO_4$//mesoporous carbon	1 M LiTFSI	2.1	0.1	17.9	[34]
Mn_3O_4/Ni(OH)$_2$//AC	1 M KOH	1.6	0.5	15.3	[35]
CeO_2 nano wire@MnO_2 //AGO	1.0 M Na_2SO_4	2.0	0.5	27.5	[9]

6.5. Conclusions

In conclusion, an effective positive electrode for an asymmetric supercapacitor was created using MFP-CeO_2. The asymmetric device creates a strong synergistic effect that significantly improved its electrochemical performance by combining with N-ACs as a negative electrode. The very porous shape of N-ACs and the well-adhered coating of CeO_2 on the surface of MFP were advantageous in facilitating easy ion-diffusion paths at the electrolyte/electrode contact, which can boost specific capacitance. The MFP-CeO_2//N-ACs had good cycling stability (69.8%) after 15 000 cycles and could function reversibly at a maximum voltage of 2.1 V.

Additionally, it has a low Rct and a high specific energy of 23.8 Wh/kg at a specific power of 525.6 W/kg. These remarkable results demonstrate the significant potential for developing high-performance supercapacitors with MFP-CeO_2.

References

[1] S. Ishimoto, Y. Asakawa, M. Shinya, K. Naoi, Degradation Responses of Activated-Carbon-Based EDLCs for Higher Voltage Operation and Their Factors, J Electrochem Soc. 156 (2009) A563.

[2] F. Zhan, H. Wang, Q. He, W. Xu, J. Chen, X. Ren, H. Wang, S. Liu, M. Han, Y. Yamauchi, L. Chen, Metal-organic frameworks and their derivatives for metal-ion (Li, Na, K and Zn) hybrid capacitors, Chem Sci. 13 (2022) 11981–12015.

[3] J. Zhang, Y. Cui, G. Shan, Metal oxide nanomaterials for pseudocapacitors, 2017.

[4] B. Li, F. Dai, Q. Xiao, L. Yang, J. Shen, C. Zhang, M. Cai, Nitrogen-doped activated carbon for a high energy hybrid supercapacitor, Energy Environ Sci. 9 (2016) 102–106.

[5] O.K. Oyeniran, H. Pretoria, Synthesis and characterization of carbon-based nanostructured material electrodes for designing novel hybrid supercapacitors, 2018.

[6] J. Yang, K. Qiu, Development of high surface area mesoporous activated carbons from herb residues, Chemical Engineering Journal. 167 (2011) 148–154.

[7] A. Rashid, S. Mondal, P. Ghosh, Development and Application of Ruthenium(II) and Iridium(III) Based Complexes for Anion Sensing, Molecules. 28 (2023).

[8] N. Ahmad, A.A. Alghamdi, H.A. Al-Abdulkarim, G.M. Mustafa, N. Baghdadi, F.A. Alharthi, Structural, morphological, and electrochemical performance of CeO2/NiO nanocomposite for supercapacitor applications, Applied Sciences (Switzerland). 11 (2021) 1–12.

[9] S.J. Zhu, J.Q. Jia, T. Wang, D. Zhao, J. Yang, F. Dong, Z.G. Shang, Y.X. Zhang, Rational design of octahedron and nanowire CeO2@MnO2 core-shell heterostructures with outstanding rate capability for asymmetric supercapacitors, Chemical Communications. 51 (2015) 14840–14843.

[10] E.M. Abebe, M. Ujihara, Influence of Temperature on ZnO/Co3O4Nanocomposites for High Energy Storage Supercapacitors, ACS Omega. 6 (2021) 23750–23763.

[11] S. Britto, V. Ramasamy, P. Murugesan, B. Neppolian, T. Kavinkumar, Graphene based ceria nanocomposite synthesized by hydrothermal method for enhanced supercapacitor performance, Diam Relat Mater. 105 (2020).

[12] Y. Luo, T. Yang, Q. Zhao, M. Zhang, CeO2/CNTs hybrid with high performance as electrode materials for supercapacitor, J Alloys Compd. 729 (2017) 64–70.

[13] T. Brezesinski, J. Wang, R. Senter, K. Brezesinski, B. Dunn, S.H. Tolbert, On the correlation between mechanical flexibility, nanoscale structure, and charge storage in periodic mesoporous CeO2 thin films, in: ACS Nano, 2010: pp. 967–977.

[14] A.S. Dezfuli, M.R. Ganjali, H.R. Naderi, P. Norouzi, A high performance supercapacitor based on a ceria/graphene nanocomposite synthesized by a facile sonochemical method, RSC Adv. 5 (2015) 46050–46058.

[15] A. Jeyaranjan, Cerium Oxide based Nanocomposites for Supercapacitors, 2020.

[16] F. Béguin, V. Presser, A. Balducci, E. Frackowiak, Carbons and electrolytes for advanced supercapacitors, Advanced Materials. 26 (2014) 2219–2251.

[17] K. Fic, G. Lota, M. Meller, E. Frackowiak, Novel insight into neutral medium as electrolyte for high-voltage supercapacitors, Energy Environ Sci. 5 (2012) 5842–5850.

[18] E. Zhen, J. Jiang, C. Lv, X. Huang, H. Xu, H. Dou, X. Zhang, Effects of binder content on low-cost solvent-free electrodes made by dry-spraying manufacturing for lithium-ion batteries, J Power Sources. 515 (2021).

[19] S. Hunpratub, T. Chullaphan, S. Chumpolkulwong, N. Chanlek, S. Phokha, Characterization and electrochemical properties of Carbon/CeO2 composites prepared using a hydrothermal method, Mater Chem Phys. 303 (2023).

[20] C. Pan, D. Zhang, L. Shi, J. Fang, Template-free synthesis, controlled conversion, and CO oxidation properties of CeO2 nanorods, nanotubes, nanowires, and nanocubes, Eur J Inorg Chem. (2008) 2429–2436.

[21] L. Yan, R. Yu, J. Chen, X. Xing, Template-free hydrothermal synthesis of CeO2 nano-octahedrons and nanorods: Investigation of the morphology evolution, Cryst Growth Des. 8 (2008) 1474–1477.

[22] Z. Ji, X. Wang, H. Zhang, S. Lin, H. Meng, B. Sun, S. George, T. Xia, A.E. Nel, J.I. Zink, Designed synthesis of CeO 2 nanorods and nanowires for studying toxicological effects of high aspect ratio nanomaterials, ACS Nano. 6 (2012) 5366–5380.

[23] H. Li, Y. Qu, X. Zhang, The gas sensor utilizing CeO2 nanorods for the low temperature detection of hydrogen, Inorg Chem Commun. 130 (2021).

[24] Y. Ono, H. Fujii, Low-temperature synthesis of cerium oxide nanorods and their suppressive effect on photocatalysis of titanium dioxide, Ceram Int. 41 (2015) 15231–15234.

[25] P.W. Menezes, A. Indra, V. Gutkin, M. Driess, Boosting electrochemical water oxidation through replacement of Oh Co sites in cobalt oxide spinel with manganese, Chemical Communications. 53 (2017) 8018–8021.

[26] N. Nzimande, A. Haruna, P. Mwonga, B. Rasche, F. Cummings, K.I. Ozoemena, Ceria-Spiderweb Nanosheets Unlock the Energy-Storage Properties in the "Sleeping" Triplite (Mn2(PO4)F). ACS Appl. Energy Mater. 4 (2021) 13085-13097.

[27] M.A. Langell, C.W. Hutchings, G.A. Carson, M.H. Nassir, High resolution electron energy loss spectroscopy of MnO(100) and oxidized MnO(100), Journal of Vacuum Science & Technology A: Vacuum, Surfaces, and Films. 14 (1996) 1656–1661.

[28] R. Tholkappiyan, A.N. Naveen, K. Vishista, F. Hamed, Investigation on the electrochemical performance of hausmannite Mn3O4 nanoparticles by ultrasonic irradiation assisted co-precipitation method for supercapacitor electrodes, Journal of Taibah University for Science. 12 (2018) 669–677.

[29] R. Kumar, A. Agrawal, R.K. Nagarale, A. Sharma, High Performance Supercapacitors from Novel Metal-Doped Ceria-Decorated Aminated Graphene, Journal of Physical Chemistry C. 120 (2016) 3107–3116.

[30] C. Zhong, Y. Deng, W. Hu, J. Qiao, L. Zhang, J. Zhang, A review of electrolyte materials and compositions for electrochemical supercapacitors, Chem Soc Rev. 44 (2015) 7484–7539.

[31] B. Shaku, T.P. Mofokeng, N.J. Coville, K.I. Ozoemena, M.S. Maubane-Nkadimeng, Biomass valorisation of marula nutshell waste into nitrogen-doped activated carbon for use in high performance supercapacitors, Electrochim Acta. 442 (2023).

[32] T. Brezesinski, J. Wang, R. Senter, K. Brezesinski, B. Dunn, S.H. Tolbert, On the correlation between mechanical flexibility, nanoscale structure, and charge storage in periodic mesoporous CeO2 thin films, in: ACS Nano, 2010: pp. 967–977.

[33] S. Nagamuthu, S. Vijayakumar, K.S. Ryu, Cerium oxide mixed LaMnO3 nanoparticles as the negative electrode for aqueous asymmetric supercapacitor devices, Mater Chem Phys. 199 (2017) 543–551.

[34] P.F.R. Ortega, G.A. Dos Santos Junior, L.A. Montoro, G.G. Silva, C. Blanco, R. Santamaría, R.L. Lavall, LiFePO4/Mesoporous Carbon Hybrid Supercapacitor Based on LiTFSI/Imidazolium Ionic Liquid Electrolyte, Journal of Physical Chemistry C. 122 (2018) 1456–1465.

[35] Q.Q. He, H.Y. Wang, N. Lun, Y.X. Qi, J.R. Liu, J.K. Feng, J. Qiu, Y.J. Bai, Fabricating a Mn3O4/Ni(OH)2 Nanocomposite by Water-Boiling Treatment for Use in Asymmetric Supercapacitors as an Electrode Material, ACS Sustain Chem Eng. 6 (2018) 15688–15696.

CHAPTER 7

7. Conclusions and Recommendations

7.1. Conclusions

In this study, nitrogen-doped activated carbons was synthesised and characterised to serve as a electrode material for symmetric and asymmetric supercapacitor. The research focused on enhancing the performance of hybrid supercapacitors by combining N-ACs EDLCs with pseudocapacitive (K^+/MFP, Li^+/MFP and MFP-CeO_2) materials. The research included two main components: (i) synthesis of nitrogen-doped ACs for improved symmetric supercapacitor performance in alkaline and neutral electrolyte; (ii) the synthesis and characterization of K^+/MFP, Li^+/MFP and MFP-CeO_2 cathode material for hybrid supercapacitors. Investigations into the structural, morphological, porosity, and compositional characteristics of the as-synthesised materials were conducted using X-ray powder diffraction (XPD), Raman spectroscopy, scanning electron microscopy (SEM), transmission electron microscopy (TEM), Brunauer-Emmett-Teller (BET) analysis, and X-ray photoelectron spectroscopy (XPS). Electrochemical properties of the as synthesized materials were evaluated by using cyclic voltammetry (CV), galvanostatic charge-discharge (GCD) and electrochemical impedence spectroscopy (EIS). The results of N-ACs in a symmetric system showed higher energy density of 17.7 Wh/kg in 2.5 M KNO_3 operated at 1.8 V. The material demonstrated practical application by pwering an LED bulb.

A novel potassium intercalation on manganese fluorophosphate (K^+/MFP) for asymmetric supercapacitors with high energy density of 26.9 Wh/kg in 1 M KNO_3 and high capacitance retention of 144.2% which show remarkable stability of the material was demonstrated.

Li^+/MFP was also successfully synthesised and applied in asymmetric supercapacitors as a cathode material with N-ACs as an anode material. The asymmetric system gave energy density of 18.8 Wh/kg.

A composite of MFP-CeO_2 was synthesised with rods formation of CeO_2 coated on MFP. CeO_2 showed improved capacitance when coated on MFP as compared to pristine MFP which indicated improved redox properties when introducing more oxygen vacancies. MFP-CeO_2 was used in asymmetric supercapacitor with N-ACs and this electrode material gave energy density of 23.8 V in 1 M K_2SO_4.

In summary, the development of nitrogen containing carbon nanostructures with superior properties, particularly as electrode materials, continue to grow. Biomass valorisation offer a facile route to produce nanostructured carbons in higher yields and their properties can be easily tailored, which makes them excellent candidates for multidisciplinary applications such as energy storage. On the other hand, manganese fluorophosphates materials containing increased interlayer spacing is another way of allowing more electrolyte diffusion for an increase in energy storage.

7.2. Recommendations for future work

- Investigation of different concentrations of KOH and LiOH for intercalation on MFP.
- Investigation of different percentages of CeO_2 for coating on MFP.
- Further study the structure of alkali intercalated MFP using other characterizations techniques.
- Study the alkali intercalated MFP with other anode materials in an asymmetric assembly for further increase of energy storage.

APPENDIX

Supplementary Information

Table S3. 1. Calculated %yield of activated carbons after KOH impregnation.

Type of material	Initial mass (m_i) (g)	Final mass (m_f) (%)
AMNW-0.5	3.0	43.3
AMNW-1	3.0	34.4
AMNW-2	3.0	25.0
AMNW-3	3.0	6.3

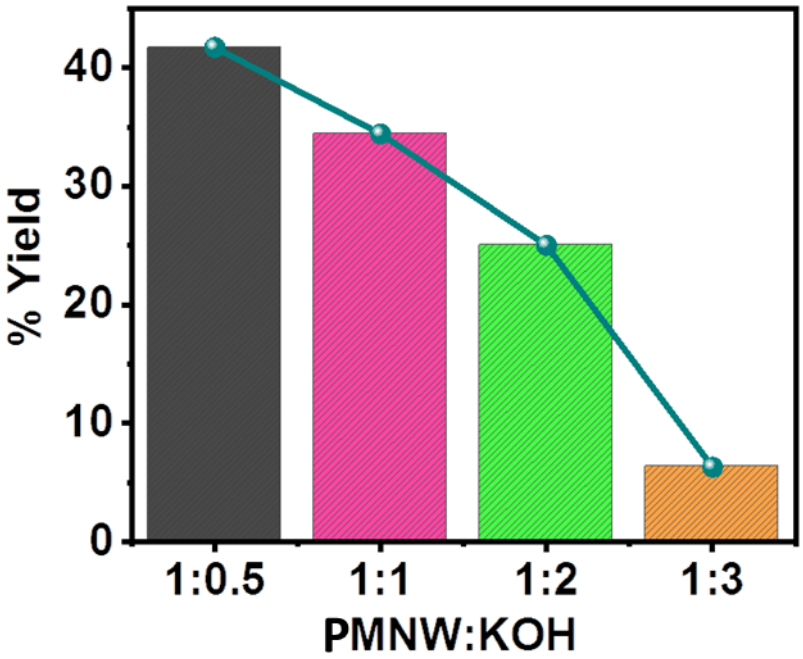

Fig. S3. 1: Effect on KOH ratio on the carbon yield obtained from marula nutshell waste

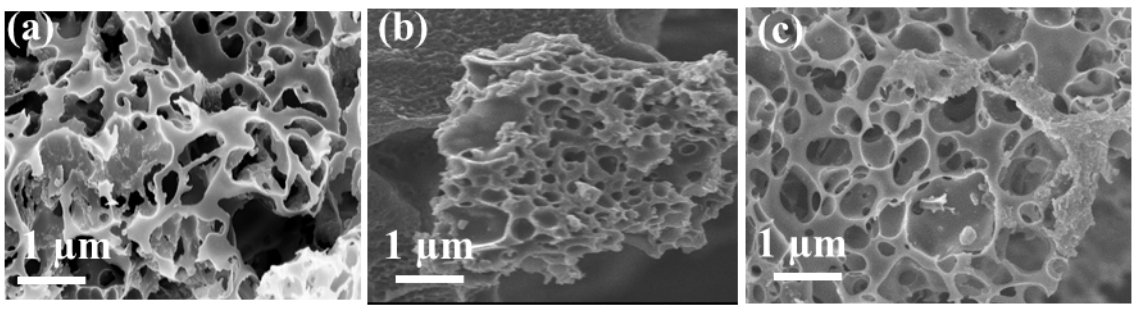

Fig. S3. 2. SEM images of (a) AMNW-0.5, (b) AMNW-1 and (c) AMNW-3.

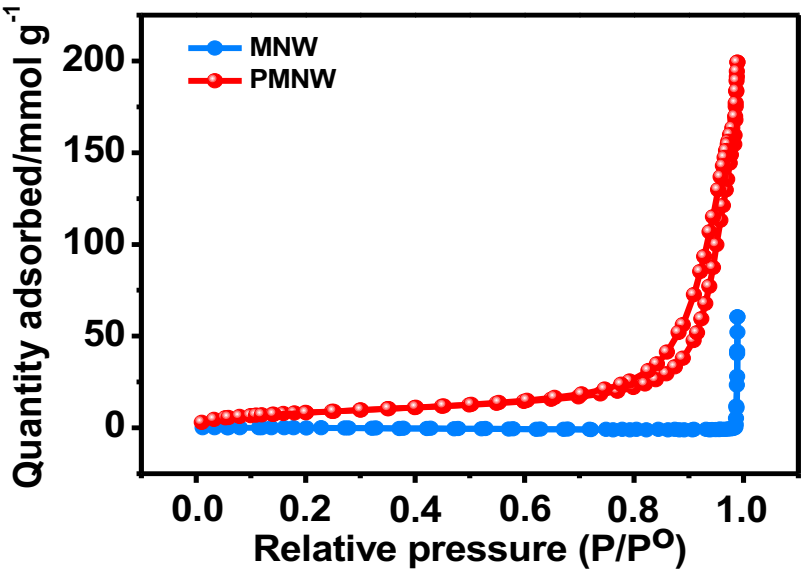

Fig S3. 3. N_2 adsorption-desorption of MNW and PMNW.

Table S3. 2. BET surface area of the pristine, pretreated activated and nitrogen doped marula nuts waste.

Type of material	BET Surface Area/m^2 g^{-1}	Micropore Surface Area/m^2 g^{-1}	Pore volume/cm^3 g^{-1}	Pore size/nm
MNW	0.011	-	0.08	165
PMNW	31.1	-	0.29	38.0
AMNW-0.5	1111	953	0.47	7.9
AMNW-1	1353	1025	0.65	3.3
AMNW-2	1266	1049	0.46	5.2
AMNW-3	1236	1029	0.39	8.9
N-ACs	1427	1012	0.31	2.6

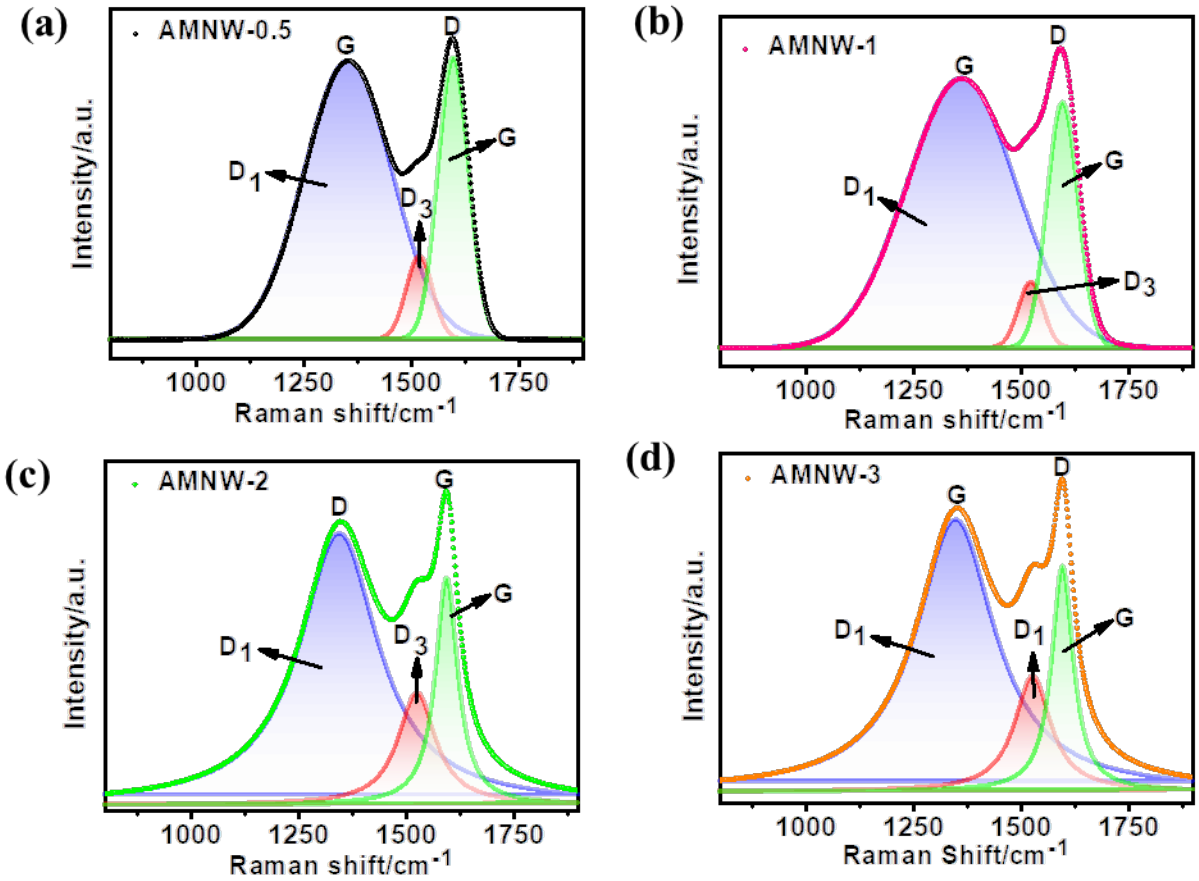

Fig. S3. 4. Deconvolution of (a-d) Raman spectra of activated carbons.

Table S3. 3. Raman data of activated carbons and nitrogen doped material.

Type of material	Raman shift/cm^{-1}		D_1/G
	D-band	G-band	
AMNW-0.5	1353.9	1598.9	2.9
AMNW-1	1348.2	1599.1	3.9
AMNW-2	1345.2	1595.5	4.3
AMNW-3	1348.7	1597.6	4.5
N-ACs	1348.0	1603.6	3.5

Table S3. 4. Summary of % concentration of bond types in the samples.

Sample	sp^2 C-C/sp^2 C-N	sp^3 C-C/sp^3 C-N	C-O	C=O	O-C=O/N-C=O	Pyri-N	Pyrr-N	Gra-N	Oxy-N	Chemi-N	O-C-O	O-C=O	Metal oxide
AMNW-2	52.7	26.4	7.0	8.8	5.1	1.2	5.4	93.4	-	-	51.3	33.2	15.5
N-ACs	31.4	18.9	13.9	14.5	21.4	22.9	31.8	13.3	11.2	20.9	11.5	88.5	

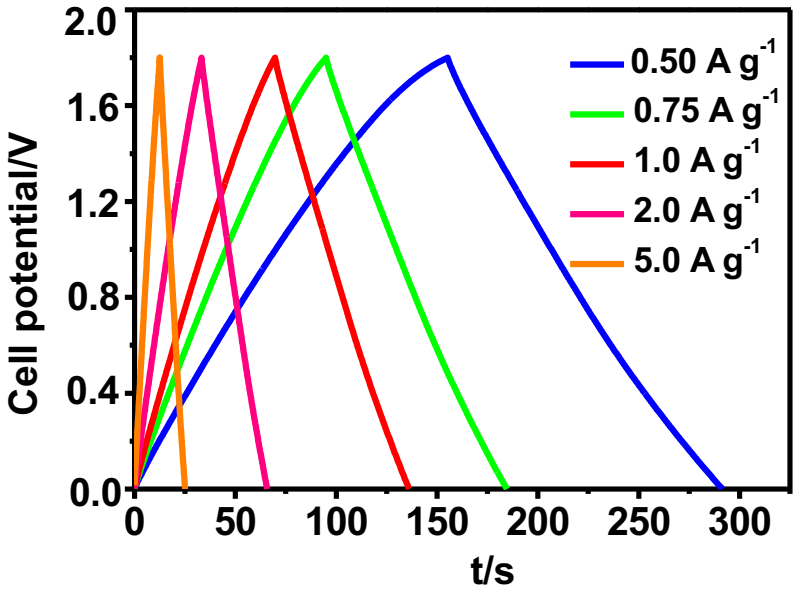

Fig. S3. 5. GCD of N-ACs in 2.5 m KNO_3.

Table S3. 5. Capacitance (F/g) of the materials in 6 M KOH and 2.5 M KNO_3.

Materials	6 M KOH electrolyte				
	Capacitance/F g^{-1} at different current densities				
	0.5 A g^{-1}	0.75 A g^{-1}	1.0 A g^{-1}	2.0 A g^{-1}	5.0 A g^{-1}
AMNW-0.5	85.3	78.6	75.8	70.0	60.8
AMNW-1	155.7	149.3	145.4	140.0	133.6
AMNW-2	292.2	272.4	259.8	242.0	229.1
AMNW-3	139.7	137.0	135.1	130.8	121.8

N-ACs	358.2	315.0	290.1	259.4	230.7

2.5 M KNO_3 electrolyte					
	Capacitance/F g^{-1} at different current densities				
	0.5 A g^{-1}	0.75 A g^{-1}	1.0 A g^{-1}	2.0 A g^{-1}	5.0 A g^{-1}
AMNW-0.5	41.1	38.5	37.7	35.5	31.8
AMNW-1	129.7	117.3	113.6	105.0	95.4
AMNW-2	193.4	175.3	168.6	153.6	124.7
AMNW-3	115.3	107.5	102.5	95.6	88.8
N-ACs	240.1	223.8	217.6	202.6	191.4

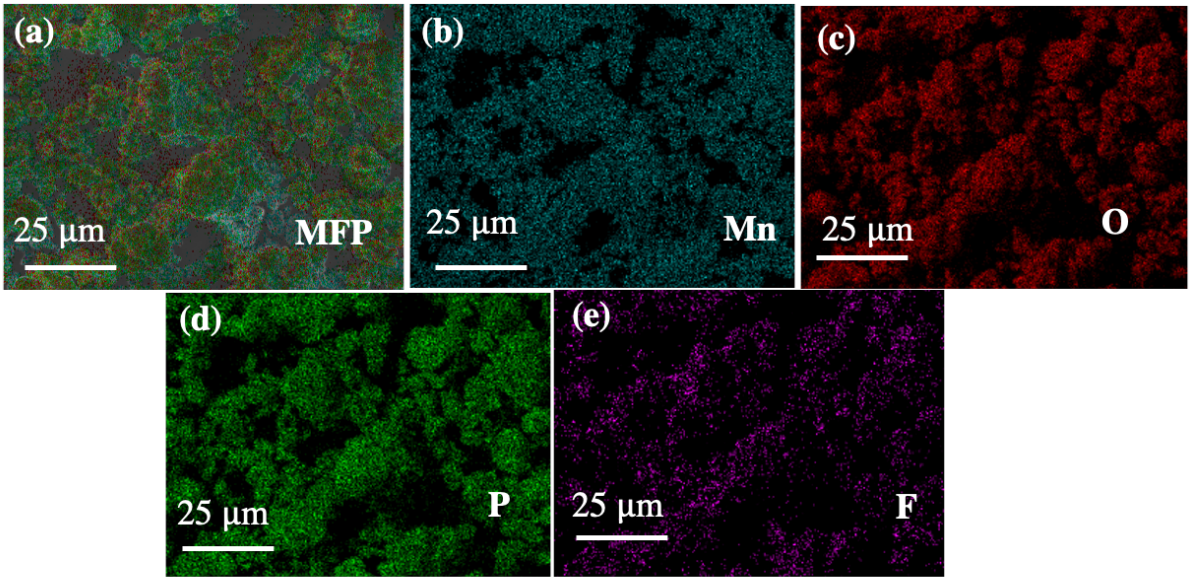

Fig. S4. 1. SEM-EDS mapping (a-e) of MFP.

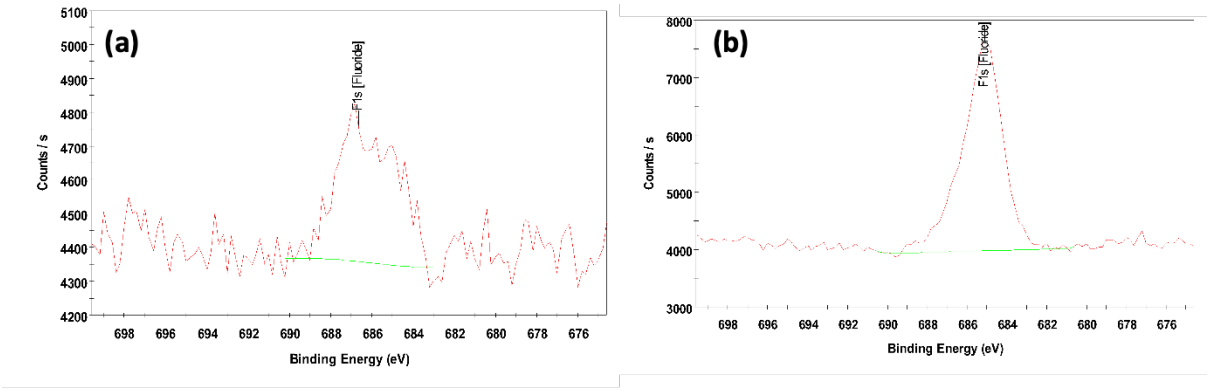

Fig. S4. 2. (a) F1s of MFP and (b) F1s of K^+/MFP.